A MODEL-BASED CORTICAL PARCELLATION SCHEME FOR HIGH-RESOLUTION 7 TESLA MRI DATA

OTTO VON GUERICKE UNIVERSITÄT MAGDEBURG

INF FAKULTÄT FÜR INFORMATIK

A MODEL-BASED CORTICAL PARCELLATION SCHEME FOR HIGH-RESOLUTION 7 TESLA MRI DATA

Dissertation
zur Erlangung des akademischen Grads
Doktoringenieurin (Dr.-Ing.)

angefertigt am Max-Planck-Institut für Kognitions- und Neurowissenschaften, Leipzig

angenommen durch die Fakultät für Informatik der Otto-von-Guericke Universität Magdeburg

von Dipl.-Ing. Juliane Dinse
geb. am 04.08.1985 in Wolgast

Gutachterinnen/Gutachter:
Prof. Dr.-Ing. Bernhard Preim
Prof. Dr.-Ing. Dorit Merhof
Prof. Dr. habil. Guido Gerig

Magdeburg, 30. Juli 2015

Wenn du über irgendeine Frage im Zweifel bist und still hältst und zwingst dich nicht zu glauben, dass etwas Unerwiesenes bewiesen sei, und du versuchst nicht, etwas zu verwerfen, oder als falsch zu erklären, wovon das Gegenteil nicht bewiesen ist, und du trachtest nicht, das zu erkennen, was du nicht zu erkennen vermagst, so hast du damit bereits die menschliche Vollkommenheit erreicht.

— MOSES MAIMONIDES (1135 - 1204)

Ich widme diese Arbeit meiner Mutter und meiner Oma, weil sie immer für mich da sind und sie mir gezeigt haben, dass es im Leben nicht darauf ankommt, was man hat, sondern was man daraus macht.

EHRENERKLÄRUNG

Ich versichere hiermit, dass ich die vorliegende Arbeit ohne unzulässige Hilfe Dritter und ohne Benutzung anderer als der angegebenen Hilfsmittel angefertigt habe; verwendete fremde und eigene Quellen sind als solche kenntlich gemacht. Insbesondere habe ich nicht die Hilfe eines kommerziellen Promotionsberaters in Anspruch genommen. Dritte haben von mir weder unmittelbar noch mittelbar geldwerte Leistungen für Arbeiten erhalten, die im Zusammenhang mit dem Inhalt der vorgelegten Dissertation stehen. Ich habe insbesondere nicht wissentlich:

- Ergebnisse erfunden oder widersprüchliche Ergebnisse verschwiegen,
- statistische Verfahren absichtlich missbraucht, um Daten in ungerechtfertigter Weise zu interpretieren,
- fremde Ergebnisse oder Veröffentlichungen plagiiert,
- fremde Forschungsergebnisse verzerrt widergegeben.

Mir ist bekannt, dass Verstöße gegen das Urheberrecht Unterlassungs- und Schadensersatzansprüche des Urhebers sowie eine strafrechtliche Ahndung durch die Strafverfolgungsbehörden begründen kann. Die Arbeit wurde bisher weder im Inland noch im Ausland in gleicher oder ähnlicher Form als Dissertation eingereicht und ist als Ganzes auch noch nicht veröffentlicht.

Magdeburg, 30. Juli 2015

Juliane Dinse

ABSTRACT

This thesis originates from the increasing interest in advanced methods in brain segmentation and cortical architectural studies. The aim of the presented work is to bridge the gap between the cortical microanatomy revealed by classical histology and the macroanatomy visible in Magnetic Resonance Imaging (MRI).

This thesis presents a novel approach to model laminar myelin patterns in the human cortex as measured using brain MRI on the basis of known cytoarchitecture. For the first time, it is possible to estimate intracortical contrast visible in quantitative ultra-high resolution MRI data in specific primary and secondary cytoarchitectonic areas. These estimated patterns are used in automated cortical parcellation and applied to study the quantitative T_1 values within the cortex. The presented technique reveals different area-specific signatures which may help to investigate the relationship between the distribution of cortical T_1 values and of cortical myelin in general. It may lead to a new discussion on the concordance of cyto- and myeloarchitectonic boundaries, given the absence of such concordance atlases.

The modelled myelin patterns are quantitatively compared with data from human ultra-high resolution in-vivo 7 Tesla brain MRI (19 subjects). For verification, the results are compared to one postmortem brain sample and its ex-vivo MRI and histological data. Additional experiments are carried out to investigate the discriminative power of such a model in future applications.

Details of the analysis pipeline are provided and discussed.

ZUSAMMENFASSUNG

Diese Arbeit ist aufgrund des steigenden Interesses sowohl an modernen und hochleistungsfähigen Segmentierungsmethoden für Gehirndaten als auch an Studien über den kortikalen Aufbau entstanden. Ziel ist es, die bestehende Lücke zwischen mikrozellulärer Anatomie, beschrieben durch Histologie, und makroskopischer Anatomie, gemessen mit MRT, zu schließen.

In dieser Arbeit wird ein neues Verfahren vorgestellt, welches MRT-relevante laminare Myelinmuster im menschlichen Kortex auf Grundlage von zytoarchitektonischem Wissen modelliert. Mit dieser Arbeit wird erstmals gezeigt, dass der in quantitativen hochaufgelösten MRT-Daten sichtbare intra-kortikale Kontrast in Primär- und Sekundärarealen abschätzbar ist. Die modellierten Muster werden für i) kortikale Parzellierungen sowie ii) der Analyse von kortikalen T_1 Relaxationszeiten im Kortex eingesetzt. Die vorgestellte Methodik lässt erste areal-spezifische Signaturen erkennen. Diese Signaturen erlauben es, die Beziehung zwischen der Verteilung der T_1 Relaxationszeiten im Kortex und der generellen Verteilung von Myelin im Kortex zu untersuchen. Die Ergebnisse dieser Arbeit erlauben neue Einblicke in der Überlappung von zytoarchitektonischen und myeloarchitektonischen arealen Grenzen. Atlanten, die diese Korrespondenzen beschreiben, sind gegenwärtig nicht existent.

Die Methodik wird auf hochaufgelösten 7 Tesla MRT-Daten von menschlichen Gehirnen (19 Probanden) quantitativ analysiert. Zur weiteren Prüfung wird die Methodik mit MRT- sowie Histologiedaten eines postmortalen Gewebeblockes verglichen. Zusätzlich durchgeführte Experimente zeigen das Differenzierungspotential einer solchen Methodik im Hinblick auf zukünftige Anwendungen.

Details zur Umsetzung und Implementierung werden intensiv beschrieben und diskutiert.

PUBLICATIONS

Main ideas and figures have appeared previously in the following publications (chronological order):

Juliane Dinse, Pablo Martin, Andreas Schäfer, Stefan Geyer, Robert Turner, and Pierre-Louis Bazin. *Quantifying differences between primary cortical areas in humans based on laminar profiles in in vivo MRI data*. In *Bildverarbeitung für die Medizin*, pages 39–44, 2013.

Miriam Waehnert, **Juliane Dinse**, Marcel Weiss, Markus Streicher, Phillip Waehnert, Stefan Geyer, Robert Turner, and Pierre-Louis Bazin. *Anatomically motivated modeling of cortical laminae*. In *NeuroImage*, 93, pages 210–220, 2013.

Pierre-Louis Bazin, Marcel Weiss, **Juliane Dinse**, Andreas Schäfer, Robert Trampel, Robert Turner. *A computational framework for ultra-high resolution cortical segmentation at 7 Tesla*. In *NeuroImage*, 93, pages 201–209, 2013.

Juliane Dinse, Miriam Waehnert, Christine Tardif, Andreas Schäfer, Stefan Geyer, Robert Turner, and Pierre-Louis Bazin. *A histology-based model of quantitative T1 contrast for in-vivo cortical parcellation of high-resolution 7 Tesla brain MR images*. In *Medical Image Computing and Computer Assisted Intervention (MICCAI)*, Part II, pages 51–58, Japan, 2013.

Christine Tardif, **Juliane Dinse**, Andreas Schäfer, Robert Turner, and Pierre-Louis Bazin. *Multi-modal surface-based alignment of cortical areas using intracortical T1 contrast*. In *Lecture Notes in Computer Science: Multimodal Brain Image Analysis*, 8159, pages 222–232, 2013.

Juliane Dinse, Nina Härtwich, Miriam Waehnert, Christine Tardif, Andreas Schäfer, Stefan Geyer, Bernhard Preim, Robert Turner, and Pierre-Louis Bazin. *A Cytoarchitecture-driven Myelin Model reveals Area-specific Signatures in Primary and Secondary Areas in Human Cortex using Ultra-High Resolution In-vivo Brain MRI*. In *NeuroImage*, 114, pages 71–87, 2015.

Christine Tardif, Andreas Schäfer, Miriam Waehnert, **Juliane Dinse**, Robert Turner, and Pierre-Louis Bazin. *Multi-contrast Multi-scale Surface Registration for Improved Alignment of Cortical Areas*. In *NeuroImage*, 111, pages 107–122, 2015.

Miriam Waehnert, **Juliane Dinse**, Andreas Schäfer, Stefan Geyer, Pierre-Louis Bazin, Robert Turner, and Christine Tardif. *A subject-specific 3D intracortical framework for in-vivo myeloarchitectonic analysis using high resolution quantitative MRI*. In *NeuroImage*, 2015 (under revision, 3rd revision cycle).

DANKSAGUNG

Eine Arbeit wie diese kann nur mit tatkräftigen Unterstützern entstehen.

Ich möchte mich ganz besonders bei Matthias bedanken, der mir stets den Rücken stärkte und darauf Acht gab, dass ich der Mensch bleibe, der ich bin. Außerdem möchte ich mich bei meiner Schwester Ulrike ganz lieb bedanken, für all die Momente, an denen sie an meiner Seite stand. Ein besonderer Dank gilt auch meiner wie Matthias' Familie, die einem Ende dieser Zeit mindestens genauso entgegenfiebern wie ich.

Ein herzlicher Dank geht an die Otto-von-Guericke Universität Magdeburg, allen voran an Prof. Bernhard Preim für seine ausgezeichnete fachliche wie auch persönliche Unterstützung. Du hast immer mit Rat und Tat geholfen und dir für all meine Belange Zeit genommen. Für die auftretenden Probleme stand deine Tür ganz weit offen. Außerdem möchte ich mich gerne bei Prof. Myra Spiliopoulou und ihr fachliches Feedback zum Thesis Proposal bedanken. Die Diskussionen haben dieser Arbeit viele interessante Aspekte gegeben. Zudem verdienen Petra Specht, Petra Schumann und Stefanie Quade vom Sekretariat des Instituts für Simulation und Grafik ein großes und vor allem herzliches Dankeschön.

Ich möchte mich hiermit auch bei meinen Kollegen am Max-Planck-Institut in Leipzig bedanken. Allen voran Prof. Robert Turner, der mir die Möglichkeit gab, meine Arbeit in seiner Abteilung Neurophysik bis Februar 2014 durchführen zu können. Zudem durfte ich meine Arbeiten international vorstellen und mein Netzwerk ausbauen. Ferner möchte ich mich bei Prof. Arno Villringer bedanken, der die Finanzierung meiner Arbeit nach Prof. Turners Emeritierung für mein drittes Jahr übernommen hat. Ich möchte darüber hinaus Pierre-Louis Bazin für das Ermöglichen dieser Arbeit danken sowie für die fachliche und technische Unterstützung. Außerdem möchte ich Miriam Wähnert für die gute Zusammenarbeit zu ihrem Projekt danken, welches Grundlage meiner Arbeit war. Ferner haben Prof. Rudolf Nieuwenhuys, Prof. Almut Schüz, sowie Dr. Bernhard Hellwig mit vielen spannenden Diskussionen und konstruktiver Kritik diese Arbeit mit ihren umfangreichen neuroanatomischen Erfahrungen bereichert.

Das Projekt wäre ohne Daten nur halb so viel wert. Aus diesem Grund geht ein großes Dankeschön an Andreas Schäfer für die strukturelle Datenerhebung und die Diskussionen, die mir einen grundlegenden Einblick in wesentliche MRT-Problematiken gegeben haben. Außerdem möchte ich mich bei Elisabeth Wladimirow und Domenica Wilfling für das Scannen und Rekrutieren weiterer Probanden bedanken. Ein besonderer Dank gilt Dr. Stefan Geyer, Marcel Weiss, Daniel Rose und speziell Katja Reimann für die tolle Unterstützung bei den postmortalen Gewebestudien. Ich möchte zudem Esther Kühn für die Nacherhebung der funktionellen MRT-Daten danken. Ein großer Dank gilt Enrico Reimer, für seine Geduld bei Rekonstruktions- und IT-Fragen.

Darüber hinaus haben Praktikanten das Projekt einzigartig unterstützt. Allen voran möchte ich Nina Härtwich und Pablo Martinez für ihren großen Beitrag zu den Experimenten danken. Weiterhin haben Paul Liebenow, Gabriela Mianowska

sowie Agnieszka Olbrich zahlreiche manuelle Segmentierungen auf Gehirndaten vorgenommen, die einen unschätzbaren Wert haben.

Zudem möchte ich gerne Marcus und Matthias Müller sowie Clemens Hentschke für die sehr guten Anmerkungen und Korrekturen danken, die diese Arbeit sicher noch ein Stück lesenswerter machen.

CONTENTS

ACRONYMS

ACA anterior cerebral artery

ACE Anatomically consistent Grey Matter Enhancement

AD Alzheimer's Disease

BOLD blood-oxygen-level dependent

CBF cerebral blood flow

CNR Contrast-to-Noise Ratio

CNS central nervous system

CSF cerebrospinal fluid

CT Computed Tomography

DTI Diffusion Tensor Imaging

EM expectation-maximisation

FCM Fuzzy C-means

FID free induction decay

FLASH Fast Low Flip-Angle Shot

fMRI functional Magnetic Resonance Imaging

FOV field-of-view

FWHM Full Width at Half Maximum

GM grey matter

GRE Gradient Echo

GVF gradient vector flow

HD Huntington's Disease

k-NN k-nearest neighbour

MCA middle cerebral artery

MGDM Multi-Compartment Geometric Deformable Model

MNI Montreal Neurological Institute

MPRAGE Magnetisation-Prepared Rapid Acquisition Gradient Echo

MP2RAGE Magnetisation-Prepared 2 Rapid Acquisition Gadient Echo

MRI Magnetic Resonance Imaging

PCA posterior cerebral artery

PET Positron Emission Tomography

PD Parkinson's Disease

PNS peripheral nervous system

PV partial voluming

RF radio frequency

ROI region of interest

ROIs regions of interest

rs-fMRI resting-state functional Magnetic Resonance Imaging

SNR Signal-to-Noise Ratio

SVM Support Vector Machine

WM white matter

1 MOTIVATION AND CONTRIBUTIONS

1.1 INTRODUCTION

The human brain is the most complex organ in the human body. It serves as the center of the nervous system and, as such, it is responsible for vital functioning of other organs. It is in close vicinity to primary organs associated with sensory functioning such as vision, hearing, taste, smell, and balance.

The **brain** mainly consists of two structures: the cerebrum, i. e., the superior-most region of the central nervous system (CNS) and the cerebellum, i. e., a smaller inferior region of the CNS. Cognitive processing of information occurs in the **cortex**, a 2–5 mm thick sheet representing the outer surface of the brain. Most research focuses on the cerebral cortex, i. e., the outer sheet of the cerebrum.

The cerebral cortex is the largest part of the cerebrum, consisting of millions of neuronal cells. These cells change in type, number and size through the depth of the cortex, providing a **layered structure**. Each cell is further associated with a single myelinated axon perpendicularly leaving the cortex and myelinated axonal collaterals running parallel within it. These parallel fiber structures change in number and size through the depth of the cortex, replicating a slightly similar layered pattern as represented by cells. The cortical architecture can thus be described by the **cytoarchitecture**, representing the cell organisation, or by the **myeloarchitecture**, representing the corresponding fiber organisation within the layers of the cortex.

It is known today that these representations change across the cortex, yielding a subdivision of the brain's surface into distinct areas. This is called a **cortical parcellation**. The structural subdivision into cortical areas is related to specific functional processing. Investigating these structure-function relationships led to a better understanding on how the brain works in tasked- or resting states and in healthy and diseased states.

The cytoarchitecture of the brain is well studied and cellular-based parcellations presented by different scientists are in agreement on the spatial arrangement of the cells. However, the research in the field of myeloarchitecture is difficult and parcellations based on the fiber distribution in the cortex are incomplete, inconclusive, or even contradictory.

But cyto- and myeloarchitecture are two aspects of the same anatomical reality, both reflecting cortical microarchitecture. It is reasonable to assume that there is a relationship between these two microstructural domains. This is supported by findings related to neurodegenerative diseases that are linked to cellular death or fiber deformation. However, it is currently impossible to image the living brain at the resolution of cells, although the cortical cytoarchitecture is well defined. In contrast, myelin is measurable in the brain using Magnetic Resonance Imaging (MRI) methods, although a defined knowledge on the myeloarchitecture is only available in fragments.

A correspondence mapping between cyto- and myeloarchitecure depends on a precise parcellation. A complete parcellation based on myeloarchitectonic criteria does not exist. Thus, analysing correspondences between the two architectures is possible in very limited ways today. But mapping myelin in the brain would allow one to study myeloarchitecture. Most importantly, it would enable researchers to draw conclusions from changes in myelin to changes in the cell configuration in the cortex.

1.2 MOTIVATION AND LEADING QUESTIONS OF THE THESIS

The aim of this thesis is to provide an architecture-based methodology to parcellate the human cortex based on myeloarchitectonic features. The parcellation scheme builds on an existing concept by Hellwig [1993].

When building such an architecture-based parcellation method, problems arise from three different aspects:

STRUCTURAL IMAGING Currently, the gold standard in architectural studies still refers to analysing postmortem brain tissue on two-dimensional sections. These techniques are inadequate due to their two-dimensional and only limited qualitative nature. Additionally, histological stainings allow no corresponding studies on brain function. Measuring structure and function of the living brain using MRI methods is very difficult. The in-vivo techniques used to acquire whole-brain data are not able to exhibit a resolution in the sub-millimetre range which would allow one to sample intracortical features. Research into the direction of MRI methods that are capable of detecting quantitative features associated with myelin just recently started.

PARCELLATION SCHEMES Existing (semi-)automatic parcellation schemes are based on morphological shape features or connectivity properties of the brain. Morphology-based parcellation methods are too constrained by marcoscopical features, which are insufficient to reliably detect cortical areas. Connectivity-based methods may be limited by the input data. Both morphology- and connectivity-based approaches are often outperformed by manual segmentations.

CORTICAL LAYERING Analysing properties of the cortical areas based on the layered nature of the cortex requires an appropriate layering model. However, current layering models are not able to follow the true anatomical layering found in the cortex. Samples derived from data using these models are highly distorted.

Therefore, an architecture-based parcellation method applied to in-vivo MRI data may only be successful when two prerequisites are fulfilled:

1. a MRI method needs to be developed that reflects myeloarchitectonic patterns at a resolution that allows sub-millimetre sampling of these features, and,
2. a layering model needs to be designed that follows the real anatomical layering in the cortex.

Given the prerequisites, the leading questions of this thesis are:

- Is it possible to build an architecture-based model that describes intracortical myelin as measured in MRI and histology?
- Is the model able to automatically parcellate the human cortex and reliably detect cortical areas in in-vivo MRI data?
- Which parameters of the model define its performance?
- What other causes, such as MRI artefacts, may influence the performance of the model?
- What is the theoretical performance of such a model to be expected in future applications under the condition of even higher resolution data being available?

1.3 CONTRIBUTIONS

Based on the aforementioned motivation and leading questions, this thesis provides the following results and novel contributions:

- a reimplementation and adaptation of an existing concept provided by Hellwig [1993]. In general, the method transforms area-specific cytoarchitectural a-priori information into information regarding the myelin content.
- the development of a normalization pipeline that allows an application of Hellwig's concept to in-vivo MRI data. The pipeline transforms the myelin content profiles into profiles described by the T_1 relaxation time which is assumed to reflect myelin in the cortex. The pipeline considers area-specific differences in terms of these T_1 times and respects limitations set by the image acquisition such as resolution and partial voluming effects.

In addition, to make an application of such an architecture-based parcellation method possible, the following results and contributions considering the prerequisites are achieved in collaborative projects:

- an optimisation of an in-vivo MRI sequence at 7 T to measure whole-brain data at an unprecedented resolution of 0.5 mm.
- the development of additional processing steps necessary to efficiently and accurately compute the new high-resolution MRI data.
- the implementation and validation of a novel layering technique that allows proper sampling of image intensities in the cortex. The layering model is able to follow the shifting behaviour of anatomical layers in gyral crowns and sulcal fundi.

This thesis represents the first contribution towards an automatic architecture-based parcellation model being applied to in-vivo MRI data. The work gives clear

indication that it may overcome the limitations of existing parcellation schemes. Incorporating architecture-relevant information such as the geometry of anatomical layers plays a key role for the success of this model.

This thesis is part of fundamental research and dedicated to emblase new insights to myeloarchitecture. Therefore, only healthy human subjects have been considered. Further research investigations are needed to discover additional architectural properties that may improve such architecture-based parcellation schemes.

1.4 STRUCTURE OF THE THESIS

The thesis is structured into three parts and nine chapters. At first, background information is given about brain anatomy, brain imaging and the context of cortical parcellations. The main part outlines the actual contributions followed by a summary and discussion. The last part comprises the Appendix which includes general illustrative information and information relevant to this thesis's prerequisite about the layering model.

CHAPTER 2 describes the **brain anatomy**. It presents macroscopical as well as microscopical properties such as cytoarchitecture and myeloarchitecture. The chapter also encompasses and describes classical findings taken from historical literature. The relationship between the architectures is briefly highlighted in the context of neurodegenerative diseases.

CHAPTER 3 presents the **physical background** on Magnetic Resonance Imaging and highlights the latest developments leading to quantitative anatomical data assessment. The focus is on myelin mapping. Although cyto- and myeloarchitecture are interlinked, MRI is currently not able to image at cell size resolution. In addition, other MRI methods as well as classical histological staining methods are explained.

CHAPTER 4 provides a general overview on methods commonly used in **image segmentation and analysis**. The chapter concentrates on deformable models in particular. It is fundamental for the next chapters.

CHAPTER 5 describes the current **state-of-the-art in cortical parcellation** methods. With the increasing diversity on brain data, many different parcellation methods have evolved. The advantages and disadvantages of the methods are discussed to draw conclusions for a new parcellation scheme.

CHAPTER 6 deals with the data acquisition and processing. It outlines the **acquisition parameters** of in-vivo MRI as well as ex-vivo MRI and histology data. This chapter also illustrates the data **processing pipeline** and describes the individual steps of it including preprocessing, brain segmentation, and cortical surface reconstruction on high-resolution MRI data. In particular, it introduces and explains the new **layering model** developed.

CHAPTER 7 presents the **architecture-based cortical parcellation model** which has been developed in this project. The model aims at overcoming limitations set by current parcellation methods.

CHAPTER 8 describes the experimental design of the **validation**. The validation targets three major fields: the application of the model to in-vivo data, the comparison to classically-derived histological data and, finally, theoretical experiments on the discriminative power in the light of different imaging resolutions. It presents and discusses all **results**.

CHAPTER 9 summarises the work conducted in this thesis. In addition, it discusses future work tasks and remaining challenges in order to develop more sophisticated parcellation methods.

Part I

Background

2

ANATOMY OF THE HUMAN BRAIN AND THE CEREBRAL CORTEX

This chapter shall give a general overview on the brain, its anatomy and function (Section 2.1). Specifically, the focus is put on the cerebral cortex, i. e., a 2–5 mm outer tissue surface of the brain. Since more than 200 years, scientists try to relate structure and function to investigate brain development in normal healthy and diseased states (see Section 2.2). The discussions on the structure-function relationship in the brain evolve from analysing the cortical architecture (see Section 2.3). The two most commonly known architectures are the cytoarchitecture which describes the neuronal cell configuration within the cortex, and the myeloarchitecture which describes the intracortical myelinated fibre network. The interplay between these architectures is highlighted in Section 2.4. It is followed by a short overview of the clinical perspective. Finally, a summary of relevant information is presented and conclusions considering this thesis are drawn.

Detailed reading on neuroanatomy and brain function are provided in Bear et al. [2007]. All other literature is cited accordingly in the text.

2.1 GROSS ORGANISATION OF THE HUMAN BRAIN

The nervous system of all mammals has two main divisions: the central nervous system and the peripheral nervous system (PNS). The brain together with the spinal cord form the CNS which consists of the parts of the nervous system that are encased in bone. The brain lies entirely within the skull. On a sideview of the brain, it becomes apparent that the brain consists of three parts: the cerebrum, the cerebellum and the brain stem (see Fig. 2.1).

THE CEREBRUM (Latin for *brain*) is, phylogenetically seen, the newest structure, with mammals having the largest and best-developed structures among all species. It has a complex folded outer surface called cerebral cortex. The cerebrum is clearly split down in the middle into two cerebral hemispheres, separated by a deep sagittal groove called medial longitudinal fissure. The right cerebral hemisphere receives sensations from, and controls movements of, the left side of the body. Respectively, the left cerebral hemisphere receives sensations from, and controls movements of, the right side of the body.

THE CEREBELLUM (Latin for *little brain*): is behind the cerebrum, and is split sagittally by a fissure as well. Although this structure is very small and dwarfed by the cerebrum, it contains as many neurons as the cerebrum. Like the cerebrum, it has a complex folded outer surface called cerebellar cortex. Primarily, it is a movement control center and is extensively connected with the cerebrum and brain stem. In contrast to the cerebrum, the right cerebellar hemisphere controls movements of the right side of the body. Respectively, the left cerebellar hemisphere controls movements of the left side of the body.

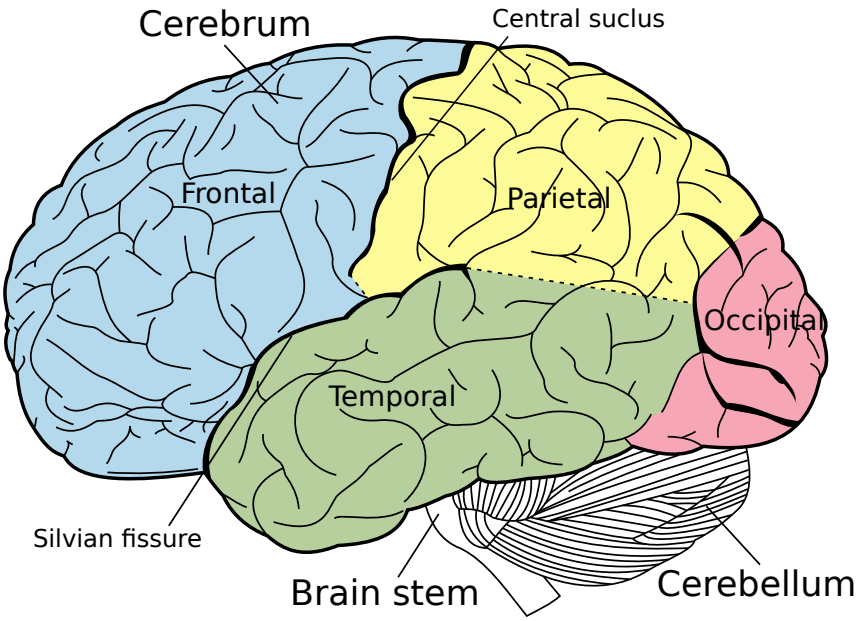

Figure 2.1: Lateral view onto the human brain consisting of the cerebrum, the cerebellum and the brain stem. The coloured regions depict the different functional lobes of the cerebral cortex. Lines indicate folds. The central sulcus divides the frontal and the parietal lobe while the Sylvian fissure separates frontal and temporal lobe. Image is a reproduction of a lithograph plate from Gray [1918]. (Image source: Wikepedia: `http://en.wikipedia.org/wiki/File:Lobes_of_the_brain_NL.svg`)

THE BRAIN STEM forms the stalk from which the cerebrum and cerebellum originate. It is a complex nexus of fibres and cells and serves to relay information from the cerebrum to the spinal cord and cerebellum, and vice versa. The brain stem regulates vital functions, such as breathing, consciousness, and the control of body temperature. It is considered the most primitive part of the brain, but at the same time it is the most important to life. One can survive damage to the cerebrum and cerebellum, but damage to the brain stem usually leads to rapid death.

The largest distinction between the brain stem and both the cerebrum and the cerebellum is the outer appearance of these structures. The cortical surfaces of the cerebrum and the cerebellum reveal a highly complex folding pattern (see Fig. 2.1). Outward folded structures are called **gyri** (singular: gyrus) and the grooves inbetween are called **sulci** (singular: sulcus). Specifically, the top of a gyrus is called **crown** while the deepest point of a sulcus is called **fundus of a sulcus** (plural: fundi). The stretch reaching down from the crown to the fundus is called **sulcal wall**.

2.1.1 *Meninges and the Cerebrospinal Fluid*

The CNS, i. e., the brain and the spinal cord, are enveloped by meninges (Ancient Greek meaning *membranes*) filled with cerebrospinal fluid (CSF). Taken together, the

meninges and the CSF act as primary mechanical and immunological protectors of the brain. The membranes are located between brain matter and skull (see Fig. 2.2A). In mammals, the meninges consist of three layers: the dura mater, the arachnoid mater, and the pia mater. The dura mater (Latin for *tough mother*, also meaning *hardest* or *thickest* tissue) is attached to the skull and is comparable to a "sac" that envelops the arachnoid mater. The **dura mater** consists of two layers: an thin membrane that covers the outer surface of all bones, and a meningeal layer, i. e., the actual dura mater. The dura mater is composed of dense fibrous tissue and surrounds and supports the CNS. It holds the cerebrospinal fluid in which large vascular vessels reside which provide blood supply to the brain. The arachnoid mater is between dura mater and pia mater, but attached to the dura mater. Both dura mater and arachnoid mater do not follow the folding of the cortex, except for the longitudinal fissure which separates the cerebrum into the left and the right hemisphere. The space between arachnoid mater and pia mater is called subarachnoid space. It acts as an effective morphological and physiological meningeal barrier that allows the blood circulation to the brain and holds the CSF. The pia mater (Latin for *soft mother*, meaning *softest* or *thinnest* tissue) is firmly connected to the surface of the brain, and in contrast to dura mater and arachnoid mater, it follows the cortex's complex folded contours of gyri and sulci. Pia mater and arachnoid mater are in close contact on gyral crowns. In the sulcal basins between two gyral crowns the subarachnoid space opens up in which the vascular tissue and the CSF interface each other and constitute the blood brain barrier.

The CSF can be found in the ventricular system inside and around the brain and spinal cord. This bodily fluid fills the ventricles which reside in the brain, the sulci of the brain, as well as the central canal of the spinal cord.

2.1.2 *Vasculature of the Brain*

The brain's vasculature plays another important role. Blood supply is provided by two main sets of vessels: the right and left common carotid arteries and the right and left vertebral arteries. The common carotid arteries divide further into the external carotid arteries, i. e., supplying the face and the meninges with blood. The internal carotid arteries supply blood to the anterior 60 % of cerebrum. The vertebral basilar arteries supply the posterior 40 % of the cerebrum, part of the cerebellum, and the brain stem.

At the base of the brain, the carotid and vertebral basilar arteries form a circle of communicating arteries known as the *Circle of Willis*. These circular arteries work as a "back-up system" and presumably improve the chances of any brain region to continuously receive blood if one of the major arteries is occluded. The **anterior cerebral artery (ACA)**, the **middle cerebral artery (MCA)**, and the **posterior cerebral artery (PCA)** arise from the *Circle of Willis* and travel to all parts of the brain. The anterior cerebral artery extends upward and forward and supplies the frontal parts of the brain. The middle cerebral artery is the largest branch of the internal carotid and supplies a portion of the frontal brain and the brain's lateral surface. The posterior cerebral artery stems in most individuals from the basilar artery but sometimes originates from the internal carotid artery. The posterior cerebral artery supplies the posterior parts of the two cerebral hemispheres. The comparatively

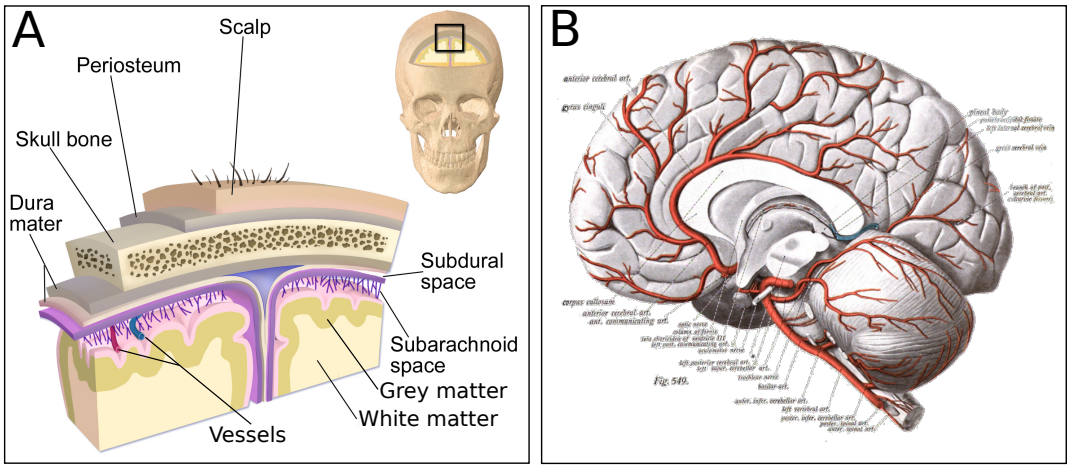

Figure 2.2: The images depict surrounding structures and tissues of the brain. A: The meninges of the brain enclosed in the skull. The dura mater and the CSF in the subarachnoid space are important in this thesis as they influence the data processing. (Image created by Blausen Medical Communications, Inc.. Image source: http://goo.gl/FDmIHQ) B: Medial view onto the human brain showing a vessel tree of the cerebral arteries. Larger vessels run on the gyral crowns and bifurcate into the sulci. (Image published in Sobotta and Playfair McMurrich [1908]. Image source: http://goo.gl/gPYjAC)

smaller lenticulostriate arteries branch from the middle cerebral artery and penetrate deep into the brain.

The arteries bifurcate to a vascular tree spanning the whole cortical surface (see Fig. 2.2B). The main vessels run on the gyral crowns, and their branches reach down into the sulcal basins. With each branch, the diametre of the blood vessels decreases, finally allowing small arteries to penetrate into the brain tissue.

2.1.3 *Structural Organisation of the Cerebrum*

When the cerebrum is cut in any direction, the inside reveals two main tissue divisions: the white matter (WM) and the grey matter (GM). The GM, the outer cortical surface of the cerebrum, is composed of numerous nerve cells arranged in six cellular layers and primarily associated with processing and cognition of incoming information. The WM forms the inner part of the cerebrum and is composed of many myelinated nerve cell processes, i. e., called axons. These axons are also called fibres, fibre bundles, or tracts, and carry nerve impulses between the neurons.

Neurons are the main component of the CNS. The cerebral cortex contains 19–23 billion nerve cells which make up only 20 % of the total number of nerve cells in human brains [Pakkenberg et al., 2003; Pakkenberg and Gundersen, 1997]. The nerve cells process and transmit information through electric and chemical signals within the brain and between brain and peripheric organs. In this section, a brief and schematic description of a typical cell structure and its function is given, as there are many exceptions to it.

The neuron usually consists of a cell body, called soma, which contains the nucleus (see Fig. 2.3). The soma can reach a size of 4–100 µm. A typical neuronal cell

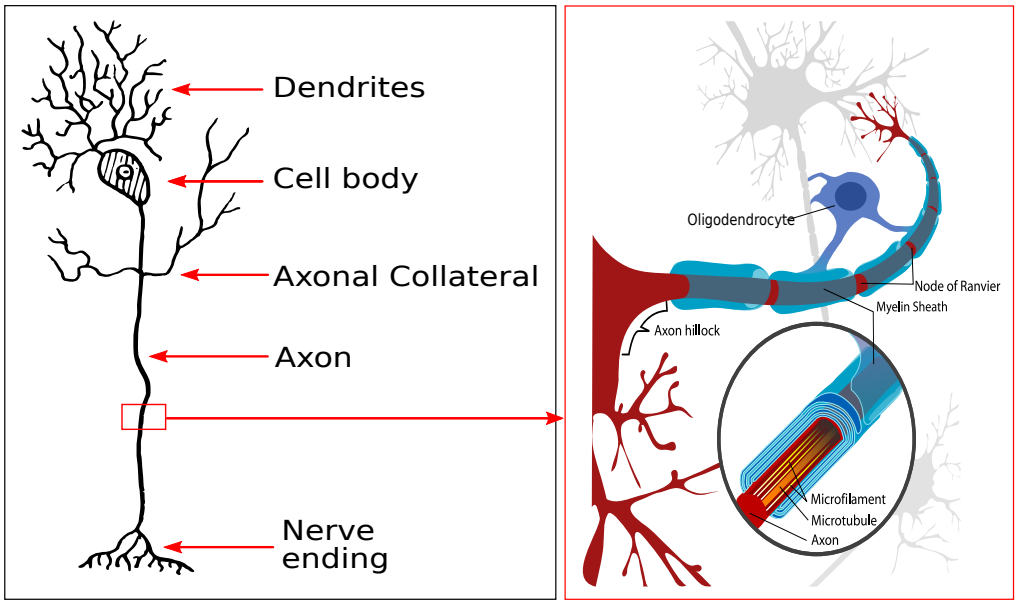

Figure 2.3: Left: The image schematically illustrates a neuronal cell with its dendritic tree, its axon and axonal collaterals. The enlargement to the right shows the myelin sheaths around the axon. These are produced by the oligodendrocytes and are arranged in segments that are interrupted by the node of Ranvier. (Left image is created by Pearson Scott Foresman. Image source: http://goo.gl/Cye2qc. Right image is derivative work of image by Mariana Ruiz Villarreal: http://goo.gl/eBkAkn. Image source: http://goo.gl/IG8hna)

has many dendrites and an axon, also known as nerve fibre. Soma and dendrites receive signals from other neurons while the axon transmits information signals to other neurons, muscles and glands. The transmitting element sending the signals from an axon of a nerve cell to the dendrites of another cell is called synapse. In the cerebral cortex 10^{15} synapses can be found.

The drendrites and axons serve different functions, but they vary a lot in features such as shape and length. Dendrites are thin unmyelinated structures which arise from the cell body multiple times. They branch into a "dendritic tree", becoming thinner and thinner with every branch and extending only hundreds of micrometre in the cortex. Thus, they act in a very restricted area around the cell body. Axons are myelinated nerve cell processes which arise only once at the axon hillock. They have a diametre of <1–6 µm. Like dendrites, they branch but maintain their diametre along the distance they travel. Myelinated branches of an axon within the cortex are called axonal collaterals. Usually, axons can extend out of the brain as far as 1 m. Within the brain, axons can span a network of 150.000–180.000 km [Pakkenberg et al., 2003; Pakkenberg and Gundersen, 1997].

The myelin around the axon is a layer of insulating substance composed of 70–80 % lipids and 20–30 % protein. The purpose of the so-called myelin sheath is to increase the speed of the propagated signals along the myelinated fibre. The myelin itself decreases the capacity across cell membranes and increases the electrical resistance. Thus, the electrical impulses cannot leave the axon. The myelin sheath gets produced by oligodendrocytes and the process of it is called myelination.

Each axon shows short myelinated segments, periodically interrupted by unmyelinated segments, i. e., the nodes of Ranvier (see Fig. 2.3). At these nodes, the axon diametre is decreased and an action potential can be generated. These electrical currents are conducted with little attenuation to the next node in transmit direction where they are strong enough to generate another action potential. Rather than following the myelinated fibre directly as a line, action potentials "jump" from node to node, bypassing the myelinated segments in between. This saltatory conduction results in an even faster propagation speed. The diametre of an axon is known to be directly linked to the conduction velocity [Hursh, 1939].

The white matter has long been understood as a passive part of the brain, but it actually has an active influence on how the brain learns and functions. The WM modulates the distribution of action potentials. Thus, it acts as a relay and coordinates communication between different brain regions. The so-called fibre tracts can be categorised into three different types:

PROJECTION TRACTS connect regions within the brain as well as with spinal cord. They transmit information between the cerebrum and the peripherals of the body.

COMMISSURAL TRACTS pass through the corpus callosum which connects the two cerebral hemispheres and enable them to communicate with each other. Others tracts pass through the anterior and posterior commissures, i. e., structures serving as a bridge between hemispheres.

ASSOCIATION TRACTS connect regions within the same hemisphere and usually link memory and perceptual regions of the brain. There are two types of association tracts: long range association tracts connect different lobes of the same cerebral hemisphere to each other, and short range association fibres connect folds within a single lobe.

2.1.4 *Functional Organisation of the Cerebrum*

The cerebral cortex is only present in mammals. In larger mammals, the cerebral cortex is highly folded which have allowed the cortex to expand in surface area without taking up much greater volume. Therefore, it is proportionally the largest in humans.

Deeper sulci are called fissures. The biggest of them is the (medial) longitudinal fissure dividing the cerebrum into the two cerebral hemispheres. **Fissures and sulci** divide each hemisphere into conventionally five different *lobes* named after the bones of the skull that lie over them (see Fig. 2.1):

- the **central sulcus** divides the *frontal* lobe from the *parietal* lobe.
- the *temporal* lobe lies ventrally to the **deep lateral (Sylvian) fissure**.
- the *occipital* lobe forms the very back of the cerebrum. It borders directly to the temporal lobe. The **parieto-occipital sulcus** separates the occipital lobe from the parietal lobe.

- the *limbic* lobe consists of the cortex around the corpus callosum, primarily the cingulate gyrus, the cingulate sulcus, the isthmus of cingulate gyrus, the rhinal sulcus and some substructures of the hippocampal formation (according to *Terminologia Anatomica*).

In addition to the five mentioned lobes, scientists regard the *insular cortex* as separate lobe. If margins of the lateral fissure are pulled apart, a portion of the cortex folded deep within the lateral sulcus is revealed, called the insular (Latin for *island*), or insular cortex or even insulae. Thus, it somehow borders and separates the temporal and frontal lobe.

In these different lobes, the organisation of cells and axonal collaterals changes, yielding a subdivision of the cortex into structurally and functionally distinct **cortical areas**. The structural division relates to specific functional processing in the areas of these lobes [Bear et al., 2007]. Considering the areas, we distinguish between **primary**, **secondary**, and **tertiary** areas. Usually, primary cortical areas receive raw information and deliver processed information to the secondary areas, which, in turn, deliver further processed information to the tertiary areas. Hence, primary, and secondary areas process raw information while tertiary areas are responsible for higher order functional processing. Tertiary areas are therefore called **association areas**.

From here on, the focus is on the cerebrum, and in particular, on the outer surface, i. e., the cerebral cortex. In the literature, the cerebral cortex is often called neocortex, isocortex, cortical sheet, cortical ribbon or cortical surface. In this work, the term **cerebral cortex** or **cortex** will be used.

2.2 MAPPING STRUCTURE AND FUNCTION IN THE CORTEX

The cerebral cortex of humans is topologically seen a thin sheet that is on average 3 mm thick and has a surface area of around 900 cm^2 per hemisphere of which only one third is visible because the remaining two thirds are buried in the sulcal folds [Henery and Mayhew, 1989; Ono et al., 1990; Makris et al., 2005]. The complex convolutions of the cortical surface allow the brain to fit into a compact space of about 18 cm length, 13 cm height and 14 cm total width.

The main goal in neuroscientific research is to correlate the structure and function in the cortex in order to understand how the brain works in different functional states (rest vs. task-evoked states) or how it changes in pathology. These structure-function mappings have been a topic of investigation since more than two hundred years. Over the 20^{th} century, cortical cartographers[1] investigated the number, arrangement, and laminar and internal organisation of anatomically and functionally distinct areas of the cortex. Two main disciplines evolved: the studies of **cytoarchitecture** and **myeloarchitecture**. The cytoarchitecture deals with the cellular arrangement and organisation of neuronal cells in the brain, and more specifically in the cortex. The discipline of myeloarchitecture examines the cortical

1 Early brain scientists studied the brain from the outside to the inside. The first descriptions are reported in terms of the topology of the brain. Thus, the scientists "cartographed" the shape of the brain like geographers the landscape of countries, and like-wise they called themselves "cartographers". Later, the study of brains lead to an independent discipline, nowadays known as *Neuroanatomy*.

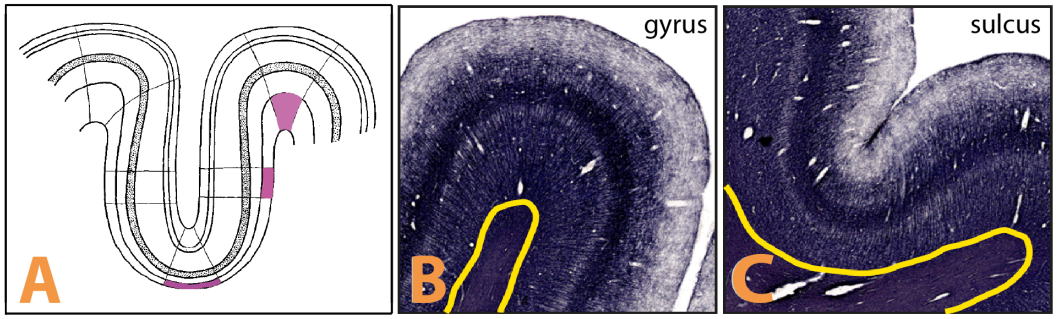

Figure 2.4: The images depict the layering in the cortex and its shifting behaviour in gyral crowns and fundi of sulci. A) Cortical layering schematically illustrated by Bok [1929]. B) and C) show myelin stains of a coronal section taken in the primary visual area. Here, the calcarine sulcus region is depicted which includes the stria of Gennari, a densely and distinct myelinated band. The WM boundary is shown in yellow. B) In the gyral crown, the inner cortical layers near the WM become thick and push the stria towards the outer cortical boundary. C): In the sulcus, the inner cortical layers become thin and the stria lies more towards the WM boundary. The changing thickness of the layers obeys the equi-volume principle as proposed by Bok [1929]. (Myelin stains kindly provided by Dr. Stefan Geyer and Katja Reimann.)

structures and anatomical features associated with the myelin sheaths of neuronal axons.

2.2.1 *Macroscopical Features: Cortical Layering, Thickness and Gyrification*

The main interest in cortical architectural studies was to investigate the lamination pattern of the six cortical layers. Bok [1929] found that to compensate cortical folding, cortical layer segments preserve their local volume fraction while the layer thickness adapts to local cortical curvature (see Fig. 2.4).

Bok studied cyto- and myeloarchitectonic layers in the fully developed adult human brain and analysed the relationship between cortical folds and layer geometry. Specifically, he investigated the question how the cortical layers behave in locations of gyri and sulci in different cortical areas. Bok divided each cortical layer into segments that were bounded by the principal dendrites of neurons. He found by measurements on postmortem histological cell-stained sections that the volume of a segment within a given layer is kept constant with respect to curvature. As a result, neighboring segments in one layer have the same volume, whether they are located on a gyral crown or in the fundus of a sulcus. The thickness of the cortical segment adjusts to adapt to the curvature, thus compensating for the folding. Simply said: Going along a cortical boundary surface, the layers appear to be squeezed and are relatively thick in locations with high curvature. Layer segments at places of small curvature appear to be stretched and are relatively thin.

Besides the lamination pattern, other macroscopical features have been intensively studied, too: the **cortical thickness** and cortical folding pattern, i. e., **gyrification**. The variability of thickness within the cortex is large and ranges from 4.5 mm in locations of thick cortex to 1.5 mm in locations of thinner cortex. There is no correlation between cortical thickness and cortical areas. The thickness is

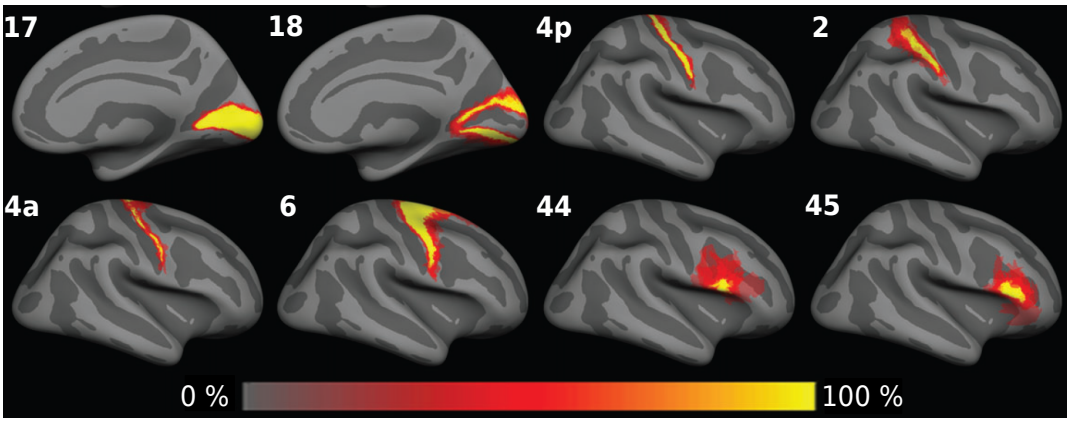

Figure 2.5: The variability of areal extent of 10 postmortem brains according to gyral or sulcal landmarks: in primary visual (17) and anterior and posterior motor (4a and 4p) areas the variability of the areal extent is small. In secondary cortices of vision (18), sense (2) or premotor function (6) the variability increases at the boundaries of each area. But in association areas such as Broca's region (44 and 45), the variability of areal extent is very high. (Image published in Geyer and Turner [2013] and by courtesy of Springer Verlag, Berlin-Heidelberg)

smallest in medial sides of the brain. Towards the occipital and frontal poles, the cortical thickness decreases. Locally, the cortical thickness is larger in gyral crowns than in sulcal fundi. The cortical thickness progressively and gradually decreases from gyral crown to sulcal fundi, in some locations by 40–50 %. This decrease depends on the depth of the sulcus: the deeper the sulcal fundus, the larger the decrease of cortical thickness. The largest cortical thickness of up to > 4 mm can be found in the precentral gyrus, especially, in its posterior wall, i. e., the primary motor region. In location of the calcarine sulcus in the primary visual region the cortical thickness can even be as small as 1.2 mm.

Measuring cortical folding patterns has gained increased interest in the study of cortical areas. The boundaries of primary areas in mammals consistently coincide with cortical folds:

- the primary motor area is contained in the precentral gyrus (frontal lobe),
- the primary somatosensory area is located in the postcentral gyrus (parietal lobe), and,
- the primary visual area is contained in the calcarine sulcus (occipital lobe).

However, the variability of gyrification increases in association cortical areas, i. e., the areal extent of these areas coincide not necessarily with cortical folds (see Fig. 2.5). The characteristic shape of cortical folds and the arrangement of the cortical areas may be explained by an evolutionary design strategy for the minimisation of axonal length [Van Essen, 1997; Kennedy et al., 1998; Klyachko and Stevens, 2003; Karbowski, 2003]. Cortical areas process information through inter-areal and inter-hemispheric connections, e. g., the cortical network. These cortical networks are optimised in such a way that they reduce the wiring costs and save energy and time during the signaling process. In larger brains, longer fibres are required to communicate between distant cortical areas. Theoretically, there must

be a decrease in inter-hemispheric connectivity when brain size increases, due to the increasing time constraints related to the inter-hemispheric conduction delay. Hence, a larger local clustering of inter-areal connections is required [Ringo, 1991; Ringo et al., 1994]. The tension-based theory by Van Essen [1997] suggests that tension along axons in the WM between nearby cortical areas is the primary driving force for cortical folds at specific locations in relation to its areal boundaries.

Today, we know that age has a profound influence of all the measures [Hogstrom et al., 2013]. Cortical thickness, gyrification, as well as cortical surface area are negatively correlated with age. The reduced gyrification in aging appears to parallel reductions in surface area. Both surface area and thickness change continuously with age, but the relationship between these two measures is relatively stable throughout healthy adulthood. Yeatman et al. [2014] found that properties of human brain tissue change across the lifespan. Specific properties of growth of new brain tissue during the maturation approaching maturity may predict the rate of degeneration in aging. According to Yeatman et al. [2014] the relationship is mirror-symmetric. In contrast, fibre development in WM follows an asymmetric behaviour: while changes in childhood happen at a very rapid rate, the decline in old age happens at a slow rate. All together, Yeatman et al. [2014] showed that several biological processes define changes in WM over lifespan.

2.2.2 *Classical Works*

Structural changes within the cortex have been observed even before Brodmann's well-known studies on cytoarchitecture [Brodmann, 1909]. In 1858, Berlin [1858] has provided descriptions on six cortical layers in the human cortex which change their lamination pattern based on variations in cell size and type. A decade later, Meynert [1868] published a subdivision of the cortex into various functional regions. Other early investigations include the work of Betz [1874], who discovered the giant pyramidal cells in the primary motor region. Many publications dealing with the change in cellular lamination pattern in the cerebral cortex followed [Lewis, 1878, 1880; Hammarberg, 1895].

Brodmann [1909] considered the published work of his colleagues in detail and investigated their inconsistencies. He discovered 44 functional areas which match in their areal extent as well as their cell configuration (see Fig. 2.6).

Smith [1907] presented a detailed atlas of human cortical localisation encompassing 50 areas (see Fig. 2.7). He distinguished the areas based on architectural patterns on freshly cut brains. Publications by Campbell [1904] and Flechsig [1920] follow the same trends.

Oskar and Cécile Vogt followed a different concept: parcellating the cortical surface based on myeloarchitecture. According to Vogt, myeloarchitecture reveals more details than cellular localisation. The Vogts provided the most circumstantial descriptions of myeloarchitecture by subdividing the cerebral cortex into more than 200 areas (see Fig. 2.8).

Von Economo and Koskinas [1925] reviewed the publications. They studied the quantitative cellular configuration and accordingly reviewed the myeloarchitectonic descriptions by the Vogts in over 107 cortical and subcortical areas. They merged the findings in their own mapping (see Fig. 2.9). In addition, they pub-

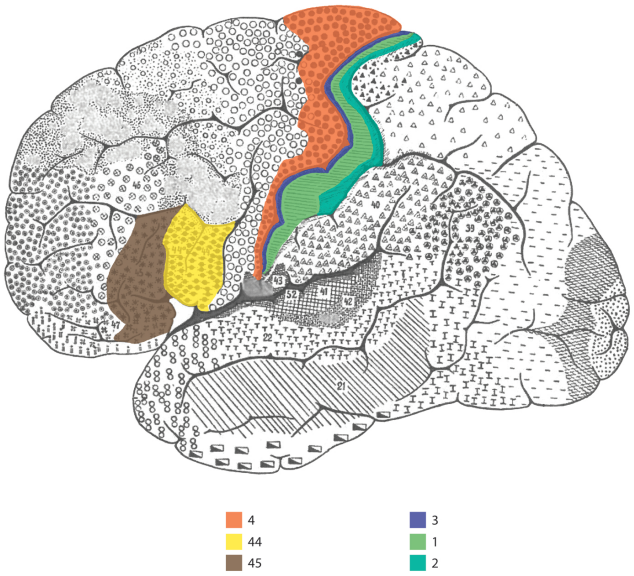

Figure 2.6: Brodmann's cytoarchitectonic parcellation of the brain surface. The division into 52 areas is based on structural changes in the cellular composition within the cortex. Lateral view onto the surface highlighting the primary motor-somatosensory areas 4, 3, 1 and 2, and Broca's region consisting of areas 44 and 45. (Image source: von Economo and Koskinas [1925])

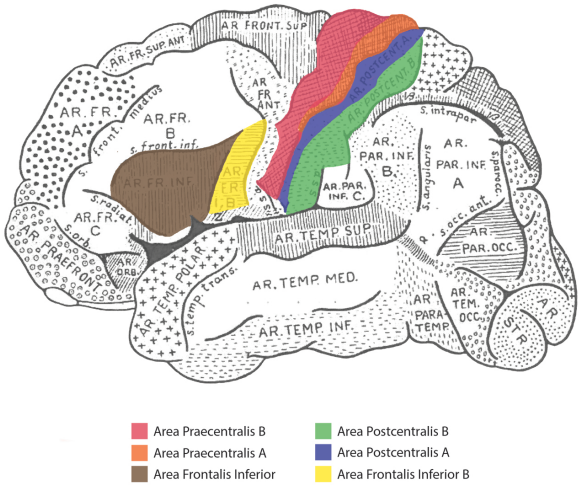

Figure 2.7: Grafton Elliot Smith parcellation of the brain surface. The division into 50 areas is related to different architectonic patterns visible on fresh cut brain material. Lateral view onto the surface highlighting the primary motor-somatosensory areas 4, 3, 1 and 2, and Broca's region consisting of areas 44 and 45 (nomenclature and colour coding adopted from Fig. 2.6). (Image source: von Economo and Koskinas [1925])

lished the first table consisting of 52 areas describing quantitative measures per layer including the relative thickness, cell size, and cell density.

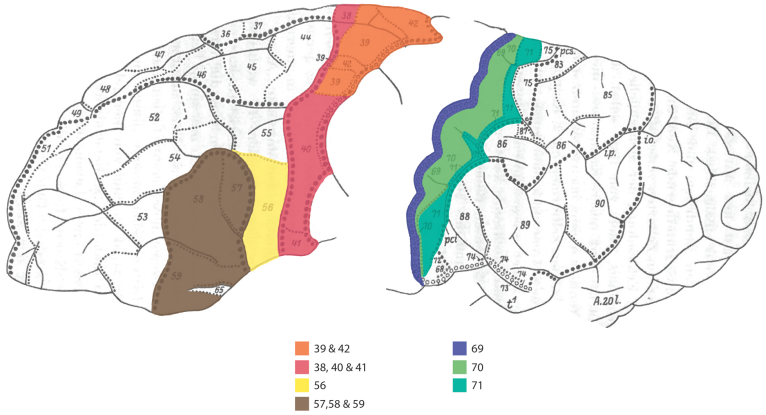

Figure 2.8: Cécile and Oskar Vogts myeloarchitectonic parcellation of the brain surface in lateral view. The division into more than 200 areas and subareas is based on subtile changes in the arrangement and organisation of myelinated horizontal and radial fibre structures in the cortex. The image depicts the primary motor-somatosensory areas 4, 3, 1 and 2, and Broca's region consisting of areas 44 and 45 (nomenclature and colour coding adopted from Fig. 2.6). (Image source: von Economo and Koskinas [1925]).

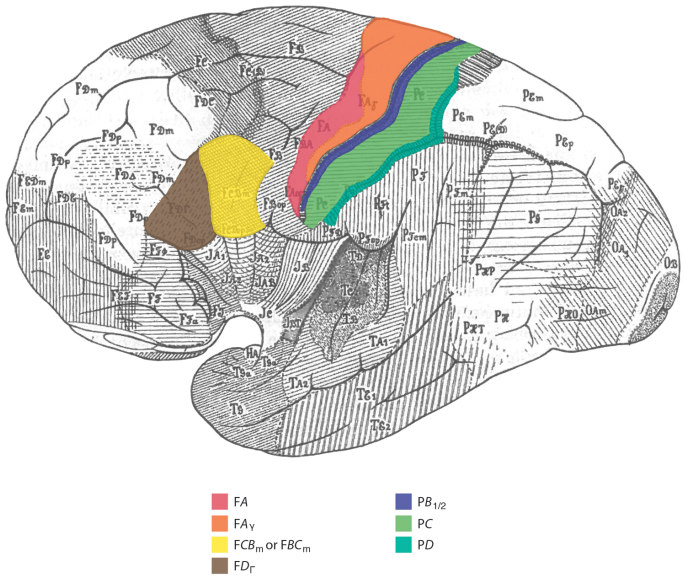

Figure 2.9: Von Economos' and Koskinas' cytoarchitectonic parcellation of the brain surface. The division into 107 areas is based on structural changes in the cellular composition that follow structural changes in the myeloarchitecture described by the Vogts Vogt and Vogt [1919a,b,c]. Lateral view onto the surface highlighting again the above named regions (nomenclature and colour coding adopted from Fig. 2.6). (Image source: von Economo and Koskinas [1925].)

With quantitative methods such as photometric reproductions of stained brain tissue sections available, Hopf [1968, 1969, 1970] and Braitenberg [1962] were the first to report quantitative myelin density profiles, i. e., traverses running from the

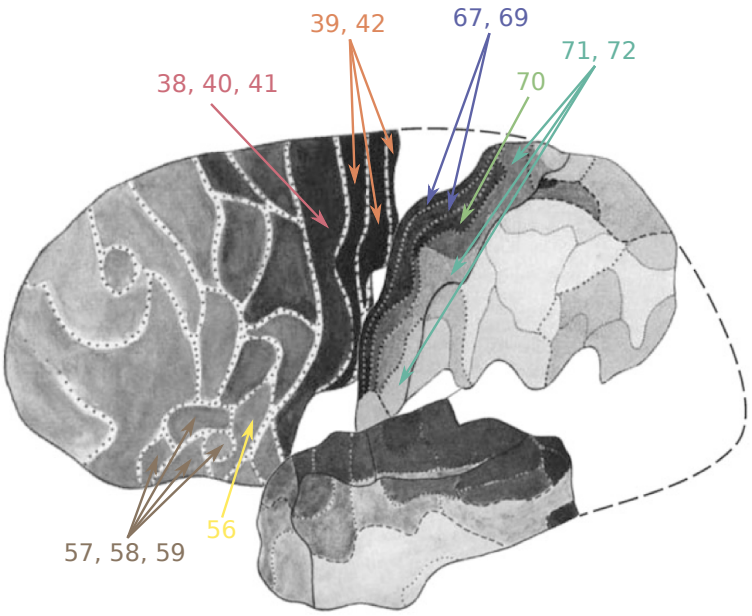

Figure 2.10: Adaptation of Hopf's individual lobe maps as presented in Hopf [1955, 1956]; Hopf and Vitzthum [1957] merged to one single surface in lateral view (nomenclature and colour coding adopted from Fig. 2.6). The separation agrees with structural changes in the myeloarchitecture described by the Vogts Vogt and Vogt [1919a,b,c]. The grey level codes the myelin concentration in each area with dark being strongly myelinated and light grey being less myelinated. (Image published in Geyer and Turner [2013] and by courtesy of Springer Verlag, Berlin-Heidelberg.)

inner to the outer cortical boundary along which intensity values were sampled. Based on the findings, Hopf [1955, 1956] and Hopf and Vitzthum [1957] created precise myeloarchitectonic mappings (see Fig. 2.10).

HISTORIC MAPPINGS The historic maps depict the similarities and differences in cyto- and myeloarchitecture. The illustrations were taken from von Economo and Koskinas [1925] and were complemented with visual highlights in the selected regions of interest: M1/S1 region. For additional comparison, Broca's area has been highlighted as well. In the Appendix A, all maps are shown from lateral and medial side to allow a full comparison.

The historic mappings indicate location and extent of certain areas or functional zones as seen by the different cartographers. Although no common map existed for the early pioneers, the similarities between the different maps are distinct. To create the mappings, sulcal landmarks were used as guidelines. The sulcal landmarks are depicted as black solid or dotted lines in the illustrations. Line width has been adjusted or dots vary in size indicating major or minor sulci. The anatomical landmarks helped the early anatomists localising the areas. These landmarks can now be seen as a historic remainder from times in which scientists discovered the relationship between cortical folding pattern and cortical areas. Today it is known, that this relationship exists in location of primary areas such as the primary motor-somatosensory region M1/S1, but it is less distinct in association areas such as Broca's region (see Fig. 2.5).

The similarities between the cytoarchitectonic mappings are higher compared to the similarities between myeloarchitectonic mappings. It is worth to note that Brodmann well described the occurrence of the giant pyramidal cells (German: "Betz'sche Riesenzellen"). However, he added no further distinction of it in area 4 in his map. The reason why Brodmann's map is similar to the one of von Economo and Koskinas [1925] is that the latter followed up on the developments in both disciplines. Von Economo and Koskinas [1925] tried to incorporate knowledge from both fields of research: cytoarchitecture and myeloarchitecture. The main contribution of von Economo and Koskinas [1925] are the tabulations on quantitative measures such as cortical thickness as well as cell density and cell size in 52 cortical and subcortical areas.

The areal extent of areas is similar across the different illustrations, albeit not the same, between cyto- and myeloarchitectonic mappings. The reader is admonished to visually inspect the historic maps in order to discover the singularities of each individual map and the differences between them in Appendix A.

2.2.3 *Regions of Interest within the Thesis*

Within the next sections, the different aspects of cyto- and myeloarchitecture are explained in detail. To analyse the architectures in conjuction, regions of interest (ROIs) were defined in the left hemisphere that correspond to the primary motor-somatosensory region.

The primary motor-somatosensory region, also called M1/S1 region, can be found along the central sulcus which is one of the main fissures separating the cerebrum into frontal and parietal lobes. This region contains cortical areas belonging to the precentral gyrus, the central sulcus, and the postcentral gyrus. In the M1/S1 region, area 4, 3, 1 and 2 (according to the nomenclature of Brodmann [1909]) can be found in anterior-posterior direction. Strictly speaking, area 3 is divided into area 3a, contained in the fundus of the central sulcus, and 3b, contained in the anterior wall of the postcentral gyrus [Geyer et al., 1999]. The location of these areas with respect to sulcal and gyral landmarks is consistent across subjects. The areal structural boundaries mainly coincide with macroscopical landmarks such as the gyral crowns or sulcal fundi (see Fig. 2.5). All areas are located in a relatively small region of the brain. The central sulcus can be 10–12 cm long and reach a sulcal depth of 1–1.5 cm. Considering myeloarchitectonic parcellation approaches, Vogt [1910] suggested four main types of myeloarchitecture to separate in human cortex. These types are constant across brains, and the areas in the selected region of interest (ROI) located in M1/S1 region specifically exemplify each of these basic types.

2.3 CORTICAL ARCHITECTURES

In this section, cyto- and myeloarchitecture are explained in general. Specific features in regions-of-interest are highlighted.

When describing the cortex the focus is on the **cerebral cortex**.

2.3.1 *Cortical Cytoarchitecture*

In the neuroscientific field, cytoarchitecture (Greek from *cyto* meaning cell, also cytoarchitectonics) is the discipline that analyses the cellular arrangement and organisation of neuronal cells in the brain, and more specifically in the cortex.

Brodmann [1909] pioneered these studies. He produced the first qualitative layer-dependent descriptions and provided quantitative measures of cell size and thickness of layers in different cortical areas. His mapping of structural changes onto the brain surface is the most popular existing mapping. A decade after Brodmann's publications, von Economo and Koskinas [1925] published a full set of tables for 52 cortical and subcortical areas, taking into consideration the absolute and relative values for different measures per layer including cortical thickness, cell size and cell numbers. More recently, Eickhoff et al. [2005b] provided a 3-dimensional (3D) digital probabilistic cytoarchitectural atlas related to the Brodmann mapping based on stained histological sections of 10 postmortem brains. These were registered into a standard reference space. Neuroscientists commonly regard such cytoarchitectonically-derived probabilistic Brodmann maps as useful guides to cortical localisation.

The cytoarchitecture is an exciting and ongoing field of investigation, continuously providing new insights and developments. The question arises: what does cytoarchitecture describe in detail?

The neuronal cells in the cortical surface form six tangential layers named with Roman numerals I to VI. Structural diversity in the cortex is visible when cell density and cell size within the layers and relative thickness of the layers change. From the outer surface of the cortex, i. e., the pial surface, to the boundary between GM and WM we distinguish between [Graumann and Sasse, 2005]:

LAMINA I , i. e., the molecular layer (*stratum moleculare*) that contains only a few nerve cells, many endformations of dendritic trees, mostly from layer III and V and very few ascending fibres, which are incoming afferent fibres. They originate in different cortical areas or ascend from unspecific thalamic nuclei, i. e., a structure residing deep in the brain.

LAMINA II , i. e., the external granular layer (*stratum granulare externum*) that is composed of many small granular neurons. The granular appearance of the cells give this layer its eponymous character. fibres are mainly incoming afferent fibres originating in neighboring cortical areas or ascending from the specific thalamic nuclei.

LAMINA III , i. e., the external pyramidal layer (*stratum pyramidale externum*) that mostly consists of small triangular-shaped cells, called pyramidal cells. Association fibres, i. e., cell-leaving fibres, appear in this layer for the first time. They project and connect within the area or to neighboring cortical areas.

LAMINA IV , i. e., the internal granular layer (*stratum granulare internum*) that is composed of many granular cells. Most afferent fibres, i. e., fibres from the thalamic nuclei, association fibres and commissural fibres end in this layer.

LAMINA V , i. e., the internal pyramidal layer (*stratum pyramidale internum*) that contains huge pyramidal cells and sometimes also giant pyramidal cells called

"Betz cells". However, it is a very sparse layer leaving much space between cells. The dendritic trees of these cells receive their impulses from fibres in layer I and II as well as from association and commissural fibres. In this layer most of the projection fibres originate and connect to the thalamus, the brain stem and the spinal cord.

LAMINA VI , i. e., the multiform layer (*stratum multiforme*) that consists of small, but sometimes densely packed cells which control outgoing fibres in this area.

Often, a division into three sublayers can be observed in layer III into layers IIIa, IIIb, and IIIc. Usually, the size of the cells progressively increases with cortical depth and the cell density decreases. The same is true for layer V, except that it is split into two layers Va and Vb. Also, layer VI sometimes gets divided into VIa and VIb. However, in this case the cell size and the cell density decrease at the same time.

The six layers can further be differentiated into [Graumann and Sasse, 2005]:

- two mostly receptive layers: the internal and external granular layers,
- two mostly efferent layers: the internal and external pyramidal layers, and,
- two modulating layers coordinating and controling the integration and processing of afferent and efferent impulses: the molecular and multiform layers.

The arrangement in layers is recognizable throughout the cerebral cortex, but reveals structural regional differences. The differences between locally neighboring areas are sometimes much larger than those between areas far apart. If areas are connected to each other, their architectural design is likely to be more similar, too, than compared to areas which are not connected.

The main cytoarchitectonic features associated with structural diversity in the cortex are cell size and cell density. The general size of the pyramidal cells can vary between individual brains. The cell size varies most in pyramidal cell layers III and V. The cell density varies most in granular layer IV. Combining cell size and cell density within a layer with the layer thickness primarily determines the characteristics of an area.

According to the thickness of individual layers and the change of cell density in granular layers, the brain surface can be divided into different types of cortex: **homogeneous** and **heterogeneous** cortex. In the homogeneous cortex all layers are equivalently represented. There is no predominance of pyramidal cell layers over granular cell layers or vice versa. This type of cortex can usually be found in association areas. In the heterogeneous cortex, pyramidal cell layers or granular cell layers predominate the respectively other cell layer resulting in an **agranular** cortex or a **granular** cortex. In locations of agranular cortex we find many pyramidal cells in layer III and V, combined with a relative increase in cell size, cell number and thickness of these layers. At the same time, the granular cell layers become thinner. Agranular cortex describes areas that process motor signals such as the primary motor area M1. In the granular cortex the granular cell layers outbalance the

pyramidal cell layers. The latter ones become very small or seem to completely disappear. Sometimes layer IV is divided into additional sublayers. Granular cortex usually processes sensory input information such as in the primary somatosensory areas. In these areas we can also observe a vertical arrangement of cells known as cell columns. Incoming fibres connecting to these areas are densely packed and push away cells which, in turn, "squeeze" into the columnar space left.

Von Economo and Koskinas [1925] have provided detailed and precise descriptions for some, but not all areas in German language. There are in general more descriptions for primary areas, i. e., for the primary motor-somatosensory region M1/S1 than compared to association areas. Here, a shorter, but essentially focused summary is given in English language.

If not stated otherwise, all features mentioned have been reported on a microscopical level.

2.3.1.1 *Cytoarchitectonic Definitions of the M1/S1 Region*

Cytoarchitectonically seen, the structural changes between neighboring or opposing cortical areas are so ultimately diverse only in the location of the M1/S1 region in the cerebral cortex. Additional cytoarchitectonic extremes related to measures such as cortical thickness, layer thickness, cell density or cell size can only be found here.

PRIMARY MOTOR AREA: M1 The primary motor area, i. e., M1 (Brodmann [1909]: area 4, von Economo and Koskinas [1925]: F*A*) covers the precentral gyrus along the anterior and posterior wall. In this work, the location of the primary motor cortex will be referred to as cortical area 4. It is the thickest cortical area within the cortex and can reach up to 3.6–4.2 mm [von Economo and Koskinas, 1925]. The thickness decreases, step by step, laterally. Usually gyral crowns are significantly thicker than sulcal walls. However, area 4 is an exception. The wall is only slightly thinner than the top of the gyral crown which is characteristic for this area. The boundary between GM and WM is unsharp, independent on the gyral crown or the sulcal wall. Compared to all cortical areas across the human brain, area 4 has an average cell density. The outer cellular layers are more cell dense than the inner layers. However, cell sizes in every layer are on average higher than compared to other regions in the cerebral cortex. Microscopically seen, there is no distinct lamination visible, i. e., layers merge without clearly revealing boundaries between single layers. Additionally, area 4 is agranular, i. e., cytoarchitectonic layer II and IV are obscured or not existing. Thus, this area appears as one thick single layer in which the lamination pattern of six cytoarchitectonic layers is not visible.

In layer V the giant pyramidal cells can be found, called "Betz'sche Riesenzellen" (German), which can reach a size of 60–100 µm. The giant pyramidal cells are the largest cells in the human cortex and are macroscopically visible. Taken together, layer III and V make up 70 % (2.5–2.9 mm) of the total cortical thickness, of which layer III alone covers 40–45 %. Hence, three quarters of the cortical depth of area 4 consist of pyramidal cells. However, the giant pyramidal cells only cover certain locations within area 4 which leads to a division of area 4 into two parts: F*A* (nomenclature borrowed from von Economo and Koskinas [1925]) which describes locations containing normal-sized pyramidal cells and FA_γ, describing locations

containing the giant pyramidal cells. F*A* laterally covers the posterior wall of the precentral gyrus. FA_γ covers the posterior wall of the precentral gyrus and medially also the gyral crown of the precentral gyrus. In general, the distribution of the giant pyramidal cells varies from medial to lateral direction. While there are many and large cells in medial parts, their size and number decreases laterally. Large cells can still be found in gyral crown and posterior wall in the location of the motor handknob, an overhanging bulge of cortex of the gyral crown reaching down into the central sulcus in area 4. Right behind this structure, the giant pyramidal cells only sparely exist or none at all. But continuing further lateral, the giant pyramidal cells reappear but can only be found in the posterior wall and not in the gyral crown any longer. Their size and number has decreased. The surface area that these cells cover laterally becomes smaller such that at the most lateral part of area 4, on top of the Sylvian fissure, no giant pyramidal cells can be found anymore. The historic cytoarchitectural mapping of von Economo and Koskinas [1925] reflects this behaviour (see Fig. 2.9).

PRIMARY SOMATOSENSORY AREA: S1 Opposite of M1, the primary somatosensory area, S1 (Brodmann [1909]: area 3, von Economo and Koskinas [1925]: PB_2) can be found. It separates from M1 by the central sulcus. In this work, the location of primary somatosensory cortex will be referred to as cortical area 3b. This area is purely located within the sulcal wall and its specific cell arrangement never reaches the gyral crown of the postcentral gyrus. Area 3b has a noticeable small cortical thickness. Sometimes it is below 2 mm which is twice as thin as in the primary motor area. In fact, area 3b is among those which have the smallest cortical thickness in the cortex. The cortex is clearly distinguishable from WM. The main characteristic features are the small cell sizes combined with a high cell density. In general, area 3b reveals a homogeneous type of cortex with a granular cell pattern. A few radial cell columns are visible which are caused by incoming fibres that push away the cells. Layer II and IV are considerably more cell dense. Layer III is composed of very small pyramidal cells that are on average smaller than everywhere else in the cortex. Layer V and VI are extraordinary thin which lets the outer cortical layers (I-III) appear much broader than compared to the inner cortical layers (IV-VI). In extreme cases, PB_2 (nomenclature borrowed from von Economo and Koskinas [1925]) reveals an even stronger granular cortex and deforms into PB_1. In PB_1, the triangular shape of pyramidal cells and their abnormal small size may lead to the conclusion that layer III may contain granular cells only. However, these cells are still pyramidal cells. In this extreme case, layer III becomes thinner in support of layer II and IV. These extremes may appear as lamellar islands running parallel to the central sulcus or even cover the entire anterior postcentral wall. The extent and the boundary between PB_2 and PB_1 is hard to determine.

SOMATOSENSORY REGION: AREA 1 The crown of the postcentral gyrus contains another area belonging to the somatosensory region: area 1 (Brodmann [1909]: area 1, von Economo and Koskinas [1925]: P*C*). In this work, the gyral crown of the postcentral gyrus will be referred to as cortical area 1. It parallels the stretch of the central sulcus at the top. The area has a relatively large cortical thickness given that cortical thickness is in general larger at gyral crowns. Its boundary

to WM is unsharp. It reveals a proper granular lamination pattern with radial cell columns which have a fan-shape appearance. Area 1 is very similar to areas in the frontal region such as the premotor cortex (Brodmann [1909]: area 6, which equals von Economo and Koskinas [1925]: F*B*) or higher association areas such as Broca's region (Brodmann [1909]: areas 44 and 45 which equal von Economo and Koskinas [1925]: F*CBm* and FD_γ). Only the great granularity in layer IV distinguishes this area from the frontal regions. Apparently, area 1 contains the most remarkable pyramidal cells posterior of the central sulcus. In superior and dorsal parts of this area these cells are larger than compared to other locations within this area. Layer III, specifically IIIc, reveals medium- to large-scaled pyramidal cells. In layer V, there are still giant pyramidal cells and Betz pyramidal cells. They are medium scaled and regularly distributed. Von Economo and Koskinas [1925] even proposed a division of P*C* into P*C* and PC_γ. Like in style of the primary motor area, P*C* would describe locations with regular cellular appearance, and, PC_γ, locations containing the giant pyramidal cells. However, the extent of PC_γ is very arbitrary and the formation is independent of macroscopical landmarks such as gyral crowns or sulcal fundi. Layer VI is very thick compared to other parietal areas. The transition between anterior PB_2 and P*C*, and, P*C* and the posterior successive area (area 2, P*D*) is obsolescent. Von Economo and Koskinas [1925] proposed the possibility of area 1 and 2 being one and the same area.

SOMATOSENSORY REGION: AREA 2 Area 2, (Brodmann [1909]: area 2, von Economo and Koskinas [1925]: P*D*) of the somatosensory region is contained in the posterior sulcal wall of the postcentral gyrus. In this work, this area will be referred to as cortical area 2. It has a very thin cortex which can compete against the thickness in area 3b. The boundary to WM is sharp. In general, area 2 is cell dense with decreased cell size. The lamination is not as clearly visible as in other locations. There is no radial arrangement of the cells. In layer IIIc there are medium to high scaled pyramidal cells which contrast the thin cortex. Layer IV is relatively thick. The boundary between area 1 and area 2 is very hard to identify. Depending on the brain, area 1 sometimes reaches down into the sulcal wall of area 2, sometimes area 2 reaches up into area 1, i. e., the crown of the postcentral gyrus. The posterior boundary of area 2 is very hard to determine, too. This area runs towards the postcentral sulcus.

2.3.2 *Cortical Myeloarchitecture*

In contrast with cytoarchitecture, myeloarchitecture has been largely neglected during the past hundred years. This discipline examines the arrangement of tangentially and radially oriented myelinated fibres in preparations stained for myelin sheaths. Research in this field is very difficult.

MYELOARCHITECTONICS NOW AND THEN Quantitative methods were not available to the pioneers in this field, Cécile and Oskar Vogt [Vogt and Vogt, 1919a,b; Vogt, 1923]. The Vogts characterised most of their findings using highly subjective terms as "thin to thick", "poorly to highly dense" or "less to fully present", which

do not lend themselves to reproducible assessments. Little has been done since then to develop more objective measures and criteria.

Adolf Hopf and Valentin Braitenberg were the first to report quantitative cortical profiles associated with myelin [Hopf, 1968, 1969, 1970; Braitenberg, 1962]. A cortical profile describes a traverse running from the inner to the outer cortical boundary along which intensity values were sampled. Their work is based on the photometric reproduction of sections stained for myelin. However, Braitenberg studied the fibre density in cortical areas whereas Hopf studied the myelinisation in the cortex which describes the development of the myelin sheath around a nerve fibre. Fibre density and myelin are certainly interlinked. But Hopf was convinced that the content or concentration of myelin in the cortex does not necessarily only depend on the fibre density, but also on the fibre caliber. Only recently, Nieuwenhuys et al. [2014] published a unique myeloarchitectonic mapping incorporating information from the Vogt-Vogt school. The mapping is a non-digital 2D projection onto the standard Montreal Neurological Institute (MNI) reference brain.

To date, a widely-accepted comprehensive myeloarchitectural reference atlas does not exist, and little is known about the concordance between cortical cytoarchitectonic and myeloarchitectonic boundaries.

THE BANDS OF BAILLARGER The Vogts focused on classifying patterns of fibres radial to the underlying white matter, and on subtle cortical layer dependent details, which led to a confusing proliferation of categories and subcategories. By contrast, Hopf followed Smith [1907] in noting that different patterns of myeloarchitecture were well discriminated by variations in the myelination of deeper cortical layers. Hopf especially focused on the so-called **bands of Baillarger** [Baillarger, 1840]. These bands describe two heavily myelinated transverse layers. The outer band usually coincides with cytoarchitectonic layer IV (internal granular layer) and the inner band with cytoarchitectonic layer V (internal pyramidal layer) [Vogt, 1910] (see Fig. 2.11A). These myelinated layers resemble a dense fibre network within the cortex, created by axonal collaterals of the neurons. In analysing the appearance of the bands of Baillarger, Hopf utilised the Vogts' most practical criteria: comparing local features of the Baillarger stripes of one cortical area globally to other areas. It becomes obvious that differences between locally neighboring areas may be much larger than those of areas far apart. Thus, myeloarchitecture can be largely defined by the bands of Baillarger, i. e., by their depth within the cortex, their thickness, and their intensity of myelination. In the mid-20th century, Hopf first used these criteria to systematically parcellate the cortical surface and generate a myeloarchitectonic map [Hopf, 1955, 1956; Hopf and Vitzthum, 1957] (see Fig. 2.10).

From comparative histological studies it is known that there is a very close relation between the two domains [Nieuwenhuys, 2013]. However, in contrast to cytoarchitecture, approaches to microstructurally parcellate the cerebral cortex based on myeloarchitecture are not well established.

MYELOARCHITECTONIC DEFINITIONS Vogt [1910] categorised myeloarchitectonic areas into four main types: **bistriate**, **unistriate**, **unitostriate** and **astriate**, depending on whether two horizontal myelin-rich bands are visible, only one band,

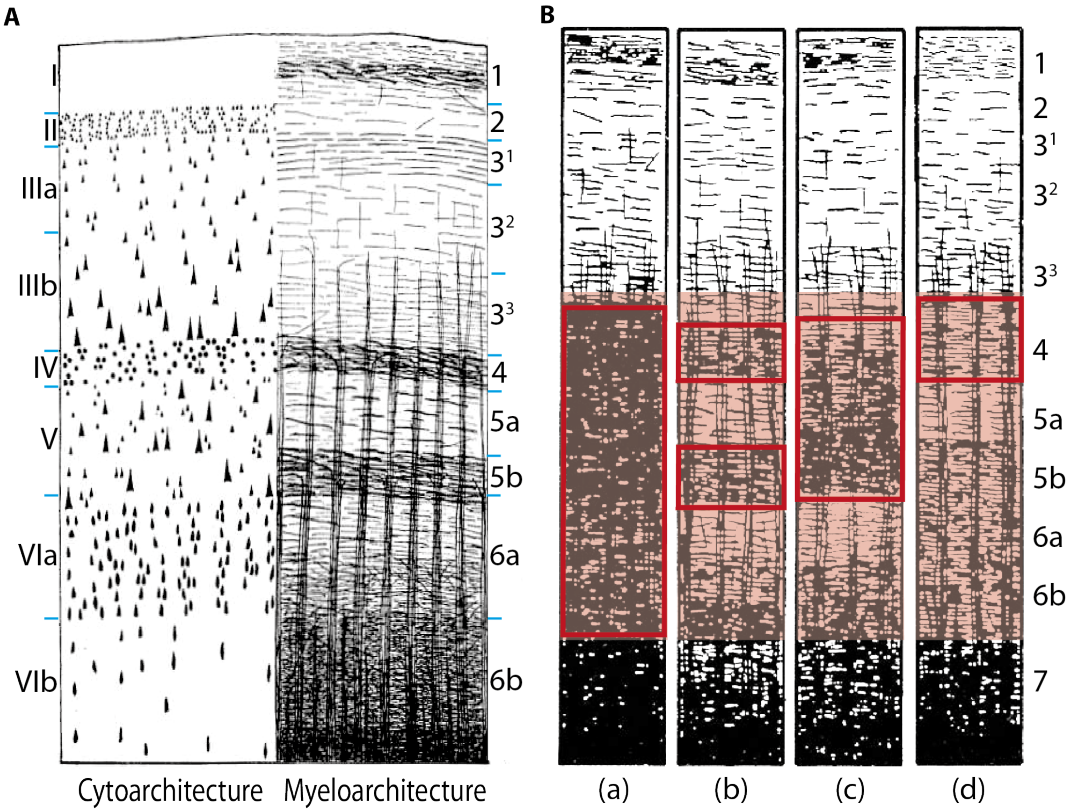

Figure 2.11: A) The two images illustrate the relationship in cortical microarchitecture between cyto- and myeloarchitecture. On the right side, we can see the two (darker) bands of Baillarger [Baillarger, 1840], two heavily myelinated transverse layers. The outer band usually coincides with cytoarchitectonic layer IV (*Lamina granularis interna*) and the inner band with cytoarchitectonic layer V (*Lamina pyramidalis interna*) [Vogt, 1910]. B) The illustrations depict the four different types of myeloarchitecture remodelled from Hopf [1956] and Hopf and Vitzthum [1957]: a) astriate, b) bistriate, c) unitostriate and d) unistriate.

or no striation at all (see Fig. 2.11B). The unistriate and unitostriate type both describe one band being visible. The unistriate type (Latin from *unus* meaning one) covers only a single band while the unitostriate type (Latin from *unite*) describes the fusion of multiple layers to a single visible one. The bistriate type has two visible bands. In contrast, the astriate type is so heavily myelinated that no individual bands are discernible.

By analysing the bands of Baillarger and their position in cortical depth, their thickness, and their intensity of myelination, Hopf found an additional local categorisation into three minor types: an **inner**, an **outer** and an **equally dense** myelinated type, depending on whether one of the bands, inner or outer, is more highly myelinated or whether both are equally myelinated.

In conclusion, the upper cortical layers (1–3) are less myelinated than the lower cortical layers (4–6).

In myeloarchitectonic studies, scientists always referred to the layers using Arabic numerals 1 to 6.

2.3.2.1 *Myeloarchitectonic Definitions of the M1/S1 Region*

In general, all areas contained in the M1/S1 region belong to two types of myeloarchitecture. Area 4, in the precentral gyrus, is of astriate type while all areas in the postcentral gyrus are of bistriate type. Here, the Baillarger stripes are very distinct.

PRIMARY MOTOR AREA: M1 With respect to myeloarchitecture, the primary motor area 4 (Vogt and Vogt [1919a,b,c]: areas 38-42) is the strongest myelinated region within the cortex. The myelination pattern within this area can be divided into two divisions closely following the cytoarchitectural distinction between locations containing large pyramidal cells and locations containing giant pyramidal cells by von Economo and Koskinas [1925]. The lower cortical layers are stronger myelinated correlating with the distribution of pyramidal cells. Due to these highly myelinated lower layers, area 4 is of astriate type. Very rarely, the outer Baillarger stripe is distinguishable. According to Hopf [1956] area 4 is equally dense myelinated. The boundary towards WM is unsharp. The outermost layer 1 reveals some tangential, myelinated fibres which are more characteristic in locations containing giant pyramidal cells. In layer 4, the myelination gradually increases towards WM. Below layer 4 the myelination becomes even stronger such that lamination in terms of Baillarger striping is not distinguishable.

PRIMARY SOMATOSENSORY AREA: S1 In area 3b, i. e., Vogts' area 69, the boundary between GM and WM is very sharp. Rarely, thick radial incoming fibres are visible. Layer 1 and 2 are poor in fibres. In layer 3 Vogt observed medium-sized single fibres, whereas layer 4 is composed of many thick horizontal single fibres. Thus, the outer Baillarger stripe appears visually stronger, relatively thicker, but not densely myelinated. Layer 5a is bright and small. In contrast, layer 5b appears dark, densely myelinated and contains to a large portion thick single fibres. Layer 6a appears brighter. Hence, both Baillarger stripes are visible, but the inner one is more pronounced.

Other authors find no agreement with Vogts' published results. Actually, Smith [1907] and Mauss [1911] results contradict those of the Vogts in particular in area 3b. Elliot Smith claimed that area 3b is of externodense type, i. e., the outer band of Baillarger is higher myelinated. Mauss even states, that area 3b is of astriate type, i. e., no stripe of Baillarger is visible due to a very dense myelination in the lower cortical layers. This debate shows again that results and studies on myeloarchitecture highly depend on the subjective opinion of the scientist and on the used staining technique which reveal high differences in the anatomical structural images and bring confusion into their interpretation, too. These issues will be discussed in further detail in Chapter 3. To the pioneers of myeloarchitectonic studies quantitative methods were not available in the early 20^{th} century. In cytoarchitectonics, the published trends of quantitative measures such as the cell counts, the cell sizes and the layer thickness follow the same characteristics. Thus, the results provided by Meynert [1868], Betz [1874], Brodmann [1909] and von Economo and Koskinas [1925] are in much better agreement with each other.

SOMATOSENSORY REGION: AREA 1 Posterior of area 3b, area 1 can be found at the gyral crown, i. e., Vogts' area 70 [Vogt and Vogt, 1919a,b,c]. This area reveals

an unsharp boundary between GM and WM, is of bistriate type and equidense with large single fibres in layer 4 and 5b. Thus, both Baillarger stripes are visible and none of them predominates the other.

SOMATOSENSORY REGION: AREA 2 Area 2, i.e., area 71 in Vogt and Vogt [1919a,b,c], is contained in the posterior sulcal wall of the postcentral gyrus. This area is of bistriate type, too, and externodense. The outer Baillarger stripe is more pronounced than compared to the inner one.

2.4 RELATIONSHIP BETWEEN CYTO- AND MYELOARCHITECTURE

Cyto- and myeloarchitecture reflect cortical microarchitecture [Nieuwenhuys, 2013] and, hence, there might be a relationship between these two domains.

Nowadays, cytoarchitecture is the best analysed architecture of the cortex. Information includes quantitative measures on cell configuration and even 3-dimensional (3D) probabilistic atlas mapping in standard MNI reference space [Eickhoff et al., 2005b]. The discipline of myeloarchitecture has been largely neglected since the classical works. Information is passed on in form of descriptions or hand-drawn illustrations. Little has been done up to now to develop more objective quantitative measures and criteria. Myeloarchitectonic mappings are still incomplete or contradict each other.

As a conclusion, Campbell [1904] already suggested that cytoarchitecture and myeloarchitecture have to be analysed in conjunction as they are both part of the same cortical architecture. Furthermore, Brodmann considered the Vogt's work as a basis to further subdivide cytoarchitectural zones into smaller functional fields. This discussion is related to the degree of spatial localisation and is not intended to let cyto- and myeloarchitecture diverge.

Half a century later, Sanides [1962] found that:

1. "the total amount of myelin in a given area is positively correlated to the cell body sizes in this area" and

2. "in regions where a cortical layer containing large cell bodies is situated above a layer in which the neurons are smaller or less densely packed, a horizontal stripe of myelinated fibres appears above a layer where horizontal fibres are less evident".

Sanides' second finding has been further investigated by Braitenberg who tried to explain these phenomena with the help of horizontal myelinated fibres [Braitenberg, 1962, 1974]. These fibres correspond to axonal collaterals of pyramidal cells. As observed in Golgi preparations, the majority of these axonal collaterals branch off the descending main axon 200–300 µm below the cell body. The pyramidal cells, most conspicuous in cytoarchitectonic layers III and V of Nissl preparations, thus produce two maxima of horizontal fibres. These maxima, shifted downwards relative to layers III and V by 200–300 µm, account for the two stripes of Baillarger (see Fig. 2.11A). Braitenberg's explanation was supported by several other studies [Le Gros Clark and Sunderland, 1939; Creutzfeldt et al., 1977; Gatter et al., 1978; Colonnier and Sas, 1978].

Indeed, there is a structural mismatch between cyto- and myeloarchitectonic layers. The axonal collaterals of larger cells (especially pyramidal cells in cytoarchitectonic layers IIIb and V) form fibre bundles in deeper myeloarchitectonic layers (see in Fig. 2.11A, compare cytoarchitectonic layer IIIb and V to myeloarchitectonic layer 4 and 5b). First quantitative measures on the distribution of such axonal collaterals were provided by Paldino and Harth [1977].

Up to now, a 3D probabilistic myeloarchitectonic atlas mapping is inexistent. However, the question targetting the correspondence between cytoarchitectonic and myeloarchitectonic boundaries can only be answered with an atlas.

EXPECTATIONS REGARDING IN-VIVO ANALYSES When investigating the intracortical features in human brains, any imaging data needs to correctly reflect the anatomical relationships. Given, that modern in-vivo imaging yields a resolution of up to 0.5 mm, the aforementioned descriptions of cells, their size and density in specific layers translate into a more general expectation on the distribution of myelin in the cortex.

The size of the cells can vary between individual brains. Within a single brain, the cell size varies most in pyramidal cell layers III and V. The cell density varies mostly in granular layer IV. The features primarily defining the characteristics of an area are cell size, cell density and the relative thickness of the layer they can be found in.

Primary areas are stronger myelinated. Non-primary areas containing large pyramidal cells, like in Broca's region, are higher myelinated, too. When the WM/GM boundary is hard to determine in cytoarchitecture, the boundary should be less distinct in myelin representations, too. When imaging the brain in-vivo, these expectations should be represented.

The bands of Baillarger should be detectable in area 1 and Broca's region as the bands easily cover 30 % of cortical thickness. In area 4, no distinct lamination is expected, but a thick strong myelinated stripe covering the bands of Baillarger to appear. Given that area 1 and 4 are similar in their cytoarchitectonic definition, they should reveal similarities in myelin distribution, too. Von Economo and Koskinas [1925] proposed that area 1 and 2 could be one single area. This leads to the expectation that area 1 and 2 may be hard to distinguish using different imaging modality.

2.5 NEURODEGENERATIVE DISEASES: A CLINICAL PERSPECTIVE

Neurodegenerative diseases are diseases or disorders related to neurodegeneration. The word "neurodegeneration" refers to "neuro" as in nerve cells and to "degeneration" as in progressive damage. In general, neurodegeneration is involved in several clinical conditions that lead to progressive loss of brain structure and function. These damages affect many of our everyday life actions such as movement, talking, thinking or even vital functions such as breathing or cardiac function [MedlinePlus, 2014]. Neurodegenerative diseases have various causes [Bear et al., 2007]. They may:

- include medical conditions such as a tumor or a stroke.

- be related to drug consumption (alcohol, nicotine, soft and hard drugs).
- include toxins, chemicals, and viruses.
- be genetically related.

There are also diseases that have an unknown cause.
Some well known neurodegenerative disorders are:

- Alzheimer's Disease (AD)
- Parkinson's Disease (PD)
- Huntington's Disease (HD)

The neurodegenerative diseases are serious and, depending on type, even be life-threatening. They have no cure and current treatments can only help to improve the symptoms, to relieve the pain, and to increase the mobility.

All three diseases show different clinical features. However, in all three cases the disease starts at the cellular level [Gerlach et al., 1994; Wilms et al., 2007]. In PD, dopamine-generating cells die in the substantia nigra, a region of the midbrain and cause stiffness, rigidity and tremors in the major muscles of the body. In AD, deposits of tiny protein plaques damage different parts of the brain and lead to progressive loss of memory. HD is a progressive genetic disorder that affects major muscles of the body leading to severe motor restriction and eventually death.

FOCUS OF RESEARCH Research focuses on the similarities in neurodegeneration that occur in all of these three diseases. Cell death and deposition of abnormal proteins and plaques is a feature common to all the mentioned disorders. In general, the disorders become apparent, when functional or behavioural symptoms and impairments are visible, e. g., at a stage when the brain is already damaged. New hope rises through better imaging technology. Up to now, imaging at cell level in living brains is impossible. New imaging techniques allow to map quantitative physiological parameters such as myelin in the brain. If myelin content changes in certain areas of the brain, it is preceded by cellular structural changes.

These advanced imaging techniques raise hope that the clinical conditions and their effect on the structure-function relation in the brain will be understood better in the future. This will, in turn, help:

- to identify the onset of the diseases by looking at structural changes in the brain using high-resolution in-vivo magnetic resonance imaging, and,
- to understand the physiological and chemical signaling changes in the brain during the development of such diseases.

Ultimately, such a development leads to an improvement in therapy towards the specific needs of each patient. It may further suppress and delay disabling effects such as cognitive impairments or comprised mobility.

HEALTH ECONOMY ASPECTS The disabling effects related to the diseases such as cognitive impairments and/or compromised behavioural activity or mobility may continue for years or even decades when being first diagnosed. The overall disease burden[2] is therefore much greater than would be suggested by mortality figures alone. Brain disorders emerge as leading contributors to global disease burden. Economic costs of brain diseases are comparatively large. In Europe, Andlin-Sobocki et al. [2005] estimated the brain disorders' total cost to be 386 € billion per year in 2004 (this figure includes direct costs of treatment and care plus indirect cost of lost workdays and lost productivity). This figure is twice the estimated cost of cancer. More recently, [Gustavsson et al., 2011] estimated the total cost in 2010 to be 798 € billion (including a wider range of disorders and costs, and new EU member countries), of which 60 % was attributable to direct costs and 40 % to lost productivity.

Specifically, AD and other dementias have a disproportionate impact on countries with longer life expectancies. They represent the fourth highest source of overall disease burden in the high-income countries, according to World Health Organisation (WHO) statistics. Worldwide, Alzheimer's Disease International [2014] estimated that there are 35.6 million people with AD worldwide as of 2010, and that this number will grow to 115.4 million people by 2050. The economic cost of AD is already enormous, and is expected to grow rapidly as more people live to a greater age with more serious impairments. Also, Alzheimer's Disease International [2014] estimated that for 2010 the global cost of dementia (of which Alzheimer's is the major cause), including medical costs and cost of formal and informal care, is $604 billion - about 1 % of world gross domestic product. The costs are disproportionatetly high in wealthy countries. In the US, for example, the Alzheimer's Association estimated that the cost of providing care for AD patients is $200 billion per year, as of 2012. If present trends continue, this cost is projected to grow to $1.1 trillion per year by 2050 (in US $ by 2012).

2.6 SUMMARY AND CONCLUSIONS

In this chapter, the fundamentals of cortical architecture, namely cyto- and myeloarchitecture, have been described. It has been shown that they generally interlink each other. But analysis methods, may they be of manual or computational nature, are mostly established for cytoarchitecture only. A precise common understanding of the myeloarchitectonic representation in the human cortex and quantitative measures relating to it do not exist yet.

Brain diseases directly relate to deformations of one or even both architectures. With new imaging methods, it is possible to detect changes at sub-millimetre level already. This enables scientists to derive first in-vivo descriptions of the myeloarchitecture and allows them to study architectures in a combined setting. This will gather a better understanding of the brain, its organisation and function in healthy and diseased states.

2 A disease burden respects all negative effects besides suffering due to the manifestation of illness. They include the cost of treatment and the lost productivity of patients. But they also cover costs related to caregivers, who look after their chronically disabled family members.

This thesis aims at using intracortical myelin-based features to build new analysis tools in order to support structure-function mappings and cortical parcellation methods.

The fundamental discussions in the field of structure-function mapping, that directly link to cyto- and myeloarchitectonics, are related to the number and extent of cortical areas:

- Is a transition zone between two clearly separable areas an independent area itself?
- And, if so: what do these newly defined areas represent?

Another issue addresses the correspondence between cytoarchitectonically and myeloarchitectonically defined boundaries:

- To what extent and where do the areal boundaries of cytoarchitectonically and myeloarchitectonically defined regions overlap?
- To what extent and where do they disagree?

The most interesting question in the neuroscience community is: "why?". This thesis does not aim and cannot answer the "why?"-question. However, the aforementioned questions have no common consistent answer yet. Without consistency and/or agreed knowledge in the definition of myeloarchitecture, correlations between cyto- and myeloarchitecture cannot be well studied. The ongoing discussions are not meant to disproof findings in one or the other discipline. New findings are driven by the goal of finally understanding these structures as one cortical unity. Data, reflecting the myelin distribution in the cortex, and proper parcellation approaches that respect the cortical anatomy may be helpful as a first step towards understanding the myeloarchitectonic patterns in the brain.

3 BRAIN IMAGING TECHNIQUES

There are many ways to study and look into the brain. In the past, postmortem derived brains were cut into pieces or sections and stained to study the brain's anatomy and composition known as classical histology. Nowadays, the main goal is to investigate the living brain. Noninvasive techniques like Magnetic Resonance Imaging (MRI) allow to study the structure-function relationship in the brain as well as diagnostic imaging and imaging over the course of an applied therapy.

Although Computed Tomography (CT) and Positron Emission Tomography (PET) provide high resolution 3-dimensional (3D) data in a very short time at relatively low costs, those techniques are associated with high risks for the patients as they are exposed to the image forming radiation. The primary drawback of CT and PET is the low contrast in soft tissue matter. When investigating the brain, soft tissue matter such as GM and WM are the main target.

MRI techniques are able to provide good contrast when imaging brain tissue. They are noninvasive, but more complex and expensive. Recently, MRI has caught up in image resolution as well as comparability and reproducibility of contrast which have been a major problem in the past. In addition, MRI helps to further optimise structural imaging by relating imaging parameters and outputs to classical histology. These investigations answer questions regarding the feasibility of imaging even smaller microstructures in the brain.

This chapter is dedicated to brain imaging methods, in particular to structural Magnetic Resonance Imaging. MRI has strong underpinnings in physics which will be described in Section 3.1. The focus is put on up-to-date quantitative imaging methods (Section 3.2). The different contrasts used will be explained as well as imaging artefacts and current imaging limitations. An overview of other MRI techniques used in cortical area studies and their underlying physical phenomenon will be briefly presented in Section 3.3. Classical histology is still regarded as gold standard to identify changes in the structural configuration of areas. In this thesis, conventional histology is used for verification purposes. Therefore, staining methods, their advantages and disadvantages will be shortly described in Section 3.4. The chapter closes with a summary.

As this thesis focuses on fundamental research, only healthy brains have been investigated. No contrast agents or sedation have been applied to the subjects. The following sections will disregard these additional techniques. Waters and Wickline [2008]; Merbach and Tóth [2001] and Mayhew [2005] provide details on using contrast agents and sedation for MRI.

3.1 MAGNETIC RESONANCE IMAGING

This section describes the underlying physics of MRI and includes topics of signal generation and localisation as well as final image reconstruction. The section further introduces how different contrasts are generated. Finally, relevant scan-

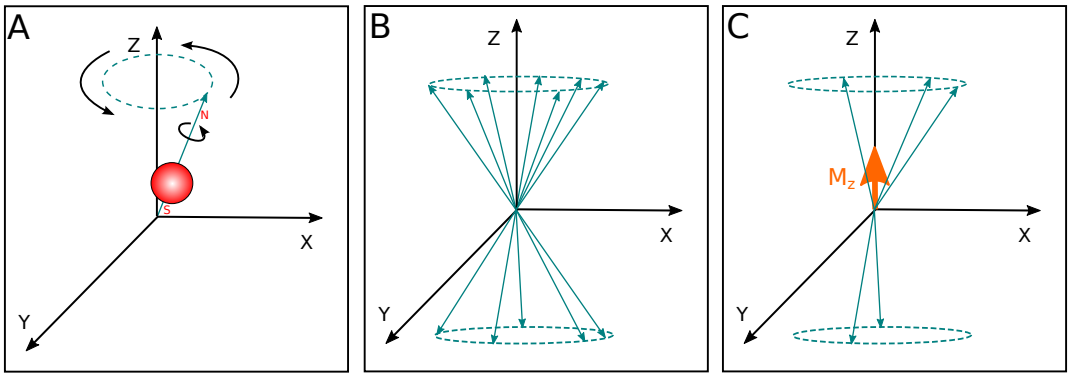

Figure 3.1: A) The image depicts a proton (simplified as red sphere) spinning around its own axis (green arrow) due to the magnetic moment. The magnetic moment describes the alignment of the proton within an external magnetic field, here assumed to be in z-direction. When an external magnetic field is applied, a secondary spin, called precession, is produced (dashed circle around z-axis). B) shows the alignment of several protons within a magnetic field: parallel (preferred direction) or anti-parallel (negative z-direction) to the main magnetic field. C) Protons in different states have equal but opposite magnetic moments. They cancel each other out yielding a macroscopic magnetisation M_z pointing into the direction of the main magnetic field.

ning parameters defining the relationship between signal and data resolution are discussed.

3.1.1 *Physical Framework*

Every substance or object is made up of atoms. Every atom is composed of electrons and a nucleus which in turn is made of protons and neutrons. The orbiting electrons cause the atoms to have a magnetic moment associated with an intrinsic angular momentum called **spin** (see Fig. 3.1 A). As a result of the orbiting electrons in atoms, the matter the atoms reside in develop a magnetic property. Protons and neutrons pair up in the nucleus and cause the cancellation of their individual angular moments. Atoms with an odd number of protons and/or neutrons have a property call magnetic (dipole) moment. The magnetic moment describes the alignment of the spinning proton with an external magnetic field and can therefore be seen as a small bar magnet. As all bar magnets, the protons have two poles, i. e., a north and a south pole, and are therefore also called dipoles. Hydrogen-1, i. e., H^1, has no neutrons. As H^1 is mainly used for human body imaging and specifically exploited to image the brain in this thesis. The term **protons** and **nucleus** will be used synonymously.

If an external magnetic field is applied to the substance or object with non-zero nuclear spin, two processes happen:

- the protons **align** with the applied magnetic field, and
- the external magnetic field exerts a torque on the magnetic moment, causing a precession of the protons around the main magnetic field (see Fig. 3.1 A).

In MRI, the precessional frequency is called **Larmor frequency** and describes the rate of precession of the magnetic moment of the proton around the external magnetic field.

When placing a substance into a static magnetic field B_0, the precessional frequency of protons in the substance can be calculated from the Larmor Equation as follows:

$$\omega = \gamma B_0 \tag{3.1}$$

where ω refers to the Larmor frequency (in MHz), γ describes the gyromagnetic ratio (in MHz/Tesla), and B denotes the strength of the main magnetic field (in Tesla). The gyromagnetic ratio of H^1 is $42.5\,\mathrm{MHz\,T^{-1}}$ and implies a rate of 42.5 million precessions per second when a hydrogen proton is placed in a magnetic field of strength 1 T.

From the aforementioned equation, the frequency of precession is proportional to the strength of the magnetic field. Changing the field strength will affect the Larmor frequency at which the protons precess.

In brain imaging, human clinical MRI scanners typically use field strengths between 0.1–3 T. In comparison, the strength of the earth's magnetic field is about 50 µT, i. e., about 2000–60 000 times smaller. In research, human brain scanning is performed at >11 T, non-human brain scanning even reaches >21 T [Sharma, 2009]. Imaging capacities will be further investigated in future to study the human brain using ultra-high field structural and functional MRI [Duyn, 2012].

If a strong external magnetic field is applied, the protons align corresponding to the field in one of two directions parallel to the direction of the field:

- protons align to the direction of B_0, i. e., parallel to the external magnetic field, or
- protons align to the opposite direction of B_0, , i. e., anti-parallel to the external magnetic field.

Two hydrogen protons in **parallel** and **anti-parallel** states have equal but opposite magnetic moments and cancel each other out (see Fig. 3.1 B). The protons preferably align parallel to the magnetic field, as they are at a lower energy level in this position. For every 1 000 000 protons, there are about seven additionally parallel aligned protons. This yields a macroscopic magnetisation in the direction of the external field (see Fig. 3.1 C).

The two different alignment states correspond to an energy difference, ΔE. For typical magnetic resonance applications, the energy difference ΔE is equivalent to the energy of electromagnetic radiation in the radio frequency region of the electromagnetic spectrum.

3.1.2 *Relaxation and Contrasts*

Placing a tissue sample in a magnetic field of 1 T and exposing it to radio waves at $42.5\,\mathrm{MHz\,T^{-1}}$, i. e., a radio frequency (RF) pulse, the protons of the tissue will get excited from the parallel to the higher energy anti-parallel state. They can switch

between higher and lower energy state, e. g., they are susceptible to this radiation only, if their precession frequency is close to the frequency of the applied RF pulse. This phenomenon is called **resonance** and gives the here discussed imaging modality its name: magnetic resonance imaging. Strictly speaking, MRI techniques exploit the processes following the excitation of protons. When the RF pulse is switched off, the protons fall back to the aforementioned equilibrium state. This process occurs spontaneously over a time period that is characteristic of individual tissues and/or their various pathological conditions.

Those gradual flip back transitions between the energy states cause the emission of radiation from the tissue sample and decrease in amplitude over time. Hence, it produces what is known as a **free induction decay**, i. e., a decay signal of characteristic time constant.

There are various time constants in MRI that can be determined and encoded into images (discussed next sections). The emitted signals are detected through receiving devices and can be reconstructed when the signal origin is known.

Here, the processes of signal induction in the tissue and their defining contrasts in MRI will be discussed.

THE NET MAGNETISATION The net magnetisation vector M in MRI refers to the sum of all magnetic moments of the individual hydrogen protons in a discrete spatial environment. If an external magnetic field is absent, the individual magnetic moments are randomly oriented and their magnetisation vector is approximately zero. If the external magnetic field B_0 is applied, the magnetic moments of the protons align with the direction of the magnetic field. The magnetic moments of parallel and anti-parallel protons cancel each other out (see Fig. 3.1 C).

Conventionally, the spatial z-axis is thought to be in the direction of the external magnetic field. Hence, the net magnetisation vector can be referred to as **longitudinal magnetisation**. As there are always a tiny number of more hydrogen protons parallel to B_0, a longitudinal magnetisation establishes in a substance inside the magnet of an MRI scanner (see Fig. 3.1 C). The longitudinal magnetisation is defined by M_z, i. e., the z-component of the net magnetisation vector.

EXCITATION OF PROTONS On a macroscopic level, applying an RF pulse with the Larmor frequency to the protons in the substance causes two independent processes to occur simultaneously:

REDUCTION OF M_z: some protons resonate with the applied RF pulse and change to the anti-parallel state. Parallel and anti-parallel protons cancel each other out resulting in a reduction of the longitudinal magnetisation (see Fig. 3.2 A).

PHASE COHERENCE: magnetic moments of individual protons align with each other in phase which in turn creates a new component of the net magnetisation vector M in the X-Y plane, i. e., transverse to the main magnetic field. This established magnetisation is called **transverse magnetisation** M_{xy} (see Fig. 3.3 A).

In essence: when a substance is placed into a magnetic field of sufficient strength, a longitudinal magnetisation is established. By applying an 90° RF pulse with the

resonant frequency, the longitudinal magnetisation is reduced and a transverse magnetisation component is created. M_z rotates away from the B_0 field from a longitudinal position into the transverse. M_z rotates a distance proportional to the time length of the RF pulse. If a 90° pulse is applied, M_z rotates 90° and lies in the transverse. Using other degrees of the RF pulse are possible, but will result in different contrasts [Bernstein et al., 2004].

In MRI, only the transverse magnetisation can be detected. The angle that M rotates is called the **flip angle** (or tip angle). A small detectable magnetisation in the z-plane will remain, if the angle is greater than or less than 90°.

For MRI image acquisition, the net magnetisation vectors are now of greatest interest.

RELAXATION OF PROTONS By absorbing RF energy at the resonant frequency, the protons are excited. When protons return to their lower energy state, they emit energy in form of electromagnetic radiation over time. This emission phase is called **relaxation**. The relaxation time denotes how fast the magnetisation vector M recovers to its ground state within the main magnetic field B_0 when the RF pulse is switched off. The return of excited protons from a high energy state to a lower energy state is associated with a loss of energy to the surrounding environment called "lattice" or neighboring protons. When the RF pulse is switched off, protons start to dephase due to external and internal magnetic field inhomogeneities. The external magnetic field, B_0 slightly varies and causes different precession frequencies. Internally, every protons is subject to the the magnetic properties of the surrounding protons. Neighboring protons are randomly distributed and cause different precession frequencies.

There are three forms of relaxation called T_1 relaxation, T_2 relaxation and T_2^* relaxation. Given the individual properties of tissues, the main goal of using MRI is to characterize tissue types based on their relaxation times.

Here, both longitudinal and transverse magnetisation will be discussed.

LONGITUDINAL RELAXATION: After the application of the RF pulse, the net magnetisation vector M_z is zero. Progressively, excited protons return to their lower energy state, i. e., the parallel alignment with the main magnetic field, (see Fig. 3.2) which yields a re-establishment of the longitudinal magnetisation M_z.

TRANSVERSE RELAXATION: After the application of the RF pulse, the transverse net magnetisation vector M_{xy} is at maximum and the individual magnetic moments are in phase coherence with each other. Progressively, the excited protons loose coherence and the transverse magnetisation decreases to zero (see Fig. 3.3).

The $\mathbf{T_1}$ **relaxation time** measures how fast the z-component of the magnetisation vector M, recovers to its ground state and is therefore called longitudinal relaxation time. The recovery of M_z can be modelled as an independent and exponential process.

T_1 describes the time until 63 % of the original longitudinal magnetisation is recovered and thus the average lifetime of a proton at the excited energy state. T_1 relaxation rate is defined as $1/T_1$.

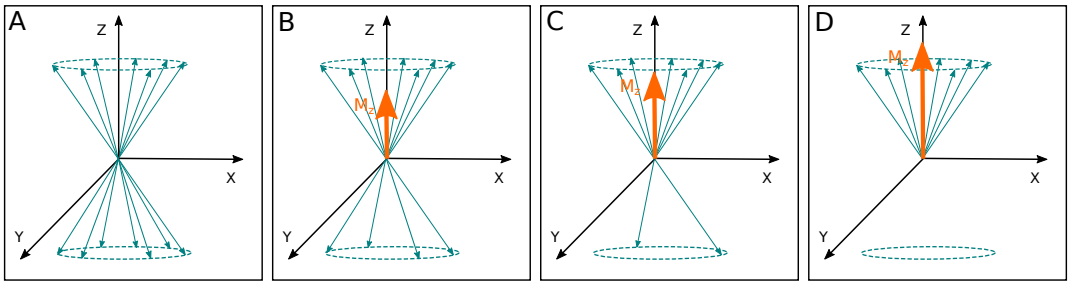

Figure 3.2: The images depict the recovery of the longitudinal magnetisation M_z after the RF pulse has been applied. A) The net magnetisation vector is zero. Excited protons are on a higher energy level. Progressively (B-D), the excited protons return to their lower energy state, i. e., the parallel alignment with main magnetic field, until the longitudinal magnetisation is fully recovered.

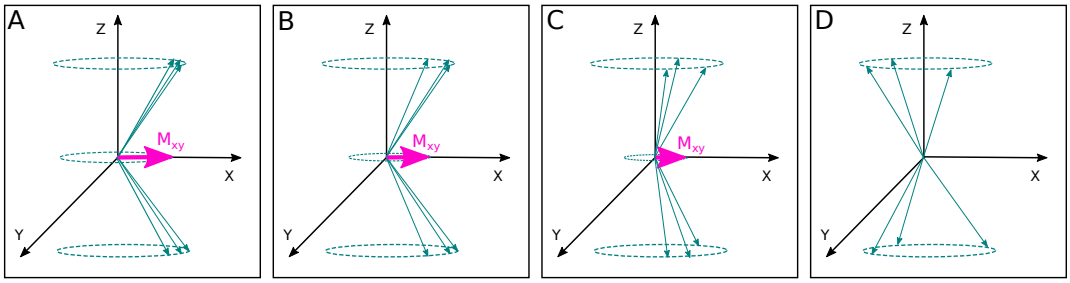

Figure 3.3: The images depict the decay of the transverse magnetisation M_{xy} after the RF pulse has been applied. A) The net magnetisation vector is at maximum. Excited protons are in phase coherence. Progressively (B-D), the excited protons loose their coherence and the transverse magnetisation fully decays to zero.

In different structures, T_1 relaxation times are different. On a molecular level, all protons in any sort of material are enclosed in an environment, the so-called lattice or lattice structure. T_1 relaxation is also referred to as spin-lattice relaxation. In this lattice, the protons are subject to vibration and rotation. This movement within the lattice generates a complex magnetic field, called lattice field. Protons from higher and lower energy states can interact with each other, causing a distribution of energy of the higher energy state among protons. The energy absorbed from the RF pulse is released back into the lattice field and increases the fluctuation of the lattice, i. e., rotation and vibration of protons. High mobility means low binding energy between respective atoms. If the mobility of the lattice field increases, the frequency of vibration and rotation of protons increase. When the frequency of the moving protons in the lattice reaches its Larmor frequency, it allows the protons to switch back from high energy state to low energy state. Thus, T_1 relaxation depends on magnetic field strength (see Eq. 3.1). With increasing field strength, T_1 relaxation times increase, too (see Fig. 3.4 A).

The **transverse relaxation time T_2** describes the decay constant for the component M_{xy} of M that is perpendicular to B_0. The initial magnetisation in x-y-plane at time zero, i. e., directly after the RF pulse, is at maximum and will decay to zero exponentially.

T_2 describes the decrease of the transverse magnetisation to 37 % of its original magnitude. The T_2 relaxation rate is again given by $1/T_2$.

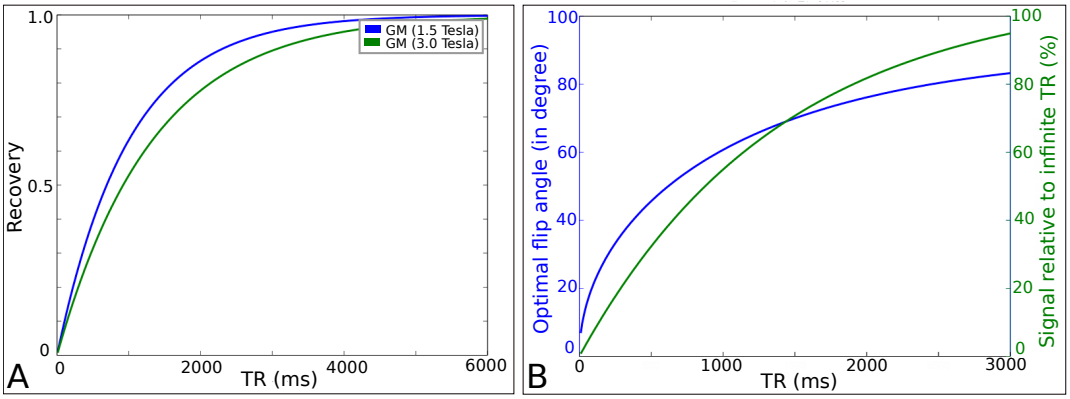

Figure 3.4: A) T_1 relaxation time in GM shown at 1.5 T (blue) and 3 T (green). T_1 relaxation times depend on the field strength used for imaging. With increasing field strength, T_1 relaxation times increase. (Image adapted by work of Chris Rorden: http://www.mccauslandcenter.sc.edu/CRNL/teaching/mri.)

T_2 relaxation is a very complex phenomenon and characteristic for certain tissues. It corresponds to the progressive dephasing, i. e., the increasing decoherence of the transverse magnetisation of the protons. The main contribution are random fluctuations of the local magnetic field of one proton caused by the surrounding protons. Therefore, it is often called spin-spin-relaxation time. Inhomogeneities in the local magnetic field of a proton lead to random variations in the precession frequency of the surrounding protons. This process leads to a progressive loss of phase coherence, until (theoretically) phases are disordered in the x-y-plane and i. e., M_{xy} is zero. T_2 values are generally much less dependent on the magnetic field strength, B_0, than T_1 values.

In an idealised system, all protons in a given lattice environment precess with the same frequency when being exposed to a homogeneous magnetic field. In reality, minor field fluctuations occur which lead to a distribution of resonance frequencies. Over time, these differences lead to dephasing and loss of net magnetisation, i. e., a free induction decay. This "relaxation" impairs the majority of MRI experiments.

Dephasing due to magnetic field inhomogeneity is not an actual relaxation process. This dephasing is not random and depends on the location of the protons in the magnetic field. Protons that aren't moving reveal a consistent deviation from an ideal relaxation over time. The transverse relaxation time including the inhomogeneity dephasing is called T_2^* and is much smaller than T_2.

SIGNAL AND CONTRAST DEPENDING PARAMETERS In the previous section, a single signal measurement has been considered in which the net magnetisation vector has been rotated into the transverse plane and therefore M_z is set to zero. After a certain time, a change of magnetisation, e. g., a signal, is available to be measured. As mentioned above, various tissues have characteristic relaxation times. Therefore, the signal depends on these relaxation times, but also on the proton density within the tissue. The measurement of the signal is called TE, i. e., the "time to echo", representing the time that provides the best contrast, e. g., largest signal difference, between different tissues. If TE is chosen to be short, not much difference between the signal amplitudes of tissues will have developed. When

using longer TE, however, a larger difference between the signal amplitudes of tissues will have developed. Thus, using a longer TE enhances the differences in signal originating from differences in the T_2 relaxation of tissues. Using a longer TE produces so-called T_2-weighted images.

In MRI, a large number of such single signal measurements are required. Applying multiple RF pulses in a row yields a so-called **pulse sequence**: the net magnetisation vector is rotated into the transverse plane, an amount of time TE is waited for to allow M_z to recover, followed by the next rotation into the transverse plane for the next signal measurement. The time waited before conducting the next repetition is called TR, i. e., the "time to repeat". Using a short TR leads to the development of a large difference between the magnetisation of tissues. Using a longer TR yields a reduced difference between the signal amplitudes of tissues. An application of a shorter TR enhances the differences in signal originating from differences in the T_1 relaxation time of tissues. Using a shorter TR generates so-called T_1-weighted images.

"Weighting" of the images only describe that the image taken is dominated by one specific tissue parameter to the exclusion of all others. Nearly all images have mixed contributions from all the different tissue parameters such as T_1, or T_2, or from imaging artefacts (see Section 3.2.4).

In general, the signal and contrast of any MRI data can be defined and optimised using appropriate parameter settings of TR and TE in a pulse sequence. To do so, measures of signal and image quality need to be defined: The Signal-to-Noise Ratio (SNR) defines the ratio of signal power S to the power of background noise o as:

$$\mathrm{SNR} = \frac{S}{S_o}. \tag{3.2}$$

Contrast-to-Noise Ratio (CNR) determines the image quality and relates to the general ability to separate structures rather than the pure signal intensity. CNR is similar to SNR, but before taking the ratio, a term is subtracted off. This is important when there are significant biases or inhomogeneities influencing the image. CNR is defined by:

$$\mathrm{CNR} = \frac{|S_A - S_B|}{\sigma_o} \tag{3.3}$$

where S_A and S_B represent the signal intensities for the signal producing structures A and B in the region of interest and σ_o is the standard deviation of the image noise. With biases present in the image, it may have high SNR, but will have low CNR.

In MRI, the main goal is to increase SNR and CNR simultaneously. When a higher SNR is needed, the following parameters can be tuned:

- field strength: increasing field strength will increase the T_1 relaxation times in all tissues. Higher field strength can also be used to increase the image resolution.
- scan time: with longer scan times SNR increases. Increasing scan time is commonly exploited when imaging postmortem material.

However, when scanning living subjects, the main goal is to reduce scan time, as longer acquisition times decrease image quality due to motion artefacts (see Section 3.2.4).

3.1.3 *Signal Localisation and Image Reconstruction*

Located inside the main magnet are three so-called gradient coils which produce the desired gradient (magnetic) fields. These fields are used to alter collectively and sequentially the influence of the static magnetic field B_0 on the imaged object by increasing or decreasing the field strength along the applied direction. As each proton resonates at a different frequency depending on the magnetic field it is subjected to, selective spatial excitation and spatial encoding is possible.

The signal generated is called **gradient echos** and refers to echo of the protons by using bipolar gradient fields. The signals are sampled during this gradient echo, i. e., the time when tissues are experiencing T_1 relaxation.

The gradient field can be applied in any direction and there is no need to reposition the subject. As many gradient fields as wanted can be applied.

To relate spatial location of a proton to its emitted signal, MRI divides the sample into a 3D grid consisting of slices, columns and rows.

First, a slice is selected by using a so-called **slice select gradient**. The gradient field has a slope and modifies the magnitude of the main magnetic field along the applied direction. The steeper the slope of the gradient field, the thinner the slices to be acquired. The slice select gradient field will be applied during the RF pulse.

To localise a certain point within the slice two additional gradient fields are used. These fields are called **frequency** and **phase encoding gradient fields**.

The frequency encoding gradient will be applied after the slice selection gradient in y-direction of the x-y-plane, i. e., transverse to the longitudinal direction of the main magnetic field. This gradient yields differences in precession frequencies along the y-direction, and, hence, results in frequency differences of the signal.

The second gradient is the phase encoding gradient which will be applied after the RF pulse in the x-direction of the x-y-plane. It yields differences in precession frequencies along the x-direction. When the gradient field is switched off, protons will slow down to their original frequency. However, due to the applied gradient in x-direction, protons have the same frequency but are phase incoherent. The different phases determine the location of the signal in x-direction. The directions of the frequency and phase coding gradient can be varied. The signals are defined as complex values by frequency and phase.

The signals are aligned in the gradient magnetic field, e. g., the B_1 field and detected by **transmit and receive coils** within the MRI setup. The transmit coil transmits the generated RF pulse, i. e., sends an electromagnetic wave, into the object to be scanned. The receive coil picks up the signal, i. e., another emitted electromagnetic wave, from the protons in the object. The coils are arranged in a transmit/receive system. Sent and detected signals are referred to as transmit B_1^+ and receive B_1^- fields.

A computer now reconstructs the data using a Fast Fourier Transformation that converts the frequency and phase signals into discrete space.

3.2 STRUCTURAL IMAGING OF MYELOARCHITECTURE USING MRI

The main goal in MRI sequence development for the imaging of myeloarchitecture is to find a technique that characterises intracortical properties which relate to a biological substrate. Hence, a technique has the requirements of:

1. producing quantitative measurements of physiological parameters such as the T_1 and T_2 relaxation times,
2. providing sufficient resolution.

Simultaneously, the total scan time should be reduced in order to decrease motion artefacts arising from motion of the subject or motion due to vital functioning of the body such as breathing or heart beat. Finally, a high SNR is favorable, since it allows for automatic segmentation and parcellation of the cortex.

Recent publications provide evidence that MRI techniques, both in-vivo and ex-vivo, are indeed able to reproduce classical results from histology (see next section). In contrast to classical postmortem analyses, in-vivo MRI techniques provide information about the living brain, albeit not at the high resolution of histological images, but still sufficient enough resolution to detect structural as well as functional layer-dependencies in the cortex [Polimeni et al., 2010b,a; Huber et al., 2014; Trampel et al., 2012]. The results allow new discussions on the specific roles of input and output layers. More importantly, there are existing techniques that are able to map myelin, which gives contrast in MRI. Although MRI is not yet able to provide data at "cell" resolution, myelin maps can be used in future applications to relate back to cell organisation as these are interlinked structures (see Section 2.4).

Using MRI techniques to derive maps of myeloarchitecture already allows to study brain development and pathology across population and age.

3.2.1 *State-of-the-Art Methods in Myelin Mapping*

Intracortical contrast was first observed in T_2-weighted and T_1-weighted images. It is argued that T_2-weighted images, created with spin-echo sequences, gain most of their contrast from T_1, proton density differences, and from magnetisation transfer effects, e. g., transfer of longitudinal magnetisation from motion-restricted protons to protons that move with many degrees of freedom [Turner et al., 2008].

Walters et al. [2003] first presented visible layering in the human cortex in postmortem brain samples using T_2-weighted images. The bands visible on the MRI data were verified to be myelinated bands using myelin stained sections. Trampel et al. [2011] were able to capture the stria of Gennari, i. e., a densely and distinct myelinated band in the primary visual cortex, using T_2-weighted in-vivo imaging.

Eickhoff et al. [2005a] presented intracortical bands visible on T_1-weighted images using in-vivo MRI. They provided evidence that these bands correspond to myelinated bands on histological sections. Walters et al. [2003] further related in-vivo cortical structure on T_1-weighted images to its function. Myeloarchitectonic patterns have been shown in-vivo by Clark et al. [1992] and have been confirmed using postmortem analysis, e. g., ex-vivo MRI in combination with histological staining. Similar findings have been presented by Bridge and Clare [2006]; Bridge et al. [2005]; Clare and Bridge [2005]; Hinds et al. [2009]; Annese [2012].

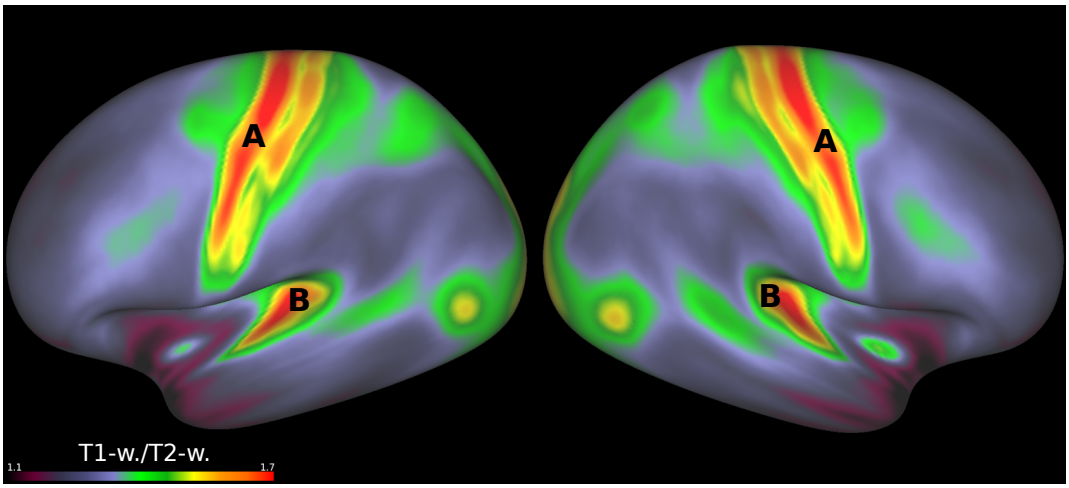

Figure 3.5: The image depicts the left and right hemispheres in lateral view of a group average (N=440) myelin map acquired using a ratio of T_1-weighted/T_2-weighted (in ms) imaging at 0.7 mm resolution [Glasser and Van Essen, 2011]. Highly myelinated regions are shown in red such as primary motor and sensory area (A) and primary auditory area (B). Image prepared by Estrid Jakobsen using the open source Human Connectome Workbench: `http://www.humanconnectome.org/software/connectome-workbench.html`.

The most common way to produce in-vivo average myelin maps is using the ratio of T_1-weighted/T_2-weighted images [Glasser and Van Essen, 2011] (see Fig. 3.5).

Iron and myelin both contribute to T_2^* contrast. The contrast between GM and WM is very high in T_2^* images as iron and myelin often co-localise (see Fig. 3.6). Iron is used by the oligodendrocytes which produce the myelin sheaths around an axon. To which degree either iron or myelin contribute to the MRI contrast is a current field of research [Cohen-Adad, 2014; Stueber et al., 2011]. Iron dominates the contrast in GM [Deistung et al., 2013; Fukunaga et al., 2010; Stüber et al., 2014]. Images of high intracortical CNR are able to reveal bands in various regions of the cortex that correlate with myelinated bands on histological stains [Fatterpekar et al., 2002]. At 7 T, it is possible to acquire T_2^*-weighted magnitude images that are able to reveal layer-specific details in-vivo in reasonable scan times. Deistung et al. [2013] obtained such whole-brain images within a scan time of 17 min. T_2^*-weighted images at 0.4 mm isotropic resolution are able to capture the stria of Gennari in the primary visual cortex [Deistung et al., 2013; Sánchez-Panchuelo et al., 2012]. Cohen-Adad et al. [2012] showed intracortical patterns on T_2^* maps.

A very new research stream follows quantitative mapping of T_1 properties. Due to their clear relation to myeloarchitecture, T_1 maps have been used in a range of studies to visualise the myelination pattern across hemispheres [Sereno et al., 2012; Marques and Gruetter, 2013; Tardif et al., 2013]. Myelination patterns have been used to map primary cortical structures, e. g., in auditory and visual areas, and have been combined with MRI data measuring the function (see Section 3.3) [Dick et al., 2012; Sigalovsky et al., 2006]. Another study compared ex-vivo T_1 values sampled in the primary motor and primary somatosensory cortex with

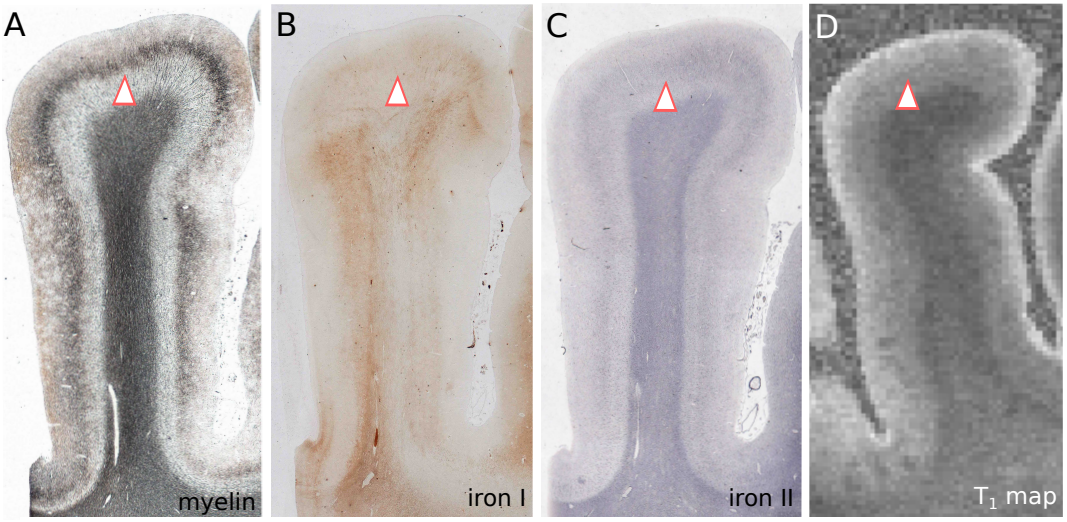

Figure 3.6: Iron and myelin co-localise. Postcentral gyrus stained for myelin (A), iron (classical Perls stain, B), iron (ferritin, C), and scanned with the MP2RAGE sequence at 7 T (D). Image by courtesy of Carsten Stüber.

histology [Geyer et al., 2011]. Primary area classification based on T_1 values is already possible [Waehnert et al., 2013b].

In the following sections, the technological developments towards in-vivo quantitative mapping and their advantages and limitations will be explained and discussed.

3.2.2 *From Weighted Imaging to Quantitative MRI Data*

When scanning living human brains, two parameters need to be balanced:

SCAN TIME: the scan time is mainly given by the sequence and its TR. Leaving resolution and scan-area unchanged, TR needs to be reduced in order to reduce scan time. Reducing the scan time will reduce the amount of motion-related artefacts.

SNR: the quality of every image highly depends on the SNR. Increasing SNR will have a direct influence on other parameters.

IMPACTS OF HIGHER SNR Recent technological innovations in the domain of ultra-high magnetic fields at 7 T lead to better image acquisitions with an increased SNR which permits to get quantitative measurements of relaxation times. Higher SNR can be used to acquire images with higher CNR, or to achieve image resolutions in the sub-millimetre range revealing intracortical details. Higher SNR can also be used to decrease scan time in order to reduce artefacts from subject motion.

USING T_1 TO MAP MYELIN When using a Gradient Echo (GRE) sequence in imaging, typically the free induction decay (FID) will be examined. T_2^* is the characteristic decay time constant associated with the FID. The contrast and the signal that are generated by a GRE depend on two parameters:

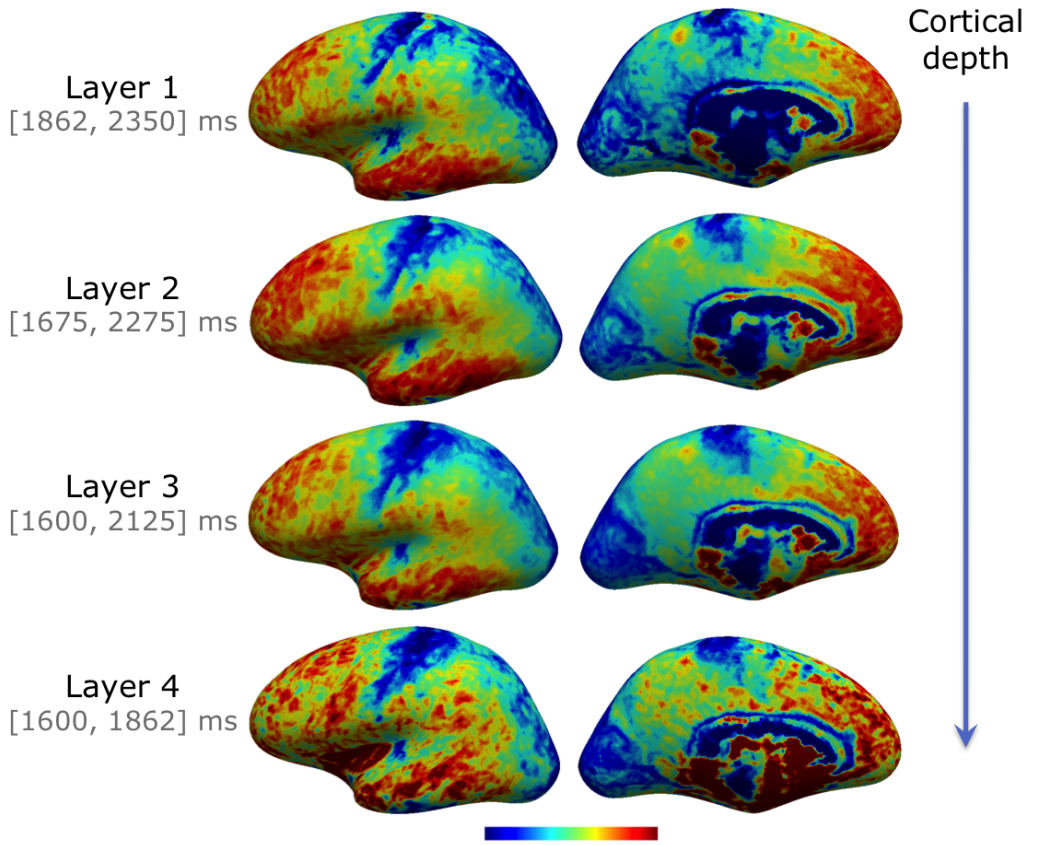

Figure 3.7: Unsmoothed group average T_1 map (N = 5) at 0.4 mm isotropic resolution shown for four different cortical depths. The T_1 time generally becomes longer towards the GM/CSF surface. Thus, the T_1 scales are chosen differently for each layer to highlight the inter-layer differences in T_1 contrast. Image courtesy by Tardif et al. [2013].

1. the magnitude of the longitudinal magnetisation M_z, and
2. the flip angle.

Iron and myelin both contribute to T_2^* image contrast where GM and WM have highest contrast difference. Turner et al. [2008] argued that sequences generating T_2-weighted images gain most of their contrast from T_1, proton density differences, and from magnetisation transfer effects. Stüber et al. [2014] and Turner [2013] provided evidence that in postmortem studies T_1 images gain most of their contrast from myelin. The free water protons near myelin sheaths transfer their magnetisation to the myelin's cell membranes [Turner, 2013; Koenig, 1991]. Thus, T_1 is much shorter for water near the myelin sheaths than further away. Turner [2012] showed that the contrast of an in-vivo T_1 mapping is similar to that of a myelin stain. Myelin-rich regions have lower T_1 values, and are usually hyperintense on T_1-weighted images. Hence, GRE sequences are a promising candidate to map myelin. In general, GRE sequences are more sensitive to field inhomogeneities, but T_1-weighting can be maintained by reducing the TR.

REDUCING SCAN TIME BY DECREASING THE FLIP ANGLE Additionally, the flip angle can be traded against TR (see Fig. 3.4B). When using a reduced flip angle, some longitudinal magnetisation remains. To also account for the effects of transverse coherence, the GRE sequence can be modified to use even lower flip angles which shortens the TR again. These sequences are called Fast Low Flip-Angle Shot (FLASH) sequences. After each echo, a gradient will be applied that spoils any remaining transverse magnetisation by causing a spatially dependent phase shift. Now, TR can be extremely reduced. This kind of sequence offers a key benefit: extremely high T_1 contrast can be obtained by imaging with TR times as short as 20–30 ms. At the same time, reasonable signal levels are maintained.

The T_1 contrast achieved with these fast GRE techniques depends on the TR and on the flip angle. Choosing smaller flip angles and short TR yields a proton density map. Long TR results in T_2^*-weighting. Using large flip angles and short TR produces T_1-weighted images.

The major drawback of T_1-weighting is the creation of images that are only qualitative (or "weighted"). The images are dominated by one specific tissue parameter to the exclusion of all others, but they incorporate mixed contributions from all the different tissue parameters. In locations of signal and contrast inhomogeneities, the image data cannot be trusted. Hence, when computationally processing the data these inhomogeneity artefacts may lead to tissue misclassifications.

To achieve reliable signal and contrast quality and allow for automatic segmentation, quantitative mapping techniques are required. Main advantages of using quantitative MRI data is the reduction of inter-subject and inter-scan variability and the possibility of analysing the data automatically. In addition, comparison with data acquired at scanners from different vendors is much easier [Weiskopf et al., 2013]. Quantitative measures require several image acquisitions that will be averaged retrospectively.

A so-called T_1 map is a quantitative spatial representation of the T_1 time. These maps are to a large degree homogeneous. In-vivo T_1 images can be acquired using fast T_1-mapping techniques [Preibisch and Deichmann, 2009; Marques et al., 2010; Lutti et al., 2014]. The MP2RAGE sequence designed by Marques et al. [2010] allows to obtain a T_1 map of the whole brain at a resolution of 0.7 mm isotropic at 7 T in only 11 min. A single hemisphere can even be imaged at even 0.5 mm isotropic resolution in 28 min [Bazin et al., 2013a]. Because of their high homogeneity and clear relation to myeloarchitecture, T_1 maps exclusively computed from a MP2RAGE sequence are used in this thesis.

The MP2RAGE is based on the Magnetisation-Prepared Rapid Acquisition Gradient Echo (MPRAGE) sequence, a fast GRE using a magnetisation preparation pulse. In T_1-weighted GRE imaging, TR and TE are very short such that tissues reveal a poor imaging signal. More importantly, using these short TR and TE yields poor contrast. Therefore, the magnetisation is "prepared" during a preparation step. This preparation is usually applied as an initial 180° inversion pulse which causes the protons to rephase. The inversion pulse is executed once. It allows the imaging technician to center the subsequent GRE data acquisition around the inversion time TI where the tissues of interest exhibit very little signal because its longitudinal magnetisation M_z is passing through zero.

The MP2RAGE now uses two inversion pulses for two different tissues of interest. In cortical analyses, the tissues of interest are GM and WM. Hence, two images are acquired, each at a TI where the corresponding tissue has very little signal. By using both images, the contrast between the tissues can be maximised as shown by Marques et al. [2010].

Since the main data source of this thesis are images acquired by MP2RAGE sequences, the advantages and drawbacks of this technique are presented in more detail in the next section.

3.2.3 *The MP2RAGE Sequence*

At static magnetic fields of <3 T, the resulting image data is influenced by intensity variations (bias field effects) due to the increased inhomogeneity of the transmit and receive, e. g., B_1^+ and B_1^-, fields (see next section on imaging artefacts). These bias field effects severely affect the image quality at ultra-high fields (>7 T) and render segmentation and quantitative analysis difficult.

In order to acquire bias field-independent, or inhomogeneity-free images, transmit and receive inhomogeneities have to be addressed separately as they have different origins and implications on the signal intensity and contrast.

Receive inhomogeneities, i. e., the B_1^- field, affect the amplitude of the signal by a multiplicative factor that is related to the coil sensitivity. Transmit inhomogeneities, i. e., the B_1^+ field, are more complicated. T_1-weighting of a sequence is related to the flip angle. To reduce the transmission inhomogeneity, the amplitude of the RF pulses used in the sequence needs to be carefully adjusted such that the resulting contrast depends less on the local flip angle accuracy [Thomas et al., 2005; Van de Moortele et al., 2008].

In a conventional MPRAGE, the signal depends not only on T_1 contrast but also on proton density and T_2^* effects. Both a lower proton density and shorter T_2^* reduce the T_1 contrast of the MPRAGE image. If two MPRAGE images are acquired at two different inversion times TI but with identical sequence parameters, the two acquired images will be affected in the same manner by effects from B_1^-, proton density and T_2^*. Hence, a combination of the images by means of a ratio will be independent of B_1^-, proton density and T_2^* [Van de Moortele et al., 2009].

The Magnetisation-Prepared 2 Rapid Acquisition Gadient Echo (MP2RAGE) acquires two MPRAGE images at TI_1 and TI_2. Those images are combined as follows:

$$\text{MP2RAGE} = \frac{\text{GRE}_{TI_1}\text{GRE}_{TI_2}}{\text{GRE}_{TI_1}^2 + \text{GRE}_{TI_2}^2} \tag{3.4}$$

The MP2RAGE sequence offers three main advantages:

1. the images are independent of bias field effects, and therefore almost inhomogeneity-free,
2. the quality of images and the resulting T_1 values are highly reproducible,
3. the data offer superior tissue contrast than compared to conventional imaging.

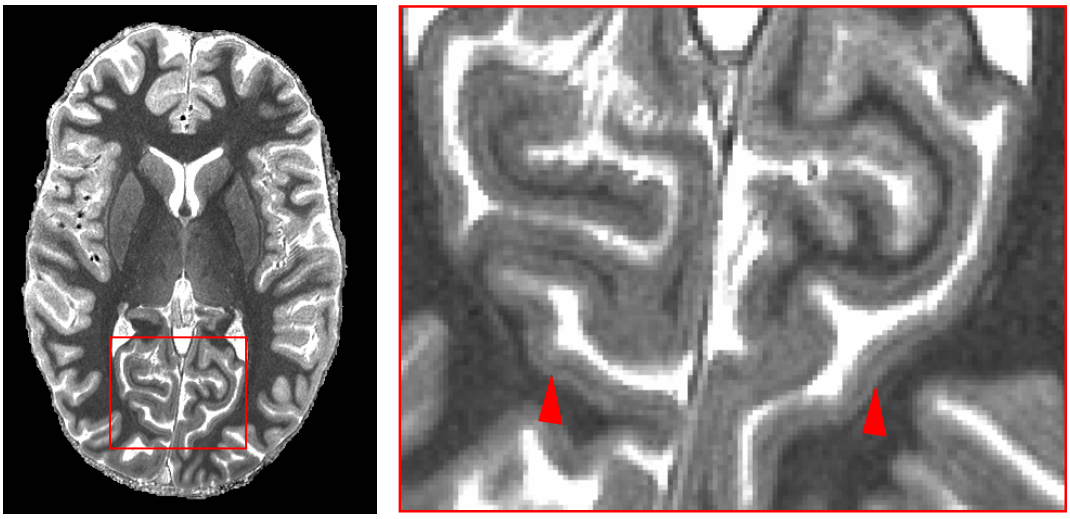

Figure 3.8: T_1 map obtained from the MP2RAGE sequence. The data is scanned at 7 T with an isotropic resolution of 0.5 mm. The strongly myelinated bands of Baillarger (red arrow heads) appear within the cortex.

To finally compute a T_1 map, optimal sequence parameters as given in Marques et al. [2010] were taken into account as well as the inversion efficiency of the inversion pulse. Bloch simulations were performed for the MP2RAGE sequence in order to model the longitudinal relaxation. The T_1 value at each voxel was then fitted to the exponential function (see Fig. 3.4).

INFLUENCES ON IMAGE QUALITY The above equation limits the possible values of the MP2RAGE into a range from -0.5 to 0.5, yielding a predefined range of image intensities (even in regions dominated by noise). Image combinations may lead to a reduction of SNR in the final image. However, it may not necessarily affect the CNR of the combined image. The dependence on proton density and T_2^*, reducing the contrast in a MPRAGE, was removed from the combined MP2RAGE image (see Appendix 1 in Marques et al. [2010] for further details).

This imaging sequence is of great use when scanning at high fields (>3 T). Furthermore, there is no need to perform a co-registration between the two acquired images. Although they have significantly different contrasts, the sequence ensures that the images are inherently co-registered as they are scanned in the same session.

ROBUSTNESS AND REPRODUCIBILITY Resulting T_1 values are highly reproducible both across subjects and within the same subject using different scanning parameters. T_1 values obtained with a MP2RAGE are in agreement with previous reports at 3 T [Lu et al., 2005; Wansapura et al., 1999; Wright et al., 2008] and studies at 7 T [Rooney et al., 2007]. Acquired images can be computed online, e. g., during the scan session, without the need of an extra post-processing step. Hence, the sequence is able to perform whole-brain scans in clinically acceptable times. Using slab-wise image acquisition and image registration methods may additionally increase the resolution to 0.5 mm and above (see Fig. 3.8).

TISSUE CONTRASTS FOR IMAGE SEGMENTATION Arteries appear bright in MP2RAGE contrast at 7 T and consequently the T_1 maps show very low T_1 values in these locations. Hence, arterial blood has a particular contrast in the MP2RAGE images. This may help to further improve the outcome of segmentation and classification approaches which often struggle with distinguishing brain matter from arteries [Fischl et al., 2004a]. By eliminating the dependencies on proton density and T_2^*, MP2RAGE images furthermore provide good contrast between GM and dura mater and specifically tissue contrast for separating between GM, WM, and CSF. These observations, together with the enhanced representation of arteries, render the MP2RAGE images suitable for applications requiring automated segmentation.

In addition, the inter-subject reproducibility suggests that this technique can be very useful in longitudinal studies or group comparison studies.

3.2.4 *Image Artefacts*

Features in images that are not present in the structure to be scanned are called image artefacts. They have different origins and can be classified into three groups:

- patient-related artefacts,
- signal processing-dependent artefacts, and
- hardware (machine)-related artefacts.

It is crucial to know about the potential sources and the physical basis of these artefacts as they influence or even distort the acquired images and render data segmentation and analysis methods difficult. Investigations and understanding of the artefact's origin and effects can lead to:

- further improvements in MRI to reduce or even overcome the effects using newly designed sequences.
- the development of advanced image segmentation methods that can deal with a certain type of artefact.

Here, the discussion is limited to artefacts occurring in structural imaging. More precisely, this section will relate to artefacts that primarily occur using the MP2RAGE sequence at 7 T. In this thesis, slab-wise image acquisition is used to image the two brain hemispheres separately at higher resolution in one scanning session.

Only normal healthy subjects are considered in this thesis. No pathological scanning or application of contrast agents was performed. Artefacts, related to these conditions, are not discussed here.

An overview of artefacts in general can be found in Somasundaram and Kalavathi [2012] and Erasmus et al. [2004].

3.2.4.1 *Patient-related Artefacts*

MOTION The most common artefact in MRI is caused by motion. Motion can be distinguished into two categories:

- motion due to vital functions: heart beating and breathing are part of physiological movements of our body and organs that cannot be suppressed. They are of milliseconds to seconds duration and usually occur periodically.
- subject motion: moving an arm or rotating the head are movements of our body that can be avoided. Usually, they occur spontaneously, i. e., non-periodically.

Due to the significant difference between acquisition time in the frequency- and phase-encoding directions, the phase-encoding direction is mainly affected.

Only a single echo (milliseconds) is needed for frequency-encoded sampling. Phase-encoded sampling lasts several seconds (or even minutes). As movements due to vital functioning takes millisecond to seconds duration, they are too slow to have an effect on frequency-encoded sampling. However, they appear in the phase-encoding direction. Blood vessels and pulsation in CSF cause ghost images. Non-periodic movements cause blurring in images (see Fig. 3.11 A and B).

There are several methods available to reduce motion artefacts. Among these are patient immobilisation, cardiac and respiratory gating, signal suppression of the tissue causing the artefact, and swapping phase and frequency-encoding directions to move the artefact out of the field of interest. Only recently, online motion correction systems have been incorporated [Schulz et al., 2012].

FLOW ARTEFACTS Flow artefacts are caused by liquid dynamic structures, i. e., flowing blood or CSF in the brain and the body.

Flow artefacts are altered intravascular signals. They occur due to inflow effects causing flow-related signal loss, or due to flow-related artefacts causing ghost images or spatial misregistration.

The inflow effect is caused by fully magnetised protons in liquids flowing through a slice. They can experience an RF pulse and already be out of the slice by the time the signal is recorded. These protons do not contribute to the echo. Thus, they manifest as a so-called signal void or flow-related signal loss.

Spatial misregistration describes a displacement of an intravascular signal in the phase-encoding direction. The intensity of the artefact depends on the signal intensity from the vessel.

In T_1 maps, vessels have very low T_1 values (see Section 3.2.3). However, vessels may appear as ghosts in the cortex as a result of a spatial misregistration (see Fig. 3.9).

3.2.4.2 *Signal Processing-dependent Artefacts*

The artefacts are a result of how the signals are sampled, processed and mapped out on the image matrix. When scanning structures, the continuous world is discretised into a space forming a 3D image grid. This grid consists of voxel, i. e., 3-dimensional cubes representing the environment into which the scanned structure is mapped.

PARTIAL VOLUMING EFFECT The partial voluming (PV) effects are a problem at any resolution in imaging. Therefore, PV effects have to be taken into account in further data processing and image analysis steps.

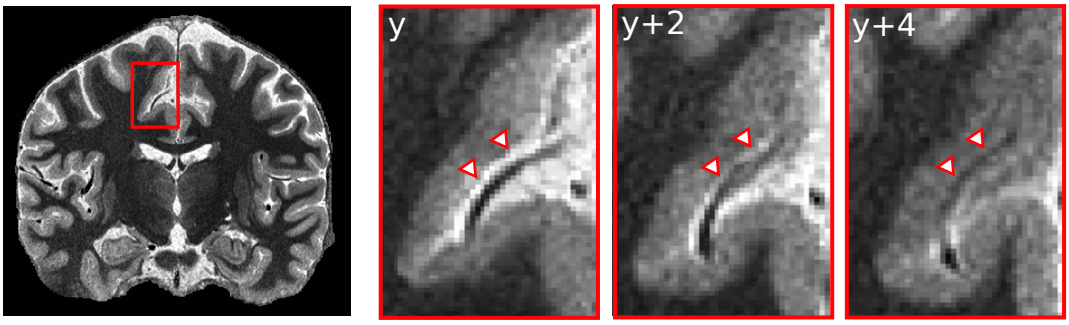

Figure 3.9: The images depict ghost images of vessels in the cortex. Vessels generally have very low T_1 values. The three images on the right highlight a zoomed-in location visible in the coronal section (left). Although the underlying cortical structure slowly changes when progressing in posterior direction (plus two slices each), the vessel remains at the same location (red arrows). Usually, vessels run *tangentially on* the cortical surface and penetrate *perpendicular into* the cortical surface. Thus, the vessel depicted in the images is a ghost as it runs *tangentially in* the cortex.

In general, PV artefacts occur when the feature to be imaged has a smaller size than the image voxel. Due to limited resolution, large intensity differences between neighboring tissues cannot be properly reconstructed. In imaging data consisting of small discretised voxel, each voxel contains a fraction of two materials, A and B. The reconstructed MRI signal of the entire voxel will then represent the weighted average of the signals originating from A and B. The PV effects are most prominent when the two neighboring structures have very different intensities. Considering the cerebral cortex, PV are more prominent at the outer cortical surface where CSF and GM interface each other, and less strong at the inner cortical surface where WM and GM interface each other.

In addition, partial voluming is particularly a problem in locations of tightly folded sulci in which the CSF resides in a little cavity created by two gyral folds being literally "back-to-back" to each other.

GIBBS RINGING Gibbs ringing, also known as truncation, ringing, or spectral leakage artefact, appears in locations of sharp intensity edges, i. e., where two tissues with high intensity difference interface each other [Czervionke et al., 1988]. The ringing presents itself as a series of regularly spaced lines parallel to the tissue boundary. The effect alternates between bright and dark signal and slowly fades with distance. The artefact occurs as a result of using Fourier transforms for image reconstruction, i. e., transforming frequency signals into spatial image intensities.

In theory, an infinite summation of sine waves of different amplitudes, phases, and frequencies can represent any signal. In MRI, sampling is restricted to only a finite number of frequencies. The image must be approximated in its Fourier representation using only relatively few harmonics. The Fourier series used is cut short or "truncated".

Due to its nature, Gibbs ringing occurs in both the phase- and frequency-encoded directions. Its effect can be reduced by filtering the frequency space prior to Fourier transform or by increasing the resolution for a given field-of-view (FOV) [Block

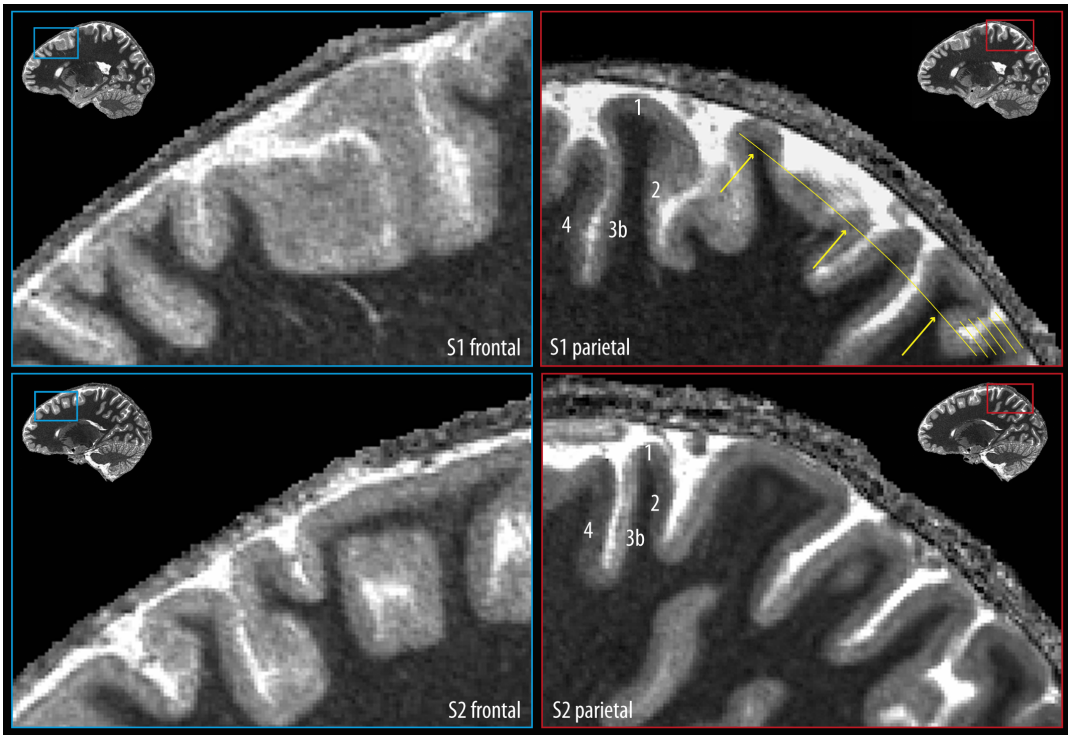

Figure 3.10: Two T_1 maps of different subjects (top and bottom row) showing different imaging quality in regard to ringing artefacts. Ringing artefacts occur only in parietal-occipital regions (top, right) and not in frontal regions (top, left). The second T_1 map shows no ringing in frontal nor parietal regions (bottom). The images are acquired at 7 T with 0.5 mm isotropic resolution.

et al., 2008]. Those techniques are effective, but come with slight loss of image quality. However, the effects can never be entirely removed.

The hemispheric slabs acquired in this thesis have a disproportionate size as they only contain one hemisphere. In particular, Gibbs ringing only occurs in parietal-occipital regions between high-contrasting tissues such as GM and CSF (see Fig. 3.10). The effects usually affect the imaging data in location of the cortical surface up to a depth of 1.5 cm.

ALIASING AND WRAP-AROUND ARTEFACT Measuring a signal's frequency using an inadequate sampling rate yields so-called aliasing effects. Sampling a signal with an insufficient number of data points leads to an underestimation of its true frequency. As a result, the "underestimated" signal will be identical to another signal having the true lower frequency. The "underestimated" signal is called "alias" to a true lower frequency signal.

In MRI, aliasing is an important phenomenon and the source of the phase wrap-around artefact [Axel and Morton, 1989]. It occurs whenever the dimensions of an object exceed the defined FOV. The wrap-around artefact can be recognised as a folding over of anatomic parts to the opposite side of the image usually containing the area of interest (see Fig. 3.11 C). Although this phenomenon may occur in the frequency-encode direction, it is generally more severe along the phase-encode axis.

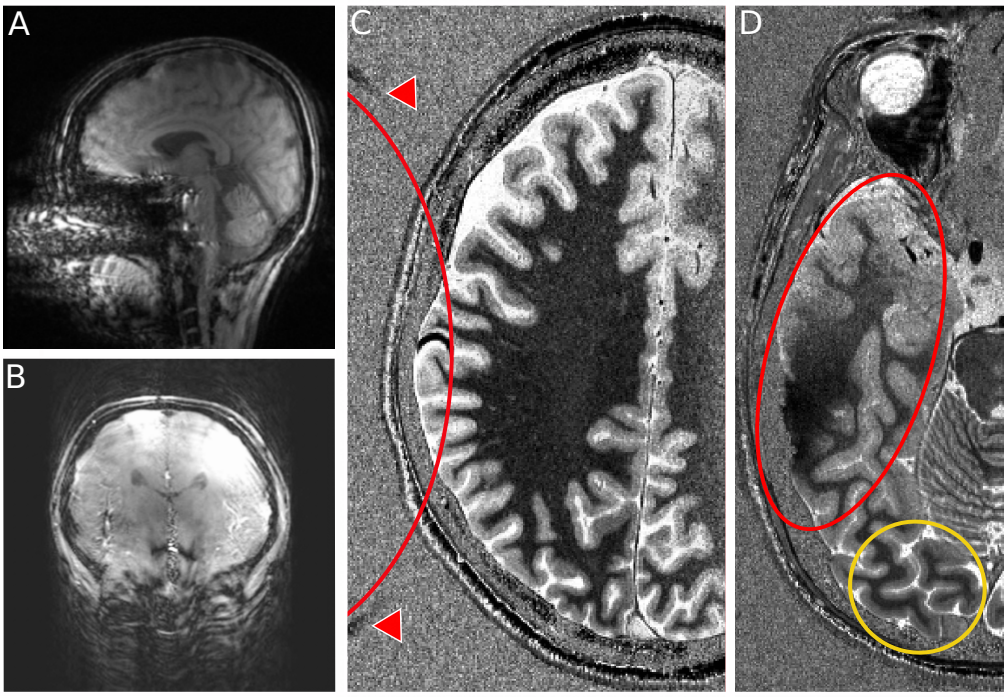

Figure 3.11: The images depict examples of various imaging artefacts. A) and B) highlight ghosting and blurring when the brain moves in sagittal (top) and coronal (bottom) view. Repetitions of the skull are clearly visible. C) shows a raw hemispheric slap of a computed T_1 map. The brain hemisphere that is out of FOV wraps into the data on the opposite site (see red line and arrows). D) reveals B_1 inhomogeneities in temporal regions (encircled red). There is insufficient signal to outline the cortical surface. It appears as if the cortex is missing. This region is generally more noisy compared to regions exhibiting enough signal (encircled yellow).

When acquiring slabs of one side of the brain, the FOV only contains one hemisphere. The other hemisphere may be wrapped around into the actually scanned brain half.

3.2.4.3 *Machine- and Hardware-related Artefacts*

The artefacts described here are due to functional problems of the MRI machine and hardware setup or caused by other problems influencing the scanning procedure.

B_0 INHOMOGENEITIES In MRI, the B_0 magnetic field is assumed to be homogeneous. Inhomogeneities in the B_0 magnetic field cause image distortions. These can either be intensity related, spatially related, or both.

Intensity distortions are caused by field inhomogeneities within the object to be imaged. Here, the field is stronger or weaker at a certain location than that in the rest of the object or tissue. Hence, T_2^* at this location is different, and therefore the signal will tend to be different.

Spatial distortion are caused by long-range field gradients in B_0 which are constant in time. Gradients cause the spins to resonate at Larmor frequencies other

than those assigned by the sequence. In an ideal setup, protons spinning at a certain position should experience a certain magnetic field and resonate at a characteristic frequency. With an inhomogeneous gradient field, there is no linear relationship between the position and the frequency the protons spin at. The result is a distorted image because linearity is assumed in the imaging process.

B_1 INHOMOGENEITIES B_1 artefacts are very similar to B_0 artefacts. These artefacts arise from a deviating gradient system and will distort the images. Usually, the artefact occurs when the gradient coil is damaged or abnormal currents pass through the gradient coils.

These inhomogeneities increase with increasing field strength and, thus, are an issue at 7 T and above. Using the MP2RAGE sequence extinguishes the inhomogeneities of the receive field, B_1^-, when computing the T_1 map. However, B_1^+ inhomogeneities (see Fig. 3.11 D) need to be taken into account in further processing steps.

RF INHOMOGENEITIES AND RF NOISE An RF inhomogeneity artefact presents itself as an undesired variation in signal intensity across an image. There are different causes to this artefact such as:

- failure of the RF coil,
- non-uniform B_1 field,
- non-uniform sensitivity of the receive only coil, or
- presence of non-ferromagnetic material in the imaged object, e. g., metal close to the object to be scanned.

Some RF coils, such as surface coils, naturally have variations in sensitivity and will always display this artefact.

MRI systems are surrounded by an RF shielding that prevents external noise from getting into the detector. However, RF pulses and precessional frequencies of MRI instruments have the same frequency bandwidth as common sources from our every-day life such as a TV, radio, and computers. A failure of the RF shielding can cause an RF noise artefact. The appearance of the artefact in the final image highly depends on the source of noise. Appropriate site planning, proper installation and RF shielding eliminate stray RF interference.

3.3 OTHER MRI TECHNIQUES USED IN CORTICAL AREA STUDIES

This work focuses on building a new cortical parcellation scheme. Cortical areas can be described by physiological parameters related to the structural organisation or underlying functional processing of the brain. MRI allows one to study these parameters in order to detect patterns that may correlate with areas. In turn, these parameters may be helpful in designing new parcellation schemes.

In this section, two imaging types are briefly highlighted:

- diffusion Magnetic Resonance Imaging which analyses the structural connectivity in the brain, and

- functional Magnetic Resonance Imaging (fMRI) which measures brain activity. The fMRI techniques address brain activity when performing a task or when the brain is at rest, i. e., so-called resting-state functional Magnetic Resonance Imaging (rs-fMRI).

Structurally connected brain regions, i. e., regions that are anatomically attached to each other by a fibre bundle running from region A to region B, do not have to be functionally connected. Functionally connected brain regions, i. e., regions that are spatio-temporally active, do not have to be structurally connected.

When examining connections and their correlations in the brain using diffusion or functional MRI data, a seed- or ROI-based approach may be very useful (see Fig. 3.14B). In this case, the data from only a few voxel, called the seeds or ROI, are taken into account to further compute their relationship with other voxel in the brain. This approach provides a better focus on structural as well as functional connectivity in brain areas of interest.

This section only gives a brief overview of the techniques mentioned above.

3.3.1 *Diffusion MRI*

Structural connectivity can be measured using diffusion MRI [Behrens and Johansen-Berg, 2005]. It is a MRI technique that utilises the local microstructural characteristics of water diffusion by measuring the random Brownian motion of water molecules within the tissue. Generally, the motion of water molecules follows the direction of least resistance. This motion exceeds its limitation when facing membranous boundaries. In white matter, motion of water molecules follows the WM fibres, i. e., the myelin sheath of axons. Boundaries or barriers can be cell membranes, myelin, crossing axons or fibre bundles.

Diffusion Tensor Imaging (DTI) [Basser et al., 1994b,a] extends diffusion MRI by additionally determining the white matter tract orientation along which water molecules move. The final reconstructed image then describes the direction of maximum diffusivity along the white matter fibres. DTI is describing a full characterisation of molecular diffusion in 3-dimensional space [Le Bihan et al., 2001; Jones and Leemans, 2011; Assaf and Pasternak, 2008]. **Isotropic** diffusion describes equally free diffusion into all directions. If the diffusion is restricted by membranous boundaries, it becomes uneven and is called **anisotropic** diffusion.

Anisotropy can be measured by using a ratio called fractional anisotropy, FA. FA=0 describes a perfect sphere and FA=1 represents ideal linear diffusion. Often, the shape becomes an ellipsoid as there is a direct relationship between the number of fibres and the degree of anisotropy. The FA ratio cannot provide information on the direction of the fibres, e. g., does the fibre represent a region-incoming or region-leaving fibre? However, the predominant direction of the fibre in 3D space can be determined using tensors. It is very difficult to represent and perceive this information on 2D grey-scaled projections (see Fig. 3.12). A colour code is introduced following the types of fibre tracts described in Section 2.1.3. The colour code maps the orientation of the fibre to a certain colour:

- red colours represent fibres connecting right and left hemisphere, i. e., commissural tracts.

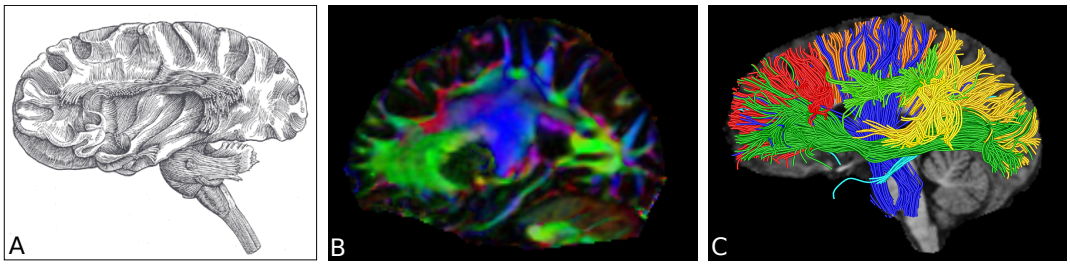

Figure 3.12: Original drawing of brain fibres presented by Gray [1918] shown in (A) and compared to in-vivo diffusion MRI data (B). From these, fibre tracts can be computed (C). The different colours in B and C correspond to different types of fibres. Images were created with the freely online accessible brainnetworks tool: http://openscience.cbs.mpg.de/brainnetworks [Heuer et al., 2014].

- green colours describe fibres running in posterior-to-anterior direction or vice versa, i. e., association tracts.
- blue colours highlight fibres running in foot-to-head direction or vice versa, i. e., projection tracts.

Calculating these 3D fibres from DTI data is called tractography. A 3D representation of the calculated fibres is called tractogram. The information in the data can be mapped to a cortical surface and represented in an adjacency matrix, e. g., a so-called connectivity matrix. This matrix describes which locations on the cortical surface are connected. The connections can be weighted to include the strength in connectedness.

Further details on diffusion methods can be found in Johansen-Berg and Behrens [2009].

3.3.2 *Functional MRI*

To obtain functional information of brain activity fMRI techniques are used. These methods are capable of detecting subtle changes in cerebral blood flow (CBF) in response to a stimulus or action. The fMRI techniques rely on the change in magnetisation between oxygen-poor and oxygen-rich blood. Therefore, fMRI methods are also called blood-oxygen-level dependent (BOLD) imaging methods.

The fMRI data is usually corrupted by noise. Statistical procedures are needed to extract and emphasize the underlying signal. Pre-processing of fMRI data commonly includes: slice-timing correction, motion correction, spatial and temporal filtering, and normalisation. Data processing usually involves independent component analysis, in which the user selects the relevant components to be investigated. Alternative analysis methods include clustering algorithms and pattern classification (see next chapter).

The resulting brain activation (see Fig. 3.13)[1] can be mapped onto a surface or to a connectivity matrix. The use of colour-coding highlights the strength of activation across the brain (or specific region studied).

1 fMRI data corrected at a voxel-wise threshold of $p < 0.001$, with a minimal cluster size of 5; functional data are then family-wise error-corrected at a threshold of $p < 0.05$ (FWE-corrected).

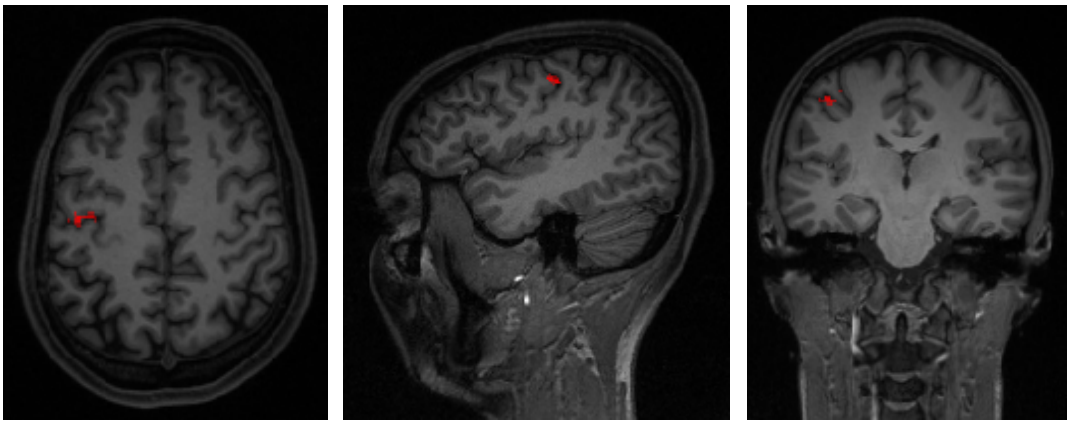

Figure 3.13: Functional activity in primary somatosensory area, S1, during a tactile stimulation task of the index finger. No movement of hand or fingers involved. fMRI data measured at 7 T (resolution: 1.5 x 1.5 x 1.5 mm) and superimposed on structural data measured at 7 T (resolution: 1 x 1 x 1 mm). Images by courtesy of Esther Kühn.

3.3.2.1 *The BOLD Effect*

The blood flow in the brain is highly locally governed considering oxygen and carbon dioxide usage in cortical tissue. When the brain is solving a task, specific cortical regions increase in activity. These regions suddenly extract more oxygen from the local capillaries which yields

- an initial drop in oxygenated haemoglobin, and,
- an increase in local carbon dioxide (CO_2) and deoxygenated haemoglobin.

After about 2–6 s, the cerebral blood supply in this region increases. An additional portion of oxygenated haemoglobin is provided, replacing the deoxygenated haemoglobin. BOLD fMRI makes use of this large rebound in local tissue oxygenation and relies on regional differences in CBF to delineate regional activity.

Due to the fundamental difference in the paramagnetic properties of oxygenated and deoxygenated haemoglobin, fMRI methods are able to detect this change. Deoxygenated haemoglobin is paramagnetic. Oxygenated haemoglobin is not paramagnetic. This has a direct influence on the T_2^* properties in tissue: deoxygenated haemoglobin causes dephasing of local protons. Thus, the signal from the tissues in the immediate vicinity is reduced. T_2^*-weighted sequences are able to capture this change.

In addition to the number of limitations related to imaging sequences themselves (see Section 3.2), there are limitations using fMRI and closely related imaging techniques which measure functions in terms of CBF:

- CBF is an indirect measure of activity. It provides no direct visualisation of activity in the cortex.
- CBF increase is a response to an increase in activity. There is a delay of 2–6 s.
- fMRI techniques can localise activity spatially within millimetre range but temporally no better than a few seconds.

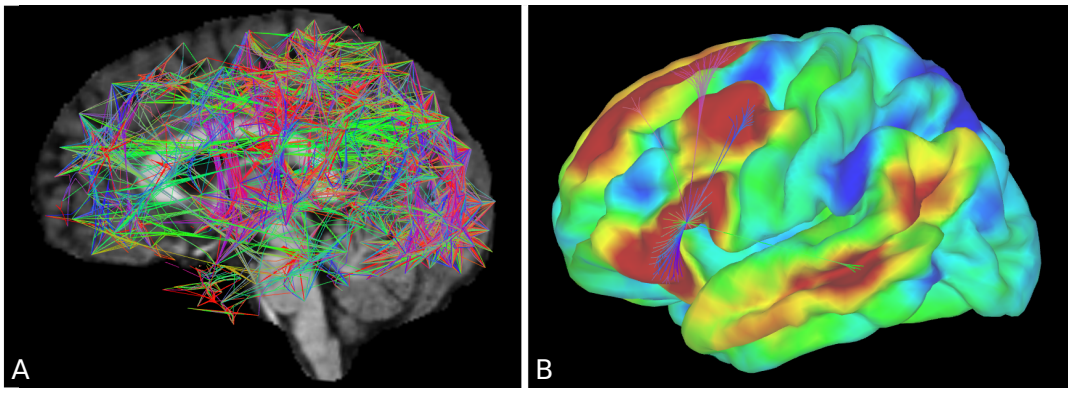

Figure 3.14: Functional network computed from rs-fMRI data shown as 3D connectivity graph in (A). Functional activity colour-coded by strength of activity shown in (B). Locations indicated by red colour are synchronously active at a resting state of the brain. Here, the focus is on area 45 (Broca's region). The connections, i. e., lines projecting to other areas, are part of the connectivity graph. The mapping changes when a different location is selected as area of interest (seed-based approach). Images were created with the freely online accessible brainnetworks tool: `http://openscience.cbs.mpg.de/brainnetworks` [Heuer et al., 2014].

3.3.2.2 *Data Acquisition*

A typical fMRI scan may be designed in two different ways.

In a scan using block design, the subjects need to deal with repeated blocks of activity. These blocks are either alternating between different activities or separated by blocks of inactivity (resting phase). In an event-related scanning session specific individual events are included. These events can be randomly distributed during the scan phase.

Hence, the design of a functional scan always focuses on primary functioning of the brain, i. e., tasks related to vision, senses, speech, memory or motor skills. The activity performed or the stimulus received, evokes a cortical response in the brain. These responses are analysed to elucidate neuroscientific questions. However, fMRI scanning is limited by its own design: to analyse functional properties of the entire cortex, many scan sessions are necessary.

3.3.2.3 *Resting-state fMRI*

A special technique of fMRI is rs-fMRI that allows to study the regional functional interactions that occur when the brain is at rest, i. e., not performing an explicit task (see Fig. 3.14). The measured "resting" brain activity relies, as in fMRI, on changes in CBF, and thus, on the BOLD effect.

Using rs-fMRI methods, scientists can investigate the functional connectivity between brain areas which is independent of structural connectivity. A number of networks were consistently found in healthy subjects, at different stages of consciousness and across species. These networks represent specific patterns of synchronous activity.

3.4 IDENTIFYING AREAS USING CLASSICAL HISTOLOGICAL METHODS

The classical method to structurally image brains is based on staining tissue samples extracted from postmortem material. Conventional staining is still respected as ground truth or so-called "gold standard". In the thesis, material is stained to allow a qualitative verification with structural MRI data. In-depth details on staining histological material can be found in Mulisch and Welsch [2010].

In this section, the general workflow of staining material is explained. But these conventional methods have many drawbacks that are outlined at the end of this section.

CHEMICAL FIXATION OF TISSUE MATERIAL To preserve brain tissue from degeneration, tissue samples have to be chemically treated. This process is called fixation. A fixation of cell tissue maintains the structure of the cells and of sub-cellular components. Regarding light microscopy, the most commonly used fixative is 10 % neutral buffered formalin (4 % formaldehyde in phosphate buffered saline). Fixatives preserve tissues or cells mainly by irreversibly cross-linking amino groups in proteins. They build up bridges made of methylene. Keeping the structural integrity of the cells damages the biological functionality of the proteins. Histological staining can, therefore, only analyse tissue according to structural properties.

PREPARATION: DEHYDRATION, CLEARING, INFILTRATION In order to analyse sections of tissue samples, the extracted tissue blocks need to be cut into slices of only a few micrometre thickness. As such thin slices rip apart very easily, the tissue has to be adequately prepared for cutting in advance. The aim of tissue preparation is to remove water from tissue in order to replace it with a hard enough medium that allows cutting of thin sections. Typically, 5–30 µm thick sections are used for light microscopy.

As a hard medium, paraffin wax is most frequently used, as it is immiscible with water. Water is the main constituent of biological tissue. In the process of dehydration, water will first be removed. During this process, samples are treated in container baths of progressively more concentrated ethanol. The transfer from low to high ethanol removes the water from the tissue. This process is followed by a hydrophobic clearing agent that removes the ethanol again. During this step, called infiltration, melted paraffin wax will be used as a replacement to stabilise the tissue structure.

EMBEDDING OF TISSUE After the preparation, tissues have to be externally embedded. The tissue is placed into containers together with liquid embedding material such as agar, gelatine, or wax, in which the tissue then hardens. In the case of paraffin wax, the hardening process is achieved by cooling. Finally, the tissue block is ready to be sectioned.

Formalin-fixed and paraffin-embedded tissues can be stored at room temperature for an indefinitely long time, which makes them an important resource for studies in anatomy and medical studies.

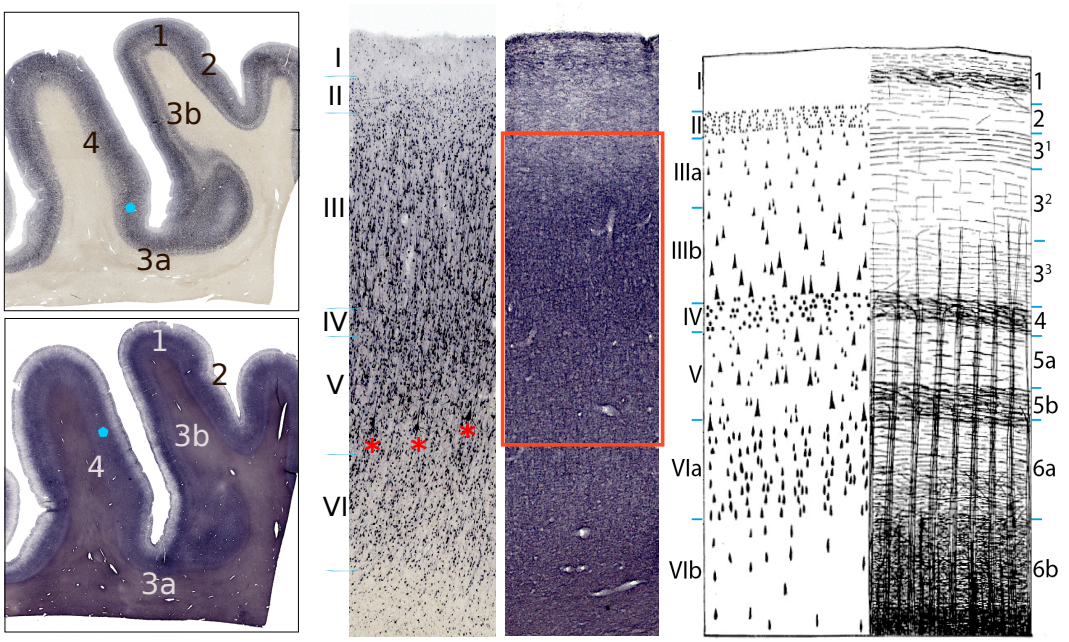

Figure 3.15: The images on the left depict two consecutive 30 µm thick cytoarchitectonic (top) and myeloarchitectonic sections (bottom) of the primary motor-somatosensory region M1/S1 (2.58 µm in-plane resolution). The layering of the cortex is visible in the cell stain as well as the myelin stain. The location between area 3a and 3b indicates a region that was not cut perpendicular to the cortical surface. Here, features, such as layer thickness, are distorted. The enlargements (middle) were taken from the primary motor area (location indicated by the blue dots). Triangular-shaped giant pyramidal cells ("Betz'sche Riesenzellen") are visible (red coloured *) in the cell stain. Area 4 shows an increased myelination between layer III and V obscuring the bands of Baillarger (red rectangle). The microscopy images can be compared to historic drawings of cell and myelin stains (right) taken from Vogt [1910]. Microscopy images are by courtesy of Dr. Stefan Geyer and Katja Reimann.

SECTIONING OF TISSUE BLOCK Sectioning is the most crucial process when analysing the underlying microstructure of a tissue block. It can only be done in limited ways. The surface of the tissue needs to be vertically cut. Using an incorrect angle of cutting may yield distortions of the real microstructural relations, i. e., layers of the cortex may appear thicker than they are in the real object.

For light microscopy, a steel knife mounted on a machine called microtome is used to cut the extremely thin tissue sections. The cut sections are put into single molds.

STAINING OF SECTIONS Staining allows to highlight particular characteristics of the tissue. The staining agent used can be designed in a way that only specific features of the tissue will absorb it. Consequently, only these features are highlighted in the final section.

Only recently, antibodies start to play a major role in staining procedures. They allow to specifically visualise proteins, carbohydrates, and lipids. The discipline is referred to as immunohistochemistry. The method offers new ways to identify categories of cells using a microscope.

VISUAL INSPECTION AND ANALYSIS Microscopes that are equipped with high-resolution digital cameras are used to capture histological images. This allows to further study the features of interest. Fig. 3.15 highlights cell and myelin stained sections of the primary motor and somatosensory region M1/S1.

DRAWBACKS OF HISTOLOGICAL METHODS Staining techniques only allow the examination of (mostly) older and dead brains. The staining approach provides no functional analysis of brain tissue. Although improvements on the actual staining techniques are available, staining may be inconsistent due to undissolved particles of the staining agent or impairments of the underlying tissue due to age or (often unknown) diseases. Overall, the staining process is very sensitive: consecutively cut sections treated with the same staining agent according to the same staining protocol may have different outcomes due to minimal timing issues or deviations in agent concentration. When cutting the tissue, the angle of cutting is most crucial. If the tissue block is not cut perpendicular to the cortical surface, features of the cortex are distorted such as layer thickness or cell size.

Histology has further limitations towards myelinated axons, which are the structure of interest in this thesis. Here, it is worth noting that the linear nature of myelinated axons and the planar dimensionality of a myelin-stained cadaver brain section limit the opportunity of reconstructing 3D data directly from histology. Sections are spatially distorted due to the staining process. Finding the corresponding myelinated axons in consecutively stained sections poses an extremely difficult task. Representing quantitative myelin concentration in the cortex is downright impossible due to saturation effects. The method cannot determine absolute values of myelin because even a highly standardised myelin staining process is not a quantitative method due to the saturation effect in the tissue.

3.5 SUMMARY AND CONCLUSIONS

Recent developments in high-field MRI lead towards better image quality regarding SNR as well as CNR. MRI can reveal the underlying physical phenomena, and, thereby, characterise the human cortex microstructurally in living human brains. The results are in agreement with histological preparations. With increased resolution, the new MP2RAGE sequence is able to reflect myeloarchitectonic intracortical features.

It has been shown that conventional histological methods cannot compete with these developments. They only allow the examination of generally older brains in two dimensions (2D). Additionally, histological staining for myelin provides no quantitative measure due to saturation effects of the staining agent.

In contrast, using quantitative MRI methods enables scientists to study the brain longitudinally across lifespan and to consider in-vivo examinations of healthy and diseased brains in three dimensions (3D). Thus, MRI is becoming an invaluable tool for studying the human brain.

4

IMAGE SEGMENTATION AND ANALYSIS

Image segmentation and analysis play a more and more important role in todays medical imaging. Results of the tasks are now widely used in different applications such as the study of anatomical structures, localisation of pathology, diagnosis, treatment planning, quantification of tissue volume or even partial volume and imaging artefact correction.

Image segmentation remains a difficult task because the image quality, e. g., image resolution, artefacts, motion of subjects, imaging modality, as well as the tremendous object shapes to be segmented vary highly, e. g., the brain and its complex folded structures, the liver and its segments, the bones and their capsules, the heart and its chambers.

Here the structure of interest is the cerebral cortex. The main computational challenges of the thesis are:

1. to segment the entire brain such that the cortex can be extracted from the whole-brain MRI data,
2. to reconstruct the boundary surfaces of the cortex such that they align with topological constraints,
3. to allow an estimation of intermediate surfaces in-between the boundary surfaces describing the anatomical layering, and,
4. to subdivide the cortex into smaller meaningful entities corresponding to functional cortical areas.

The process of further segmenting the cortex into smaller sub-segments is also called **cortical parcellation**.

Regarding the segmentation of brain data, clustering and classification methods are appropriate as they allow membership definitions between WM and GM, and GM and CSF. Clustering and classification are introduced in Section 4.1. Their advantages and disadvantages are discussed, too.

Given the assignments of voxel belonging to a certain object may yield topological inconsistencies. With additionally applying a deformable model, topology-correct boundaries of the interfacing tissue structures of the cortex can be derived. The two classical types, i. e., *parametric* and *geometric* deformable models, and their individual characteristics will be presented in Section 4.2.

Using high-resolution data demands the use of efficient methods such as the geometric deformable model, specifically the level set functions. Level set functions are an ideal candidate for constructing an anatomically-motivated layering model. They allow accurate computation of curvature which is a necessity for the highly curved cortex. Using such a framework allows the computation of **cortical profile trajectories** which range from one boundary surface to the other. Along these trajectories, precise sampling of image intensities is possible, yielding so-called **cortical profiles**.

The here highlighted methods are fundamental for the following chapters of the thesis. Clustering and classification methods that are used in state-of-the-art cortical parcellation schemes are explained in the next chapter. Geometric deformable models are used throughout data processing in this thesis.

4.1 CLUSTERING AND CLASSIFICATION IN IMAGE SEGMENTATION

Image segmentation describes the process of dividing image data into multiple segments. These can be sets of pixel in 2D, but also voxel in 3D. The goal of every segmentation task is to change and/or simplify the information given in the image data to more meaningful and easier-to-analyse representations. Segmentation methods are used to locate objects and boundaries, i. e., lines and curves in 2D or surfaces in 3D. For simplicity, explanations in the thesis will refer to the 2D case, i. e., defining regions and curves in 2D rather than volumes and surfaces in 3D. Approaches considering application to 3D imaging data are more sophisticated, but can be implemented just as accurately and efficiently as in 2D with higher computational cost due to the third dimension.

Image segmentation specifically describes the process of assigning a label to every pixel in an image such that the pixel having the same label share certain characteristics. The result of an image segmentation is a set of segments or classes, or set of contours extracted from the image data. Clustering and classification techniques allow one to make such assignments.

CLUSTERING belongs to **unsupervised** learning techniques and, as such, they try to find an intrinsic grouping in a set of unlabelled data. Clustering methods can be utilised as an **exploratory** data analysis. The aim is to sort different objects into groups. The intra-group variance shall be minimised while the inter-group variance is maximised with respect to a certain criterion. Thus, clustering methods are useful to discover structures in data without providing an explanation, interpretation or high-level a-priori information.

CLASSIFICATION methods belong to **supervised** learning techniques. They are common in statistics and machine learning, but also in image data analysis or pattern recognition. In contrast to clustering methods, classification itself can be seen as a form of **categorisation**. As such, it describes the process in which objects are recognised, differentiated, and understood. In image analysis, most commonly statistical classification methods are used. These methods identify to which of a set of categories a new observation belongs. The decision is based on a training set of data or an observation (or instance) whose category membership is known.

SIMILARITIES Clustering and classification methods are able to divide the image data into multiple segments. The analysis methods themselves address no specific algorithm, but the general task to be solved. Segmentations can be of **binary** or **multi-class** type. In a binary segmentation, the object to be identified will be separated from the background. In multi-class segmentations, multiple objects are detected at the same time. The result can be of two types: a **hard** or a **soft** segmentation. A hard segmentation assigns only one label to each voxel while a

soft segmentation assigns k labels (with k representing the maximum number of segments) to each voxel defining the membership value for each segmented class k to this voxel.

DIFFERENCES When clustering data, the resulting set of segments is of interest. Clustering relates to an exploratory investigation of the data to address the questions "if" and "how" data groups. In classification tasks, the resulting discriminative power of a set of segments to other sets is of interest. The procedure categorises data into groups based on a-priori information asking whether the final grouping is meaningful and correlates with a certain assumption. The prior information is usually derived from initial samples or specifically through training of samples. Indeed, the differences between the methods often lead to misunderstandings when using the same terminologies and algorithms with different intended goals.

REQUIREMENTS In general, clustering and classification algorithms shall satisfy certain main requirements. They need to deal with different types of attributes or input observations. Segmentation techniques need to have the ability to work with higher dimensional data and to be robust towards noise and outliers. Clusters with a complex shape need to be detected.

The algorithms may not address all requirements adequately and, most commonly, not at the same time. The effectiveness of the techniques highly depends on the chosen similarity criterion or features used to separate objects. In case, a similarity metric does not exist, it has to be defined by the user. This is a crucial choice as an inappropriate metric may lead to incorrect results. When dealing with high dimensional data or a large number of input items, the complexity and the computational cost increase.

NUMBER OF CLASSES A more critical problem is to identify how many groups or classes exist. Usually, this information is not known in advance. Unfortunately, there is no general solution that can determine the optimal number of classes for any given data set. A simple solution is to set the number of classes a-priori, either manually or using (semi-)automatic methods. Another solution is to run the algorithms multiple times each with a different number of classes to identify the best result according to a criterion [Pena et al., 1999; Bradley et al., 1998]. Other solutions incorporate statistics or advanced models [Eltibi and Ashour, 2011].

In this section, representative algorithms of clustering and classification techniques will be briefly described and discussed.

4.1.1 *Clustering Methods*

When clustering data, the segmented classes are called clusters. Clustering methods can be divided into four categories:

EXCLUSIVE CLUSTERING: one object belongs to one, and only one, segmented cluster.

OVERLAPPING CLUSTERING: uses fuzzy descriptions to cluster data. Thus, an object may belong to two or more clusters with different degrees of membership.

HIERARCHICAL CLUSTERING: is based on iteratively merging two clusters based on a criterion.

PROBABILISTIC CLUSTERING: uses statistical techniques. It is close to statistical learning methods or supervised learning approaches (see next section).

In the thesis, the following clustering algorithms will be briefly presented:

- K-means,
- Fuzzy C-means,
- Hierarchical agglomerative clustering,
- Model-based clustering.

Each of these algorithms represents one of the categories listed above. The approaches are most commonly used in cortical parcellation schemes (presented in the next chapter) and represent the building block in the data processing pipeline (see Chapter 6.2).

The general question of any clustering technique is to decide what a good clustering is constituted of. The decision is based on a similarity criterion. Two objects from one cluster have more similar characteristics than two objects from different clusters. There are various characteristics to define the similarity. Most commonly, distance is used.

4.1.1.1 *K-Means Clustering*

K-means [MacQueen, 1967] is one of the simplest unsupervised learning algorithms. The method is a type of exclusive clustering in which a certain object belongs to only one cluster. A number of clusters k has to be fixed a priori. The grouping is based on the barycenter of each cluster. Therefore, k-means clustering is also known as centroid-based clustering.

Given an a-priori defined set of k clusters and n objects to group into these, k-means algorithm minimises the objective function:

$$S = \sum_{j=1}^{k} \sum_{i=1}^{n} \|x_i^{(j)} - c_j\|^2. \tag{4.1}$$

It is a squared error function where $\|x_i^{(j)} - c_j\|^2$ represents the Euclidean distance measure between a data point $x_i^{(j)}$. The cluster center c_j indicates the distance of data points from their respective cluster centers.

The k-means algorithm starts to group the data as follows:

1. Define k points in the data space. These points represent initial group centroids (see Fig. 4.1 A).

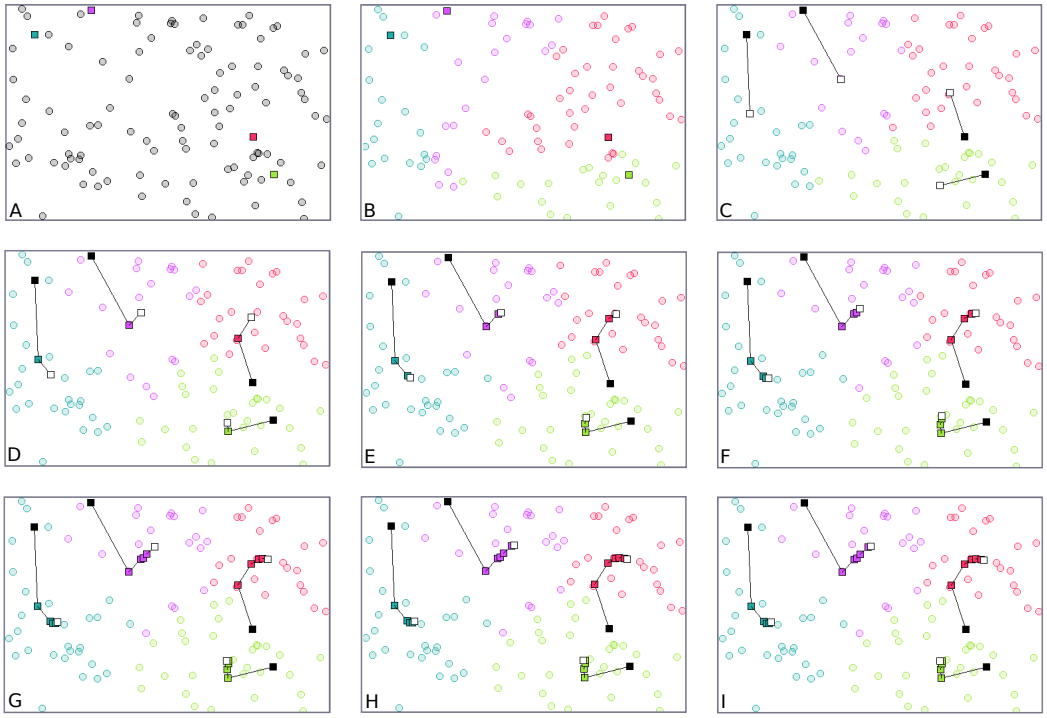

Figure 4.1: Data is clustered into four groups using k-means. A) shows the initial group centroids as small rectangles. B) shows the initial grouping. C) depicts the first recalculation of the group centers. The white rectangles are the new centroids. D)-I) highlight the evolving clusters. Images created with free online applet: http://home.deib.polimi.it/matteucc/Clustering/tutorial_html/AppletKM.html.

2. Find for each unlabelled object the closest centroid.
3. Group objects belonging to the same centroid (see Fig. 4.1 B).
4. Recalculate positions of the k centroids according to the grouping in the previous step (see Fig. 4.1 C).
5. Repeat steps 2–4 until the position of the centroids no longer changes (see Fig. 4.1 D-I).

The definition of the initial k points can be done manually or automatically. But the algorithm highly depends on the initially selected cluster centers. If the initial cluster centers are not well distributed over data space, the k-means algorithm may not find the most optimal solution. Running k-means multiple times may reduce this effect. However, there is a remaining chance that the set of samples closest to the centroid is empty and the position of the k centroid cannot be updated (see step 2). This needs to be taken into account in the implementation. A more critical problem is to identify the number of potential clusters k a-priori. A simple solution is to run k-means multiple times each with a different number of clusters. The best result is then chosen according to a given or defined criterion.

4.1.1.2 *Fuzzy C-Means Clustering*

Fuzzy C-means (FCM) clustering is similar to k-means but allows an object to belong to two or more clusters leading to a non-binary membership decision which explains the term "fuzzy". This method has been developed by Dunn [1973] and was improved by Bezdek [1981]. FCM is a frequently used technique in pattern recognition. Given an a-priori defined set of K clusters and N items to be clustered, FCM minimises the objective function:

$$S_m = \sum_{i=1}^{N} \sum_{j=1}^{K} u_{ij}^m \|x_i - k_j\|^2 \quad \text{for} \quad 1 \leqslant m \leqslant \infty \tag{4.2}$$

where u_{ij} is the degree of membership of x_i in the cluster j, x_i is the i-th of d-dimensional measured data, k_j is the center of the cluster, and $\| * \|$ is any norm expressing the similarity between the measured data and the center.

The fuzziness coefficient is denoted by m and must be a real number greater than 1. It measures the tolerance of the clustering, e. g., how much the clusters overlap with one another. The higher the value of m, the larger the overlap between clusters.

Fuzzy partitioning is carried out through an iterative optimisation of Eq. 4.2, with the update of the membership u_{ij} as follows:

$$u_{ij} = \frac{1}{\sum_{t=1}^{K} \left(\frac{\|x_i - k_j\|}{\|x_i - k_t\|} \right)^{\frac{2}{m-1}}}. \tag{4.3}$$

The cluster centers k_j are updated as follows:

$$k_j = \frac{\sum_{i=1}^{N} u_{ij}^m x_i}{\sum_{i=1}^{N} u_{ij}^m} \tag{4.4}$$

with t determining the number of iterations used. The iteration will stop when:

$$\max_{ij} \left\{ |u_{ij}^{t+1} - u_{ij}^t| \right\} < \varepsilon. \tag{4.5}$$

ε is a termination criterion between 0 and 1. This procedure converges to a local minimum or a saddle point of S_m. Initialising the algorithm differently may provide a different solution. But, a different initialisation may converge to the same result but at higher costs. 20 data points can be grouped into three clusters very quickly (see Fig. 4.2 B). Using a fuzziness coefficient of $m = 2$ and a termination criterion set to $\max_{ij} \left\{ |u_{ij}^{t+1} - u_{ij}^t| \right\} < 0.3$, the initial data (Fig. 4.2 A) is clustered in only 8 steps. When increasing the accuracy by setting ε=0.01, the clustering takes 37 steps (Fig. 4.2 C).

4.1.1.3 *Hierarchical Agglomerative Clustering*

A hierarchical clustering, defined by Johnson [1967], respects the inherent connectivity in the data. Therefore, hierarchical clustering is also known as connectivity-based clustering.

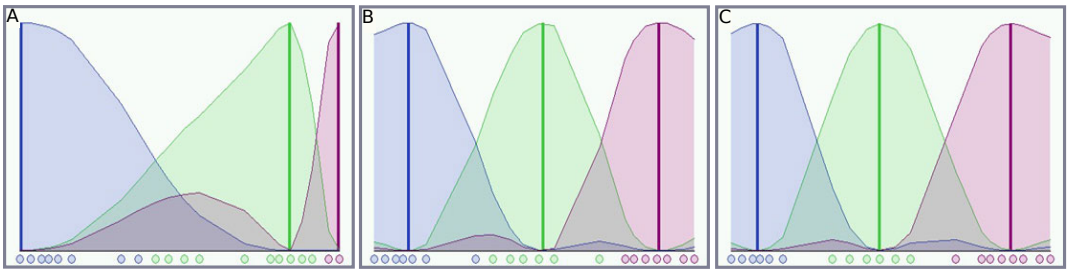

Figure 4.2: Grouping 20 data points into three clusters using the Fuzzy C-means (FCM) algorithm. The cluster curves (blue, red and green) describe the membership value of each data point belonging to a certain cluster. As clusters overlap each other, data points belong to a certain degree to a single cluster. A) shows the initial data. B) A quick FCM result after 8 steps allowing less accuracy. C) FCM result after 37 steps. Using higher accuracy yields higher computational costs. Images created with free online applet: http://home.deib.polimi.it/matteucc/Clustering/tutorial_html/AppletFCM.html.

Hierarchical approaches are iterative and start with the condition of setting every object as a cluster. After the final iteration i_{end}, all objects belong to one cluster. To chose the clustering wanted, the result at $i < i_{end}$ is chosen. Thereby, they bring a certain order into the clustering. Clusters on higher levels are constituted of clusters on lower levels.

Given a set of N items and a $N * N$ similarity (or distance) matrix, the basic hierarchical clustering algorithm starts to group the data as follows:

1. Assign each single item to a single cluster, such that $\#_{items} = \#_{clusters}$.
2. Define the similarity between two clusters as the similarity between the items these clusters contain.
3. Find the most similar (or closest) pair of clusters.
4. Merge pair into a single cluster. The $\#_{clusters}$ decreases by 1.
5. Compute the similarities (distances) between the new defined cluster and each of the old clusters.
6. Repeat steps 3–5 until all items are clustered into one single cluster of size N.

Finally, when the hierarchical tree is completed, the k defined clusters can be derived by cutting the $k-1$ longest link in the tree.

Three strategies are mainly used in hierarchical schemes: single linkage clustering, complete-linkage clustering and average-linkage clustering (see Fig. 4.3).

SINGLE-LINKAGE CLUSTERING is called the minimum method (or connectedness method). The distance between two clusters is considered to be the shortest distance. In case a similarity metric is used, the similarity between the two clusters is considered to be maximum.

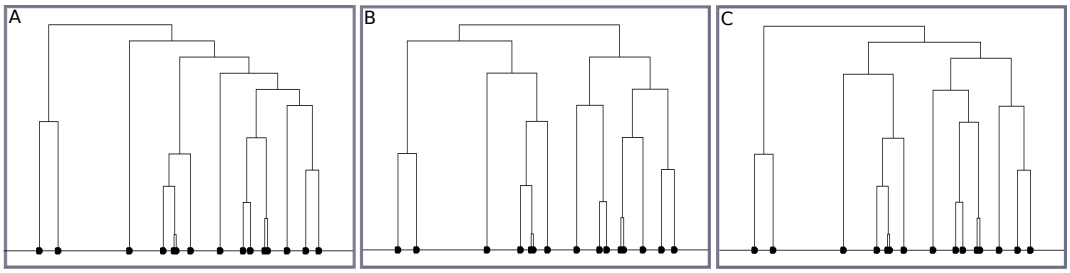

Figure 4.3: Hierarchical clustering of 15 data points using the single-linkage (A), complete-linkage (B) and average-linkage clustering (C). Images created with free online applet: http://home.deib.polimi.it/matteucc/Clustering/tutorial_html/AppletH.html.

COMPLETE-LINKAGE CLUSTERING is called the maximum method (or diametre method). The distance between two clusters is considered to be the maximum distance. In case a similarity metric is used, the similarity between the two clusters is considered to be minimum.

AVERAGE-LINKAGE CLUSTERING considers the distance between two clusters to be the average distance.

Hierarchical clustering methods are also called agglomerative clustering because clusters are iteratively merged together.

The main problem of these clustering methods is their irreversible nature: once a label is assigned to an object, it will not change again. When using k-means, labels of an object may change when iterating towards the solution.

4.1.1.4 *Model-based Clustering*

Clustering problems can be solved using a model-based approach. The models used aim at representing clusters within the entire data. Model-based clustering approaches need no observed data (training data) to identify the cluster to which an unobserved instance belongs. These methods use an assumption about a cluster described by a certain model that is adequately represented by the data. The algorithm then aims at optimising the fit between data and model.

Practically, a cluster in the data can be mathematically described by a parametric distribution. Often, Gaussian distributions are used to represent continuous data [Shental et al., 2004]. An individual distribution used to describe a certain cluster is referred to as a *component* distribution. With different clusters being present in the data, a mixture of the models then represents the entire data.

Using so-called mixture models is meaningful when:

- the modelled distributions, i. e., the components, are appropriately distributed (small variance around a significant peak in the distribution, no large overlap between components),
- the data is covered well by the mixture of the models (components are able to capture dominant patterns).

Model-based approaches have several advantages: depending on the data, the distribution used for clustering can be adequately chosen. Using a-priori defined models allows to obtain a density estimation for each cluster. Hence, model-based clustering techniques are also referred to as density-based clustering methods.

MIXTURE OF GAUSSIAN Most commonly, mixture models describe a mixture of Gaussian distributions [McLachlan and Peel, 2004]. Clusters are modelled as Gaussian distributions centered on their barycenter.

In the data, k components are given by R data points. The i-th component, $i = 1 \leqslant i \leqslant k$ is called ω_i. Each component ω_i is assumed to generate data from a Gaussian distribution with a probability $P(\omega_i)$. The Gaussian distribution is defined by a mean vector μ_i and its covariance matrix $\sum_i$. Now, each unlabelled data point x_i is generated as follows: using component ω_i with probability $P(\omega_i)$:

$$x_i \sim N(\mu_i, \sum_i). \tag{4.6}$$

The algorithm fits the mixture models to the data for the unknown mean vectors μ_i. The probability of each component and data point need to be maximised by calculating the first derivative. This is complicated and the logarithmic likelihood estimation serves as a surrogate. Due to its monotone nature, it provides a maximum at the same location as a non-logarithmic likelihood estimation. A detailed description on how to maximise the probability is given in Moore [2001].

Logarithmically maximising the probability, creates a circularity that can be interpreted as two different problems:

1. if μ_j is given, then the probability for each ω_j and x_i could be computed.
2. if for each data point we knew that for each component the probability that μ_j belongs to component ω_j is of a certain probability, then μ_j could be easily computed.

To solve this circularity, an iterative expectation-maximisation (EM) approach can be used [Moon, 1996]. The expectation-step computes the "expected" components of all data points yielding a membership distribution. Thus, at each data point a vector indicates the membership value to the components. The maximisation-step computes the maximum likelihood of μ given the class membership distribution of the data.

4.1.1.5 *Summary*

The above mentioned clustering methods represent the most commonly used algorithms. Advanced implementations include a-priori information about the data such as the number of clusters or combine the different advantages of the methods to design application-driven methods.

The success of a certain clustering method highly depends on the appearance of the clusters in the data. As centroid-based method, k-means is able to find the barycenter of a cluster. The method can detect differently-sized clusters in a data set. However, if the clusters in the data are only describable based on density, and

not by shape or size, k-means fails. When clusters can be described by a specific size or shape, model-based clustering techniques work well.

4.1.2 *Classification Methods*

As in clustering, classification describes no specific algorithm, but the general task to be solved. An algorithm implementing a classification, i. e., a categorisation of objects or observations, is called a classifier. A simple mathematical function can be defined as classifier.

Usually, the individual observations are evaluated according to (quantifiable) properties, called features. The vector storing the features is called feature vector. The space associated with these vectors and used for classification is called feature space. These features can be of different types:

- real-valued, e. g., a measurement of body temperature,
- integer-valued, e. g., the number of sunny days per year,
- ordinal, e. g., "hot", "warm" or "cold",
- categorical, e. g., "dog", "cat" or "fish" as part of animal classes.

In other cases, classifiers compare the observations to previous observations by using a similarity metric, e. g., a distance measure.

4.1.2.1 *Linear Classifiers*

Linear classifiers use linear functions to assign a score to each possible category k. Most commonly, the feature vector of the object is combined with a vector of weights using the inner product. The object is assigned to the category with the highest score.

The function used is known as linear predictor function and has the following form:

$$\text{score}(\mathbf{X}_i, k) = \boldsymbol{\beta}_k \cdot \mathbf{X}_i \tag{4.7}$$

where $\mathbf{X}_i$ describes the feature vector of object i. $\boldsymbol{\beta}_k$ is the vector of weights corresponding to category k, and $\text{score}(\mathbf{X}_i, k)$ is the predicted score of object i in respect to each category k.

Algorithms using this basic function are known as linear classifiers. They only differ by their training, i. e., on how to determe the optimal weights for the data separation.

4.1.2.2 *k-Nearest Neighbor*

The k-nearest neighbour (k-NN) algorithm is one of the simplest instance-based, supervised learning techniques [Altman, 1992]. k-NN estimates its results based on a uniform kernel that is applied only locally [Terrell and Scott, 1992]. k-NN algorithms can be seen as non-parametric density-based classification approaches.

k-NN consists of two phases:

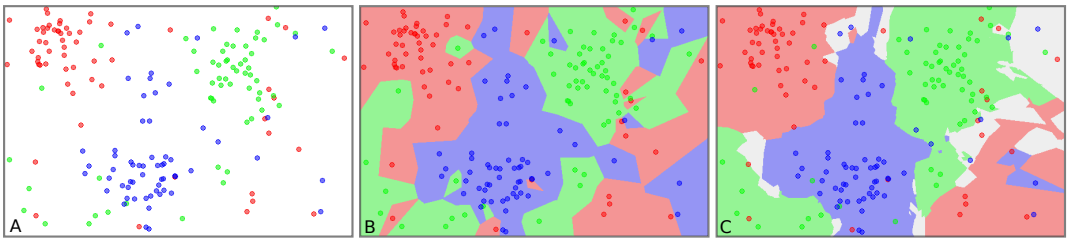

Figure 4.4: k-NN applied to the data shown in A) with k=1 (B) and k=5 (C). Using larger values of k reduces the noise effect on the classificaion, i. e., the classification is less patchy. However, boundaries are less distinct. Images created with free online applet by Mirkes [2011].

TRAINING PHASE The training examples are vectors in a multi-dimensional feature space. Each training example is assigned to a class label. The training phase involves storing the feature vectors and class labels of the training samples.

CLASSIFICATION PHASE In the classification phase, an unlabelled instance is assigned to a label based on majority voting. k-NN identifies the most frequent label among the k training samples nearest to the actual observation based on a similarity criterion (see Fig. 4.4).

The k-NN classification algorithm categorises the data as follows:

1. Define a set of k clusters a-priori, e. g., by training.
2. Select an unlabelled instance.
3. Find the k training samples closest to the new instance.
4. Find the label most common among the training samples.
5. Assign this label to the unlabelled instance.
6. Repeat step 2–5

The k-NN algorithm is applied only locally, and as such, very sensitive to the local structure of the data.

If the class distribution is skewed or the features scale inconsistently with their importance, a simple "majority voting" may lead to misclassifications. This problem can be solved by incorporating distance-based weighting in the classification phase: the classes of the k nearest neighbors of the actual instance are multiplied by a weight that is proportional to the inverse of the distance from the actual unlabelled observation [Coomans and Massart, 1982a]. Using these distance-based criteria, k-NN can be modified for direct density estimation [Coomans and Massart, 1982b].

4.1.2.3 *Support Vector Machines*

A Support Vector Machine (SVM) is a non-probabilistic classification method. It performs data classification based on finding a hyperplane that maximises the distance between the samples in each class [Vapnik, 1963; Vapnik and Chervonenkis, 1964]. The vectors defining the hyperplane are called support vectors. Multi-class

separation is performed by dividing the individual multi-class problems into multiple binary classification problems.

There are two basic types: linear and non-linear SVM.

LINEAR SVM Considering a SVM for data classification into two classes, we have a training set T containing n data points described as follows:

$$T = \left\{(\mathbf{x}_i, y_i) \mid \mathbf{x}_i \in \mathbb{R}^d, y_i \in \{-1, 1\}\right\}_{i=1}^{n}. \tag{4.8}$$

The data points are either 1 or -1 depending on the class they belong to and $\mathbf{x}_i$ is a d-dimensional vector. The goal is to find a hyperplane that maximise the distance between the samples in each class. A hyperplane can be defined by:

$$\mathbf{w} \cdot \mathbf{x} - b = 0. \tag{4.9}$$

Here, $\cdot$ defines the dot product. The distance between the classes is determined by the offset b of the hyperplane from the origin along the normal vector $\mathbf{w}$ (see Fig. 4.5A). From Eq. 4.9, the distance is defined as $\frac{b}{\|\mathbf{w}\|}$ and called *margin*. If the training data are linearly separable, there are two other hyperplanes that separate the data such that no training sample falls into the margin. These hyperplanes can be defined by:

$$\mathbf{w} \cdot \mathbf{x} - b \geqslant 1, \text{ (for } x_i \text{ of class one), and } \mathbf{w} \cdot \mathbf{x} - b \leqslant -1, \text{ (for } x_i \text{ of class two).} \tag{4.10}$$

The distance between the two hyperplanes is $\frac{2}{\|\mathbf{w}\|}$. The aim is to minimise $\|\mathbf{w}\|$.

The optimal separating hyperplane can be defined by the following problem: find $\mathbf{w}$ and b that minimise $\|\mathbf{w}\|$ such that for all data points (x_i, y_i):

$$y_i(\mathbf{w} \cdot \mathbf{x_i} + b) \geqslant 1. \tag{4.11}$$

The support vectors constrain the width of the margin and are the x_i on the boundary for which $y_i(\mathbf{w} \cdot \mathbf{x_i} + b) = 1$. Finally, the goal is to minimise the objective function:

$$\min \frac{1}{2}\|\mathbf{w}\|^2, \tag{4.12}$$

that finds $\mathbf{w}$ and b using quadratic programming. If the data is linearly separable, there is a global minimum value. The approach produces a hyperplane that separates the data into two non-overlapping classes. The simplest method to group the data into two categories is using a straight line (in 2 dimension), a flat plane (in 3 dimensions) or an N-dimensional hyperplane.

It may occur that there is no hyperplane that separates the data under the constraint of not allowing samples to be within the margin. Sometimes, misclassification occurs. A solution to these problems can be achieved by using a soft margin constraint.

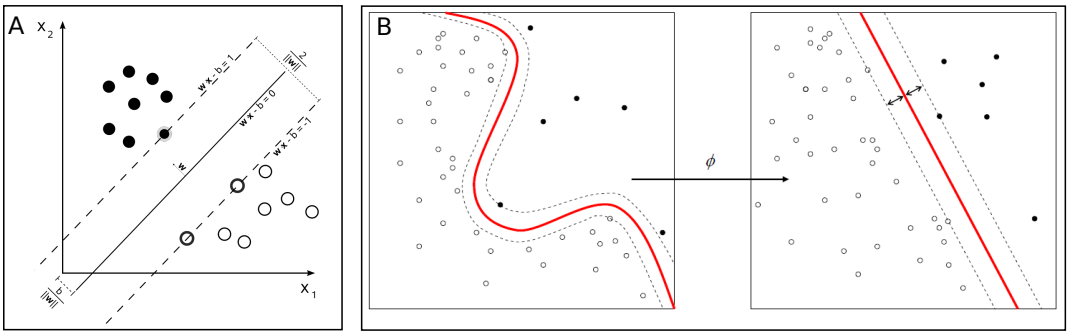

Figure 4.5: The images depict a support vector machine for linear (A) and non-linear separation tasks (B and C). A) The hyperplane (solid line) separates the data such that no training sample falls into the margin defined by the planes in normal direction. (Image source: Wikipedia: http://goo.gl/dvUTxR.) B) The image represents data that can be separated non-linearly. C) The data can be transformed into a feature space where it is linearly separable using the kernel trick. (Image source: Wikipedia: http://goo.gl/rnZ2pV.)

SOFT MARGIN METHODS A "soft margin" approach is used when there is no solution to an ideal hyperplane such that misclassification occurs [Cortes and Vapnik, 1995]. The method still maximises the distance to the nearest regularly split samples but tries to minimise misclassifications. To do so, a slack variable ζ_i is introduced into the constraint. It allows instances to fall of the margin, but penalises these. In general, the approach keeps the slack variable to zero while maximising the margin.

NON-LINEAR SVM Separating data linearly is sometimes impossible for more complex problems and a non-linear separation of data is required. Boser et al. [1992] suggested a way to create non-linear classifiers by applying the so-called kernel trick [Aizerman et al., 1964].

The kernel trick applies a non-linear kernel function that transforms the data into a higher dimensional feature space where the linear separation can be performed. The algorithm is similar except that the dot product is substituted by a non-linear kernel function. Hence, the method transforms the hyperplane in a transformed feature space.

A linear SVM equals the dot product of vectors:

$$y(x_i, x_j) = x_i \cdot x_j. \tag{4.13}$$

A non-linear SVM maps the vectors using a transfer function ϕ into a feature space in which the kernel trick then uses the transformed vectors to separate the data (see Fig. 4.5B):

$$k(x_i, x_j) = \phi(x_i) \cdot \phi(x_j). \tag{4.14}$$

Kernel functions depend on the application and, hence, are customizable. Examples on design can be found in Hearst et al. [1998].

4.1.3 *Limitations of Clustering and Classification Methods*

Clustering and classification approaches in the discipline of medical image processing aim at grouping or classifying the image pixel to anatomical structures. However, the assignments may yield topological inconsistencies when compared to the true anatomy. The segmentation may be divided up into several pieces rather than being one connected compartment or it may contain holes or handles. Therefore, a topologically correct reconstruction of the structure's boundary is important. The reconstruction provides a geometric representation that is in alignment with the true geometry of the anatomy of this structure.

In this thesis, the structure of interest is the cortical surface. An accurate surface reconstruction therefore agrees with the true definition of the cortical sheet given its varying thickness, the different lobes, the gyral folds, and narrow sulci. Thus, a cortical reconstruction describes the localisation and representation of one or even more of these mentioned cortical surfaces. The task is very challenging given the very complex nature of the brain.

4.2 IMAGE SEGMENTATION USING DEFORMABLE MODELS

Medical images are often contaminated by imaging artefacts and noise which can cause considerable difficulties when applying classical segmentation methods. The applied techniques either fail completely or require some pre- or post-processing to correct or remove inaccurate or invalid object boundaries in the segmentation result. Explanations will again refer to the 2D case.

These difficulties are addressed by deformable models. Deformable models describe curves which are defined in the image domain. They move under the influence of forces.

INTERNAL FORCES are defined within the curve itself and are designed to keep the model smooth during the deformation process. The internal forces describe the tension or bending behaviour of the curve.

EXTERNAL FORCES are computed from the image data directly and govern the model movement towards an object's boundary or other desired features within an image. External forces are called image-based forces.

Deformable models are robust to image noise and boundary gaps by constraining the extracted boundaries to be smooth and to incorporate prior information about the object shape. The models integrate all boundary elements into a consistent and coherent mathematical description. Deformable models are defined implicitely on the image grid. This allows the resulting boundary representation to achieve sub-pixel accuracy, a highly desired feature for medical imaging application.

The concept of deformable models date back to Fischler and Elschlager's spring-loaded templates [Fischler and Elschlager, 1973] and Widrow's rubber mask technique [Widrow, 1973a,b]. The definition of deformable models first appeared in the work by Terzopoulos and Fleischer [1988]. The popularity of deformable models is constituted by the famous paper by Kass et al. [1988]: "Snakes: Active Contour

Models" and related work by Teraopoulos [1987] and Terzopoulos et al. [1988]. Deformable models have become one of the most successful and active research streams in image segmentation. To refer to deformable models various names are used in literature: snakes, active contours (surfaces in 3D domain, respectively), balloons, deformable contours (or surfaces in 3D, respectively).

There are two different classes of deformable models: **parametric deformable models** [Kass et al., 1988; Miller et al., 1993; Amini et al., 1990; Cohen, 1991] and **geometric deformable models** [McInerney and Terzopoulos, 1995a; Caselles et al., 1993; Malladi et al., 1995; Caselles et al., 1997].

Level set methods are synonymously used to describe geometric deformable models.

Within the next section, parametric and geometric deformable models will be briefly presented. A specific focus is given to level set methods as they provide the fundamental basis for the work conducted in the thesis.

4.2.1 *Parametric Deformable Models*

Parametric deformable models describe curves explicitly in a parametric form. Thus, a direct interaction with the model in this representation is possible. Adapting the topology of the model, i. e., splitting or merging parts during the deformation is difficult when using parametric models.

There are two types of formulations for parametric deformable models:

1. an energy minimising formulation, and,
2. a dynamic force formulation.

The first formulation is advantageous as its solution satisfies a minimum principle. The second formulation allows for more flexibility in using more general types of external forces. The most commonly applied formulation is the energy minimising formulation which will be explained in this section.

4.2.1.1 *Definition of Parametric Deformable Models*

The parametric curve is initialised within the image domain to find the object boundary. The aim of a deformable model based on an energy minimising formulation is to find a parameterised curve which minimises the weighted sum of internal and external forces. Minimising the total energy will cause two effects. On the one hand, the curve is hold together (elasticity forces) and kept from bending too much (bending forces) through internal forces. On the other hand, the curve is attracted towards the desired object boundaries.

In mathematical notation, a deformable contour is a curve $\mathbf{X}(s) = (X(s), Y(s))$ with $s \in [0, 1]$, that moves in the spatial domain of an image and minimises the energy function ϵ such that [Xu et al.]:

$$\epsilon(\mathbf{X}) = S(\mathbf{X}) + P(\mathbf{X}) \rightarrow min. \tag{4.15}$$

The first term $S(\mathbf{X})$ denotes the internal force and defines the tension or smoothness of a contour as:

$$S(\mathbf{X}) = \frac{1}{2}\int_0^1 \alpha(s)\left|\frac{\partial \mathbf{X}}{\partial s}\right|^2 + \beta(s)\left|\frac{\partial^2 \mathbf{X}}{\partial s^2}\right|^2 ds. \tag{4.16}$$

The first-order derivative prevents stretching and allows the model to behave like an elastic string. The second-order derivative constrains bending and imitates the behaviour of a rigid rod. The strength of the model's tension and rigidity can be controlled by $\alpha(s)$ and $\beta(s)$.

The second term $P(\mathbf{X})$ denotes the external energy, called potential energy. It is defined over the image domain and takes smaller values at object boundaries. Thus, it typically possesses local minima at the image intensity edges that occur at object boundaries. In Eq. 4.15, $P(\mathbf{X})$ integrates a potential energy functional $P(x, y)$ along the contour $\mathbf{X}(s)$ such that:

$$P(\mathbf{X}) = \int_0^1 P(\mathbf{X}(s))ds. \tag{4.17}$$

Given a grey-level image $I(x, y)$, a common potential energy function considered to move a deformable model towards edges is defined as [Xu et al.]:

$$P(x, y) = -w_e \left|\nabla \left[G_\sigma(x, y) * I(x, y)\right]\right|^2 \tag{4.18}$$

in which w_e is a weighting parameter, $G_\sigma(x, y)$ is a two-dimensional Gaussian function with standard deviation σ, ∇ is the gradient operator, and $*$ the convolution operator. Increasing σ broadens the attraction range of the moving deformable model and can cause a shift in the final boundary location, leading to a less accurate result.

Overall, the problem of finding a contour $\mathbf{X}(s)$ that minimises the energy function ϵ is known as a variational problem [Courant and Hilbert, 1953]. Kass et al. [1988] and Cohen [1991] have shown that the curve minimising the energy function must satisfy the Euler-Lagrange equation:

$$\frac{\partial}{\partial s}\left(\alpha\frac{\partial \mathbf{X}}{\partial s}\right) - \frac{\partial^2}{\partial s^2}\left(\beta\frac{\partial^2 \mathbf{X}}{\partial s^2}\right) - \nabla P(\mathbf{X}) = 0. \tag{4.19}$$

To understand the physical behavior of deformable contours, Eq. 4.19 can be interpreted as a force balance equation:

$$\mathbf{F}_{int}(\mathbf{X}) - F_{ext}(\mathbf{X}) = 0 \tag{4.20}$$

in which the internal energy is defined as:

$$\mathbf{F}_{int}(\mathbf{X}) = \frac{\partial}{\partial s}\left(\alpha\frac{\partial \mathbf{X}}{\partial s}\right) - \frac{\partial^2}{\partial s^2}\left(\beta\frac{\partial^2 \mathbf{X}}{\partial s^2}\right) \tag{4.21}$$

and the external energy is defined as:

$$\mathbf{F}_{ext}(\mathbf{X}) = -\nabla P(\mathbf{X}). \tag{4.22}$$

The internal force $\mathbf{F}_{int}(\mathbf{X})$ prevents stretching and bending of the contour while the external force $\mathbf{F}_{ext}(\mathbf{X})$ pulls the contour toward the desired object boundaries.

To find a solution to the Euler-Lagrange formulation given in Eq. 4.19, the deformable contour is made dynamic. $\mathbf{X}(s)$ is treated as a function of time t as well as s yielding $\mathbf{X}(s, t)$. The partial derivative of $\mathbf{X}$ with respect to t is set equal to the left-hand side of Eq. 4.19:

$$\gamma\frac{\partial \mathbf{X}}{\partial t} = \frac{\partial}{\partial s}\left(\alpha\frac{\partial \mathbf{X}}{\partial s}\right) - \frac{\partial^2}{\partial s^2}\left(\beta\frac{\partial^2 \mathbf{X}}{\partial s^2}\right) - \nabla P(\mathbf{X}). \tag{4.23}$$

γ is a coefficient introduced to make the units on the left side consistent with the right side. When the solution $\mathbf{X}(s,t)$ stabilises, the left side vanishes. Then, a solution of Eq. 4.19 is found. Making the time derivative term vanish is similar to an application of a gradient descent algorithm that finds the local minimum of Eq. 4.15 [Cohen et al., 1992]. In general, a solution to the minimisation problem can be found by placing an initial contour on the image domain and allowing it to deform according to Eq. 4.23.

4.2.1.2 *External Forces*

There is a huge variety of external forces. The definition of external forces depends on the application. Their common goal is to increase the attraction range for the deformable contour.

MULTISCALE GAUSSIAN POTENTIAL FORCES use the Gaussian potential force given in 4.18 at different scales (starting from large σ values down to small values) to broaden the attraction range while maintaining the accuracy of the model's boundary location. It allows to attract the curve from a long range and track it at finer scales. It overcomes the problem of setting the initialisation curve close to the final solution [Kass et al., 1988; Terzopoulos et al., 1988].

PRESSURE FORCES are used together with Gaussian potential forces. The pressure force can inflate or deflate the model. Thus, it is no longer required to initialise the model near the desired object boundary. The deformable models using an external pressure force are usually called balloons [Cohen, 1991; Ronfard, 1994; Poon and Braun, 1997]. The pressure force is defined as:

$$\mathbf{F}_p(\mathbf{X}) = w_p \mathbf{N}(\mathbf{X}) \tag{4.24}$$

where $\mathbf{N}(\mathbf{X})$ is the inward unit normal vector of the model at $\mathbf{X}$ and w_p is a constant weighting parameter. Whether the model should be inflated or deflated depends on the sign of w_p that defines the strength of the pressure force. Region information can be used to define the weighting parameter together with a spatial-varying sign in order to determine if the model is located inside or outside of the desired object. Using pressure forces in deformable models does not come without disadvantages: the pressure force may cause the deformable model to cross itself and form loops [Tek and Kimia, 1995].

DISTANCE POTENTIAL FORCES increase the attraction range and can be used by defining a distance map [Cohen and Cohen, 1993]. At each pixel the value of the distance map is obtained by calculating the distance between the pixel and the closest boundary point. Given a computed distance map $d(x,y)$ one possibility of defining a corresponding potential energy is presented in Cohen and Cohen [1993]:

$$P_d(x,y) = -w_d \exp\left(-d(x,y)^2\right). \tag{4.25}$$

The corresponding potential force field is then defined as $-\nabla P_d(x,y)$. However, difficulties remain when deforming the model into concavities of a contour.

GRADIENT VECTOR FLOW forces show an improved convergence into boundary concavities and use a vector diffusion equation that diffuses the gradient of an edge map in regions distant from the boundary. The force field is called gradient vector flow (GVF) field. The amount of diffusion adapts according to the strength of edges to avoid distorting the object boundaries. Details on GVF field definitions can be found in Xu and Prince [1998b,a].

4.2.1.3 *Limitations of Parametric Deformable Models*

Parametric deformable models have been applied in a wide range of applications. However, parametric deformable models have three main limitations:

1. When the initialisation of the model and the desired object boundary differ heavily in location, size and shape, the object may not be detected well enough. The model must be reparameterised dynamically to accurately recover the object boundary. A reparameterisation in 2D is usually straightforward. It requires only moderate computational overhead. However, a reparameterisation in 3D requires sophisticated and computationally expensive approaches.

2. Parametric deformable models have difficulties in dealing with topological adaptations. Splitting or merging of model parts, usually a useful property for detecting multiple objects or an object with unknown topology, cannot always be correctly performed. Whenever a topology change occurs, a new parameterisation must be constructed. To solve this difficulty, sophisticated approaches are required [Ďurikovič et al., 1995; McInerney and Terzopoulos, 1995b].

3. The parametric deformable models described here are defined in continuous space. Sometimes, it is more straightforward to develop deformable models from a discrete point of view [Geiger et al., 1995; Lobregt and Viergever, 1995; Nastar and Ayache, 1996].

4.2.2 *Geometric Deformable Models*

Geometric deformable models have been independently proposed by Caselles et al. [1993] and Malladi et al. [1995] and provide elegant solutions for the limitations of parametric deformable models. These models are based on the theory of curve evolution [Kimia et al., 1995; Kimmel et al., 1995; Alvarez et al., 1993] and the level set method [Sethian, 1999]. Detailed information on deformable models can be found in Xu et al. [2000].

Curves (surfaces in 3D, respectively) are evolved using only geometric features, yielding an evolution independent on the parameterisation. Using geometric deformable models, curves are represented implicitly as a level set of a higher-dimensional scalar function. Hence, topological changes are handled automatically. The evolution is coupled with imaging data to recover the object boundaries.

4.2.2.1 *Curve Evolution Theory*

The aim of the curve evolution theory is to study the deformation of curves. In this process, only geometric measures such as the unit normal direction and curvature are taken into account as opposed to the quantities that depend on the parameters such as the derivatives of a parameterised curve.

Let $\mathbf{X}(s,t) = [X(s,t), Y(s,t)]$ be a moving curve with s being any parameterisation and t defining the time. The evolution of the curve along its normal direction can be described by the following partial differential equation:

$$\frac{\partial \mathbf{X}}{\partial t} = V(\kappa)\mathbf{N}. \tag{4.26}$$

The inward unit normal vector is denoted as $\mathbf{N}$ and the curvature defined by κ. $V(\kappa)$ represents the speed function that determines the speed of the curve evolution. Curves moving in some arbitrary direction can always be reparameterised to have the same form as Eq. 4.26 [Kimia et al., 1990].

There are two types of curve deformation known in curve evolution theory:

CURVATURE DEFORMATION is described by the following function:

$$\frac{\partial \mathbf{X}}{\partial t} = \alpha\kappa\boldsymbol{N}. \tag{4.27}$$

in which α denotes a constant. The equation smoothes, and eventually shrinks the curve to a circular point [Grayson, 1989]. The effects of curvature deformation are similar to the elastic internal forces of parametric deformable models. The curvature deformation describes the deformation along the tangent according to the local curvature.

CONSTANT DEFORMATION is given by the following equation:

$$\frac{\partial \mathbf{X}}{\partial t} = V_0\boldsymbol{N}. \tag{4.28}$$

where the coefficient V_0 determines the speed and direction of the deformation.

The properties of the curvature deformation and the constant deformation are complementary to each other. Curvature deformation smoothes the curves and thereby removes singularities. The constant deformation can create singularities from an initially smooth curve.

The general idea of the geometric deformable model is to match the speed of the deformation through curvature and/or constant deformation with the imaging data. The goal is that the evolution of the curve stops at the object boundaries.

An implementation of the evolution of geometric deformable models is using the **level set method**.

4.2.2.2 *Level Set Method*

The level set method for evolving curves is describes by Sethian [1999, 1985]. The method can handle topology changes automatically and provides the basis for a numerical scheme used by geometric deformable models.

In the level set framework, a curve is represented implicitly as a set of scalar function, i. e., the level set function. This function is defined on the same domain as the imaging data. A level set determines a set of points that have the same function value. The level set method evolves the curve by updating the level set function at fixed coordinates through time, rather than tracking the whole curve through time. This approach is similar to an Eulerian formulation of motion in contrast to the Lagrangian formulation, which is analogous to the parametric deformable model.

Suppose that a curve at time t is described by the closed-contour $\Gamma(t)$. The level set framework requires a level set function denoted as $\phi(\mathbf{x}, t)$, that is related to $\Gamma(t)$ according to:

$$\Gamma(t) = \{\mathbf{x} | \phi(\mathbf{x}, t) = 0\}. \tag{4.29}$$

$\Gamma(t)$ is called the zero-level set of $\phi(\mathbf{x}, t)$. It consists of points having 0 as function value. The level set function is defined on a fixed Cartesian grid. This representation eliminates the need to parameterise the boundary and allows the level set to handle complex geometries efficiently. A huge advantage of using the level set method is that the level set function remains valid even when the embedded curve changes its topology, develops sharp corners and cusps.

Most commonly, the level set funtion is described as a signed distance function:

$$sign d(\mathbf{x}, \Gamma) = \begin{cases} -d(\mathbf{x}, \Gamma), & \text{if } \mathbf{x} \text{ inside the contour,} \\ d(\mathbf{x}, \Gamma), & \text{if } \mathbf{x} \text{ outside the contour,} \\ 0, & \text{if } \mathbf{x} \in \Gamma, \end{cases} \tag{4.30}$$

in which $d(\mathbf{x}, \Gamma)$ describes the distance of position $\mathbf{x}$ to the curve Γ. $\Gamma(t)$ can now be manipulated through the level set function $\phi(\mathbf{x}, t)$ according to:

$$\frac{\partial \phi(\mathbf{x}, t)}{\partial t} + \mathbf{v}(\mathbf{x}, t) \cdot \nabla \phi(\mathbf{x}, t) = 0. \tag{4.31}$$

The vector $\mathbf{v}(\mathbf{x}, t)$ defines the velocity of the level set moving in the outward normal direction. These velocities are called **speed functions** and can be defined by additional internal and/or external forces. Research considering level set frameworks concentrates on the application-driven design of these speed functions.

4.2.2.3 *Narrow Band Approach*

The level set method requires one to track all the level sets at the same time. However, it is more meaningful to just track those grid points which are located in a so-called **narrow band** around the zero level set [Adalsteinsson and Sethian, 1995]. This allows an evaluation of the values of the level set function only at these grid points and yields a decrease in the computational costs. With the narrow band approach, these cost now only depend on the dimension of the framework in use and the constant that corresponds to the width of the narrow band. A narrow band method is easy to build and maintains the advantages of regular level set frameworks: handling topological changes, corners and cusps and keeping high accuracy along with its desirable extension to 3D.

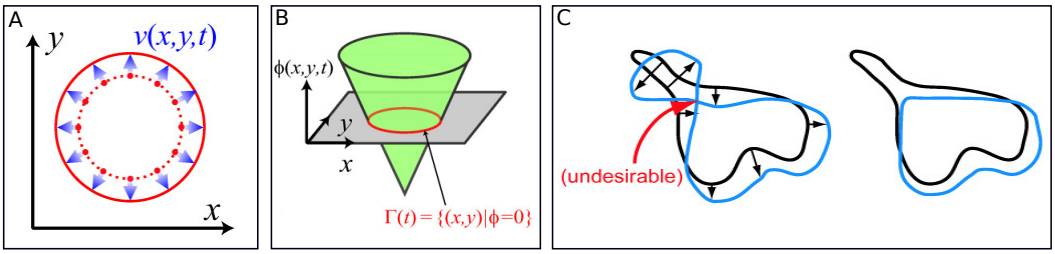

Figure 4.6: The images depict a level set function. A) shows a curve (red dotted line) consisting of points $\mathbf{x} = (x, y)$ moving with velocity $v(\mathbf{x}, t)$ yielding a new boundary (solid line). B) illustrates the zero-level set $\Gamma(t)$ which is embedded into a higher dimensional level set function $\phi(\mathbf{x}, t)$. $\Gamma(t)$ moves as $\phi(\mathbf{x}, t)$ evolves in time. C) Difficulties can arise when the geometry of the curve becomes irregular (left). The method is not capable to preserve the topology. Using level sets (right) overcomes these problems due to their implicit definition. (Image adapted from work presented by Yang et al. [2008])

4.2.2.4 *Fast Marching Approach*

The regular level set method can handle the evolution of the level set in forward and backward direction. A fast approach can be designed if the curve only moves in one direction. The method is called **fast marching method** [Sethian, 1996]. The regular level set framework is time-dependent. However, using fast marching methods allows one to operate on a stationary level. The curve is only allowed to move in one direction. Thus, fast marching methods reduce the complexity of computing a 4D function to a 3D function. When the curve moves forward and backward, the curve is not a graph of a function, e. g., it crosses and intersects itself during evolution.

4.2.3 *Summary*

Deformable models are able to handle topology and provide an implicit representation of structure in discrete space. Parametric deformable models have drawbacks that can be overcome by geometric deformable models. Most commonly, geometric deformable models are represented in the level set framework. Depending on the application, level set methods can be implemented in very efficient ways.

4.3 SUMMARY AND CONCLUSIONS

Clustering and classification techniques are often used as preprocessing step in image segmentation and data exploration. Deformable models are used to correct the topology of the identified segmented objects. They are useful when further evaluations towards certain properties such as volume, thickness, or area measurements are necessary. Depending on the application, the methods presented are very powerful tools in image segmentation and analysis tasks.

In this **thesis**, the aim is to develop a parcellation scheme that requires the fulfillment of two prerequisites:

1. an accurate segmentation of the cortex from the imaging data, and,

2. the representation of the cortical layering in surface-space.

Regarding the **segmentation** of brain data, FCM methods are appropriate as they allow fuzzy membership definitions between WM and GM, and GM and CSF. Using a deformable model such as the level set functions, topology-correct boundaries of the interfacing tissue structures of the cortex can be derived. The level set framework can further be used to construct a layering model that agrees with the anatomy. Using such a framework allows the computation of cortical profile trajectories ranging from one boundary surface to the other. These profiles are used to sample image intensities which describe laminar patterns of cortical architecture.

Parcellation approaches commonly use k-means or Fuzzy C-means clustering methods on the data. When exploring parcellations in respect to the order of primary and secondary cortices as well as association areas, hierarchical clustering and support vector machines are preferred. Parcellation approaches are discussed in detail in the next chapter.

5 STATE-OF-THE-ART IN CORTICAL PARCELLATION

This chapter describes what a cortical parcellation is and what a good parcellation is potentially able to capture. The chapter highlights the most relevant works in this field. It will explain and discuss their advantages and disadvantages of the methods. Concluding from these discussions, requirements for cortical parcellations will be outlined and motivated. The chapter will close with a summary.

5.1 WHAT IS A CORTICAL PARCELLATION?

A cortical parcellation defines the separation of the cortical sheet into its functio-anatomical areas. Popular approaches follow either macro- or microanatomical criteria:

MACROSCOPICAL APPROACHES differentiate cortical regions based on gyral or sulcal structures. Depending on the region to be identified, additional subdivisions are introduced, i. e., to delineate rostral/caudal or ventral/dorsal parts of a gyrus/sulcus separately.

MICROSCOPICAL APPROACHES use criteria on the micro-scale for cortical mapping. The cytoarchitecture of the cortex is based on differences in cell size, packing density and distribution throughout the cortical layers. Similarly, characteristics of the myeloarchitecture of the cortex, i. e., differences in fibre density between cortical layers, are used to delineate cortical areas.

The aim of a cortical parcellation is to correctly identify cortical patterns in individuals in normal healthy or diseased states. Historic parcellations are based on the examination of postmortem material (see Appendix A). Using MRI techniques, the additional demand is to show these cortical patterns in living brains to enable a correlation with brain function.

Parcellation approaches have to fulfill the following requirements:

- subdividing the cortex into structurally and functionally meaningful divisions,
- robustly detecting the cortical areas across different brains, and,
- handling individual variation regarding the extent of these cortical areas.

These requirements target specific questions on the true number of meaningful cortical areas in the brain and their variability in areal size. The results are often transformed into a probabilistic atlas that allows the study of variability in the brain.

In the following section, approaches for cortical parcellation will be presented and discussed.

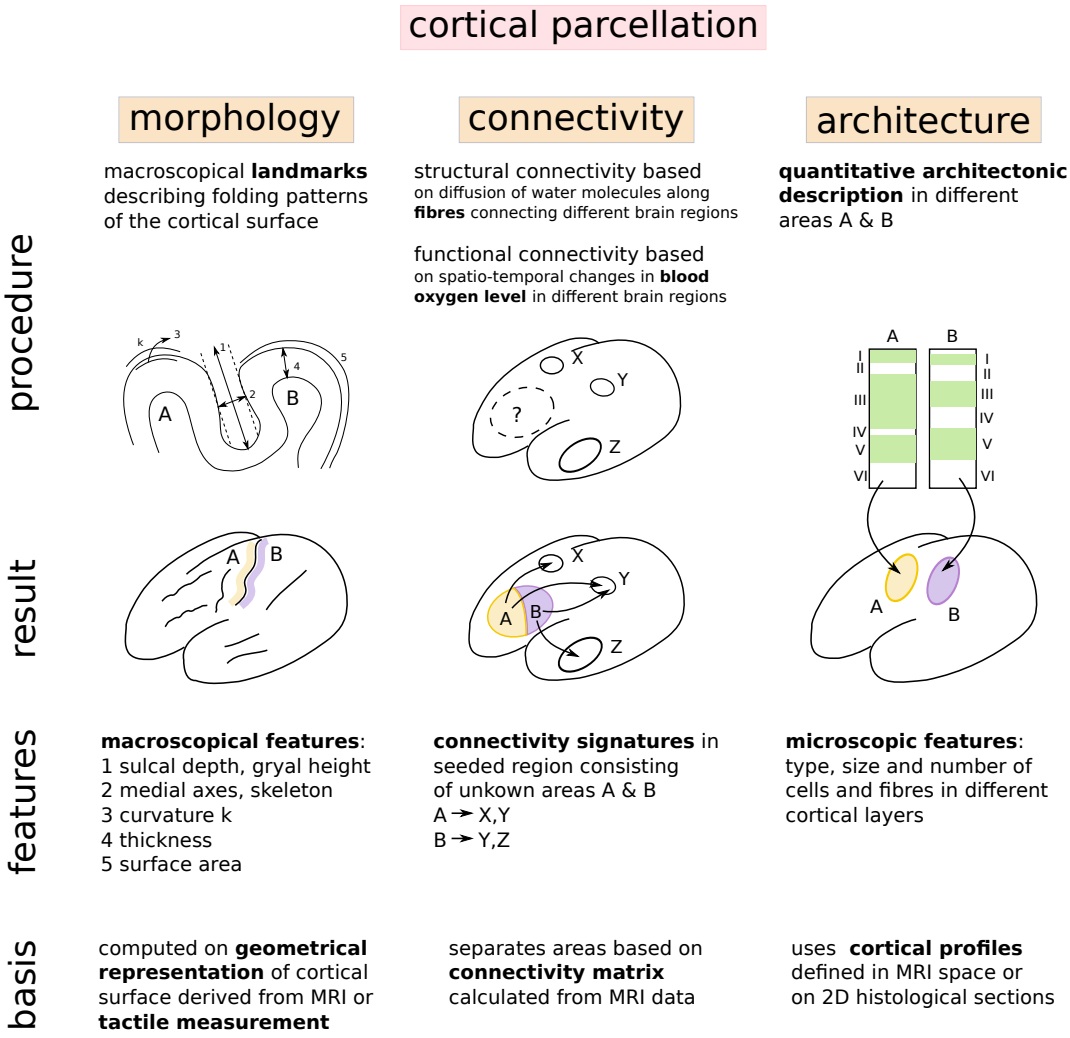

Figure 5.1: The image schematically provides an overview on existing parcellation methods presented in this chapter and compares their different basis and outputs.

5.2 APPROACHES FOR CORTICAL PARCELLATION

The goal of each method is to identify various cortical areas such that a parcellation can be derived. Based on the methodology used, the approaches can be distinguished into three categories (see Fig. 5.1):

- morphology-based methods,
- connectivity-based methods,
- architecture-based methods.

Morphology-based methods focus on macroscopical features such as the shape of the cortical surface. The shape may be defined by landmarks or pure geometrical measures. These measures may correlate with the extent of an area.

Connectivity- and architecture-based methods use information considered or provided at the microscopical level. Connectivity-based methods usually exploit the inherent structural or functional connectivity measured at micro-scale in the

brain to parcellate the cortex. Architecture-based methods incorporate information about the microstructural organisation of each cortical area. In this section, each of the three categories mentioned above will be explained and discussed in detail. Often, cortical parcellation is referred to as "cortical segmentation" which is a synonym to (sub-)dividing the cortical surface into meaningful entities.

In general, there are three major techniques that are used to derive information about the areas- or structures-of-interest in the cortex:

- manual labelling of areas or structures based on certain decision criteria,
- using a certain quantifiable and measurable feature to (semi-)automatically identify areas or structures,
- use information derived from the previous techniques to build a probabilistic atlas that is then mapped to new data for further analyses.

Although technology progressed, manual labelling of structures- or regions-of-interest is commonly performed and valid until today. The majority of the methods presented here use information derived from manual or computer-assisted delineations or its probabilistic atlas representation. The described information were used for verification, initialisation or as parameter within the parcellation method.

Please note: The resolution of the MRI data reported in the following publications was $\geqslant 1$ mm in case of 3D anatomy and on the scale of 1.5–3 mm for diffusion, fMRI and rs-fMRI scanning. Although this thesis focuses on human cortical parcellations, this chapter will include, describe and discuss techniques and approaches applied to non-human primates, too.

5.2.1 *Morphology-based Parcellation Methods*

Morphology-based methods usually focus on identifying cortical folds, i. e., the sulci. However, in neuroscience, cortical references or parcellations are gyrus-based. Mostly, primary areas are located in a gyral structure. Association areas such as Broca's region are also contained in a gyrus.

Sulcal structures can be defined simply by using topographic properties or landmarks, including the sulcal depth (gyral height, respectively), its curvature, or the medial axes, i. e., the skeleton of sulci. The general goals of a morphology-based parcellation are:

- a robust detection of folds, and,
- an adequate handling of individual variation in folding patterns.

Studying macroscopical features has lead to first descriptions of variability across cortical areas (see Section 2.2.1). Solely using measures such as thickness or areal extent alone provided no conclusive parcellation mapping. But the individual folding pattern in a brain is supposed to be in line with the organisation of functional areas. Specifically, primary areas coincide with gyral definitions. To identify these cortical areas, parcellation schemes based on the gyrification of the cortex have been developed. From a pure geometrical point of view, cortical gyri are difficult

to define. They are assumed to be delimited by two parallel sulci. Parcellation algorithms dedicated to gyral shapes therefore rely on the detection of the sulci delimiting the gyri.

PROBABILISTIC ATLASES In the early nineties, when MRI of brain structures has become more popular and feasible, neuroanatomists started to manually identify and label cortical areas based on sulcal and gyral landmarks in living brains. The main goal was to create probabilistic atlases [Ono et al., 1990; Caviness et al., 1996; Duvernoy et al., 1991; Duvernoy, 2012]. Just recently, Destrieux et al. [2010] presented a complete parcellation of the cortical surface. Neuroanatomists used internationally accepted standard nomenclature to manually delineate the brain surface on 2D anatomical MRI slices into sulcal or gyral structures. The delineations were later used to build a probabilistic sulcal-gyral atlas of the human cerebral cortex.

AUTOMATED APPROACHES USING MANUAL LABELLING
Wagenknecht and Winter [2008] segmented so-called volumes-of-interest bound by tissue borders and cortical sulci to allow a quantitative assessment of structural and functional properties in cortical brain regions. They used a semi-automatic 3D deformable model, i. e., a live-wire approach, on surface visualisations. This method is faster than manual editing on 2D anatomical MRI slices. Cachia et al. [2003] present an automated approach for the parcellation of the cortical surface into labelled gyri. These gyri were defined from a pair of sulci manually selected by the user. The parcellation is based on nested partitioning diagrams that were computed on the cortical surface using geodesic functions.

ADVANCED METHODS USING CORTICAL TOPOGRAPHIC MEASUREMENTS
More advanced methods incorporate measures of local (principal) curvature, sulcal depth, gyral height, cortical thickness, or surface area to derive a segmentation into regions describing sulci or gyri.

Sulcal Depth and Gyral Height: Lohmann and von Cramon [2000] subdivided the cortical folds into a number of substructures, called sulcal basins, in human brain MRI data sets. The sulcal basins allow a complete parcellation of the cortical surface into separate regions that are neuroanatomically meaningful. The basins were segmented using a region growing approach. The assignment to specific sulcal structures is performed by using a model matching technique based on shapes. This work has been extended to automatically extract sulcal and gyral patterns from MRI of the human brain [Lohmann, 1998]. The algorithm yields highly condensed line representations which can be used to describe the variability of individual cortical surfaces. The algorithm is applied directly to the volumetric image data. Lohmann, G. and von Cramon, D. and Colchester, A. [2008] additionally examined the deeper parts of the sulci as they generally show less interindividual variability than superficial parts. The deepest parts of primary sulci embryologically develop first and change least as the cortex expands. Along the length of the sulci the authors found one well-defined zone where depth is maximal, i. e., the sulcal pit. They showed that these pits have a more consistent relationship to func-

tional areas. Tosun et al. [2004] automatically obtained a sulci segmentation using a watershed algorithm on the buried regions of the cortex presented by Rettmann et al. [2002]. They used a measure of geodesic depth to define a suitable function describing the height of the cortex, i. e., the depth of the sulcal structures.

Thickness, Area and Curvature: Makris et al. [2006] used cortical topographic measurements such as thickness, surface area and curvature. These measurements are regionally specific and were integrated into a cortical parcellation scheme that subdivides the cortex into gyral-based units. The authors were able to show that the results were consistent with current views of cortical development and neural system organisation of human [Makris et al., 2006] and non-human primate brains [Makris et al., 2005]. Li et al. [2009] proposed an automatic cortical sulcal parcellation approach based on the geometric characteristics of the cortical surface. They applied a hidden Markov random field and the expectation-maximisation algorithm on the maximum principal curvatures of the cortical surface to derive a sulcal region segmentation. In a second step they used a principal direction flow field tracking approach on the cortical surface to perform the sulcal basin segmentation.

Skeletons: Shi et al. [2008] use sulcal skeletons as presented in Siddiqi et al. [2002] to first partition the cortical surface into sulcal and gyral regions by solving a variational problem using graph cuts. The presented method can trade off between skeleton complexity and completeness of represented folding patterns and, thus, derive a parcellation into sulcal/gyral regions automatically.

There are many more methods that provide parcellations based on skeleton extraction, sulcal/gyral pattern extraction, or geodesic depth/height estimates [Mangin et al., 1995; Le Goualher et al., 1999; Vaillant and Davatzikos, 1997; Zhou et al., 1999; Zeng et al., 1999; Riviere et al., 2002].

HYBRID METHODS USING SPHERICAL SURFACE REPARAMETERISATIONS

More recently, hybrid methods became available. These methods use probabilistic atlases to predict the locations of certain gyri or sulci patterns. Delineations of structures derived manually or semi-automatically from brains were used to build a complete atlas that describes the average probability of a data point to belong to a certain region. This atlas can be simply registered to new data in order to identify cortical areas.

Clouchoux et al. [2006, 2010] present a method to detect gyral and sulcal folding patterns across individual brains. They use a model-driven parameterisation of the cortical surface, providing an anatomically meaningful coordinate system. In this coordinate system, the arrangement of the axes follows latitudes and longitudes as on a spherical world mapping with specific meridians and parallels corresponding to the axes. An initial set of manually outlined sulcal structures is provided by the work of Cachia et al. [2003]. To fit the initial set and detect remaining structures a multi-resolution snake algorithm on the cortical surface has been developed that defines the best sulcal bottom line from a sulcal initialisation. Toro and Burnod [2003] used a similar method that establishes a one-to-one correspondence between a geometric model of axes and a cortical surface reconstruction. The parcellation

scheme incorporates landmarks based on labelled gyri and uses the axes of the model as boundary conditions to solve a set of partial differential equations over both surfaces.

Similar methods using a spherical representation of the cortical surface and probabilistic atlases to derive a sulcal-gyral parcellation were proposed by Fischl et al. [1999b]; Dale et al. [1999]; Fischl et al. [1999a]; Van Essen and Dierker [2007]; Desikan et al. [2006]. Spherical representations are also used by Hinds et al. [2008] and Fischl et al. [2004b] to predict the location of anatomical areas using intersubject surface-based registration of the primary cortical folds.

5.2.1.1 *Discussion on Morphology-based Approaches*

Using parcellation schemes that incorporate information about landmarks or folding pattern are helpful in globally identifying cortical areas and their functionally equivalent lobes. Features such as sulcal depth or height as well as the definition of medial axes or their skeletons in cortical folds were proven to be successful. However, these methods are restricted towards:

1. only identifying primary areas,
2. the topographic metrics they use, and,
3. their performance.

PRIMARY VS NON-PRIMARY AREAS Given the anatomical perspective, morphology-based approaches usually work well in primary areas, but they lack evidence in higher order cortical areas due to the increased variability of folding in such locations (see again Fig. 2.5). In addition, the architectonic boundaries also have a very loose definition in association areas which in itself allows only limited comparison between boundaries and folds. Hence, these parcellation schemes are not applicable in a cortex-wide manner as they are restricted to main morphological features.

TOPOGRAPHIC METRICS OF GYRI AND SULCI Curvature metrics locally divide a cortical fold into its gyral and sulcal component, but the architectural extent of an area is often not limited to this subdivision. The primary motor area reaches dorsally into the gyral crown of the precentral gyrus. Using such a local gyral-sulcal subdivision is inapplicable for secondary cortices or association areas as the variability of the folding pattern increases, and as such, the extent of areas, varies. Likewise, using cortical thickness solely as a measure to identify primary areas is inadequate as even primary areas show large differences in thickness. The primary motor area represents the thickest area in the human cortex and the primary visual area is the thinnest within cortex.

PERFORMANCE The performance of sulci-gyral approaches using manual labelling is questionable. The effort for training the approaches, e. g., manually labelling structures, is very high. First, all sulci patterns have to be labelled and then the negative, e. g., the gyral formation, is computed. Limitations considering

manual delineations and the construction of probabilistic atlases are discussed in Section 5.2.4.

5.2.2 *Connectivity-based Parcellation Methods*

Connectivity-based parcellation schemes are based on the connectivity in the brain which is described by structure or function. When using structural data, cortical areas with similar long-range connections encompass a region, which is segregated from neighboring regions with different connections. The structural connectivity pattern of a voxel in the cortex is approximated by a tractogram (see Section 3.3.1). If the correlation value between any two of these tractograms is high, they are likely to be connected. When using functional data, a cortical area involved in cognitive processing encompasses a region, which is segregated from neighboring regions by a different activation pattern. Usually, fMRI and rs-fMRI techniques correlate activity measures across two or more areas and examine how correlations between these areas change when participants are engaged in a cognitive process. If the correlation between any two of these voxel is high, they are likely to be involved in the processing of the same task.

COMPUTING A CONNECTIVITY MATRIX The correlation between any two voxel is assigned to an entry in a *connectivity correlation matrix*. Hence, connectivity-based parcellation schemes are also referred to as correlation-based methods. The general prerequisite of any connectivity-based parcellation technique is to compute such a *connectivity correlation matrix*. Using all data points on the cortical surface, i. e., usually 32 000, and correlate them to each other will yield a very large matrix consisting of 32 000-by-32 000 entries. Calculating such huge matrices is time consuming. Generally, it is often not reasonable to incorporate all data points. The results may prove to be inconclusive or insignificant due to the large matrix size. Usually, dimension reduction is performed on the data to allow a focused analysis. This is done by choosing a seed region that encompasses several cortical areas and contains k data points. The original matrix is then reduced to in size to k-by-32 000 entries. The goal of the parcellation scheme is to subdivide the seed region into meaningful entities that may correlate to cortical areas.

The i-th column in the matrix determines the degree of similarity between the seed voxel i and all other seed voxel. Voxel with similar connectivity patterns show a similar pattern of correlation within the connectivity matrix. In order to define collections of voxel with similar connectivity, a cluster algorithm is applied to the columns of the connectivity correlation matrix. As a consequence, this requires that the number of clusters has to be introduced beforehand.

APPROACHES USING STRUCTURAL CONNECTIVITY Croxson et al. [2005] performed quantitative investigations on the connectivity pattern in the prefrontal cortex of humans and macaques. They showed that non-invasive techniques, such as diffusion MRI, are comparable to invasive techniques, such as tracer studies, specifically when addressing association areas. Since then, the field of structural connectivity investigations has grown. Johansen-Berg et al. [2004] used diffusion-weighted MRI to examine the structure-function relations in the cortex of nine

healthy human subjects. Using no prior information, they identified distinct cortical regions having similar connectivity profiles and borders where the connectivity changed. Their results were in agreement with anatomical assignments and demonstrated for the first time a strong relationship between structure and function.

Global Connectivity derived from White Matter Fibres: Anwander et al. [2007] replicated the aforementioned technique to study the anatomical subdivision of Broca's area in six healthy human subjects. They identified cortical regions with mutually distinct and internally coherent connectivity patterns. These findings in Broca's region were supported by Klein et al. [2007] who used diffusion MRI to perform connectivity-based parcellation in nine human subjects. Tomassini et al. [2007] presented a parcellation method based on tractograms derived from diffusion MRI data. They separated the lateral premotor cortex in 17 healthy macaque monkeys into structurally and functionally distinct subregions which have distinct cytoarchitecture, function, and patterns of connectivity with both frontal and parietal cortical areas. Similar results using the same or a slightly adapted version of the approach were presented for many brain structures, including the primary motor cortex [Guye et al., 2003], the inferior parietal cortex [Ruschel et al., 2014], the cingulate cortex [Beckmann et al., 2009], the insula [Nanetti et al., 2009], the human thalamus [Johansen-Berg et al., 2005], and for connectivity mapping through the corpus callosum [Park et al., 2008].

Local Connectivity based on Grey Matter Microstructure: Zhang et al. [2010] presented a novel automatic method for cortical surface parcellation based on fibre density information assuming that fibres connecting to the same cortical region should be within the same functional brain network. Hence, their aggregation on the cortex can define a functionally coherent region.

Nagy et al. [2013] use diffusion data for a first attempt to map the individual grey matter microstructure within the entire cortex. They derived features from diffusion data considering the local cortical normal direction as well as orientationally invariant features. These features were used as fingerprints of the underlying GM structure. The authors applied a support-vector machine classifier that was able to successfully distinguish cortical areas.

APPROACHES USING FUNCTIONAL CONNECTIVITY Besides structural analyses, one can also investigate the functional connectivity in the brain. Wig et al. [2014] used functional resting state correlations to parcellate human cortical areas. They showed that the resulting parcellations agree with parcellations derived from fMRI and gyral/sulcal landmarks. Results also indicate an additional subdivision of the retrieved functional clusters defined by fMRI, i. e., so-called sub-areas.

Cohen et al. [2008] correlated rs-fMRI with fMRI data using a hierarchical clustering of connectivity data. The regions detected using rs-fMRI proved to be appropriate in size and number for the reported functional areas.

Yeo et al. [2011] studied the functional cortical networks in 1000 human subjects derived from rs-fMRI. The study showed that the functional connectivity agrees with motor and sensory areas as well as association areas.

Blumensath et al. [2013] also used rs-fMRI for parcellation. Their results confirm clusters derived from task-based fMRI. But, the connectivity-derived parcellation borders agree less to borders derived from cortical myelination and from cytoarchitectonic atlases. The authors conclude that their findings reflect inherent differences in the structural and functional intracortical organisation.

COMBINING STRUCTURAL AND FUNCTIONAL CONNECTIVITY A review of connectivity-based approaches can be found in Damoiseaux and Greicius [2009]. To allow more precise findings, these methods focus on smaller locations usually encompassing individual functional lobes. Studies were conducted in the human lateral frontal cortex [Goulas et al., 2012], the medial frontal cortex [Johansen-Berg et al., 2004; Kim et al., 2010] as well as the striatum [Choi et al., 2012; Di Martino et al., 2008]. Results of the parietal cortex were also compared to macaque brains [Mars et al., 2011].

These structure-function analyses were also examined under additional research perspectives considering different magnetic field strengths of 3 T and 7 T [Hale et al., 2010] as well as using ultra high fields to gain better resolution and decrease partial voluming artefacts [De Martino et al., 2011].

5.2.2.1 *Discussion on Connectivity-based Approaches*

Connectivity is described on the basis of structure or function. Diffusion MRI allows one to measure brain structure in-vivo and ex-vivo. Functional activation can be measured only in-vivo. Correlating structural and functional connectivity is reasonable and it has been proven that they correlate to each other. However, Blumensath et al. [2013] were able to show that functionally defined regions do not necessarily correlate with structural boundaries defined architecturally. This demonstrates that boundaries determined based on intracortical architecture and boundaries of functional activation can differ. Investigations are neccessary to study the extent and the reasons of this variability.

The discussion presented here addresses three main limitations of connectivity-based parcellation approaches:

1. limitations of the structural and functional connectivity data,
2. limitations of using the seeded regions as initialisation,
3. limitations of the methods separating correlation matrices into clusters.

DATA LIMITATIONS Diffusion MRI as well as fMRI and rs-fMRI have substantial limitations. Hence, analysing structural and functional connectivity in a combined setup has been subject to criticism. The resolution of diffusion data is usually >1 mm and >1.5–3 mm for functional activation data. But the underlying measurable physical effects occur at the micro-scale, i. e., the diffusion of water molecules and the BOLD effect (see Section 3.3). Interpretability of the data is therefore vulnerable to artefacts and has to be taken with caution. Tracts derived from diffusion data only follow (into) the gyral crown or fundus of sulci. The computed tracks never turn into sulcal walls. This is regarded as anatomically not reasonable, because in reality cortical fibres descend from and enter into the cortical surface in

sulcal walls, too [Nagy et al., 2013]. From a global perspective, diffusion MRI only maps long-range connections. Intra-area fibres, and intracortical fibres or connections between neighboring areas are only measurable to a limited extent.

In fMRI, the BOLD effect integrates into opposite regions. Although, for example, a (somato-)sensory task is used to stimulate sensory regions, it will cause an effect in the opposite primary motor region, too. This is due to blood vessels reaching into the central sulcus supplying both regions. This stimulation effect is currently investigated using so-called negative BOLD imaging which tries to separate between real and integrated BOLD effects [Huber et al., 2015]. Further concerns regarding the use of fMRI address the limited scope of brain analyses possible. When performing a task during a scan, these tasks relate to the functioning of motor, sensory, visual, speech or memory skills. These skills can rarely be analysed together. Cortex-wide task-setups are hard to design. They require multiple scanning which costs time (up to several hours). However, scanning of subjects is regulated through ethical approval and thereby restricted.

Limitations particularly addressing rs-fMRI were discussed by Buckner et al. [2013] and specifically regard the interpretation of rs-fMRI data. The problems range from questions like "What is the resting state of the brain?" to "Is mind-wandering already a task?". These questions cannot be answered at the current stage. Hence, the results derived from resting state analyses need to be judged with caution. Discussions and critical comments can be found in Deco and Jirsa [2012].

INITIALISATION Results provided by a connectivity-based parcellation method using a seed region as input is already limited by its initialisation. The region and its extent are predefined. Hence, a potential variability outside of this region cannot be measured. Additionally, the number of areas to be detected in the labelled region is also predefined. This is a critical concern. Furthermore, the seed region has to be defined either manually or automatically. General limitations of manual labelling shall be discussed in the last section of this chapter. This thesis aims at designing a method that may provide automatic labels.

METHODS Like for any clustering method, the main difficulty is to trade off between the model's consistency and its advanced sophistication. Consistency describes how well the resulting clustering characterises the structure of the data. The model's sophistication denotes the ability of a simple model to define relevant features and to ignore noise. Usually, different numbers of clusters are tested. However, since functional studies have revealed sub-areas, the question arises if these sub-areas truly exist and relate to the underlying architecture. Sub-areas can also be artificially introduced by overfitting the method used to separate the data such that the sub-areas only represent an oversegmentation of the underlying data but no true anatomical variability.

5.2.3 *Architecture-based Parcellation Methods*

Architecture-based approaches use intracortical features to parcellate the cortical surface. In more general terms, metrics are used that quantify the laminar pattern to locate areal borders. The first architecture-based parcellations used features

extracted from so-called cortical profiles, i. e., traverses running from the inner to the outer boundary along which the underlying data is sampled. Usually, these features were associated with cytoarchitecture or myeloarchitecture, i. e., size or density of cells or myelinated fibres represented in the different cortical layers. The parcellations were derived manually from 2-dimensional sections of postmortem tissue. An overview of these classical parcellations is given in Section 2.2.2.

PARCELLATIONS BASED ON LITERATURE REPORTS Classical parcellations only appeared as drawings in printed publications. A century ago, neuroanatomists had no technology available to store their results in a digital version, not to mention a standard reference space. To still make use of all reported classical findings, Nieuwenhuys [2013] started to collect knowledge from literature in order to build a first descriptive atlas based on literature findings [Nieuwenhuys et al., 2014]. This atlas uses information regarding myeloarchitecture and its spatial patterns. It is a 2D projection onto a standard reference space. However, to make it accessable as a digital 3D probabilistic atlas, further work is needed.

OBSERVER-INDEPENDENT METHODS With technological progress in automated histological staining and microscopic imaging, parcellations based on postmortem material were automated towards observer-independent analysis techniques. Schleicher et al. [1999] presented a sliding window technique that quantitatively analysed the regional and laminar organisation in cytoarchitectonically defined areas of the human primary motor-somatosensory cortex. This approach is based on cortical profiles depicting the grey level index, i. e., intensity, derived from the digitised microscopic images. The authors used the first four moments on the intensity profile and its gradient profile. These moments describe the shape of a set of points along cortical depth, including among others the mean value and point of gravity of the profile. The Mahalanobis distance was then applied to segregate the areas. This method has been successfully replicated on histological stained sections in the primary visual cortex [Schleicher et al., 2000]. Areas in the primary auditory cortex were distinguished based on myeloarchitecture [Schleicher et al., 2005]. Malikovic et al. [2007] applied the sliding window technique to correlates representing the motion-sensitive area V5 in the visual cortex. Annese et al. [2004] automatically distinguished cortical areas based on 2D sections stained to reveal myelinated fibres. The cortical profiles used in this approach were classified to belong to a certain area according to significant components that emerge from a wavelet analysis.

MANUAL DELINEATIONS Eickhoff et al. [2005b] provided a first 3D digital probabilistic atlas based on real cytoarchitecture-related data. They manually delineated 10 postmortem brains on 2D sections and registered the results to anatomical and functional MRI data. Using these cytoarchitectonic manual parcellations and surface registration methods, Fischl et al. [2008] were able to successfully provide probabilistic maps of cortical areas. Such maps are consistent with myeloarchitecture only in primary areas.

MAPPING OF STRUCTURE AND FUNCTION New MRI mapping techniques allow one to image the brain at sub-millimetre resolution. With myelin being able to capture inter-areal differences, new approaches evolved that outline areas by using fMRI data. Sereno et al. [2012] used T_1 mapping to measure the local myelination in visual areas. To detect these areas, fMRI-based retinotopy was performed in the same subjects. The outlines of functional activity were then mapped onto the subjects' structural data for identification. Lutti et al. [2014] and Dick et al. [2012] combined tonotopic and myeloarchitectonic T_1 mapping to localise primary auditory areas in individual healthy adults.

CONCEPTUAL APPROACH Hellwig [1993] provided a concept on a cytoarchitecture-driven model that estimates myelin content in different areas in the cortex based on the cellular composition in these locations as indicated by the tabulations of von Economo and Koskinas [1925]. Hellwig [1993] simplified the findings by Sanides [1962] and Braitenberg [1962, 1974] (see Section 2.4) and proposed that large neurons contribute more to intracortical myelin content than small ones, and that this relationship can be modelled using a sigmoid function. He then projected a structural shift of the laminar myeloarchitectonic pattern using data provided by Paldino and Harth [1977]. To compare his area-specific models to myelin preparations, Hellwig [1993] transformed the profiles linearly into grey values. Values located at the outer cortical surface represented 0 % myelin, values at the inner cortical surface corresponded to 100 % myelin. Although Hellwig [1993] presented a conceptual method, he was the first to report indicators of myelin concentration based on cell composition in the cortex. These qualitative myelin profiles were comparable to myelin-stained sections and the myeloarchitecture described by Vogt and Vogt [1919a,b].

ARCHITECTURE-BASED PARCELLATION MODELS A decade ago, in-vivo MRI methods started to produce imaging data with an increased resolution at sub-millimetre scale such that several voxel covered the whole cortical depth. This enabled one to sample intracortical features of laminar architectonic patterns. The main research stream focused on revealing the similarities between classical histology and MRI data (see Section 3.2). Cortical profiles have been used to compare these two disciplines [Glasser et al., 2014].

A first contribution of an architecture-based parcellation scheme in living human brains using 7 T MRI has been presented by the author of this thesis [Dinse et al., 2013b]. The method is an adaptation of the approach presented by Hellwig [1993] and includes a normalisation step towards an application to in-vivo MRI data. A first attempt of an architecture-informed parcellation scheme in a ferret brain using ex-vivo MRI data measured at 7 T has been presented by Leprince et al. [2014].

To the knowledge of this author, other architecture-informed parcellation schemes do not exist yet.

5.2.3.1 *Discussion on Architecture-based Approaches*

Most of the above-mentioned techniques deal directly with the intracortical architecture at micro-scale. These methods are closest in terms of successfully respect-

ing architectural definition. They present no restriction towards landmarks and are able to perform in secondary cortices as well as association areas.

But these methods are limted by:

1. the data,
2. the layering and profile construction, and,
3. the feature definition.

DATA LIMITATIONS The parcellation methods presented were built for or based on 2D sections of postmortem tissue. In general, staining techniques allow no precise structural assessment in 3D and provide no information about the function (see Section 3.4). Furthermore, staining techniques are vulnerable to saturation effects. So far, MRI methods were not able to catch up with the information provided by histological data. Only recently, MRI techniques became available that provide a sufficient resolution in the sub-millimetre range which allows one to sample intracortical features. Also, MRI methods start to provide contrasts that reflect intracortical architecture (see Section 3.2.1).

CORTICAL LAYERING The sliding window approach presented by Schleicher et al. [1999] incorporates features derived from cortical profiles. These profiles are based on a layering technique which is not able to respect the shifting behaviour of the intracortical layers in gyral crowns and sulcal fundi. Thus, features were sampled in locations that may not coincide with the correct laminar position. Hence, the profiles were distorted, also known to be *curvature biased*. Different layering techniques are presented and compared to each other in the Appendix B. A novel anatomically motivated layering will be presented in Section 6.2.2.5.

PROFILE FEATURES To parcellate the cortex and separate areas, Schleicher et al. [1999] and Annese et al. [2004] used features computed from the histological data rather than using layer-specific features within the data such as cell or fibre number and density. The features selected may produce unreliable results because the features may be similar to each other although they originate from different cortical areas.

Currently, cellular structures represent the only quantifiable measure of intracortical features such as size, number, type, and density of cells in given sublayers. The most promising approach has been presented by Hellwig [1993]. Indeed, his results are valid for qualitative comparisons. The estimated myelin profiles are not fully in agreement with classical works by Braitenberg [1962] and Hopf [1967, 1968, 1969, 1970]. Vogt and Vogt [1919a] and von Economo and Koskinas [1925] pointed out that there are variations in myelin in outer cortical surface as well as towards the WM boundary surface. Dinse et al. [2013a] and Tardif et al. [2013] recently showed that the myelin distribution in different cortical depths varies also in in-vivo MRI data. Adapting Hellwig's method towards a first in-vivo application is the next step towards an efficient and accurate parcellation of the human cortex.

5.2.4 *Limitations of Manual and Probabilistic Atlases*

Although technology progressed, manual labelling of material and data is commonly performed and valid until today. The majority of the methods presented here uses manual techniques or semi-automatic approaches requiring manual interaction. In general, manually labelled data is more accurate, justifying the high effort to produce these. However, a whole-brain scan can be performed in less than 30 min. In contrast, manually labelling brains requires hours. This shows the need for automated procedures.

Furthermore, the brain is the most complex and highly folded organ of the human body. Manually labelling anatomical brain structures based on visual critera is a matter of convention. Delineations are subjective and even when performed repeatedly by the same person on the same data, the result can vary.

Probabilistic atlases have been used, too. They describe how frequent certain structures appear across brains. Using these atlases raises major concerns considering:

- **the manually provided base data:** Each expert has an individual scope of knowledge and level of performance. If several experts label the same brain, the atlases include inter-rater variability because delineations of different experts may vary in their extent.
- **the automatically provided base data:** When the atlas is derived by automatic methods, results need to be taken with caution. Are those atlases reliable enough, knowing that the current methods have valid limitations?
- **the exclusion of variability:** Probabilistic atlases are often thresholded at a certain frequency prior to application. This is problematic as the variability introduced by the individually different brains is neglected.
- **the projection of atlas data:** Probabilistic atlases are constructed from a set of brains and applied to a set of different brains. The result of this projection can only be interpreted as an "assumption" that reference and target structures are similar enough. In addition, most atlases reveal a large age difference to the data sets they get compared to.

In the neuroscience community, the atlas presented by Eickhoff et al. [2005b] is used as common standard reference. The atlas is regarded as the best base that new work can get compared to. However, at the same time, the 10 brains that were used to build the atlas are insufficient to capture the anatomical variability of a species. In the research community a debate just recently started on how to estimate appropriate sample sizes [Charan and Biswas, 2013].

5.2.5 *Motivation and Requirements for Architecture-based Parcellation Methods*

The main goal of a new parcellation method is to overcome the limitations posed by existing techniques and limitations produced by manual delineations.

An ideal approach needs to:

- **incorporate architecture-relevant information:** The method shall respect the anatomical layering within the cortex, particularly the shifting behaviour of the layers in gyral crowns and sulcal fundi within an area. Ideally, the method would incorporate information at micro-level. This information may be introduced through the data the method is applied to, or a-priori by other modalities.
- **respect areal extent:** The borders of areas in the cerebral cortex are not bound precisely enough to macroanatomical landmarks such as gyri and sulci. The relationship is strong in primary areas, but more loosely defined in secondary cortices and association areas. In these areas, gyri and sulci are extremely variable. Thus, the parcellation method shall have no restrictions regarding sulcal or gyral landmark-definitions and respect the high variability in non-primary areas.
- **offer cortex-wide application:** The parcellation scheme shall be valid for all areas cortex-wide and not be custom-built for specific areas.
- **provide robustness:** When applying the method to multiple brains, it shall yield a similar result.
- **be independent of type of input data:** The method shall be independent regarding the type of the input data. It shall be applicable to in-vivo and ex-vivo data. In addition, the technique shall allow translation or scaling towards information provided by further modalities such as MRI or histology data.
- **run automatically:** The method shall compute and provide the parcellation of the cortex in an observer-independent manner, not requiring further user interaction.

By fulfilling these requirements, such a method may provide:

- **an automated procedure** that would be important for further investigations of research and clinical data.
- **labels** describing cortical areas which could in turn be used as initilisation for seed-based approaches. These labels would be more appropriate in regard to the variability of individual brains, since they were derived from the same brain they get applied to. Using these parcellation-derived labels may overcome the limitations of predefining the extent of an area manually or using projections of probabilistic atlases.

The most promising approach that may fulfill the requirements was presented by Hellwig [1993].

5.3 SUMMARY AND CONCLUSIONS

A cortical parcellation aims at separating the cortical surface into distinct areas. As such, every parcellation method addresses the same questions:

- How many areas and sub-areas can be found in the cortex?
- What is their true areal extent on the surface?

These questions are part of ongoing research and are challenging for each method presented above.

Existing parcellation methods are mainly limited by:

- **the input data:** MRI methods commonly operate at millimetre scale while histological data are vulnerable to the staining procedure itself (see Section 3.4). In addition, both methods are limited in reflecting cortical microstructure appropriately.
- **the layering model:** Using inaccurate layering models yields a distorted sampling of cortical features which are in turn used in the parcellation approaches.

In this thesis the above-mentioned limitations shall be overcome by:

- acquiring data that accurately reflects cortical myeloarchitecture,
- using a newly developed cortical layering model that respects the shifting behaviour of layers in gyral crowns and sulcal fundi in the cortex, and,
- building an architecture-driven parcellation model that provides area-specific signatures on the cortical surface.

In this thesis, Hellwig's concept will be adapted to accurately model cortical profiles representing laminar myelin density patterns in the cortex. An additional adaptation towards in-vivo MRI data is necessary.

Part II

Main Contributions

6

DATA ACQUISITION AND PROCESSING FOR CORTICAL SURFACE EXTRACTION

This chapter outlines the image acquisition procedure and processing of the data in order to extract the cortical surface.

6.1 IMAGE ACQUISITION

This chapter outlines the image acquisition of in-vivo MRI data (Section 6.1.1), postmortem MRI and histological data (Section 6.1.2).

All data were acquired at the Max Planck Institute for Human Cognitive and Brain Sciences in Leipzig, Germany, and the collaborating Paul Flechsig Institute, also located in Leipzig.

A challenge in this thesis was the relatively new mapping technique which provides quantitative data of human brains. In order to show that these data sets reflect cortical myeloarchitecture, in-vivo data needed to be compared to postmortem data. Therefore, in-vivo MRI scans were obtained from several healthy subjects. Ex-vivo MRI scanning of one postmortem tissue block has been performed. The postmortem material used in the ex-vivo scanning underwent classical histological staining to reveal the underlying intracortical cell structure and myelinated fibre pathways.

In the following sections, an outline of the imaging parameters used to acquire the different data sets is presented.

6.1.1 *Structural Imaging of Living Human Brains using MRI*

22 healthy human subjects (25.5 ± 3.4 years, 11 female subjects) were scanned with the MP2RAGE sequence [Marques et al., 2010] and a TR-FOCI pulse for inversion [Hurley et al., 2010] on a 7 T whole-body MRI scanner (MAGNETOM 7 T, Siemens, Germany) using a 24 channel phased array coil (Nova Medical Inc., Wilmington, MA, USA).

For each subject, a whole-brain quantitative in-vivo T_1 map at 0.7 mm isotropic resolution was obtained using the two GRE images D_1 and D_2 acquired at the two different inversion times TI_1 and TI_2. The GRE images were combined to a T_1-weighted image D_W following the equations given in Section 3.2.3:

$$D_W = \frac{D_1 D_2}{D_1^2 + D_2^2}, \tag{6.1}$$

The T_1 map was then calculated by fitting the T_1 values at each voxel to an exponential function describing the longitudinal relaxation (see Section 3.2.3).

The parameters used during scanning were: TE = 2.45 ms, TR = 5 s, TI_1 = 900 ms, TI_2 = 2750 ms, $\alpha_1 = 5°$, $\alpha_2 = 3°$, GRAPPA = 2. The scan time was 11 min. In the same scan session, T_1 maps at 0.5 mm isotropic resolution of each

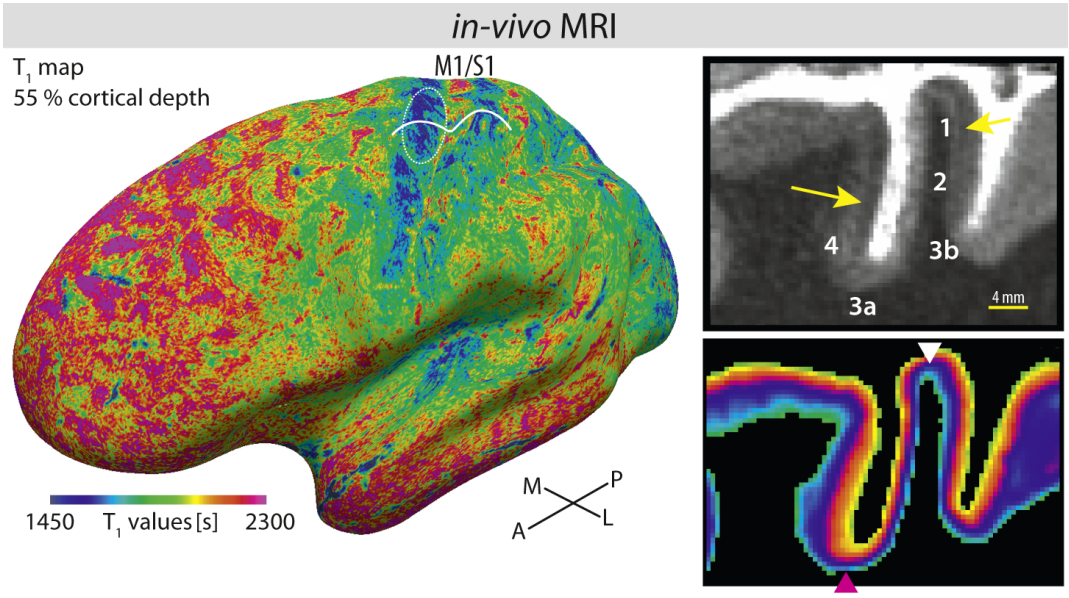

Figure 6.1: The images present an overview of in-vivo data acquired and processed in this work. Left: Inflated 0.5 mm T_1 map at 55 % cortical depth. The M1/S1 region, known to be more highly myelinated, shows lower T_1 values. Variability in T_1 values is visible across the surface but also within M1 (encircled) which is related to the location of the motor hand knob, e. g., the highest myelinated region in the brain. The white doublebow curve outlines the ROI shown in the 2D MRI slice of the in-vivo T_1 map (upper right). Brodmann Area (BA) 4 shows lower T_1 values than BA 3b. Striation (arrows) is visible. The image below depicts the cortical depth values calculated using a novel volume-preserving layering approach in the applied processing pipeline [Waehnert et al., 2013c] (see next chapter). In locations of gyral crowns (white arrowhead), the outer surfaces are compressed while the inner surfaces are stretched out. In locations of sulcal fundi (pink arrowhead), the behaviour of the surfaces changes to the opposite.

hemisphere were acquired separately (same parameters, no GRAPPA, scan time = 30 min each). The total scan time amounts to 75 min.

Fig. 6.1A depicts in anterior-posterior orientation an inflated in-vivo quantitative T_1 map of a single subjects left hemisphere. Low T_1 values (in ms, shown in blue) are associated with higher myelination.

6.1.2 *Structral Imaging of Postmortem Human Brain Material using MRI and Histology*

The ex-vivo data were acquired for verification only and information and/or results provided by the data were not used or incorporated in any way in the data processing pipeline.

An ex-vivo brain sample of the left primary motor and somatosensory region, i.e. M1/S1 region, was analysed. Fig. 6.2 shows the brain sample used. The red curve outlines the region of interest. A formalin-fixed block of human postmortem brain (age: 92 years, postmortem time: 22 h) containing the pre- and post-central gyri was obtained from an autopsy with informed consent from the patient's relatives. No neurological or psychiatric pathologies were recorded for this brain.

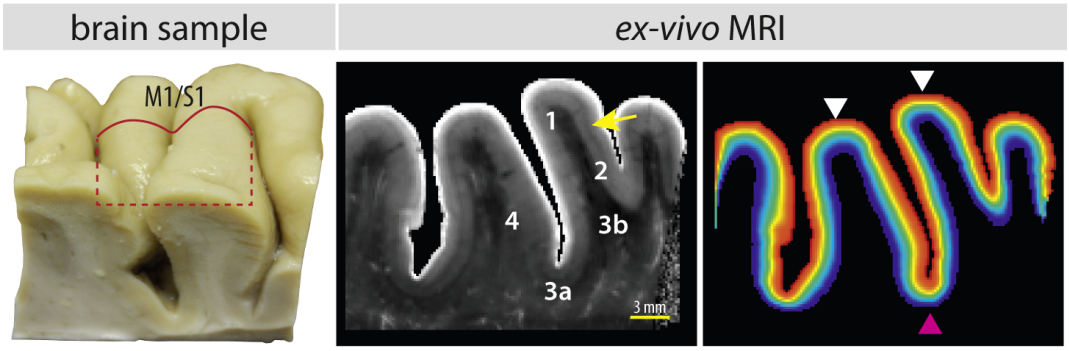

Figure 6.2: The pictures show the postmortem brain sample used (left) to derive ex-vivo data. The red doublebow curve covers the ROI which are depicted in a 2D MRI slice of the ex-vivo T_1 map (middle). Brodmann Area (BA) 4 shows again lower T_1 values than BA 3b. Striation is visible in BA 1 and 2 (arrow). The picture to the right illustrates the cortical depth values calculated during processing the data. The behaviour of the computed intracortical layers is similar as in Fig. 6.1 but much more visible due to the higher resolution of the ex-vivo MRI.

The block was scanned in Fomblin (Solvay Solexis, Bollate, Italy) with a home-built dual-loop circularly polarised radio frequency (RF) coil. The MP2RAGE sequence was used to obtain a quantitative T_1 map of the M1/S1 region with an isotropic resolution of 0.25 mm. The scan parameters were: TE = 2.94 ms, TR = 3 s, TI_1 = 325 ms, TI_2 = 900 ms, $\alpha_1 = 8°$, $\alpha_2 = 8°$, 66 averages. In postmortem scanning, longer scan times can be used as the objects scanned do not experience motion. Longer scan times achieve better signal. The acquired data blocks are retrospectively averaged. The actual scan time amounts to 11 h 43 min. Fig. 6.2 depicts the quantitative T_1 map obtained from the tissue block.

The same brain sample, containing Brodmann areas 4, 3, 1, and 2, was used for histological analysis. The block was cut with a freezing microtome (SM 2000R, LEICA Biosystems, Wetzlar, Germany). Consecutive sections were stained for myelin and cells and examined under an Axio Imager M1 light microscope (Zeiss, Jena, Germany) with a 5x objective at 2.58 µm in-plane resolution. In this work, only the myelin stains were considered (see Fig. 6.3). The cell stains were used for a general comparison of the underlying tissue structure. The sections (thickness: 30 µm) were immunostained for myelin sheaths (rabbit monoclonal antibody against myelin oligodendrocyte glycoprotein (MOG) diluted to 1:2000, avidin-biotin-peroxidase complex (ABC) method, chromogen: 3.3'-diaminobenzidine (DAB) tetrahydrochloride and ammonium nickel(II) sulfate). The floating sections were pre-treated in sodium borohydride ($NaBH_4$) for 30 min at room temperature in order to enhance the antigen accessibility [Jäger et al., 2013].

Every other section of the same block was immunostained for cell bodies (mouse monoclonal antibody against neuronal marker protein HuC/HuD diluted to 1:400, ABC method, chromogen: DAB tetrahydrochloride and ammonium nickel(II) sulfate). The floating sections were pre-treated in Tris buffer (pH 8.0) for 20 min at 90° Celsius.

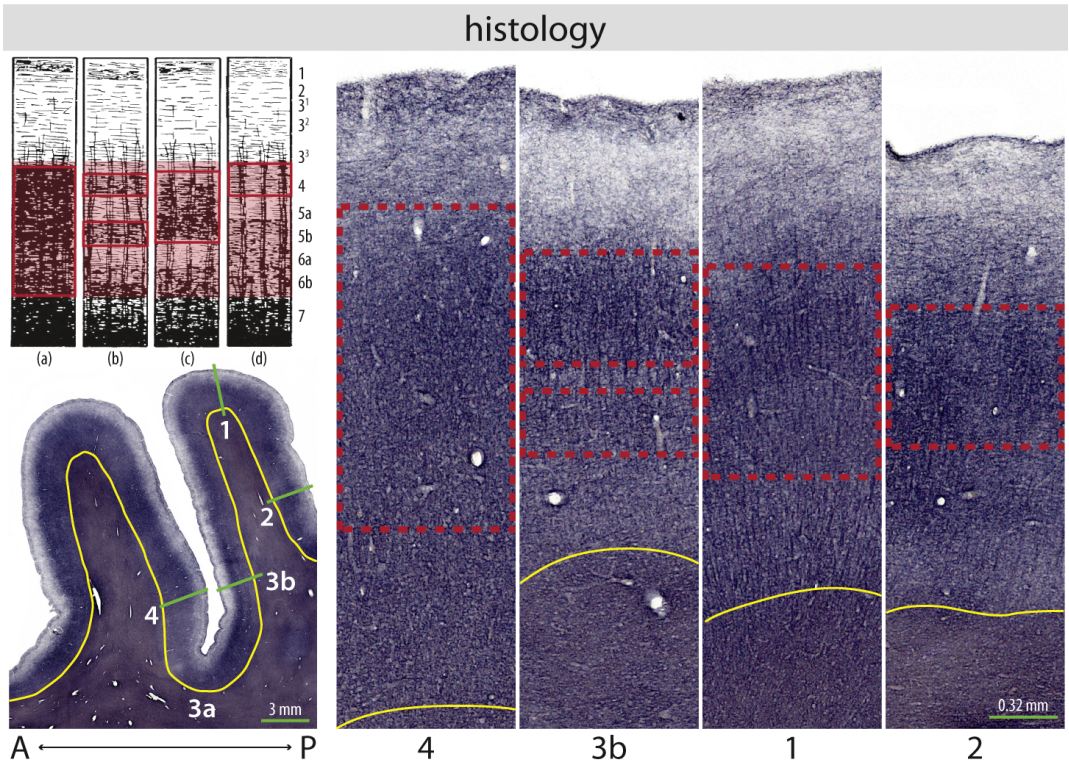

Figure 6.3: The images illustrate the myelin stain and enlargements of it in locations of the green lines. The yellow line follows the WM boundary. Red boxes depict the Baillarger banding. As direct comparison, Hopf's illustrations were included as depicted in Fig. 2.11 [Hopf, 1967].

6.2 PROCESSING OF IN-VIVO AND EX-VIVO DATA

The segmentation and representation of the human cortical surface plays an important role in neuroscience. Specifically, accurate reconstructions of the cerebral cortex from MRI data enable scientists to study and analyse cortical features of an individual subject. These features may be morphometric measurements such as grey matter volume, cortical surface area, or sulcal depth. The measures also allow careful observation of the cortical characteristics in individuals and groups of both normal development and pathological disease. For comparisons across different brains or species a correspondence, i. e., a so-called normalisation or registration, between the cortical reconstructions is essential. A registration of cortical surfaces is nowadays used in digital atlas labelling, and population-based probabilistic atlas building. Both cortical reconstruction and registration are important for structure and function mapping.

CORTICAL SURFACE DEFINITIONS Geometrically, the human cerebral cortex is a thin, complex folded sheet of 2–5 mm. As described in Section 2.1, it is bounded by WM on the inside, and CSF, vasculature and dura mater on the outside. Here, it is useful to define the cortical surfaces. The surface interfacing WM and GM will be called **WM/GM boundary surface**, or short, **inner cortical surface**. The surface interfacing GM and CSF will be called **GM/CSF boundary surface**, or short, **outer**

cortical surface. A surface running in-between these two boundary surfaces is called central or **mid cortical surface**. Here, usually the relative cortical depth the surface is located in will be defined. A **cortical profile** is represented by a traverse running from one boundary surface to the other while sampling the image values.

A cortical reconstruction describes the localisation and representation of one or even more of these mentioned cortical surfaces. Classical segmentation approaches classify the image pixel to belong to (in this case) GM or not. However, an accurate reconstruction of a cortical surface provides a geometric representation of the cerebral cortex. This representation is in alignment with the true geometry of the brain. Hence, it agrees with the different lobes, the gyral folds, and narrow sulci.

INFLUENCING FACTORS Creating a surface reconstruction can be difficult due to artefacts or influencing factors arising from the MRI imaging or the data processing.

Non-uniform radiofrequency coil sensitivity patterns cause MRI intensity inhomogeneities that result in inaccurate thickness patterns or missing components of the cortex. These issues must carefully be taken into account. Partial volume effects are most common, but also most problematic, specifically in very "tight" sulcal structures in which two neighboring folded GM banks are basically located "back-to-back" to each other, leaving little CSF in-between. Image noise may lead to segmentation artefacts due to misclassification of GM. This leads to missing or additional incorrect components which yields a representation of the cortex that is erroneous from an anatomical viewpoint.

Poorly reconstructed cortical surfaces do not allow a full assessment of statistical measures such as cortical thickness, surface area or curvature. In addition, measures along a cortical profile, i. e., a traverse running from one boundary surface to the other and sampling image values, may be corrupted. Undersampling the cortex based on missing components or oversampling it due to false additionally added pieces, yields an incorrect assignment of information to a cortical profile.

ADDITIONAL INFORMATION Most of the methods are related to the level set framework which allows a numerical analysis of surfaces and/or shapes on a fixed Cartesian grid with no need to parameterise the object(s). Detailed descriptions and discussion on parametric and geometric deformable models is given in Section 4.2.2.

This section will shortly introduce the necessary steps of the used cortical surface extraction pipeline. Given the data aquired, the focus will be on in-vivo data processing (Section 6.2.2 including the estimation of intracortical surface using the new layering method developed by Waehnert et al. [2013c]. The section will continue describing the processing steps for ex-vivo data analysis. Finally, the software used for analysis and method implementation will be outlined.

6.2.1 *General Remarks*

Improvements in the spatial resolution of structural MRI are beginning to enable the analysis of intracortical structures such as the heavily myelinated layers in 3D, a prerequisite for in-vivo parcellation of individual human brains.

To extract information from the data requires a few processing steps. The following steps are included in the processing pipeline applied in this thesis:

1. Fusion of the structural whole-brain and hemispheric slab images into a common reference space.
2. Preprocessing including skull stripping of the brain and estimation of the partial volume effects as well as local estimation of surrounding structures such as vessels or dura mater.
3. Segmentation of the brain, specifically the cerebral cortex.
4. Cortical surface reconstruction of the outer and inner cortical surfaces.

However, a cortical parcellation can only be performed precisely if the intracortical profiles used in the analysis are anatomically meaningful. Profiles are often constructed as traverses that are perpendicular to computed surfaces. In this case they are fully determined by these surfaces. In this thesis, cortical profiles are the building block of the developed methods. In order to build correct profiles and generate meaningful results from these, two additional prerequisites are necessary:

1. Development of a new layering model that computes layer-wise surfaces between the outer and inner cortical surfaces to represent the actual cortical layers.
2. Construction of 3-dimensional cortical profiles, i. e., traverses running perpendicular from one boundary surface to the other sampling image intensities along the cortical depth.

Therefore, the author of the thesis has contributed to:

- the fusion of the MRI data, principally explored the inversion times used in the MP2RAGE at ultra-high field to maximise the contrast between WM and GM on the one hand and GM and CSF on the other,
- the refinement of the cortical surface reconstruction, specifically to reduce misclassifications of blood vessels and dura mater as GM, and,
- the novel layering approach, in particular tested and validated the layering on quantitative high-resolution in-vivo and ex-vivo T_1 maps.

The approaches applied in the processing pipeline have been outlined in several publications which the author of the thesis is co-authoring. Therefore, the next sections are based on or have partially been appeared in the following publications (chronological order):

> Pierre-Louis Bazin, Marcel Weiss, **Juliane Dinse**, Andreas Schäfer, Robert Trampel, Robert Turner. *A computational framework for ultra-high resolution cortical segmentation at 7 Tesla*. In *NeuroImage*, 93, pages 201-209, 2013.
>
> Miriam Waehnert, **Juliane Dinse**, Marcel Weiss, Markus Streicher, Phillip Waehnert, Stefan Geyer, Robert Turner, and Pierre-Louis Bazin. *Anatomically motivated modelling of cortical laminae*. In *NeuroImage*, 93, pages 210–220, 2013.

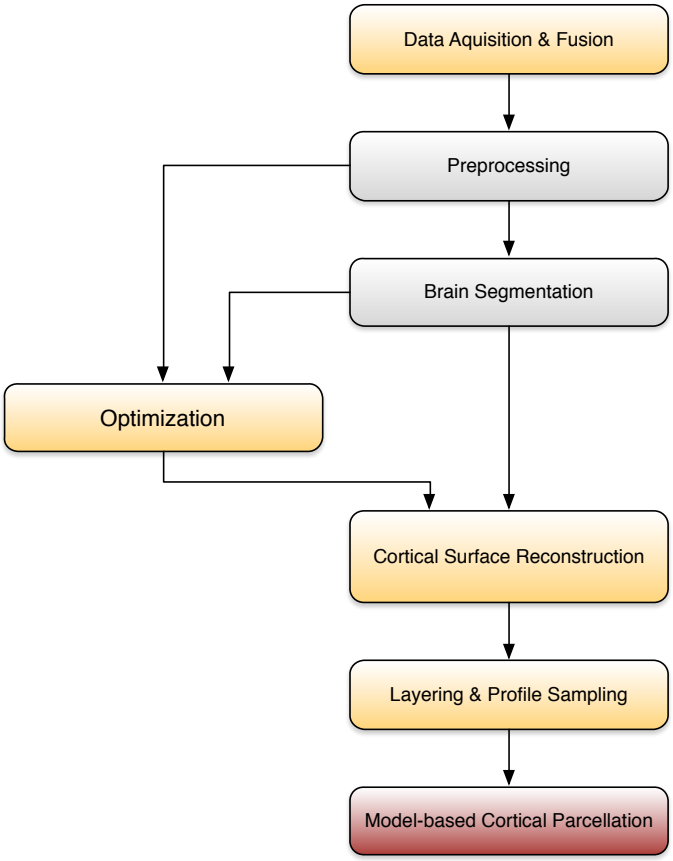

Figure 6.4: The diagram illustrates the general processing pipeline including the preprocessing and segmentation steps. The model-based cortical parcellation approach is the focus of the thesis. The author has contributed to the modules marked yellow.

Miriam Waehnert, **Juliane Dinse**, Andreas Schäfer, Stefan Geyer, Pierre-Louis Bazin, Robert Turner, and Christine Tardif. *A subject-specific 3D intracortical framework for in-vivo myeloarchitectonic analysis using high resolution quantitative MRI*. In *NeuroImage*, 2014 (submitted).

6.2.2 *Processing of In-Vivo Brain Data*

Processing the raw MRI data up towards cortical profiles encompasses several steps. These are outlined here.

6.2.2.1 *Generating a Whole-brain T_1 Map at 0.5 mm Resolution*

The three T_1 maps obtained after scanning were linearly co-registered into the standard anatomical MNI[1] reference space using FMRIB's[2] Linear Image Registration Tool (FLIRT) [Jenkinson and Smith, 2001]. The 0.7 mm isotropic resolution whole-brain T_1 map was registered to the 0.4 mm isotropic resolution MNI brain template.

1 Montreal Neurological Institute
2 FMRIB is the Oxford Centre for Functional Magnetic Resonance Imaging of the Brain.

Afterwards, the hemispheric slabs at 0.5 mm isotropic resolution were registered to the whole-brain image already being in MNI space. Using this slab-wise scanning approach allows one to obtain maps that reveal fine details of cortical and sub-cortical anatomy [Bazin et al., 2013a].

Although upsampling the data significantly increases the overall computational costs, it may achieve more accurate results in the surface reconstruction (see Section 6.2.2.4).

In order to preserve cortical geometry, a rigid registration was used that included six degrees of freedom optimised using a cost function of normalised mutual information.

6.2.2.2 *Preprocessing*

The estimation of interfacing structures serves as a prerequisite for the following brain segmentation (see Section 6.2.2.3) and cortical surface reconstruction (see Section 6.2.2.4).

To correctly initialise the brain segmentation, structures surrounding the brain, such as the skull, had to be removed. This step is known as brain extraction, i. e., skull stripping. Some filtering had to be performed to remove inhomogeneities or excessive noise originating from the image acquisition such as PV effects. In addition, the location of interfacing structures, such as vessels and dura mater, were estimated.

The information resulting from the skull stripping and the PV estimation were then used to estimate the location of the dura mater. In addition, arteries and veins were enhanced with a vesselness operator.

SKULL STRIPPING Brain extraction, or skull stripping, requires to mask out parts of the head that do not belong to the brain. It is a crucial task as any information accidentally removed cannot be recovered.

Rather than identifying the brain at a very accurate level, the intra-cranial region was targeted including the brain, blood vessels and dura mater. This region can approximately be outlined using D_2, i. e., the GRE image acquired at the second inversion time (see 3.2.3).

D_2 was thresholded at the level of background noise by fitting an exponential distribution to the background of the image and an uniform distribution to the foreground of the image, i. e., the visible scanned head. The largest component represents the region of the brain. Inside the brain, a seed region was placed at a scale coarser by a factor of 2^4. The seed region was allowed to grow at finer scales. However, the boundary constraint applied to the brain region allowed the seed region to not grow further than two voxel away from the boundary at the previous scale. The resulting mask was smoothed using a level set method that balances curvature smoothing and the distance to the original boundary (see Fig. 6.5A).

In general, the mask includes the entire brain. In some parts of the imaging data acquired the cerebellum and lower temporal lobe were missing. In this case, the B_1+ field inhomogeneities generated signal drops during image acquisition. If the sequence and reconstruction method used cannot compensate the inhomogeneities, the imaging data appears very noisy in these locations (see Fig. 3.11D).

This yields an incorrect brain mask as the thresholding will inevitably remove "noisy" background.

PARTIAL VOLUME ESTIMATION Partial voluming is a problem at any resolution in imaging (see Section 3.2.4.2). The PV effects are most prominent when the two neighboring structures have very different intensities. Considering the cerebral cortex, PV effects are more prominent at the outer cortical surface where CSF and GM interface each other, and less strong at the inner cortical surface where WM and GM interface each other. Most types of partial voluming can be addressed by using probabilistic or fuzzy membership models.

Partial voluming is particularly a problem in location of tightly folded sulci in which the CSF resides in a little cavity created by two gyral folds being literally "back-to-back" to each other. But partial voluming effects also occur in WM. Here, the sulcal walls of one fold create a narrowness that acts like a "bottleneck" into the gyral crown. PV probabilities were computed in regard to both interfacing tissue structure: WM and CSF (see Fig. 6.5B for CSF probabilities).

Here, a filter was created that mimics this case: at a given voxel, the average intensity of a T_1 map in a 3x3x3 neighborhood in a given plane and its two immediate neighboring planes was computed. Second, the difference was taken between these averages. The filter was orientation-dependent. Hence, the computation was repeated for all discrete directions in the voxel's neighborhood. The filter was related to the second derivative. Thus, the final filter selects the discrete orientation with the highest response in absolute values. This has proven to be more robust to noise and less sensitive to local curvature bending [Bazin et al., 2013b].

DURA ESTIMATION AND VESSELNESS FILTERING Due to the increased resolution and SNR at higher magnetic field strength, here 7 T, structures such as the dura mater or vessels come to the fore. It is a challenge to estimate these structures as they appear in the imaging data very close to the brain both spatially and in terms of MR intensities. It is difficult to differentiate the dura mater from the cortical grey matter based on MRI intensity alone. Often, there is only little CSF space between grey matter and dura mater.

Therefore, the dura mater had to be specifically addressed in image segmentation approaches when working with 7 T data at high resolution. The location of the dura was estimated by using the above-mentioned partial voluming filter with a probabilistic prior that decreases linearly with the distance towards the boundary of the brain mask. This helps to mask structures beyond the dura that were also included in the brain mask (see Fig. 6.5C).

In ultra-high resolution MRI data blood vessels were visible that have a diametre of 0.5 mm. Here, a filter was applied that detects tubular 3D objects [Frangi et al., 1998] yielding a probability image including values in the range $[0, 1]$ (see Fig. 6.5D).

6.2.2.3 *Brain Segmentation*

The brain segmentation method was defined as a hierarchical probability model following a Bayesian approach. The model can be broken down into conditionally independent and successive components whose parameter or group of parameters

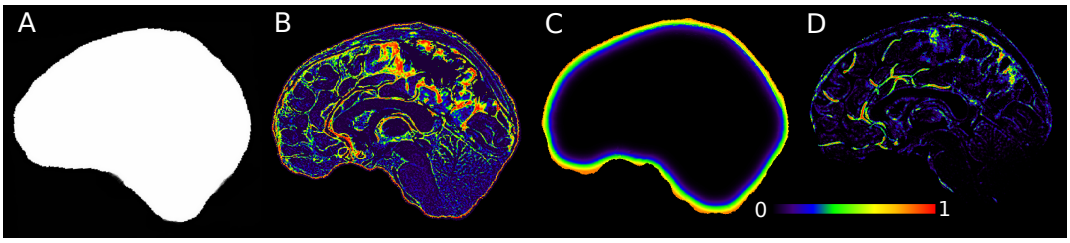

Figure 6.5: The images present the intermediate results from the preprocessing step: the brain mask (A) and probabilities of PV (B), dura mater (C), and vessels (D).

can be estimated independently with efficient and robust algorithms. Given the ultra-high resolution MR data, it is more appropriate to avoid iterative and computationally intensive schemes that alternate between the estimation of coupled parameters as in Expectation-Maximisation approaches.

The segmentation problem is defined as:

$$p(S, M, A, I \mid D, A_0, I_0) \equiv p(S \mid M, A, I, D, A_0, I_0)p(M \mid A, I, D, A_0, I_0)\times \\ p(A \mid I, D, A_0, I_0)p(I \mid D, A_0, I_0). \tag{6.2}$$

S describes the sought final segmentation of the brain. M, A, and I are estimated parameters. M specifies the membership of each voxel to given structures. A desribes the adapted shape atlas prior while I defines the intensity atlas prior. D is the image data, and A_0 and I_0 are the raw shape and intensity prior.

In general, the parameters mentioned here, follow a hierarchical dependency. In order to estimate the intensity prior I, a simple histogram segmentation of the data D was performed based on the raw priors I_0. Given the estimated intensity priors I, the raw shape priors A_0 were registered to the data and the shape atlas A was computed. Given the atlas and intensity priors A and I, the membership values can be computed on which the sought segmentation is built.

BRAIN ATLASES The brain region extracted in Section 6.2.2.2 can be defined with statistical atlases of human anatomy. These atlases describe expected shape and appearance of different structures. The brain segmentation step makes use of a composite atlas built from the IBSR[3] v.2 data set [Worth et al., 1996] and the newer Brainweb atlas [Aubert-Broche et al., 2006].

The IBSR atlas provides manual segmentations of many brain regions of 20 healthy humans. However, the atlas considers no external structures nor sulcal CSF. The Brainweb atlas models the whole head of 20 phantom brains and provides tissue separation. The final composite atlas used here, thus, includes 30 distinct regions encompassing large structures such as cerebral GM and WM but also smaller structures such as dura mater or arteries.

All structures in the atlas were represented at 2 mm resolution which provides a good compromise between complexity of the shapes and the size of the atlas data.

The boundary of single-subject atlas labels were spatially smoothed over 10 mm, and then averaged yielding a more general atlas [Bazin and Pham, 2008].

The appearance of the structures was modelled as a Gaussian distribution with mean and variance parameters. The parameters of the distribution were learned

3 Internet Brain Segmentation Repository

from sampling the manual segmentations and adjusted empirically. It is worth to note that the T_1 values given in the quantitative T_1 maps agree with brain sample measurements [Rooney et al., 2007].

The composite atlas also includes a topology template that defines the expected topology and connectivity characteristics of the atlas [Bazin et al., 2007]. The chosen scale of 2 mm resolution allows to model the topological constraints between the different structures in the brain without further approximating the anatomy.

INTENSITY NORMALISATION The intensity normalisation step provides an estimate of intensities I in order to maximise $p(I \mid D, A_0, I_0)$ (see Eq. 6.2) and, at the same time, to correct for possible distortions of the imaging intensities. The data was resampled into atlas space (2 mm resolution) and a histogram-based segmentation into WM, GM, and CSF was performed on the weighted imaging data D_w. The segmentation method used here was a standard Fuzzy C-Means algorithm initialised with the mean intensity priors I_0 from strcutures of the corresponding tissue type in the atlas.

SPATIAL NORMALISATION The spatial normalisation aims at maximising $p(A \mid I, D, A_0, I_0)$ (see Eq. 6.2). Using the WM segmentation provided in the previous step and the brain mask, derived through skull stripping (see Section 6.2.2.2), the atlas was co-registered into the subject space. The image and the atlas were transformed into label images representing these two structures only. The simplified images were then registered together in two steps, first rigidly then non-linearly, using the Demons algorithm [Vercauteren et al., 2009].

MEMBERSHIP COMPUTATION The posterior probability $p(M \mid A, I, D, A_0, I_0)$ (see Eq. 6.2) for the membership functions M, can only be computed when both shape and intensity atlas have been normalised to the subject. The membership functions describe the likelihood of a voxel to belong to a certain structure k based on the shape and intensity priors of structure k in the given atlas. The membership values were normalised into the range of $[0, 1]$.

First, the Cauchy distribution was used to model the intensity values as follows:

$$m_k = \frac{1}{1 + d_k^2}, \qquad d_k^2 = \frac{\|x - \mu_k\|^2}{\sigma_k^2}, \tag{6.3}$$

where μ_k and σ_k represent the location and scale parameters of the Cauchy distribution, and x describes the image intensity. The Cauchy distribution has several advantages. Considering this thesis, two interesting properties stand out:

- the noise distribution of MP2RAGE data is more closely related to the Cauchy distribution than to Gaussian distributions [Bazin et al., 2013b].
- the Cauchy distribution is robust to outliers.

Second, the information from the T_1-weighted image D_W, the T_1 map D_T, partial volume probability maps $p_{pv/d}$ and the statistical atlases A and I were integrated to a membership value. The contrast images were combined first as:

$$m_{I,k} = \min(m_{W,k}, m_{T,k}), \qquad \text{with } m_{W,k} = \frac{1}{1 + d_{W,k}^2}, \qquad m_{T,k} = \frac{1}{1 + d_{T,k}^2}. \tag{6.4}$$

The values of μ_k and σ_k in $d_{W,k}$ and $d_{T,k}$ are given by the intensity prior in I.

As mentioned in the previous section, partial volume effects can distort image intensities. Thus, intensities cannot be trusted in regions with higher probability of partial voluming effects, i. e., GM voxel close to CSF. Therefore, the partial volume probability maps p_{pv} were integrated in a different way:

$$m^*_{I,k} = \begin{cases} p_{pv} + (1 - p_{pv}) m_{I,k} & \text{for } k = \text{CSF, dura mater,} \\ (1 - p_{pv}) m_{I,k} & \text{for } k = \text{GM} \end{cases} \tag{6.5}$$

Finally, the membership values $m_{A,k}$ derived from the shape atlas were combined with the intensity memberships. Now, a Cauchy membership value with normalised distance $d^2 = \frac{1}{2}(d^2_{A,k} + d^2_{I,k})$ can be obtained as:

$$m_{I,A,k} = 2 \frac{m_{A,k} m^*_{I,k}}{m_{A,k} + m^*_{I,k}}. \tag{6.6}$$

CONSTRAINED MULTI-OBJECT LEVEL SET SEGMENTATION The previous estimates of the brain structures are reasonably accurate. However, the structures have still an arbitrary topology and appear noisy. The final brain segmentation was carried out using a Multi-Compartment Geometric Deformable Model (MGDM) in order to transform the prior estimates (in discrete voxel space) to smooth, topology-constrained shapes (in continuum) representing the structure's true geometry. The MGDM used here describes the extension of the topology-preserving level set framework by Han et al. [2003] to multiple objects. The advantage of using the MGDM framework is to maintain multi-object topology while performing classical level set evolution (see Section 4.2.2) for each structure [Bogovic et al., 2013; Fan et al., 2008] and automatically preventing overlaps or vaccums between objects.

A challenge for any multi-object deformable model that maintains topological constraints is the propagation of forces through multiple boundaries, when multiple structures need to be moved to achieve the desired solution. This problem was solved with an estimation scheme for the level set φ_k of structure k as follows:

$$\frac{\partial \varphi_k}{\partial t} = \alpha_k \frac{m_{I,A,c}}{1 + \max(\varphi_c, 0)^2 / s^2_\varphi} \nabla \varphi_c \varphi_k - \kappa_k |\nabla \varphi_k| \tag{6.7}$$

where c denotes the index of the structure k with "closest" membership, i. e., defined as highest membership value modulated by its outer distance to the boundary as:

$$c = \arg\max_j \left(\frac{m_{I,A,j}}{1 + \max(\varphi_j, 0)^2 / s^2_\varphi} \right). \tag{6.8}$$

κ_k describes the classical curvature regularisation term. α_k represents a weighting coefficient modulating the amount of smoothness of the different structures and is set differently for each structure k. Some brain structures are regularly shaped, i. e., the ventricles, other structures have a very complex structure, i. e., cerebral cortex and blood vessels.

The evolution of the level set method was performed in a multi-scale fashion in order to ensure smoothness and fast convergence. The scales used started in atlas

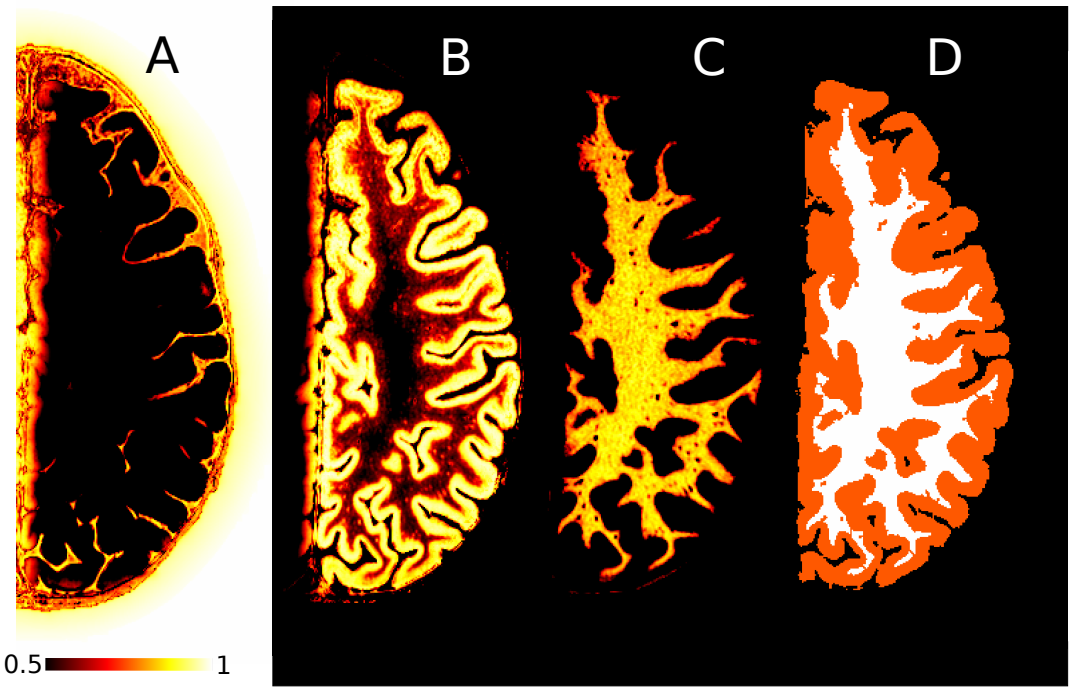

Figure 6.6: The images showcase the posterior probability estimates of CSF (A), GM (B) and WM (C) and the first segmentation of GM and WM obtained using the MGDM brain segmentation method (D). The segmentation result reveals remaining topological misclassifications and an inaccurate segmentation of cortical sulcal and gyral structures.

space and increased in steps by a factor of $\sqrt{3}$[4] up to the processing resolution in data space (here: 0.4 mm isotropic resolution referring to the registered MNI template space). To match the scale changes in the curvature, α_k is multiplied with the scaling factor.

The result of the MGDM brain segmentation is a level set interface for each structure k as well as posterior probability estimates defined as follows:

$$p_k = m_{I,A,k}\left(\frac{1}{1+\max(\varphi_k,0)^2/s^2}\right) \tag{6.9}$$

where s operates as scale parameter. The corresponding results are shown in Fig. 6.6.

6.2.2.4 *Cortical Surface Reconstruction*

The MGDM computation yields a topologically correct estimation of the different structural interfaces. However, due to noise and the "abrupt" changes that were made to correct topology, the surfaces are usually a bit rougher than desired. To finally refine the segmentations, two additional steps were applied:

1. an Anatomically Consistent GM Enhancement (ACE) (as described by Han et al. [2004]) in order to handle the partial voluming effects, specifically in sulcal banks of tightly folded gyri, and,

4 A scaling factor of $\sqrt{3}$ and larger preserves topology of the segmented image [Bazin et al., 2007].

2. a final optimisation to further reduce misclassifications of GM voxel actually belonging to WM, CSF, vasculature or even dura mater.

ANATOMICALLY CONSISTENT GM ENHANCEMENT Partial volume averaging at voxel of cortical GM, particularly in the sulcal regions where the gyral folds are virtually "back-to-back", results in wildly inaccurate estimates of both the outer cortical surface and intracortical surfaces.

Anatomically consistent Grey Matter Enhancement (ACE) presented by Han et al. [2004] aims to provide a GM representation that indicates sulcal structures where they might not otherwise exist due to the partial volume effect. ACE modifies the initial GM segmentation derived from the MGDM segmentation to create a thin, digital separation between opposing gyral folds.

The idea is to automatically locate the outer cortical boundary surface within a sulcal structure and to reduce the GM membership values towards CSF. Using the conventional Euclidean distance to separate gyral banks makes a groove into the GM, regardless of the presence of actual CSF. An improved version incorporates the presence of CSF in the definition of distance used to compute the outer cortical surface by using a weighted distance measure.

OPTIMISATION The surfaces were corrected regarding topology but, at the same time, show local residual effects, i. e., oversegmented GM voxel, due to misclassification of different structure types. Incorrectly labeled GM voxel actually belong to:

1. WM. Here, the inner cortical surface got stuck in a gyral crown because the sulcal walls of one fold create a narrowness. The MGDM is not able to penetrate upwards into the gyral crown through this "bottleneck".

2. vessels. Here, the contrast between vessel and cortical GM was not sufficient enough to clearly separate blood vessels from GM tissue.

3. dura mater. Here, the brain tissue and the dura mater were very close to each other leaving no space in-between for CSF. When applying the tissue classification, the GM segmentation leaks into locations of dura mater.

To improve the cortical surface reconstruction, the posterior probability estimates of different structures computed with the MGDM were altered. Within the preprocessing step probabilities regarding partial voluming effects, dura mater and blood vessels were computed (see Section 6.2.2.2). The probability images contain values defined in the range of $[0, 1]$.

To correct WM misclassifications, the posterior probability estimates of WM p_{WM} computed with the MGDM will be increased towards the inner cortical surface as follows:

$$p_{WM} \leftarrow \arg\max\{p_{WM}, p_{pv,WM}\}. \tag{6.10}$$

If the partial voluming probability $p_{pv,WM}$ towards the inner cortical surface (computed in the preprocessing step) is larger than the intrinsic posterior probability p_{WM} of WM only, the posterior probability p_{WM} will take the larger value of $p_{pv,WM}$. The posterior probabilities, thus, specifically increase in gyral crowns.

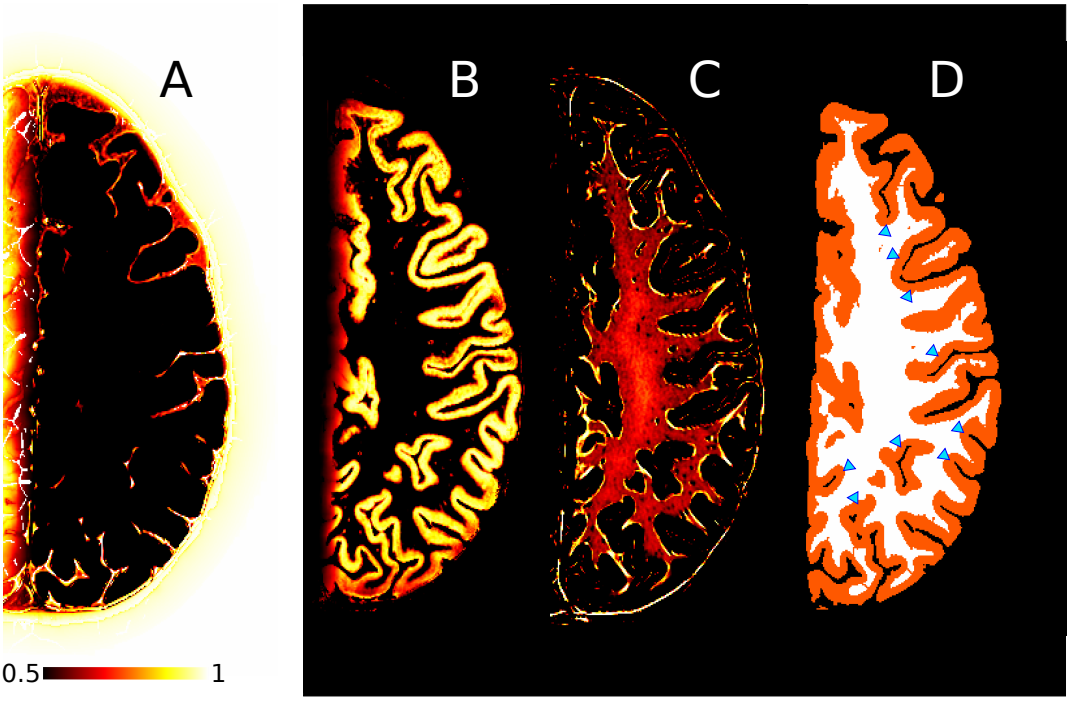

Figure 6.7: The images showcase the corrected probability estimates of CSF (A), GM (B) and WM (C) and the topology-corrected segmentation of GM and WM obtained using ACE and an additional optimisation step (D). Clearly visible are the increased probabilities as well as the accurate segmentation of cortical sulcal and gyral structures (blue arrowheads).

Correcting the CSF misclassifications caused by dura mater and blood vessels is more complicated. First, the probabilities of dura mater and vessels computed in the preprocessing were enhanced using a sigmoidal function centered at 1/3 with a slope of 1/10. Parameters of the function were empirically defined. Secondly, the probabilities were fused to form one probability image $p_{d,v}$ representing both dura and vessels such that:

$$p_{d,v} \leftarrow \arg\max\{p_{dura}, p_{vessel}\}. \tag{6.11}$$

Finally, to correct CSF misclassifications, the posterior probability estimates of CSF p_{CSF} computed with the MGDM will be increased towards the outer cortical surface as follows:

$$p_{CSF} \leftarrow \arg\max\{p_{CSF}, p_{d,v}\}. \tag{6.12}$$

If the probability of dura and vessels $p_{d,v}$ towards the outer cortical surface (computed above) is larger than the posterior probability p_{CSF}, the posterior probability will take the larger value. The posterior probabilities specifically increase in locations of blood vessels and dura mater.

SINGLE OBJECT RECONSTRUCTION Using ACE and the tuned posterior probabilities of interfacing tissues, the inner and the outer cortical surfaces will be recomputed based on a single object geometric deformable model. Hence, this step generates a full WM and GM segmentation in voxel space (see Fig. 6.7).

6.2.2.5 *Cortical Layering and Cortical Profile Sampling*

An important prerequisite of the thesis is the development of a novel layering approach aiming at generating a well-adapted coordinate system of the cerebral cortex. The system allows one to sample image intensities corresponding to the actual anatomical layering described by Bok [1929] (see Section 2.2.1). The explanations given in this thesis follow the descriptions of the corresponding publication by Waehnert et al. [2013c].

The method described in this section evolves a geometric deformable model to define a series of N =20 surfaces of constant volume, based on a local model which integrates the influence of curvature from both inner and outer cortical boundary surfaces. The surfaces were then interpolated to give a continuous layering of depth values. From the well-adapted coordinate system isocontours, i. e., contours following the same cortical depth, can be chosen to fit myelinated bands locally. These isocontours are referred to as computed surfaces. However, the layering model does not intend to recompute the anatomical layers. The main purpose of the coordinate system is to provide profiles that are anatomically meaningful to study MR intensity patterns within cortical areas and their variation across area boundaries.

The input data for any cortical layering method is a segmentation of the inner and outer cortical surfaces as provided by the previous cortical surface reconstruction.

At first, the level set functions of the two boundary surfaces were computed as described above. Using the narrow band level set method (see Section 4.2.2.3), the surface φ can be evolved to a target level set surface φ_d at a certain cortical depth:

$$\frac{\partial \varphi}{\partial t} + (\varphi - \varphi_d) \cdot |\nabla \varphi| = \epsilon \kappa |\nabla \varphi|. \tag{6.13}$$

φ can either be the level set of the inner cortical surface that is evolved outwards towards the level set of the outer surface or φ can be the level set of the outer surface to construct an inward layering. The regularisation term $\epsilon\kappa|\nabla\varphi|$ keeps the evolved level sets of the surfaces smooth and avoids shocks. The computed surfaces are close to each other. Hence, the computations are fast and memory efficient even at high resolution. Implementation details follow the classical narrow band algorithm with first order differences [Sethian, 1999].

The target level set φ_d describes a parameterised weighted average of the level sets of the inner and outer cortical surfaces φ_{in} and φ_{out}. The choice of the parameter ρ allows the target to be at any distance between the two surfaces.

$$\varphi_d = (1 - \rho) \cdot \varphi_{in} - \rho \cdot \varphi_{out}, \qquad \rho \in [0, 1]. \tag{6.14}$$

Varying ρ and hence φ_d, a set of level set surfaces $\{\varphi_d\}_{d=1,\dots,N}$ can be constructed, modelling the cortex. A computed surface represents the volume between two neighboring surfaces.

Orthogonal profile curves can be easily generated based on the level set representation. From any starting location x, the projection onto the closest surface φ_d can be obtained as:

$$x_d = x - \varphi_d(x) \frac{\nabla \varphi_d(x)}{|\nabla \varphi_d(x)|} \tag{6.15}$$

and x_d can then be projected onto the next closest surface, until a curved 3D profile is created that intersects all the computed intracortical surfaces. The classical approach for constructing profiles is to follow the gradient of the layering function.

CORTICAL LAYERS BASED ON THE EQUIVOLUME MODEL The geometry of the intracortical laminae (constructed as described above) depends on the choice of ρ in equation 6.14. If ρ is chosen to be constant, the resulting surface keeps a constant distance fraction from the segmented boundaries. This is called the **equidistant model**. In Section 2.2 it has been shown that the actual cortical layers do not maintain a constant distance from the inner and outer surfaces. Hence, the equidistant model is not appropriate. Another solution to sampling the cortical surface uses the Laplace equation. A full comparison of the here mentioned layering models including the newly developed equivolume model is provided in the Appendix B.

In order to build a layering model that parallels the cortical layers observed in cyto- and myeloarchitecture [Bok, 1929], an **equivolume** model should construct laminae that fulfill the following requirements:

1. they are thick at high curvatures and thin at low curvatures, for both cases of firstly being within one and the same layer and secondly traversing from one boundary surface to the other along a profile.

2. they keep the volume fraction in cortical segments constant.

To achieve these goals, cortical segments that approximate the local shape of the cortex have to be constructed. A segment has the form of a truncated cone with bent walls. Its flat bottom is located at the inner surface and the flat top at the outer surface.

To construct the cortical segments, cortical surfaces are computed first with the equidistant model. Cortical profiles are build perpendicularly to these, starting at one cortical boundary surface and ending at the other one. Each profile approximates the center line in a cortical segment (cf. to Fig. 6.8), which will be called the column. Now, the equivolume model transforms a desired volume fraction α of the segment volume into a distance fraction ρ of the column length.

The surfaces of each segment at the inner and outer cortical boundaries are the areas A_{in} and A_{out} that are large at small curvatures and small at high curvatures so that goal 1. can be fulfilled.

$$A_{in} = \frac{1}{1 + \operatorname{sgn}(k_{in,1} - k_{out,1}) \cdot \frac{1}{2} \cdot d \cdot k_{in,1}} \cdot \frac{1}{1 + \operatorname{sgn}(k_{in,2} - k_{out,2}) \cdot \frac{1}{2} \cdot d \cdot k_{in,2}} \tag{6.16}$$

$$A_{out} = \frac{1}{1 + \operatorname{sgn}(k_{out,1} - k_{in,1}) \cdot \frac{1}{2} \cdot d \cdot k_{out,1}} \cdot \frac{1}{1 + \operatorname{sgn}(k_{out,2} - k_{in,2}) \cdot \frac{1}{2} \cdot d \cdot k_{out,2}} \tag{6.17}$$

These areas are the products of side lengths. Each length is related to the local primary or secondary curvature k_1 and k_2. Moreover, whether the length is

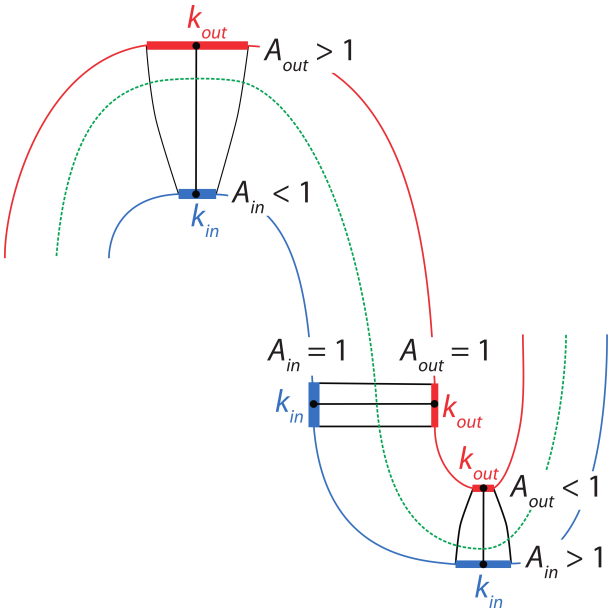

Figure 6.8: Schematic section through the cortex with the inner surface in blue and the pial surface in red. Cortical segments at the gyral crown, the sulcal wall and the fundus of the sulcus, with the centerline/column in black. A_{in} and A_{out} are the top and bottom surfaces of the segments and have different relative sizes related to the local curvatures k_{in} and k_{out} of the boundary surfaces. The intracortical surface (green) is constructed with $\alpha = \frac{1}{2}$, dividing the segments into laminar segments with equal volumes. The position of this intracortical surface on the columns ρ varies with curvature.

smaller, larger or equal to 1 depends on the relation between the curvatures of the inner and outer boundary surfaces as follows:

$$\operatorname{sgn}(k_{in,m} - k_{out,m}) = \begin{cases} +1, & \text{if } k_{in,m} > k_{out,m} \\ 0, & \text{if } k_{in,m} = k_{out,m} \\ -1, & \text{if } k_{in,m} < k_{out,m} \end{cases} \tag{6.18}$$

where k_{in} are the curvatures at the inner surface and k_{out} the curvatures at the outer surface. The subscript 1 marks primary curvatures, the subscript 2 marks secondary ones (cf. Section 6.2.2.5). d is the cortical thickness measured along the column of the segment and sgn is the sign function. Depending on which of the curvatures is larger, k_{in} or k_{out}, the area A_{in} is either larger or smaller than A_{out}. The volume of a segment in a layer next to one of the boundaries is determined by A_{in} or A_{out} and the thickness of the layer (cf. Eq. 6.21). This volume should be constant, so that the relationship described between areas and curvatures results in the relationship between layer thicknesses and curvatures described in goal 1.

The shape of the segment is determined by assuming that the area grows linearly with the height of the segment column with $h = 0$ being at the inner cortical surface and $h = d$ at the outer cortical surface:

$$A(h) = A_{in} + (A_{out} - A_{in}) \cdot \frac{h}{d}. \tag{6.19}$$

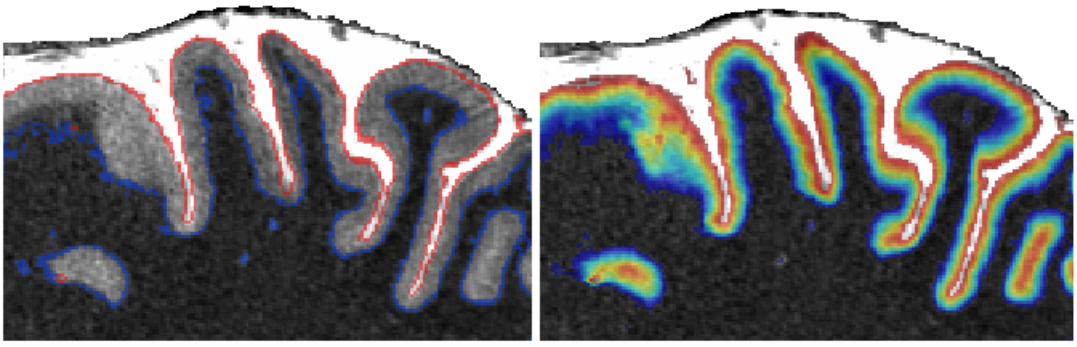

Figure 6.9: The images demonstrate the inner (blue) and outer (red) reconstructed surfaces (left) as well as cortical depth values computed using the new equivolume layering method (right). Reconstructed surfaces are accurate and computed intracortical layers follow the shifting behaviour in gyral crowns and sulcal fundi of anatomical layers.

Eq. 6.19 describes an approximation of the actual cortical shape. The current equivolume model balances robustness, accuracy and precision. As an advantage, it also yields in a closed-form solution (Eq. 6.22).

The total volume of a cortical segment can be calculated by integrating the area from the bottom face ($h = 0$) to the top face ($h = d$) of the segment:

$$V = \int_0^d A(h)\,dh = A_{in} \cdot d + \frac{A_{out} - A_{in}}{2} \cdot d. \tag{6.20}$$

An intracortical surface next to the inner cortical surface with fraction α of the total volume of the segment V is obtained by integrating the area from the bottom to a certain distance $\rho \cdot d$ on the column of the segment:

$$\alpha \cdot V = \int_0^{\rho \cdot d} A(h)\,dh = A_{in} \cdot d \cdot \rho + \frac{A_{out} - A_{in}}{2} \cdot d \cdot \rho^2, \qquad \alpha, \rho \in [0, 1]. \tag{6.21}$$

Solving Eq. 6.21 for ρ by inserting V from Eq. 6.20 gives:

$$\rho = \frac{1}{A_{out} - A_{in}} \cdot (-A_{in} + \sqrt{\alpha A_{out}^2 + (1 - \alpha) A_{in}^2}). \tag{6.22}$$

To construct a surface having a constant volume αV, ρ is determined for every segment column and thus varies with curvature and location:

$$\rho = \rho(k_{in}, k_{out}) = \rho(x, y, z). \tag{6.23}$$

Then the complete level set of one of the cortical surfaces is evolved to the target level set φ_d with the respective ρ using Eq. 6.13 and Eq. 6.14. This operation is repeated for N to be constructed intracortical surfaces with increasing or decreasing volume αV in order to obtain the final layering (see Fig. 6.9).

CURVATURE ESTIMATION A prerequisite of the equivolume model is to compute the curvatures k_{in} and k_{out} at the inner and outer cortical boundary surfaces. Curvature estimates are typically based on second order derivatives, which are very noise-sensitive. In order to provide adequate regularisation, the curvatures are estimated by fitting a centred paraboloid to the level set surface. The paraboloid at a point X is given by the following quadric equation with known parameters Q and L: $X^T QX + L^T X = 0$. The point of interest X_0 is in the center of the curvature sampling neighborhood X_n, X_n ranging between a minimum and a given maximum distance to X_0 in the three dimensions. The distance between the quadric at the voxel in the neighborhood X_n and the quadric at the point of interest X_0 is $(X_n - X_0)^T Q(X_n - X_0) + L^T(X_n - X_0)$. The distance between the level set surface at X_n and the level set surface at X_0 is $\varphi(X_n) - \varphi(X_0)$. Therefore, the coefficients $\hat{Q}$ and $\hat{L}$ have to be found that minimise the difference between the quadric distance and the level set distance at X_0:

$$\hat{Q}, \hat{L} = \operatorname{argmin} \sum_n w(X_n) \left[(X_n - X_0)^T Q(X_n - X_0) + L^T(X_n - X_0) - (\varphi(X_n) - \varphi(X_0)) \right]^2 \tag{6.24}$$

with a weighting factor $w(X_n) = \exp(-\frac{(\varphi(X_n)-\varphi(X_0))^2}{2\sigma^2})$ to lower the influence of values in the sampling neighborhood further away from X_0. The coefficients $\hat{Q}$ and $\hat{L}$ can be estimated linearly by solving a system with nine unknowns. From the geometry of paraboloids, the primary and secondary curvatures k_1 and k_2 of the paraboloid approximation to the level set surface at X_0 can be obtained as the eigenvalues of Q in the orthogonal direction to L.

6.2.3 *Processing of Ex-Vivo Brain Data*

The processing of the postmortem material is in two ways very different from the in-vivo data processing:

1. the postmortem material was cleaned and prepared before MRI scanning and histological treatment.
2. the segmentation into WM and GM compartments was performed manually both on MRI images as well as microscopic images derived from histological sections.

6.2.3.1 *Preparation of Brain Material*

The brain tissue is scanned ex-vivo and, therefore, cleaned before scanning. All parts that could distort image acquisition or influence histology were removed. A laboratory assistant manually pealed off the dura from the outer cortical surface and removed all vessels, too.

During scanning, the tissue block was surrounded by Fomblin with the advantage of keeping the tissue block moistured, in position and giving contrast only to the tissue. During histology, the tissue block is cut into sections consisting of WM and GM only.

6.2.3.2 *Cortical Surface Reconstruction, Layering and Profile Sampling using Ex-vivo MRI Data*

Estimation of the WM/GM and GM/CSF surfaces in the ex-vivo MRI data was based on a manual segmentation into WM and GM compartments. To estimate intermediate surfaces, the above-mentioned volume-preserving approach (see section 6.2.2.5) was applied to resemble observable myeloarchitectonic cortical layers. The right picture in Fig. 6.2 illustrates again the shifting behaviour of the surfaces in gyral crowns (white arrowheads) and sulcal fundi (pink arrowheads). 3D traverses were constructed and along these the postmortem MR image T_1 values were sampled to generate myelin-related profiles. For consistency, the postmortem-derived profiles are referred to as **ex-vivo profiles**.

6.2.3.3 *Cortical Surface Reconstruction, Layering and Profile Sampling using Histology Data*

Consecutive sections alternate between cell and myelin stain. A complete 3D reconstruction of myelinated fibres in the cortex was therefore impossible. However, given 3D data, the volume-preserving method implicitly provides a cortical depth estimate. Therefore, one histological section was stacked six times to recover a 180 µm thick 3D data block. The section used is shown in Fig. 6.3, lower left. The yellow line indicates the WM boundary. The zoomed-in pictures were taken from locations highlighted in green on the original stained section. Striation is visible in the zoomed-in pictures (red dashed rectangles). As comparison, Vogt [1910] originally drawn illustrations remodelled by Hopf [1967] have been included. The stacked data were manually segmented into WM and GM compartments and the volume-preserving approach was applied to estimate the intracortical surfaces. Due to the 2D nature of the histological sections and the implicitly given cortical depths estimates, the intensity values were averaged at different cortical depths to provide a myelin profile. For consistency, such histologically-derived profiles are referred to as **histology profiles**.

6.2.4 *Software*

All of the image processing tools used in this thesis to process in-vivo as well as ex-vivo data are included in the CBS Tools, a plug-in for the MIPAV software package [McAuliffe et al., 2001] and the JIST pipeline environment [Bazin et al., 2013b; Lucas et al., 2010]. The CBS Tools are freely available for download from the Max Planck Institute for Human Cognitive and Brain Sciences website [5] and from NITRC [6].

The computer used to carry out the image processing has a CPU with 32 kernels of AMD opteron 62/74 and RAM of 128 Giga Byte.

5 http://www.cbs.mpg.de/institute/software/cbs-hrt/index.html
6 http://www.nitrc.org/projects/cbs-tools/

6.3 SUMMARY AND CONCLUSIONS

The newly acquired high-resolution data requests for customised processing. The presented pipeline is able to handle the new data and implements state-of-the-art methods. In addition, processing data in volume space using deformable models allows for more accurate reconstructions of the cortical surface.

7

A CYTOARCHITECTURE-BASED MYELIN MODEL FOR CORTICAL PARCELLATION

At the core of the presented modelling approach are cortical profiles, which carry a rich information content [Bridge et al., 2005; Dinse et al., 2013a; Walters et al., 2007]. With the ultra-high in-vivo resolution used to acquire 7 T data, finer details of myelination are revealed. With the advanced data processing methods presented in the previous chapter, the cortical sheet can be computationally divided into multiple surfaces. Perpendicularly to these surfaces traverses can be constructed that run from one cortical boundary surface to the other. Along these traverses, T_1 values of a given ultra-high resolution MR T_1 map can be sampled at different depths of the cortical sheets to derive myelin-related profiles, here called **in-vivo profiles**.

In order to estimate laminar myelin density patterns as observed in quantitative T_1 maps, a model of cortical myeloarchitecture was built from known cytoarchitecture in a two-step approach. In the first step, Hellwig [1993]'s method was implemented and adapted. Quantitative properties of cytoarchitecture relevant in each cortical area found by von Economo and Koskinas [1925] were transformed into patterns representing myelin density. In a second step, the profiles were normalised into MRI space (T_1 values given in milliseconds) respecting the currently used MRI resolution and MRI limitations such as partial voluming. Fig. 7.1 depicts the conceptual design of the presented approach including intermediate results. Finally, a probabilistic function based on a Gaussian metric was built that measures the similarity between area-specific models and in-vivo profiles obtained with ultra-high resolution brain MRI.

The modelling approach presented in this chapter has been described in:

> **Juliane Dinse**, Miriam Waehnert, Christine Tardif, Andreas Schäfer, Stefan Geyer, Robert Turner, and Pierre-Louis Bazin. *A histology-based model of quantitative T1 contrast for in-vivo cortical parcellation of high-resolution 7 Tesla brain MR images*. In *Medical Image Computing and Computer Assisted Intervention (MICCAI)*, Part II, pages 51–58, Japan, 2013.
>
> **Juliane Dinse**, Nina Härtwich, Miriam Waehnert, Christine Tardif, Andreas Schäfer, Stefan Geyer, Bernhard Preim, Robert Turner, and Pierre-Louis Bazin. *A Cytoarchitecture-driven Myelin Model reveals Area-specific Signatures in Primary and Secondary Areas in Human Cortex using Ultra-High Resolution In-vivo Brain MRI*. In *NeuroImage*, 114, pages 71–87, 2015.

The method presented here deviates from the approach mentioned above regarding:

- the quality of the boundary surfaces,
- the normalisation step towards MRI data, and

- the larger number of subjects, namely 19, used in the thesis.

The modifications address previous limitations of the implemented approach.

7.1 GENERATING CORTICAL AREA-SPECIFIC PROFILES

Hellwig's approach is based on two main assumptions:

1. Large neurons contribute more to intracortical myelin content than small ones.
2. The average distribution of horizontal axon collaterals of neurons can be quantified according to data provided by Paldino and Harth [1977].

We followed Hellwig's approach by first obtaining the relative thickness, mean neuronal cell density $c_{density}$, and mean cell size c_{size} for each cortical layer from the tabulations of von Economo and Koskinas [1925]. The measures were given for locations in sulcal walls and gyral crowns. In case a Brodmann area was mainly located in a sulcal wall, we used the measures given for this location and, conversely, the measures for a gyral crown for areas mainly located on the crest of the gyrus. In von Economo and Koskinas [1925], the neuronal cell size c_{size} is defined as the ratio of $cell_{height}/cell_{width}$ of the cell body, which includes the nucleus. Note that the Nissl stain used by von Economo and Koskinas [1925] labels only cell bodies, not neurites. According to Hellwig [1993], myeloarchitecture can be estimated from cytoarchitecture by assuming that the quantity of myelin depends on the cell size, following a sigmoidal function s which describes the contribution of cells to the layer-specific myelin concentration. We modelled this relation as:

$$s(c_{size}) = \frac{1}{1 + \exp(-r(c_{size} - l))} \tag{7.1}$$

in which l describes the location of maximum cellular contribution and r the rate of change (Fig. 7.1b).

An estimate of the initial cell content (Fig. 7.1c) for each layer c_{layer} was obtained as:

$$c_{layer} = c_{size} c_{density} s(c_{size}). \tag{7.2}$$

The laminar pattern of myelinated fibres in the cortex is considered to originate mainly from axonal collaterals of neuronal cells. To include laminar projections in the area-specific profile shapes and to transform the profile from cytoarchitectonic properties into information representing the myelin content, the initial cell content of c_{layer} was convolved with a function a describing the number of axonal collaterals distributed around a cell body remodelled from Paldino and Harth [1977] (see Fig. 7.1d):

$$m_{BA}(x) = (c_{layer} * a)(x)dx. \tag{7.3}$$

The convolution is defined in the range of relative cortical depth $d \in [0, 1]$. The profiles m_{BA} give a qualitative indicator of myelin concentration in the cortex (Fig.

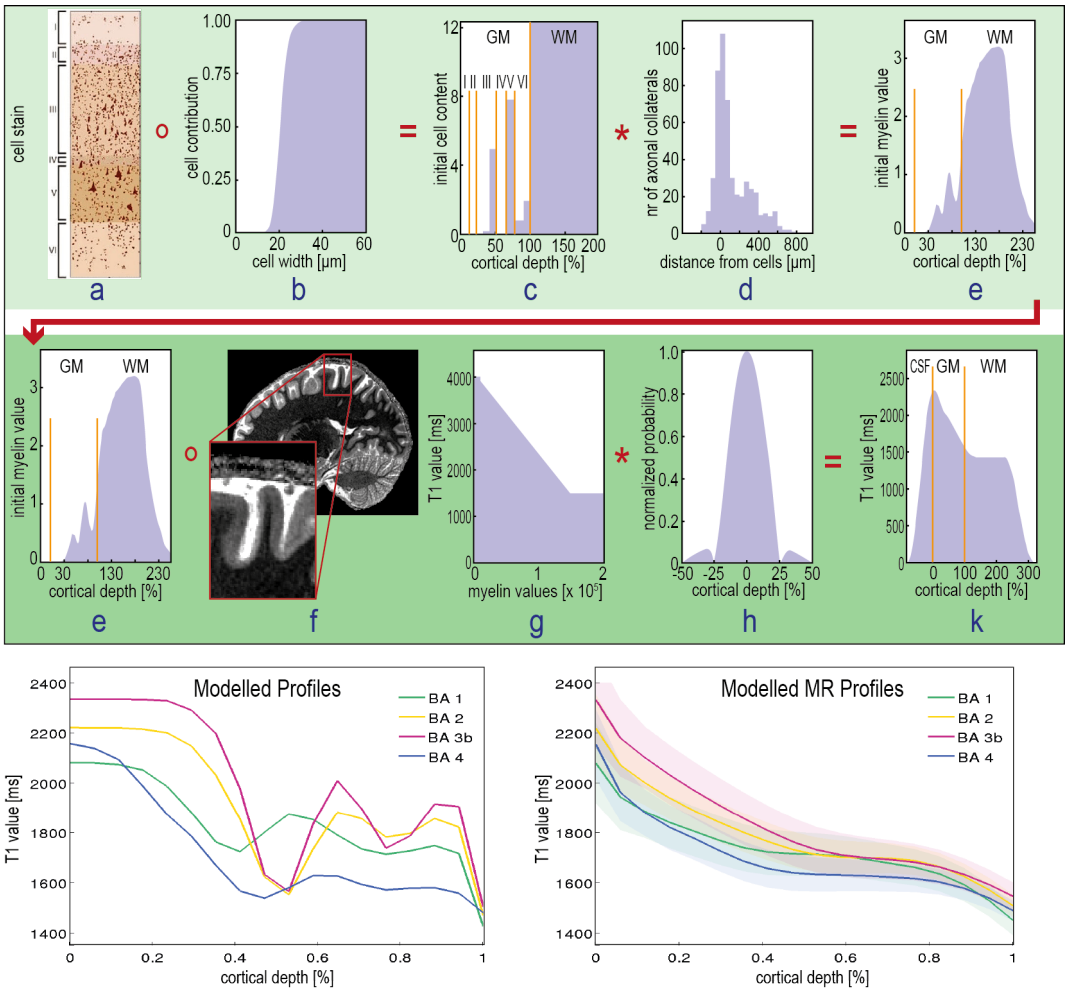

Figure 7.1: Schematic overview of the parcellation approach. The top row revisits the work of Hellwig [1993]. Quantitative measures of cellular configuration were used to estimate an initial cell content which is convolved with a model of the distribution of axonal collaterals. The second row transforms the modelled myelin-related profiles into modelled MR profiles of the T_1 intracortical contrast observable in brain MRI. In addition (bottom row), the modelled (Fig. 7.1g) and modelled MR profiles (Fig. 7.1k) for each ROI are shown.

7.1e) and are comparable to myelin-stained sections and the myeloarchitecture described by Vogt and Vogt [1919a,b].

At this stage, values located at the outer cortical surface represent 0 % myelin, values at the WM interface corresponded to 100 % myelin. This is not in agreement with classical works by Braitenberg [1962] and Hopf [1967, 1968, 1969, 1970]. Vogt and Vogt [1919a] and also von Economo and Koskinas [1925] pointed out that there are variations in myelin in the outer cortical surface as well as towards the WM boundary surface. Dinse et al. [2013a] and Tardif et al. [2013] recently showed that the myelin distribution in different cortical depths varies between different cortical areas when using in-vivo high-resolution quantitative T_1 maps. When applying the model to in-vivo MRI data, the variability at the interfacing tissue boundaries has to be taken into account.

7.2 NORMALISING AREA-SPECIFIC PROFILES INTO THE MR IMAGING SPACE

Geyer et al. [2011] demonstrated that quantitative T_1 maps obtained with 7 T MRI reveal local cortical differences reflecting the boundaries of cortical areas. Glasser and Van Essen [2011] showed that similar features could even be observed at 3T, albeit at a coarser spatial resolution, using another method to reveal myelin contrast. Similar results have also been shown in non-human primates [Bock et al., 2009]. When considering MRI data, partial voluming needs to be addressed because it poses a problem in MRI at any resolution, but becomes particularly severe in tightly folded cortical sulci. The areas in focus are located in and around the central sulcus. The processing pipeline, described in the previous chapter, handled most types of partial voluming robustly. But in locations where neighboring cortical folds were almost in contact, CSF image intensities have a high spatial dependence and differ quite strongly compared to other locations.

To allow for an application to quantitative MRI data, the area-specific models had to undergo two transformation steps.

Step 1: In step one we normalised the area-specific profiles into the MR intensity range of a quantitative T_1 map (values in milliseconds). This transformation step facilitates one to apply the model to individual subjects as well as to group data. This first transformation step has to respect further variability, i. e., partial volume effects in the cortex, originating from the rather coarse resolution of in-vivo MRI. The resulting profile is in MR intensity range, but still at the resolution of cell size (0.001 mm=1 µm) given in the tabulations by von Economo and Koskinas [1925].

The MR intensity range of the cortex is defined by the mean T_1 value and standard deviation of the boundary surfaces. We calculated these parameters directly from the WM/GM and the GM/CSF boundary surfaces, individually for each subject. However, the intensity range of T_1 values in individual areas varies and is, thus, defined as $I_{BA} = [I_{BA}^{wm}, I_{BA}^{csf}]$ for each individual Brodmann area. The area-specific range was calculated by using the cortex' mean T_1 value μ and the cortex' T_1 standard deviation σ computed at the WM/GM boundary and the GM/CSF boundary (Fig. 7.1f) as follows:

$$I_{BA}^{wm} = \hat{e}_{wm,BA}\,\mu_{wm} \qquad \text{and} \qquad I_{BA}^{csf} = \hat{e}_{csf,BA}\,\mu_{csf}. \tag{7.4}$$

$\hat{e}_{wm}$ and $\hat{e}_{csf}$ represent the estimators of the determined area-specific variation at the two boundaries. $\hat{e}$ was estimated from prior investigations on lower resolution T_1 maps (0.7 mm isotropic) [Dinse et al., 2013a] in which the behaviour of the profiles in terms of mean and standard deviation has already been observed. Subjects analysed in [Dinse et al., 2013a] do not overlap with the subject cohort used in this thesis. According to Waehnert et al. [2013a], the standard deviation decreases in higher resolution quantitative T_1 maps measured using MRI. Therefore, the estimates were adapted to follow this behaviour. Table 7.1 outlines the estimates.

The area-specific estimates $\hat{e}_{wm}$ and $\hat{e}_{csf}$ in Eq. 7.4 handle the myelin-related variability in individual areas as well as the partial volume effects. Partial volume effects become more severe when adjacent tissues such as GM and CSF differ greatly in T_1 value. Profiles of the cortex have a greater variance at the GM/CSF boundary

estimates	$\hat{e}_{BA4}$	$\hat{e}_{BA3b}$	$\hat{e}_{BA1}$	$\hat{e}_{BA2}$	σ^{modMR}_{BA4}	σ^{modMR}_{BA3b}	σ^{modMR}_{BA1}	σ^{modMR}_{BA2}
WM	0.96	0.99	0.95	0.98	60	60	60	60
CSF	0.90	0.96	0.89	0.92	205	245	210	190

Table 7.1: Estimates $\hat{e}$, used in the normalisation step (Eq. 7.4), and estimated T_1 standard deviations σ^{modMR}, used in the profile similarity computation (Eq. 7.11), are shown.

than at the WM/GM boundary because the two interfacing tissues GM and CSF differ greatly in T_1 value. Thus, the estimates $\hat{e}_{csf}$ at the GM/CSF interface have a larger spread compared to the estimates $\hat{e}_{wm}$ at the WM/GM interface.

Finally, the profiles in m_{BA} (Eq. 7.3) were normalised into the T_1 MR intensity range of grey matter:

$$T^{mod}_{1_{BA}}(x) = I^{wm}_{BA} + \frac{(I^{csf}_{BA} - I^{wm}_{BA})(m_{BA}(x) - min(m_{BA}(d))}{max(m_{BA}(d)) - min(m_{BA}(d))} \tag{7.5}$$

in which $min()$ and $max()$ define the minimum and maximum of m_{BA} along relative cortical depth $d \in [0, 1]$ (Fig. 7.1g). At this point, the modelled T_1 profiles are continuous, but resemble the cell size resolution (0.001 mm) used in the atlas of von Economo and Koskinas [1925]. For consistency, we refer to the modelled profiles $T^{mod}_{1_{BA}}$ in MR intensity range as **modelled profiles**.

Step 2: In the second step we transformed the modelled profiles into the currently used MR resolution. We build a filter function that can be understood as a translator between the model and different scales of MR resolution.

To match the limited MRI resolution, the profiles in $T^{mod}_{1_{BA}}$ (Eq. 7.5) were convolved with a windowed cardinal sine function that represents the MRI signal point-spread function (Fig. 7.1h). To take into account partial volume effects, the modelled profiles $T^{mod}_{1_{BA}}$ were extended into white and grey matter. T_1 values representing WM and CSF in MRI data similar to Rooney et al. [2007] were assigned to the profile's end points corresponding to WM and CSF. The values are highlighted in Table 7.2. The filter function intends to represent the current in-vivo MRI resolution. To account for the limiting effects of the MR resolution, we considered the relative overlap (in percent) between filter function and cortical thickness t_{BA} (in absolute value) in each Brodmann area (BA). We defined the width of the filter function as:

$$width = \frac{resMR^{in-vivo}}{t_{BA}} t_m. \tag{7.6}$$

$resMR^{in-vivo}$ is the MR resolution of the in-vivo brain data (0.5 mm isotropic), and t_m is the maximum cortical thickness (in percent). We adapted the width of

PV estimates	WM_{BA4}	WM_{BA3b}	WM_{BA1}	WM_{BA2}	CSF_{BA4}	CSF_{BA3b}	CSF_{BA1}	CSF_{BA2}
T_1 values (s)	1.25	1.25	1.55	1.25	3.0	3.3	3.3	3.3

Table 7.2: T_1 values attached as WM and CSF to the modelled profile. These estimates function as PV estimates.

the filter function for each area-specific model as the cortical thickness varies in different Brodmann areas. Mean values of absolute cortical thickness t_{BA} in the different areas were computed from the individual subject's brain data. A width factor α was numerically determined to hold the following relation:

$$sinc(x) = sinc(\alpha\, width) = 0.5 \tag{7.7}$$

where α defines the Full-Width-Half-Maximum (FWHM = 0.5) according to the cortical thickness in individual Brodmann areas. In the filter function, we used the absolute value of a truncated cardinal sine function centred in the sampling window. The final filter function for resolution adaptation had the following form:

$$filter(x) = |sinc(\alpha(x - (t_m/2))|\, H(x). \tag{7.8}$$

$H(x)$ describes a Hamming window that was used to decrease the Gibbs phenomenon. We defined $H(x)$ as:

$$H(x) = (0.54 - 0.46(\cos((2\pi x)/t_m)). \tag{7.9}$$

Finally, the modelled profiles $T_{1_{BA}}^{mod}$ were convolved with this filter function:

$$T_{1_{BA}}^{modMR}(x) = (T_{1_{BA}}^{mod} * filter)(x)dx \tag{7.10}$$

The convolution is defined in the range of relative cortical depth $d \in [0, 1]$. $T_{1_{BA}}^{modMR}$ is now a defined function of myelin-related T_1 values represented in MRI space and MRI resolution and has been modelled from known cytoarchitecture in individual Brodmann areas (BA) (see Fig. 7.1k). For consistency throughout the thesis, we refer to the MR-resolved profiles as **modelled MR profiles**.

7.3 MEASURING THE SIMILARITY BETWEEN AREA-SPECIFIC MODELS AND IN-VIVO DATA

To facilitate comparisons between the area-specific models and empirical data, we defined a metric that estimates the similarity $P(T_1^{in-vivo} \in BA)$ of an in-vivo profile $T_1^{in-vivo}$ to belong to a certain Brodmann area (BA). For this purpose, the expected variance σ_{BA}^{modMR} of the modelled MR profiles in their corresponding location was estimated empirically from Dinse et al. [2013a]. σ_{BA}^{modMR} determines the range of uncertainty (in milliseconds) by linearly interpolating empirical estimates of deviations in individual areas (see Table 7.1). Under the assumption that T_1 values, independently of their cortical depth, are normally distributed, we defined the probabilistic similarity $P(T_1^{in-vivo} \in BA)$ as a weighted Gaussian process with a prefactor $\delta = 1/2$ as:

$$P(T_1^{in-vivo} \in BA) \approx \exp\left(-\delta \int_0^1 \frac{\left(T_1^{in-vivo}(x) - T_{1_{BA}}^{modMR}(x)\right)^2}{\sigma_{BA}^{modMR}(x)^2}\, dx\right) \tag{7.11}$$

Here, P compares how similar a single in-vivo profile $T_1^{in-vivo}$ of the cortex is to the modelled MR profile $T_{1_{BA}}^{modMR}$ in individual subjects. Similarity values range between 0 and 1, indicating low and high similarity.

7.4 MODEL VALIDATION IN MOTOR AND SOMATOSENSORY REGION

In order to validate this modelling approach using MRI, ROIs in the left hemisphere were defined that correspond to primary and secondary areas of the motor and somatosensory region known as M1/S1 region. They specifically comprise Brodmann area (BA) 4, located in the posterior wall of the pre-central gyrus, Brodmann area 3b, located in the anterior wall of the post-central gyrus, Brodmann area 1, covering the gyral crown of the post-central gyrus, and Brodmann area 2, located in the posterior wall of the post-central gyrus. The location of these areas with respect to sulcal and gyral landmarks is consistent across subjects. All areas are located in a relatively small region of the brain, which allows a joint in-vivo and post-mortem study with ultra-high resolution 7 T MR brain imaging. The areas are anatomically contiguous or close neighbors, and they all have strong myelination levels. As a group, they stand out from neighboring areas of the frontal and parietal lobe. However, the microstructural differences between these areas are subtle, thus accurately separating them is challenging for observer-independent parcellation schemes. It has been shown by Geyer et al. [1999] that there are changes in cytoarchitecture within Brodmann area 3, thus forming areas 3a in the sulcal fundus and 3b in the anterior wall of the post-central gyrus. Strictly speaking, BA 3a and 3b are not areas defined by Korbinian Brodmann, but were later introduced by Vogt and Vogt. We will continue using this nomenclature as the tabulations of von Economo and Koskinas [1925] and also the descriptions of Vogt and Vogt refer back to it.

Although the Vogts' division based on myeloarchitectonics is very complex, Vogt [1910] suggested four main types of myeloarchitecture in the human cortex which are very constant across brains. The chosen ROIs specifically exemplify each of these basic types. Brodmann area 3a, located at the fundus of the central sulcus between areas 4 and 3b, was not included in this analysis. Its myeloarchitecture has not been intensively studied and is thus not assignable to one of the four main types.

For all data sets acquired, ROIs were manually labelled in the left hemisphere within the abovementioned Brodmann areas. The labelling process was guided by accepted macro-anatomical landmarks [Grefkes et al., 2001; Geyer et al., 1999]. All labels in in-vivo, ex-vivo, and histology data were used to derive mean profiles in each ROI and in each data modality. The mean profiles were compared to the area-specific models. Additionally, the manual labels on the 0.5mm isotropic T_1 maps were used to validate the area-specific models on in-vivo data.

8 EXPERIMENTS AND RESULTS

This chapter describes all experiments performed and its corresponding results. The chapter will also include a discussion on the results and the limitations of the presented modelling approach.

8.1 RESEARCH QUESTIONS AND EXPERIMENTS

The validation addresses the following major research questions:

Q1: How well do individual empirical profiles derived from in-vivo data, i. e., in-vivo profiles, fit the respective *modelled MR* profiles (Eq. 7.10)?

Q2: Can the area-specific models identify myeloarchitectonic signatures in different functional cortical areas in living subjects?

Q3: How well do the area-specific *modelled* profiles (Eq. 7.5) fit traditionally derived profiles, i. e., ex-vivo MRI and histology profiles?

Q4: How helpful are measures such as the mean value and the shape of an individual in-vivo profile separately for the identification of specific human cortical areas?

Q5: Which resolution is required to distinguish between cortical areas accurately and confidently using intracortical features measured with quantitative ultra-high resolution brain MRI?

Q6: What influence have PV effects on the data, and consequently, on the area-specific models? More precisely, how do T_1 values change under the influence of PV and how far do the effects penetrate into the cortex?

Q7: Why do signatures of both primary motor and sensory areas split into clusters?

The research questions listed above were answered using the here outlined corresponding experiments. In-vivo group analysis includes 19 of the 22 originally scanned subjects. One subject has been removed from the study due to a strong anatomical variation in the M1/S1 region known as a divided central sulcus [Schweizer et al., 2014]. Two other subjects have been removed due to unusual high motion artefacts yielding segmentation errors.

In **Experiment 1**, we compared the area-specific models quantitatively to in-vivo data. ROIs in the left hemispheric 0.5 mm T_1 map were defined and manually labelled. The samples covered between 1 and 2.5 cm^2 of the surface area in each ROI. Similarities P (Eq. 7.11) were analysed by calculating a distribution of the similarity values in each ROI subject-wise. Similarity values P are expected to be high

(approaching 1) in plausible locations, i. e., where in-vivo profiles belong to a certain Brodmann area. However, in other regions the similarities are expected to be lower (approaching 0). Thus, the distribution of similarities P in a given ROI may vary with the model used. To provide comparable measures, we approximated the given distribution with a probability density function of a beta distribution with shape parameters α and β. Subject-wise, mode and standard deviation were estimated in each ROI. The mode defines the value at which the approximated beta distribution takes its maximum value, i. e., the value that is most likely to be represented by the similarities in each ROI. Computing the mode of a beta distribution requires that the parameters α and β are greater 11. If the approximation yielded values of α and $\beta < 1$, the distribution of similarity values was skewed too much to either 0 or 1 such that the calculated beta distribution became asymptotic. In these extreme cases, the mode of the distribution (respectively the standard deviation) cannot be computed and we therefore assigned 0 to the mode and standard deviation. This validation was performed on a single-subject as well as a group-average basis.

Experiment 2 addresses the question of how well the models perform in one and the same ROI. We therefore computed for each location in the human cortex the similarity values across the area-specific models and marked the area-specific model with the highest value at that location.

Please note, in Q3-Q5 the surfaces and profiles used to compute the area-specific models and similarity maps deviate from the above described approach in respect to:

- the cortical boundary surfaces used which only include the anatomically consistent grey matter enhancement but no surface optimisation as described in Section 6.2.2.4.
- the T_1 intensity range computed in Eq. 7.4 which is adapted such that it includes the standard deviation of the cortex at the inner and outer cortical surfaces.
- the filter overlap computed in Eq. 7.6 which uses cortical thickness values as described in the tabulations by von Economo and Koskinas [1925].

In **Experiment 3**, we qualitatively compared ex-vivo and histology profiles to modelled and in-vivo profiles in order to analyse the relationship and likely similar trends in profile shapes. All profiles were transformed into a normalised space with arbitrary units to match the different contrasts and resolutions of the different data origins. The objective of this validation is to study the apparent laminar myelination change in each Brodmann area, given the different scales of resolution.

Experiment 4 deals with a more general question considering the information content of in-vivo cortical profiles. To show to what extent both a profile's mean and its shape matter, we performed additional here-called *mean-* and *shape-experiments* using these two measures separately in Eq. 7.11. In the mean-experiment, the mean T_1 value of the modelled MR profile was compared to the mean T_1 value

of an individual in-vivo profile. The mean T_1 value itself was simply computed as the average across the profile's cortical depth. In the shape-experiment, the mean distance between the profiles were calculated through cortical depth. To allow comparisons of shape only, we aligned the modelled MR profile in advance by shifting it to the mean T_1 value of the empirical profile.

The analysis of **Experiment 5** was performed among the different area-specific *modelled* profiles (Eq. 7.5). The profiles were transformed into different scales of resolution using the filter function in Eq. 7.8. In order to change the resolution at each scale, resMR, i. e., the parameter defining the resolution, was changed in 50 µm steps starting at a resolution of 1 µm and then increasing up to 1 mm. Waehnert et al. [2013a] used profiles originating from T_1 maps of different resolution. They found that the standard deviation decreases at higher resolution. In the thesis, the standard deviation was simulated to be smaller at a higher resolution and to be slightly larger at a lower resolution. A theoretical similarity P_t was calculated between the different resampled area-specific models at each scale of resolution. For application to in-vivo data, the modelled MR profiles were downsampled. The modelled profiles were used at their original cell size resolution to reduce sampling artefacts when observing changes in profile shape.

Experiment 6 demonstrates the influence of PV effects on the data in the entire cortex. As mentioned in Section 3.2.4.2, PV effects are most prominent between neighboring structures having very different T_1 values. Due to the larger T_1 difference, PV effects at the outer cortical surface, where CSF and GM interface each other, are stronger than at the inner cortical surface, where WM and GM interface each other. Therefore, the *outer distance measures*, i. e., the distance of the outer cortical surface in outward-pointing normal vector direction, is studied in relation to the T_1 values along a cortical profile. This enables one to quantify:

- the change in T_1 values depending on the "narrowness" of sulcal structures where gyral folds are close to contact, such as in the central sulcus, and,
- the cortical depth to which the effects penetrate into the cortex.

Experiment 7 has an explorative nature. Medial and lateral parts of both primary motor and sensory areas show locations of reduced myelin on the T_1 maps. These specific locations may form a structural border, i. e., septum, between different functional representations in human primary motor cortex and primary somatosensory cortex. These functional representations may relate to body movement control and touch localisation that rely on the brain's ability to distinctly represent single body parts. Rodents and monkeys are equipped with so-called *septa* to aid this process.

There is a current lack of knowledge about these border definitions in human brain. So far, it is believed that **the human sensorimotor cortex is not equipped with septa**, or similar structural borders. The T_1 maps used in the thesis provide evidence to the contrary. Therefore, the identified locations may offer a human homologue to septa as identified in the animal brain.

To investigate the "gaps", the human in-vivo layer-dependent myelin mapping (as presented throughout this thesis) was combined with BOLD functional imaging to investigate if locations of reduced myelin separate hand and face representations in human primary somatosensory cortex and primary motor cortex. Six subjects were re-invited for a functional brain scan. The data were registered to the anatomical 0.5 mm T_1 maps. The cortical surfaces were compared to observe correlations between structural and functional changes in the two different areas.

8.2 RESULTS

8.2.1 *T_1 Maps and Cortical In-vivo Profiles*

Glasser and Van Essen [2011] have already presented lower resolution (1 mm) average myelin maps. Bridge and Clare [2006] and Walters et al. [2003, 2007] earlier showed microstructural detail in individual cortical profiles. As the spatial resolution of the T_1 maps improves, finer details of myeloarchitecture are revealed. Cortical profiles derived from 0.5 mm T_1 maps clearly carry more information than the mean of a profile alone.

T_1 MAPS The T_1 maps used in this study are able to capture finer details of myeloarchitecture than average myelin maps presented by Glasser and Van Essen [2011]. The T_1 maps used provide contrast differences between primary/secondary areas (lower T_1 values) and other less heavily myelinated areas (higher T_1 values). Frontal and parietal regions clearly differ in contrast. The difference in myelination between the motor region M1 and the somatosensory region S1 is visible in Fig. 6.1A and in the mean experiment shown in Fig. 8.5 (second column). With the isotropic ultra-high resolution of 0.5 mm, the in-vivo data reveal medio-lateral structural variabilities in the primary motor and somatosensory region M1/S1. Within M1, a location with even darker T_1 values (encircled in white in Fig. 6.1A) can be detected that corresponds to the motor hand knob known to be the most strongly myelinated part of the primary motor region. These observations agree with historic maps representing cytoarchitectural distributions [Brodmann, 1909; von Economo and Koskinas, 1925] as well as myeloarchitecture [Vogt and Vogt, 1919a,b; Hopf, 1955, 1956; Hopf and Vitzthum, 1957; Smith, 1907].

T_1 PROFILES The (T_1) values of profiles in Brodmann area 4 are very low (indicating higher myelination) for each individual imaging modality (see Fig. 8.4). Area 4 has myelinated tangential fibres in upper cortical layers [Vogt and Vogt, 1919a,b]. These additionally cause a higher degree of myelination in the upper cortical layers of area 4 than in the corresponding layers of area 3b. The described myelination translates into expectations for the T_1 profile values. Low T_1 values (in *ms*) are found in deeper cortical layers of both area 4 and 3b as shown in the in-vivo average profiles of area 4 and 3b, presented in Fig. 8.1 (first column). The T_1 values for upper cortical layers of areas 4 and 3b, however, differ. The cortical profiles derived from our T_1 maps clearly display this difference. The T_1 values in the upper layers of area 4 are much lower than the corresponding T_1 values in area 3b.

Now, a comparison between cortical MRI profiles and classical histology profiles, as presented by Hopf [1967] or Braitenberg [1962], may lead to confusion. In MRI, the GM/CSF boundary is highly partial-volumed, i.e. the T_1 values in the cortex are distorted by much higher T_1 values found in CSF, which may give rise to the impression that the myelin concentration changes more strongly in upper cortical layers. Rather than expecting an almost stagnating profile shape towards the pial surface, in-vivo and ex-vivo MR profiles show a high increase of T_1 values.

8.2.2 *Comparing Models to In-vivo Brain Data (Exp. 1,2)*

The in-vivo comparison has been validated from different perspectives which are presented in this section. Fig. 8.1 illustrates the results corresponding to Experiment 1 from a single subject.

MODELLED PROFILES The strongly alternating profile shape of the modelled profiles (Fig. 8.1, left column, magenta, dashed) represents the underlying laminar myeloarchitectonic patterns at cell size resolution. Higher myelination is associated with lower T_1 values. The transparent bands of the in-vivo profiles and modelled MR profiles represent the standard deviation. The dips visible in the profiles correspond to higher myelinated intracortical structures. The area-specific MR models (shown in red) correspond well to in-vivo profiles. When the resolution is decreased, the area-specific modelled MR profiles reveal less of their characteristic structure as compared with the modelled profiles. Given a certain resolution, both the in-vivo and modelled MR profiles are different across the areas. The loss of structural features in the area-specific models with decreasing resolution is depicted in Fig. 8.4B.

SIMILARITIES ON CORTICAL SURFACE In the second column of Fig. 8.1, the similarities P are mapped onto the cortical surface for each model. The similarity values range between 0.5–1 and indicate high similarity by red to pinkish colours or low similarity by bluish to grey colours. In general, the area-specific MR models show higher similarities in primary cortical areas, but not in areas located at the frontal lobe. Some areas are highlighted in the parietal lobe and the occipital pole. These structures are more strongly myelinated than the prefrontal brain, but not as strongly myelinated as primary areas, which confirms previous research [Vogt and Vogt, 1919a,b; Hopf, 1955, 1956; Hopf and Vitzthum, 1957].

SIMILARITIES IN ROIS The right column in Fig. 8.1 shows zoomed-in results, focusing on the defined ROIs, of the same subject. The model of Brodmann area 4 shows clear results. Higher similarities (shown in red to pink) are consistently distributed in location BA 4, whereas the similarities get smaller and the distribution pattern more patchy in other areas. The results are similar for the model of Brodmann area 3b. Neighboring locations such as area 4 and 1 show lower similarity values. The model of Brodmann area 1 shows lower similarity values in location of area 3b and area 2. The model of Brodmann area 1 has high similarity values in location of area 4. The model of Brodmann area 2 does not stand out well. The discrimination between the four areas may be rather poor. In conclusion,

the similarities are generally higher in plausible locations (model and area match)

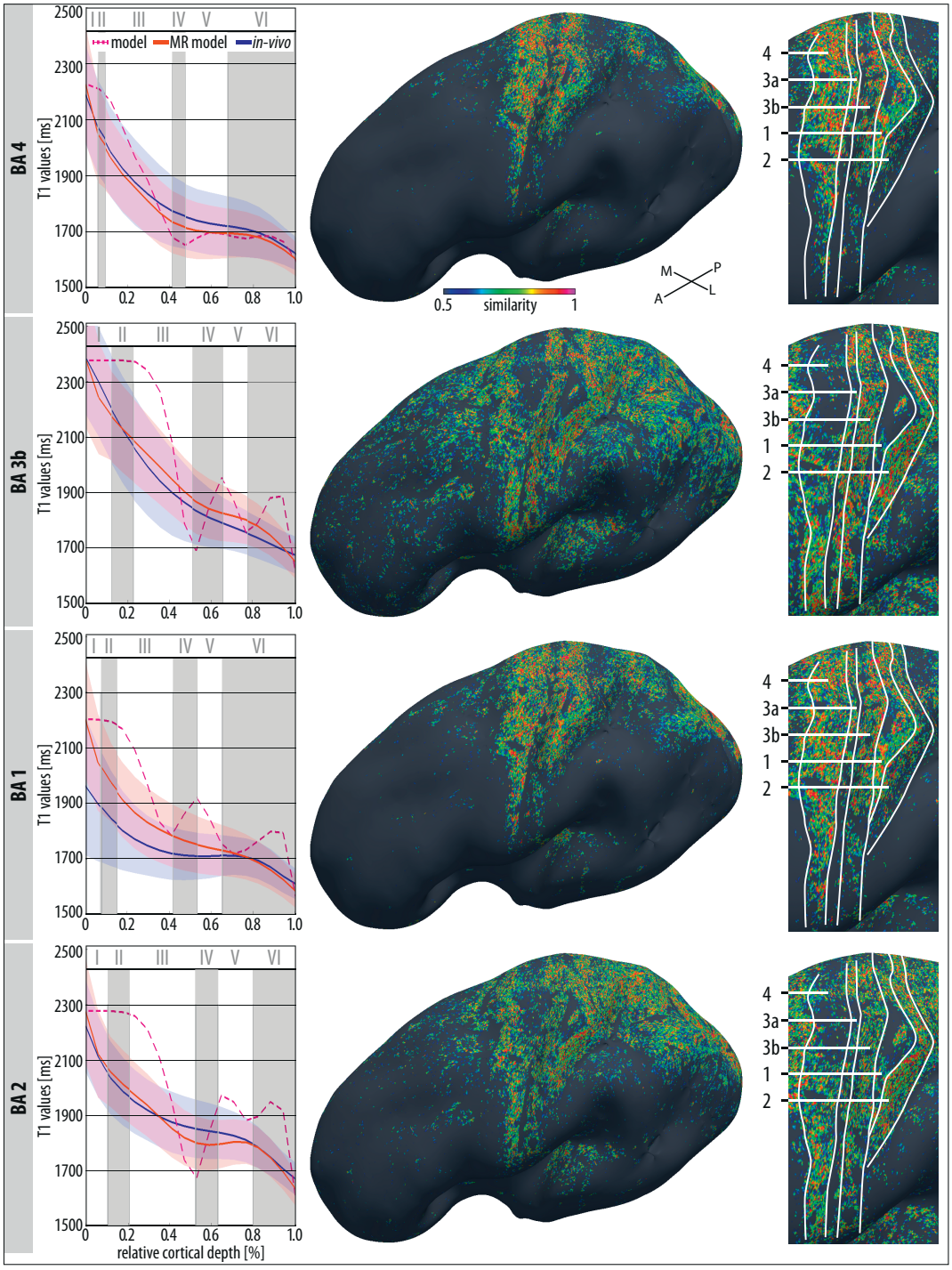

Figure 8.1: The image depicts the application of the presented model to a single subject. The left column shows area-specific modelled profiles (magenta, dashed) against mean in-vivo profiles (blue, solid) and modelled MR profiles (red, solid) in one individual subject. Lower T_1 values represent higher myelin concentration. The transparent bands represent the modelled and measured standard deviations. The area-specific MR models correspond well with the mean in-vivo profiles. (Figure caption continues on the next page.)

Figure 8.1: The second column shows maps of a single subject's similarity values, computed from Eq. 7.11 and sampled along the central cortical surface, to give a general impression of their distribution. The right column shows enlargements of the considered ROIs. The zoomed-in pictures show higher intra-ROI similarities when there is a match between a model and the respective Brodmann area. When the model and the location of an area do not correspond, the results show smaller similarities and/or inconsistent patterns.

		Single Subject				Group Average			
	BAs	4	3b	1	2	4	3b	1	2
Modelled Profiles	4	0.8431 (0.1529)	0.0 (0.0)	0.8 (0.201)	0.5556 (0.253)	0.871 (0.1807)	0.0 (0.0)	0.9412 (0.211)	0.0 (0.0)
	3b	0.4 (0.235)	0.818 (0.183)	0.0 (0.0)	0.795 (0.175)	0.357 (0.237)	0.833 (0.216)	0.45 (0.233)	0.794 (0.184)
	1	0.80 (0.166)	0.0 (0.0)	0.833 (0.216)	0.889 (0.246)	0.805 (0.171)	0.0 (0.0)	0.92 (0.188)	0.0 (0.0)
	2	0.5 (0.238)	0.718 (0.193)	0.0 (0.0)	0.796 (0.161)	0.5 (0.244)	0.643 (0.166)	0.684 (0.222)	0.781 (0.174)

Table 8.1: A summary of the quantitative comparisons between area-specific MR models and in-vivo profiles. The mode and standard deviations (given in brackets) were computed from the estimated beta distribution of the underlying similarity values in each ROI as depicted in Fig. 8.2. The diagonal boxes (blue) describe a given model at its corresponding location. Anatomically neighboring areas are highlighted in yellow. Given a certain model, it performs best in its corresponding location and outperforms directly neighboring areas.

while they are smaller in directly neighboring areas. The individual models reveal smaller similarities and/or inconsistent patterns (small different clusters) when the location of the Brodmann area and the area-specific model do not match.

QUANTITATIVE COMPARISON Quantitative comparisons between area-specific MR models and in-vivo profiles are summarised in Table 8.1. Given a certain model, it mostly performs best in its corresponding location (diagonal, coloured blue) and outperforms directly neighboring areas (coloured yellow). This is true for individual subjects as well as the group data. When the distribution of similarity values was skewed to 0 or 1, or similarity values were distributed across the entire range forming no precise peak, the approximated beta distribution becomes asymptotic. The mode and standard deviation cannot be estimated and were set to 0. The distribution of the area-specific similarities (blue) and the estimated beta distributions (red) are additionally shown in the Fig. 8.2. Graphs are illustrated for the group-average and for the single subject shown in Fig. 8.1. These graphs additionally provide information on how the underlying similarity values were distributed when the estimation of the mode and standard deviation from the beta distribution did not work. In the group results, the model of Brodmann area 4 in location of area 3b and 2 show values distributed across the entire range. Brodmann area 2 is an exception because it is not well separable across the group ($N = 19$). In the single subject results, the model of Brodmann area 3b shows a negatively skewed distribution in location of area 1.

CAUSES OF FAILURE In Brodmann area 2 the underlying data is highly variable, which arises from imaging artefacts as well as small segmentation errors.

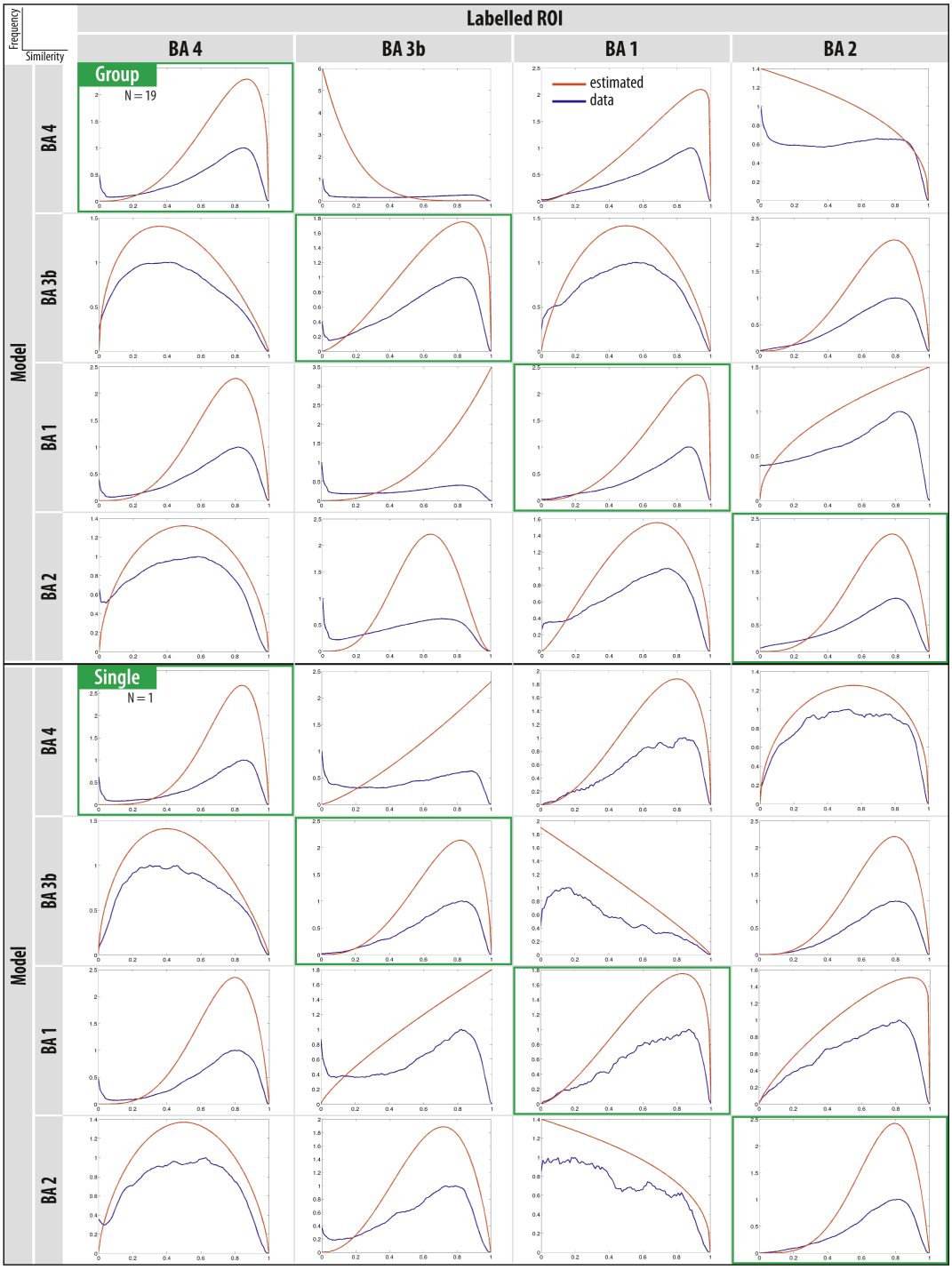

Figure 8.2: The images show the distributions of similarity values derived from the data (blue) and the approximated probability density function of a beta distribution (red) in each ROI for the given models. The beta distribution is used to compute the mode and standard deviation in each ROI on a group-average (N=19, top row) and subject-wise (bottom).

Gibb's ringing: The T_1 maps show small effects of Gibb's ringing (which is respected in our modelling approach, too, see Fig. 7.1h) that appear in the back of the brain and encompass the post-central gyrus but barely reach more into anterior regions, i.e. the central sulcus (see Fig. 3.10). The ringing artefacts do thus not affect area 3b very much and area 4 is even less affected. The effects usually intrude the imaging data in location of the cortical surface up to a depth of 1.5 cm. Therefore, all remaining areas of interest in the post-central gyrus, i.e. areas 1 and 2, show these small effects. Its influence on the final modelling result is different for the two areas, because the influence depends on the orientation and position of the area as well as its cortical thickness. The effects of ringing artefacts appear parallel in the cortex of area 1 and orthogonally in the cortex of area 2. Given the different cortical thicknesses of these locations with area 1 being thick at the gyral crown and area 2 being relatively thin in the sulcal wall, this ringing significantly affects the cortical segmentation result, and leads to larger inaccuracies when calculating the cortical profiles. In area 1, segmentation errors occur rarely, and their effects average out when the cortical profiles are calculated. In area 2, however, the segmentation of the boundary surfaces is affected by the artefact, which in turn impairs the quality of the cortical profiles. Comparing these corrupted profiles with an area-specific MR model leads to low similarity values, although intracortical contrast remains visible in this area.

Blood vessels: With the new resolution, blood vessels with a diametre of $0.5mm$ can be captured. Thus, their influence appears even stronger compared to standardly used MRI data. Segmentation errors due to blood vessels occur in various regions of the cortex. Here, the effects of segmentation errors due to blood vessels are most prominent in area 2, where the anterior parietal (or post-central sulcal) artery extends medially into the post-central sulcus. Branches of the paracentral artery reach laterally into the central sulcus region. These extensions usually follow the gyral crowns and their branches reach into the sulcal basins. Vessels on the crown have a diametre larger than the imaging resolution and are well discriminated with the segmentation methods used. However, their branches have a diametre close to or even smaller than the imaging resolution and are sometimes misclassified as belonging to grey matter. All these effects influence the performance of the model of Brodmann area 2. In the future, better methods have to be developed to capture the vessels' characteristics and to reduce segmentation errors.

AREA-SPECIFIC SIGNATURES From the aforementioned analysis, the question arises if the individual models are able to capture area-specific signatures. In Fig. 8.3 we mapped at each location the model with the highest similarity value given the values presented in Fig. 8.1. Patterns of the models overlap with the corresponding locations of these areas. In location of Brodmann area 4, the model of area 1 is slightly present. In location of area 1, the model of Brodmann area 4 dominates more. These two areas are very similar and hard to distinguish. When data quality was insufficient, the similarity values of the model of Brodmann area 2 were smaller than similarity values from other models. Thus, there was no obvious cluster representing the location of Brodmann area 2.

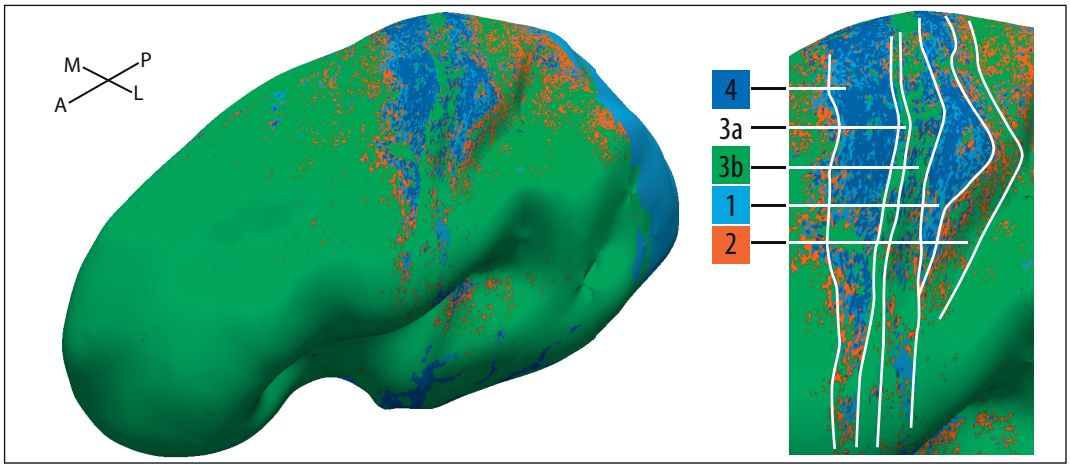

Figure 8.3: Surface and zoom-in on ROIs: At each location, the area-specific model with the highest similarity value is marked. Models reveal area-specific signatures.

8.2.3 *Comparing Models To Postmortem Brain Data (Exp. 3)*

Fig. 8.4, first row, shows a comparison between group-average in-vivo profiles (dark blue), ex-vivo profiles (light blue), histology profiles (green), and a group-average of the area-specific models (red). The comparison is shown for each ROI. Lower values are again associated with higher myelin concentration. Profiles with similar resolution should have similar profile shapes. Indeed, the modelled (red) and histology profiles (green) are qualitatively similar. They show the same trends at the same locations although the intensity of change is not the same. The ex-vivo profiles (light blue) preserve some shape characteristics, but striking features visible in the modelled and histology profiles are weakly noticeable here due to limiting resolution effects. The in-vivo profiles show less characteristic structure, but follow the general trend of the other profiles.

8.2.4 *Profile Attributes: Mean and Shape (Exp. 4)*

In Experiment 4, we investigated the information contributed separately by the mean and the shape of an individual in-vivo profile. In Fig. 8.5, first row, we schematically depict the different measures considered (from left to right): our presented approach, the mean-experiment and the shape-experiment. For comparison, the first column depicts the results of our approach on a cortical surface (as shown in Fig. 8.1).

THE UNIQUENESS OF AREA 4 In a normal adult human brain, area 4 is the most highly myelinated cortical area. Profiles found in this location have very low T_1 values, leading to very low mean values and large differences in profile shape when compared to profiles derived from other regions in the cortex. Using Eq. 7.11 with only the mean T_1 value of a profile results in high similarities in locations of area 4 and low similarities in other locations. Therefore, the three surfaces corresponding to the model of area 4 in Fig. 8.5 reveal fewer differences when comparing the effects between our approach, the mean- and the shape-experiment.

In each case, the areas are best discriminated when using our approach which not solely depends on mean T_1 value but incorporates shape differences, too.

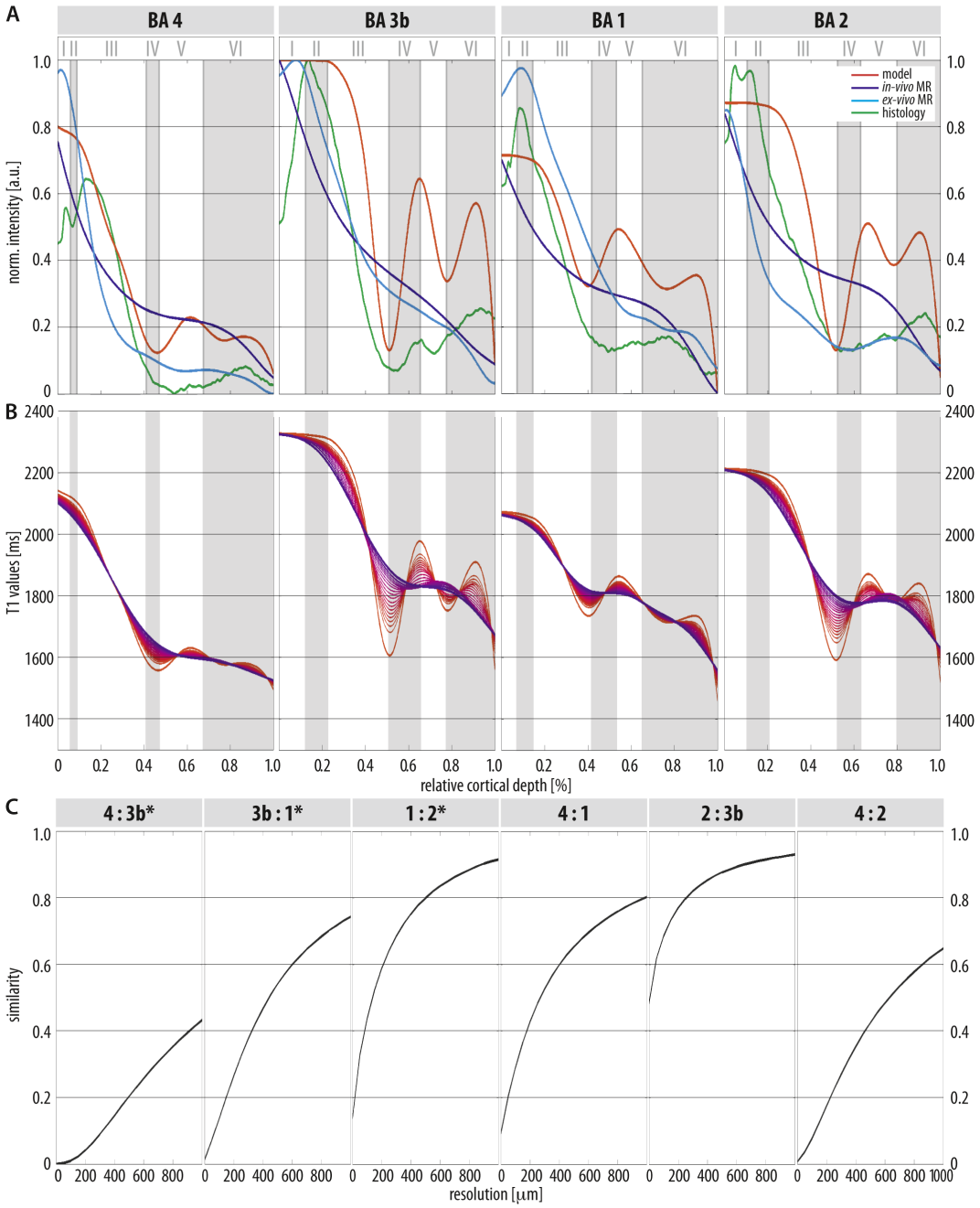

Figure 8.4: The image presents comparisons between area-specific models and in-vivo and postmortem data. The first row shows comparisons between modelled (red), group-average in-vivo (blue), ex-vivo (light blue), and histology (green) profiles. The myelination pattern agrees between the area-specific model and histology. The differences in myelination are located at similar relative cortical depths for different imaging techniques in each Brodmann area. In general, the myelination trend is also preserved in ex-vivo and in-vivo profiles. (Figure caption continues on the next page.)

Figure 8.4: Middle and bottom row show simulated experimental data. Each modelled profile (middle row) was transformed into different scales of resolution starting at 0.5 µm (red) and increasing in 50 µm steps up to 1 mm (blue). As resolution is coarsened, salient features disappear very quickly. Even at lower resolutions, profiles at the same scale are still very different across Brodmann areas. The bottom row shows the theoretical similarity P_t of how similar the area-specific models are at different resolutions.

MEAN OF A PROFILE The mean-experiment presented in Fig. 8.5 for Brodmann areas 3b and 1 show that using the mean T_1 value of a profile alone is insufficient to

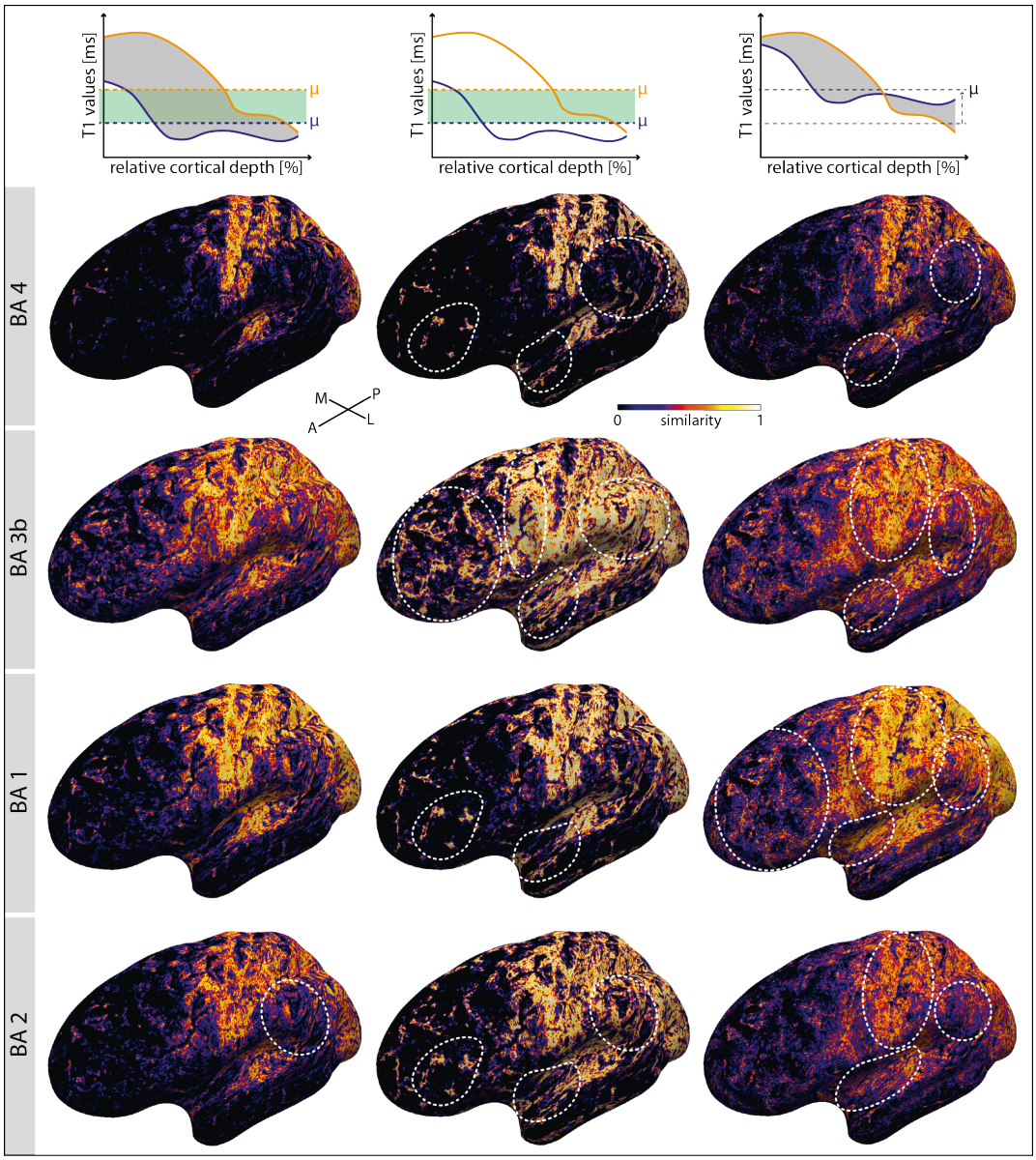

Figure 8.5: The images depict results from additional experiments comparing the use of the mean and the shape (first column), the mean (second column), and the shape (third column) of cortical profiles separately. (Figure caption continues on the next page.)

Figure 8.5: In general, the experiment using only the mean yields an almost binary result in which frontal, parietal, and temporal regions are equally similar to each other. Using the shape alone provides even less distinction in the ROIs in focus. Differences are encircled. The performance is best when using the mean and shape in a combined setup as presented in this work. It leads to high similarities when location and model match and low similarities in the case of a mismatch.

reveal area-specific signatures. Locations across the cortex are categorised as either very similar or very different, with no intermediate variation. Frontal, temporal, and parietal parts appear to be equally similar when applying the models of area 3b and area 1. A similar pattern can be observed for the shape-experiment when using the models of Brodmann area 3b and 1. Here, the selected regions of interest are poorly distinguished.

In many locations across the cortex, cortical profiles exhibit lower T_1 values in upper cortical layers and, at the same time, higher T_1 values (less myelin) in lower cortical layers. Therefore, if we compare the mean T_1 value of these profiles, there is no noticeable difference. Hence, mean values of profiles from different locations in the cortex appear similar when using the mean T_1 value alone, although their underlying real microstructure may be different.

MEAN DISTANCE BETWEEN PROFILE SHAPES The shape-experiment presented in Fig. 8.5 shows that using the mean distance between profile shapes is insufficient, too. The shapes may differ due to higher or lower T_1 values in upper or lower cortical layers. The total shape difference through cortical depth may be the same in different locations across the cortex, and, thus, the similarities differ not much. Here, the same conclusion as in the mean-experiment can be drawn: profiles from different locations in the cortex appear similar when using the shape only, although the underlying microstructure may be different.

The effects are less convincing when the model of Brodmann area 2 is applied. Possible reasons for the failure of the model of Brodmann area 2 were discussed previously in Section 8.2.2.

8.2.5 *Resolution Experiment (Exp. 5)*

Area-specific models at different scales of resolution are shown in Fig. 8.4, second row. The pictures illustrate the effect of decreasing resolution on profile shape characteristics. Strong shape features, such as turning points along the profile, vanish quickly with decreasing resolution. At 0.4–0.5 mm resolution, striking features become weaker. However, at a given resolution the profile shapes in each area are noticeably different, an observation which has already been pointed out when comparing in-vivo and modelled MR profiles in Fig. 8.1. Thus, the following question arises: Which resolution is needed to distinguish between profiles originating from different cortical areas?

THEORETICAL DISCRIMINATION OF AREAS The bottom row of Fig. 8.4 depicts the similarity P_t for directly neighboring areas 4 vs. 3b, 3b vs. 1, and 1 vs. 2 (all

marked with an $*$) as well as not directly neighboring areas 4 vs. 1, 2 vs. 3b, and 4 vs. 2. The similarity is computed on the basis of the modelled profiles. Thus, the similarity values can only be interpretated in a theoretical manner. The values are illustrated according to decreasing resolution. The challenging task for this approach is to distinguish between neighboring areas. The similarity plots show that Brodmann areas 4 and 3b can be well discriminated even at lower resolution. It is easier to distinguish Brodmann area 3b from 1 than Brodmann area 1 from 2. Brodmann areas 1 and 2 are similar at higher resolution, too. In the case of non-neighboring areas, Brodmann areas 2 and 3b are the most similar, directly followed by Brodmann areas 4 and 1. Brodmann areas 4 and 2 are the most dissimilar areas. In general, the slope of the similarity curve is high, given high resolution (except Brodmann areas 4 vs. 3b and 4 vs. 2), and starts to become smaller after 0.8 mm. At our working resolution of 0.5 mm, neighboring Brodmann areas 4 and 3b are well discernible. However, Brodmann area 2 cannot be reliably separated from other areas. Brodmann areas 4 and 1 are hard to distinguish. The outcome of the theoretical experiment here confirms results in Fig. 8.1 and 8.3, and Table 8.1.

8.2.6 *Myeloarchitecture and Area-specific Results*

There is a close relation between the cyto- and myeloarchitecture. The four myeloarchitectonic types present in the cortex are depicted in Fig. 2.11B (reproduced from Hopf [1968, 1969]). Here, we relate the results from the experiments to descriptions of myeloarchitecture.

THE PRIMARY MOTOR CORTEX M1 (BA 4) is reported to be of astriate type [Hopf, 1967]. The (T_1) values of profiles in Brodmann area 4 are very low (indicating higher myelination) for each individual imaging modality (Fig. 8.4A). The minima in the area-specific modelled profile (red) have the same strength. The difference in amplitude between minima and maxima is small. Histological data confirms this difference in myelination (see Fig. 8.4A). Due to small artefacts occurring close to the pre- and post-central gyral crowns in the ex-vivo MR data, the T_1 values in area 4 are increased in the ex-vivo profile, i.e. the difference is less apparent.

THE PRIMARY SOMATOSENSORY CORTEX S1 (BA 3B) is described to be of bistriate type, which is supported by the profile shape of the area-specific model of Brodmann area 3b (Fig. 8.4A). The outer band seems to be stronger myelinated. The area-specific model of Brodmann area 3b shows a deeper turning point (higher myelination) in layer IV in which the outer band of Baillarger is located. The same trend is visible in the histology profile of this area.

BRODMANN AREA 1 is located at the crown of the post-central gyrus and considered to be of unitostriate type (inner and outer band of Baillarger fuse together). Area 1 has equally dense myelinated layers. In Fig. 8.4A, all profiles of Brodmann area 1 appear on average less myelinated (higher T_1 values) in lower cortical layers IV-VI compared to the graphs of Brodmann area 4 and 3b. The minima in the area-specific model of Brodmann area 1 have the same depth in terms of T_1

values. The difference in amplitude between minima and maxima is small. The histology profile almost stagnates in the deeper cortical layers with almost no difference between the two bands of Baillarger being visible. Thus, Hopf's definition of Brodmann area 1 being of unitostriate type with equally dense myelinated layers is replicated here.

BRODMANN AREA 2 is located in the posterior wall of the post-central gyrus and, according to Hopf [1968, 1969], of unistriate type with an outer band of Baillarger being more pronounced. The area-specific model (Fig. 8.4A) clearly indicates higher myelination in the location of the outer band. The difference compared to the inner band is large. In the histology profile as well as in the ex-vivo profile there is a clear minimum in location of the two Baillarger bands. However, the separation into two bands is only visible in the histology profile. The data fit Hopf's definition of a unistriate type with a pronounced outer band.

8.2.7 *Results on Partial Volume Analysis (Exp. 6)*

The results in Fig. 8.6 show the spatial dependency between narrowness of structures and quantitative T_1 values. The narrowness is computed by taking the normal vector on the outer cortical surface and measuring the distance into the outward direction, until a target is hit. In theory, the distance can reach infinite values. For validation purposes, the distance was thresholded to 8 mm. In particular, this distance measure allows to compute the distance in sulcal valleys (positions marked with *1*, *2* and *3* in the schematic drawing in Fig. 8.6). The picture in the bottom of Fig. 8.6, each line represents T_1 values sampled on a surface in a certain cortical depth. The T_1 values of each line are then mapped according to their distance on the x-axis. The 21 intracortical surfaces calculated in this thesis are distributed in steps of 5 % of relative cortical depth.

An interpretation of the results and effects described here and their underlying causes is restrictedly possible at this stage as the true distribution of myelin in the cortex as measured using MRI is still under investigation.

The effects visible in Fig. 8.6 address different configurations that are schematically depicted above. The inflated surfaces show the mapped distance values computed using the normal vector. In general, there is a clear separation between gyral and sulcal structures visible on the surfaces.

GYRAL STRUCTURES Greenish regions visible on the surfaces define gyral crowns on the medial side (marked as *4* in the schematic drawing). Blue to grey colours indicate gyral crowns mostly on the lateral side of the cortex (marked as *5* in the schematic drawing). These structures are defined by distance values >3.2 mm.

SULCAL STRUCTURES Pink to red coloured regions on the inflated surfaces (marked as *1* and *2* in the schematic drawing) represent opposite gyral folds in sulcal structures which are close to contact. Yellowish regions (marked as *3* in the schematic drawing) describe deep sulcal structures which have CSF in-between. These structures are defined by distances of less than 3 mm.

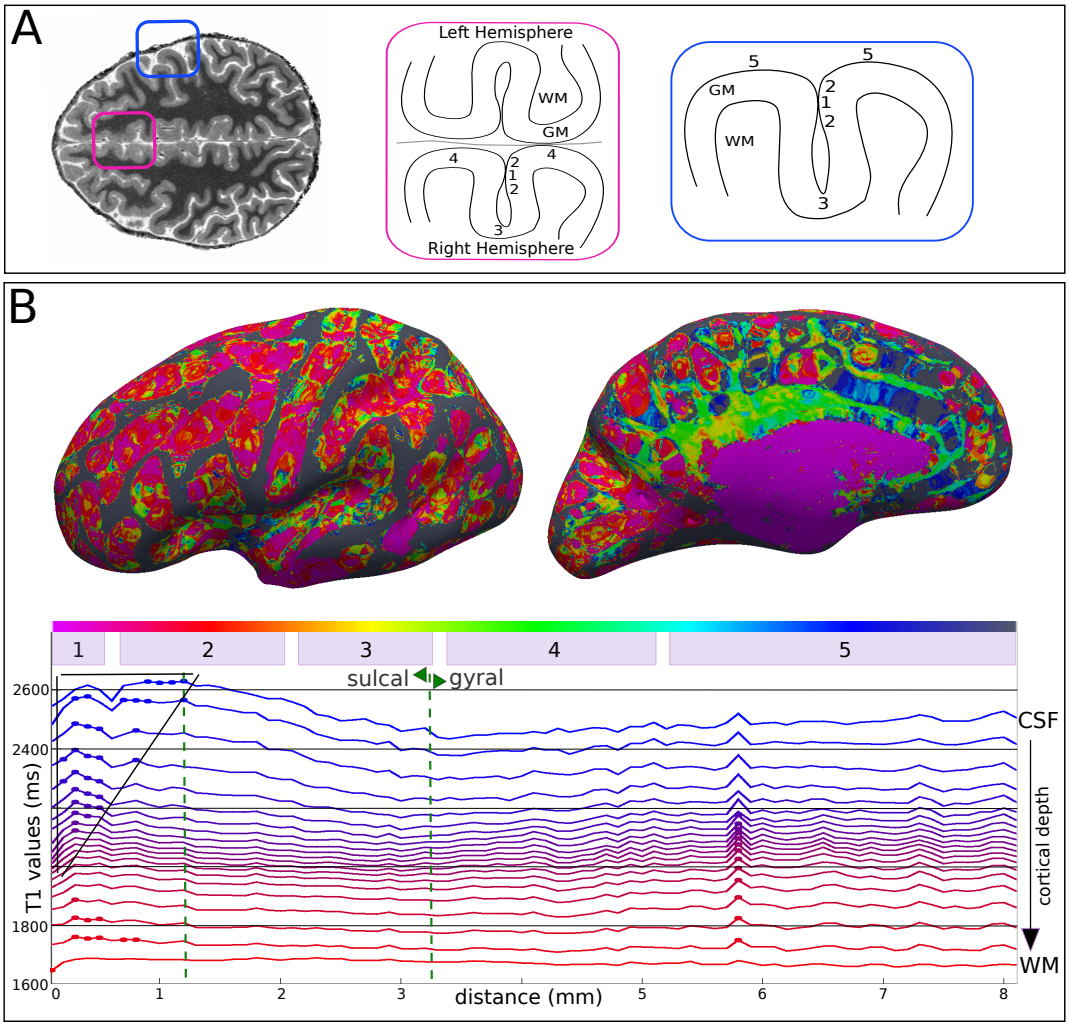

Figure 8.6: The images depict the dependency between distance of cortical structure and T_1 values. Narrow sulcal structures, where gyral folds are close to contact, show a rapid increase in T_1 values in relation to an increase in distance.

DEPENDENCE OF T_1 VALUES IN GYRAL STRUCTURES The analysis shows that there is a spatial dependence of T_1 values in section *4* and *5* defining gyral crowns on the medial (*4*) and lateral side (*5*). At the medial wall, gyral crowns of the two different hemispheres are opposite each other. The distance of opposing gyral crowns (marked *4*) is larger than compared to distances in sulcal structures. Due to less CSF as well as other structures being present between the hemishperes, such as the dura mater, the T_1 values exhibit only a slight slope. Gyral crowns on the lateral side are exposed to CSF much stronger in frontal regions yielding an additional increase in T_1 values. Although it seems that the distance is maximum (position marked as *5*), the gyral folds in the parietal regions are in contact to dura mater which has lower T_1 values. This lessens the effect of increasing T_1 values.

DEPENDENCE OF T_1 VALUES IN SULCAL STRUCTURES Sulcal structures mostly have a distance lower than <3.2 mm. The graphed curves in sulcal structures show a very different pattern than compared to gyral structures. There is also a rapid spatial dependency visible in sulcal structures as described in gyral crowns. Up

to a distance of 1.2 mm the T_1 values in each of the upper cortical layers increase. Then, they decrease again. This behaviour may be caused by definitions in the segmentation pipeline as well as the imaging resolution used. The MRI data has been registered to 0.4 mm isotropic MNI space prior to segmentation. In the preprocessing step, the PV filter was applied that uses a kernel size of 3x3x3 voxel. The resulting posterior probabilities describing potential PV effects in a voxel are more accurate in locations where the distance between folds covers the size of the partial volume filter kernel: $3x0.4 = 1.2$. This distance correlates with the peak of the top curve in the graph. The curve denotes the outer cortical surface. In locations where the distance between folds is smaller than 1.2 mm, the PV filter does not support the segmentation very well. The boundary surface separating GM and CSF is "pulled" further towards CSF. Thus, it samples actual CSF values yielding increased T_1 values. With distances between folds larger than 1.2 mm, the PV estimates are able to guide the segmentation such that it accurately outlines the boundary between GM and CSF.

The drop of T_1 values visible at a distance of 0.5 mm may indicate artefacts related to the original imaging resolution of 0.5 mm isotropic.

SIGNIFICANCE TESTING To evaluate the significance of the increased T_1 values, a z-test has been performed. The mean and standard deviation of each of the lines (representing each of the 21 intracortical layers) was calculated. The null hypothesis tests whether the T_1 value associated with a specific layer and a certain distance comes from a normal distribution defined by the calculated mean and standard deviation in this layer. The dots on the graphed curves in Fig. 8.6 depict layer-specific values at which the null hypothesis has been rejected. These points are significantly increased and may relate to the above-described segmentation artefacts. Significant points penetrate into the cortex up to 50 %, influencing all T_1 values up to this depth. The highlighted dots form a triangular shape in upper cortical layers. It shows that with an increase in distance up to 1.2 mm the effect becomes less strong and thus, penetrates less into the cortex. In addition, the triangle's upper right point matches again with the previously described necessary voxel distance of $3x0.4 = 1.2$.

8.2.8 *Segmented Patterns in Human Primary Motor and Sensory Cortex (Exp. 7)*

The observed decrease in myelin in T_1 maps coincides with the outline of receptive field representations of hand and face. The results indicate a structural gap being present between functional receptive fields. This is an unexpected finding. Such gaps were assumed to not exist in humans. As a consequence, this structural variability could not adequately been modelled in the architecture-based parcellation approach yielding a "clustered" appearance of similarities.

Further validation and analysis has been carried out to identify the underlying properties of the structural variability. The work is currently under review. Understanding the key features of the gap will aid to model the cortical architecture in future applications.

8.3 DISCUSSION AND CURRENT LIMITATIONS OF THE METHOD

8.3.1 *Aspects on the Area-specific Modelling*

In general, Hellwigs's (1993) model depends on many assumptions and parameters which he derived from the work by Sanides [1962] and Braitenberg [1962].

ARCHITECTURAL MEASURES Possible sources of uncertainty within the modelling itself may be different cell densities or cell sizes in cortical areas, given that the numbers can only be derived from postmortem material. The modelling is based on the assumption that larger cells contribute more to the myelin concentration, as their myelinated axonal collaterals carry more myelin. This relationship is modelled using a sigmoidal function. Newer cytoarchitectural data are needed describing average measures on cell size, cell number, myelination and layer thickness, but specifically providing variances for each of the measures.

CORTICAL T_1 VALUES The T_1 maps used in this study are comparatively new. In order to explore the modelling approach in a focused way, we kept several parameters constant across subjects, such as values of T_1 for WM and CSF. These were supported by previous literature. With more T_1 maps acquired and analysed, it will be possible to replace tissue values taken from Rooney et al. [2007] with reliable values derived from these new T_1 maps. In the thesis, it has been shown that the T_1 values at the CSF boundary vary depending on their location in the folded cortex and the tightness of structures. Tardif et al. [2013] additionally showed that the myelin concentration varies in the outer and inner cortical surfaces from area to area. This is due to incoming radial fibres at the inner surface and tangential fibres in the outer surface of the cortex. However, a static estimate used to model the T_1 intensity range as described in this thesis is therefore not sufficient enough to capture anatomical variability.

8.3.2 *Limitations in Validation*

The validation has several critical limitations that are discussed here.

MANUAL LABELLING IN REGIONS-OF-INTEREST The observation of segmented myelin patterns on cortical surfaces sampling structural T_1 values may effect the outcome of the validation. The area-specific models may only fit the underlying in-vivo MRI data in locations of small structural variability. The similarity values in such highly variable locations are decreased. Hence, the average similarity computed from labels given in a ROI may be decreased, too.

SIMILARITY METRICS In this thesis, we further tested the Pearson correlation in order to generate the previously shown area-specific signatures. The Pearson correlation is defined as:

$$\rho_{X,Y} = \frac{cov(X,Y)}{\sigma_X \sigma_Y}, \tag{8.1}$$

where $cov(X, Y)$ represents the covariance and σ the standard deviation of the two features X and Y being tested. The metric calculates the linear correlation between the two features. In the thesis, X and Y describe cortical profiles. When using the Pearson correlation, the crucial parameter is the covariance. It only measures the deviation from the mean of a cortical profile. However, the mean of cortical profiles itself plays a major role. In its outcome, the Pearson correlation is comparable with the shape-experiment performed in Exp. 4 (see Section 8.2.4).

FITTING OF BETA DISTRIBUTION TO UNDERLYING SIMILARITIES To provide comparable measures on the discrimination performance of the approach, a beta distribution has been fitted to the underlying similarity values in each ROI. The underlying similarity values in the ROIs follow no Gaussian distribution. Hence, computing the mean and standard deviation yields inaccurate results. In addition, the standard deviation would be very large which is not reasonable given that the range of similarity values is between 0 and 1.

Calculating the mode as average similarity is meaningful as it addresses the problem of finding the peak visible in the distributions. However, using Full Width at Half Maximum (FWHM) as standard deviation measure provides no accurate results. The estimated deviation at "half width" usually covers the entire range of similarities. It does not provide reasonable measures and cannot capture the lobe around the peak of the distribution.

Therefore, fitting a beta distribution to the data brings the best out of both options: the mode and the distribution around this mode are estimated. However, fitting the beta distribution to the data is only possible to a limited extent: if the data is too much skewed to either 0 or 1, the beta distribution becomes asymptotic.

8.3.3 *Limitations in MRI Acquisition and Data Segmentation*

The data used allows an application in limited ways.

ACQUISITION AND SEGMENTATION In the group data some subjects lack overall consistency in data quality. Small motion artefacts and image artefacts may strongly affect the results. Head motion typically has a global effect, decreasing the similarity values for each model. In contrast, image artefacts may have local effects and lead to better performance of a given area-specific model in other locations, e.g. the model of Brodmann area 4 may perform better in the location of area 1 (and vice versa) and the discrimination between area 1 and 2 may be impaired.

DATA RESOLUTION Another limitation of the approach is the current in-vivo image spatial resolution, which is constrained by the scan duration. Below a cortical thickness of 1.5 mm, the profiles generated from the empirical in-vivo data carry a smaller amount of information compared with the modelled MR profiles. In locations of small segmentation errors (oversegmentation) the empirical profiles may still carry enough information which is skewed into the profile's cortical depth. Important myelin-related intracortical features of the empirical profile are thus not well aligned with the features in the corresponding model affecting single subject as well as the group average results. Brodmann area 2 is the most incon-

sistent structure of the ROIs. Anatomical differences occurring in the individual brains may play a certain role, too. In some subjects the dura mater is almost in contact with the brain matter, other subjects have CSF between brain matter and dura mater. In these locations, the T_1 values at the CSF boundary surface have a high spatial dependence leading to strong partial voluming effects (see Experiment 6). These dependencies highly influence the results.

PERFORMANCE In general, the practical performance of the presented model is in agreement with the theoretically computed performance given in Fig. 8.4C. It appears that a resolution as high as 0.3 mm will be required to reliably distinguish the cortical areas solely based on intracortical features. At 0.3 mm the similarity values between neighboring (4 vs 3b, 3b vs 1) and non-neighboring areas (4 vs 1, 4 vs 2) are mostly below 0.5, thus, areas can more likely be distinguished. The theoretical performance calculations show that the bands of Baillarger, their location in cortical depth, and their degree of myelination are important. In addition, the experiments shown in Fig. 8.5 indicate that mean and shape in a combined setup perform best compared to mean or shape alone.

Average cortical myelin maps effectively depict primary areas even at lower resolution. But T_1 maps at 0.5 mm isotropic resolution and their derived profiles' mean and shape information bring further discriminative power when distinguishing between cortical areas. Spatial or geometrical priors, such as curvature, may be necessary in order to precisely distinguish between Brodmann areas 1 and 2 and between Brodmann areas 2 and 3b.

8.3.4 *Comparing In-vivo and Ex-vivo MRI Measurements*

There are main differences between investigations based on in-vivo measurements and postmortem brain samples:

RESOLUTION plays a major role. The difference in resolution between the imaging modalities used here is quite large and ranges from 0.5 mm isotropic resolution in in-vivo MRI measurements and 0.25 mm isotropic resolution in ex-vivo MRI measurements to 0.002 58 mm = 2.58 µm in-plane resolution in our histological experiment. Thus, differences in sampled image values may arise from different partial volume effects.

FIXATION of the ex-vivo sample may have an effect on the size of the cortical layers due to a small shrinking of the tissue during the fixation process [Mouritzen, 1978].

TRANSVERSE RELAXATION TIME is decreased after the fixation of a tissue sample. Thus, the dynamic range in the data is different. Mean T_1 values of GM derived from in-vivo MR data span a dynamic range of approximately 1500 ms. In MR data of a formalin-fixed brain sample, the mean T_1 values of GM span a range of approximately 350 ms.

AGE DIFFERENCE between the in-vivo and ex-vivo measurements is very large. A T_1 map derived from older postmortem brains may reveal slightly higher T_1 values. The change of the laminar myelin pattern across cortical depth may

loose some significance in location of the bands of Baillarger [Lintl and Braak, 1983].

Overall, age has a tremendous effect on brain structure and function. With increasing age, cells die and myelinated fibres change, and this process may be accelerated in disease states [Peters, 2002]. Cortical myelination is well known to continue into the third decade of life but gradually reduces with advancing age [Lintl and Braak, 1983]. Age may correlate with regionally specific decreases in myelin content, changes in iron [Hallgren and Sourander, 1958] and water content and ultimately with brain atrophy [Callaghan et al., 2014]. Further investigations are necessary to determine and define changes depending on age, gender, brain development, or disease.

8.3.5 *Limitations in Histology*

One should keep in mind that comparing profiles from different imaging modalities is difficult since each individual modality has its own limitations. Here, it is worth noting that the linear nature of myelinated axons and the planar dimensionality of myelin-stained cadaver brain sections pose a difficult problem. Calculating 3D quantitative profiles representing myelin concentration directly from histology is insuperable. The method cannot determine absolute values of myelin because even a highly standardised myelin staining process is not a quantitative method.

9 SUMMARY AND CONCLUSIONS

This thesis presents a cytoarchitectonically-driven model that is able to provide laminar area-specific estimates of myelin visible in quantitative T_1 maps measured using MRI. So far, computational parcellation methods based on myeloarchitecture do not exist yet. The key contribution of this work is the adaptation of Hellwigs's (1993) conceptual approach to a practical application to MRI data. As this work presented here is the first known in-vivo application of Hellwigs's (1993) method, the model can only be seen as a starting point for further investigations of cortical myelin distribution.

The model was validated by quantitatively analysing it on in-vivo data and comparing it to classically-derived information from postmortem material. The signature patterns visible on in-vivo surfaces appear to be area-specific. In addition, experiments were carried out to investigate the general discriminative power between the models itself. The results showed that sophisticated methods are necessary to precisely distinguish primary and secondary areas. Attributes, such as mean and shape, describing cortical profiles were also compared. Last but not least, partial voluming effects have been investigated by comparing the imaging intensities at the CSF boundary surface to the tightness of sulcal structures.

This model is only applicable when certain prerequisites are fulfilled. These relate to:

- the MRI data used which should reflect intracortical microstructure, and,
- the cortical layering technique used which should respect the shifting behaviour of real anatomical layers in the cortex.

In the thesis, new MRI mapping techniques were applied to obtain quantitative maps of myelin. Furthermore, a novel equivolume layering model that follows the architecture in the cortex was designed and implemented.

9.1 SUMMARY ON ACHIEVEMENTS

In Section 5.2.5, requirements for an ideal parcellation approach were formulated. Here, the outlined attributes will be compared to the achievements of the myelin-based parcellation model presented in this thesis:

- **incorporate architecture-relevant information:** The cytoarchitecture-driven myelin model respects the real cortical layering within the cortex because a new layering model has been designed. The parcellation method incorporates information at micro-level taken from the tabulations provided by von Economo and Koskinas [1925] and also models the misalignment between cytoarchitectonic and myeloarchitectonic layers.

- **respect areal extent:** The presented approach is not restricted by any sort of macroanatomical landmark. Hence, it respects the high degree of folding variability in non-primary areas.
- **offer cortex-wide application:** The parcellation scheme can be extended to areas cortex-wide without the need of area-specific custom-built designs.
- **provide robustness:** The method guarantees to be robust in the applied setting described in the thesis.
- **be independent of type of input data:** The parcellation scheme is developed as a two-step approach. As such, it is completely independent of the type of input data. It may be applied to in-vivo as well as ex-vivo data. Furthermore, the presented method can translate model-specific information into other data spaces in terms of redefining the intensity scale and the resolution. The normalisation function used can be replaced by any other function. This allows a **translation** and **scaling** towards other image modalities provided by MRI as well as histology data.
- **run automatically:** The method runs automatically without user-interaction.

In summary, this work shows that architecture-based parcellation schemes may be able to outperform existing parcellation techniques. The presented parcellation method allows to study myelin distribution in the cortex. By doing so, it may further help to understand the brain, and the relationship between number of areas and their extent.

9.2 FUTURE WORK

Based on the previous section, future work tasks are outlined here.

The next steps for such a parcellation scheme may include:

- an extension to other cortical areas, such as Broca's region.
- using the provided areal labels to further study areal extent or using them as initialisation for other parcellation approaches.
- reversing the approach in order to estimate cytoarchitecture.
- an application to clinical data.

EXTENSION TO OTHER AREAS The method can be extended to generate profiles of laminar myelin density patterns for other cortical areas. It is of most interest to evaluate the performance in locations like Broca's region which is responsible for speach processing. It contains area 44 and 45. These areas are different in their cyto- and myeloarchitectonic patterns, but are highly variable in their folding pattern (see Fig. 2.5).

UTILISING THE LABELS The area-specific signatures presented in Fig. 8.3 can be used as labels describing cortical areas. They can be used as initilisation for seed-based approaches. The labels are more appropriate in regard to the variability of individual brains. In other words: they were derived from the same brain they get applied to. Using these parcellation-derived labels may overcome the limitations of manually predefining the extent of an area or using projections of probabilistic atlases. It is of uttermost interest in the fMRI community to have such labels to study structural and functional connectivity in the brain.

ESTIMATING CYTOARCHITECTURE In turn, the approach could be easily reversed to estimate laminar quantities describing cytoarchitecture. This is specifically useful when studying sub-areas of larger cortical areas or when trying to detect new unknown areas with a deviating definite structure-function relation.

APPLICATION TO CLINICAL DATA In future, the approach could be used in studying diseased states of the brain in follow-up exams. By scanning the same brain at different time points and using the first scan as reference, the *intracortical* differences relating to the disease could be detected in a more focused way. An ultimate goal would be to quantify these changes in order to support diagnostics and therapy.

9.3 REMAINING CHALLENGES

The remaining challenges include four subjects that address:

- other tissue properties in the real brain that may drive and influence the MRI contrasts.
- further aspects to improve the parcellation model,
- the data processing to allow for an accurate and efficient segmentation.
- the imaging to optimise data quality.

TISSUE PROPERTIES In terms of T_1 values, there is an increasing interest in the neuroscience community to what extent other factors, such as iron or susceptibility, may influence the contrast of the T_1 maps. The work of Stüber et al. [2014] suggests that, within the cortex, the value of T_1 is dominated by myelin content. Further investigations are also necessary to determine and define myelin changes depending on age, gender, brain development, or disease. Incorporating new findings may improve the performance of the presented approach. Increasing the sample size and the age range of the study will help to adjust the modelling, in particular considering that changes in cell and myelin morphology occur throughout human life span [Henderson et al., 1980; Terry et al., 1987].

MODELLING ASPECTS The architecture-based parcellation model can be improved in the two different steps individually.

First step: In the first step, the models were built from cytoarchitectonic descriptions. Newer cytoarchitectural data are needed describing average measures

on cell size, cell number, myelination and layer thickness, but specifically providing variances for each of the measures. Using architecture variances may help to model the inner-areal structural variability and enhance the general performance of the model

Second step: In the second step, the models were transformed into the MRI space by adapting the T_1 intensity scale and the resolution. The results presented in the thesis show that there are differences in myelin concentration in different cortical depths between different areas. This variability has been taken into account but needs to be further investigated in-vivo. However, a relationship between T_1 values at the outer cortical surface and the tightness of structures has been presented in the thesis. Furthermore, significant inner-areal structural variability coinciding with receptive fields may exist in the primary motor and somatosensory region. So far, there is a lack of knowledge about these structural entities in the human brain. Using static estimates in the approach may therefore be inappropriate. Future architecture-based parcellation schemes would benefit from a more sophisticated modelling of CSF variability defined at the outer cortical surface that respects the individual anatomical conditions. Advanced methods also require adequate models of structural variability. This additional information may be derived from functional MRI. Spatial or geometrical priors, such as curvature, may be necessary in order to precisely distinguish between Brodmann areas 1 and 2 and between Brodmann areas 2 and 3b.

Advanced cortical registration techniques may help to increase the robustness and reproducibility of the results [Tardif et al., 2013; Robinson et al., 2013]. In particular, registered group-average T_1 maps may help in estimating a proper range of T_1 values in given ROIs. But more data sets are necessary to reliably extract and analyse the information. In addition, the approach presented could be usefully combined with other data such as probabilistic maps or gyral maps, and even task-based fMRI data to further understand the relationship between structure and function in the human brain.

DATA SEGMENTATION The data processing pipeline presented in the thesis provides the base for applying the cytoarchitecture-driven myelin model. When processing ultra-high resolution MRI data, artefacts and misclassifications of tissue cannot be avoided. Future work will include more data to better characterise and control image artefacts during the segmentation, and thus increase the performance of the approach.

IMAGING THE BRAIN Head motion is one of the biggest problems when performing MRI scanning at ultra-high resolution. The scan time is usually long and up to 70 min. Therefore, head motion introduces noise and produces blurry images. This problem can be overcome with adequate methods for removing motion artefacts, such as prospective motion correction [Schulz et al., 2012]. The true challenge is the data quality: optimising data is defined by increasing the SNR or increasing the resolution. New sequences need to be designed that are able to further increase SNR and resolution and investigate other tissue properties.

9.4 CONCLUSIONS

The approach presented offers a fresh perspective for imaging and modelling the relationship between myelo- and cytoarchitecture, in the context of the increasing interest in advanced methods for cortical parcellation.

The cytoarchitecture-driven myelin model presents a promising starting point to further investigate cortical architectural studies. It provides results of high interest to other fields in the neuroscience community.

This work specifically shows that architecture-based parcellation schemes outperform existing techniques. But on the other hand, the resolution of the imaging data is still a limiting factor. Parcellating the cortical surface has a history of more than 250 years. Finding a proper method may be as challenging as pushing the resolution in MRI.

Part III

Appendix

A

HISTORIC MAPPINGS OF CYTO- AND MYELOARCHITECTURE

In this Appendix, the historic mappings mentioned in Section 2.2.2 are presented in medial and lateral view. They depict the similarities and differences in cyto- and myeloarchitecture. The illustrations were taken from von Economo and Koskinas [1925] and were complemented with visual highlights in the selected regions of interest: M1/S1 region and Broca's area.

Brief descriptions of (individual areal) cytoarchitectonic and myeloarchitectonic features are provided in Section 2.3.1 and Section 2.3.2. Detailed descriptions (in German however) can be found in von Economo and Koskinas [1925].

First, all the three cytoarchitectonic mappings by Brodmann [1909], von Economo and Koskinas [1925] and Smith [1907] are shown followed by the myeloarchitectonic maps of Vogt and Vogt [1919a,b,c] and Hopf [1955, 1956]; Hopf and Vitzthum [1957].

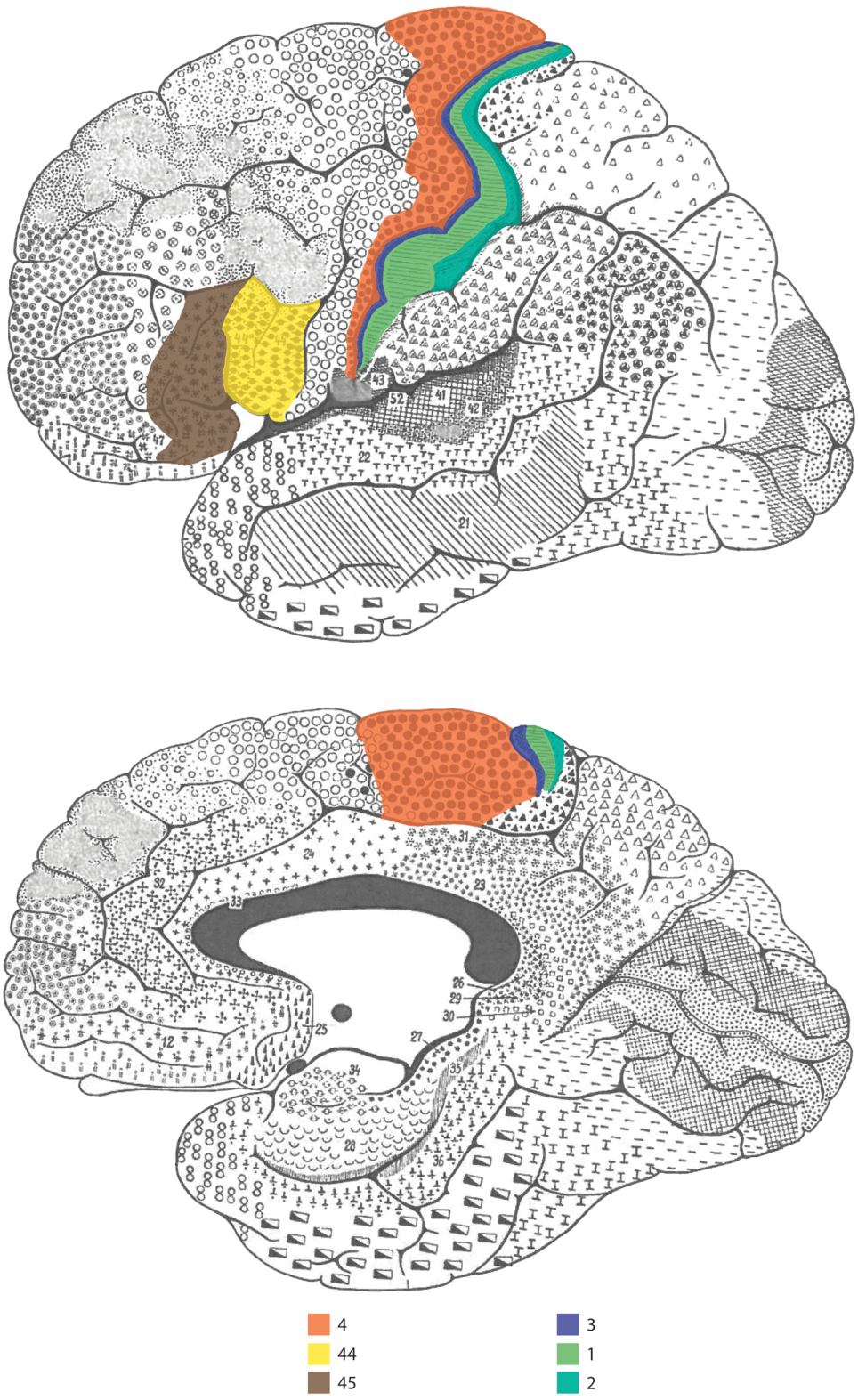

Figure A.1: Brodmann's cytoarchitectonic parcellation of the brain surface into 52 areas. Lateral view (top) and medial side view (bottom) onto the surface highlighting the primary motor-somatosensory areas 4, 3, 1 and 2, and Broca's region consisting of areas 44 and 45. Image source: von Economo and Koskinas [1925].

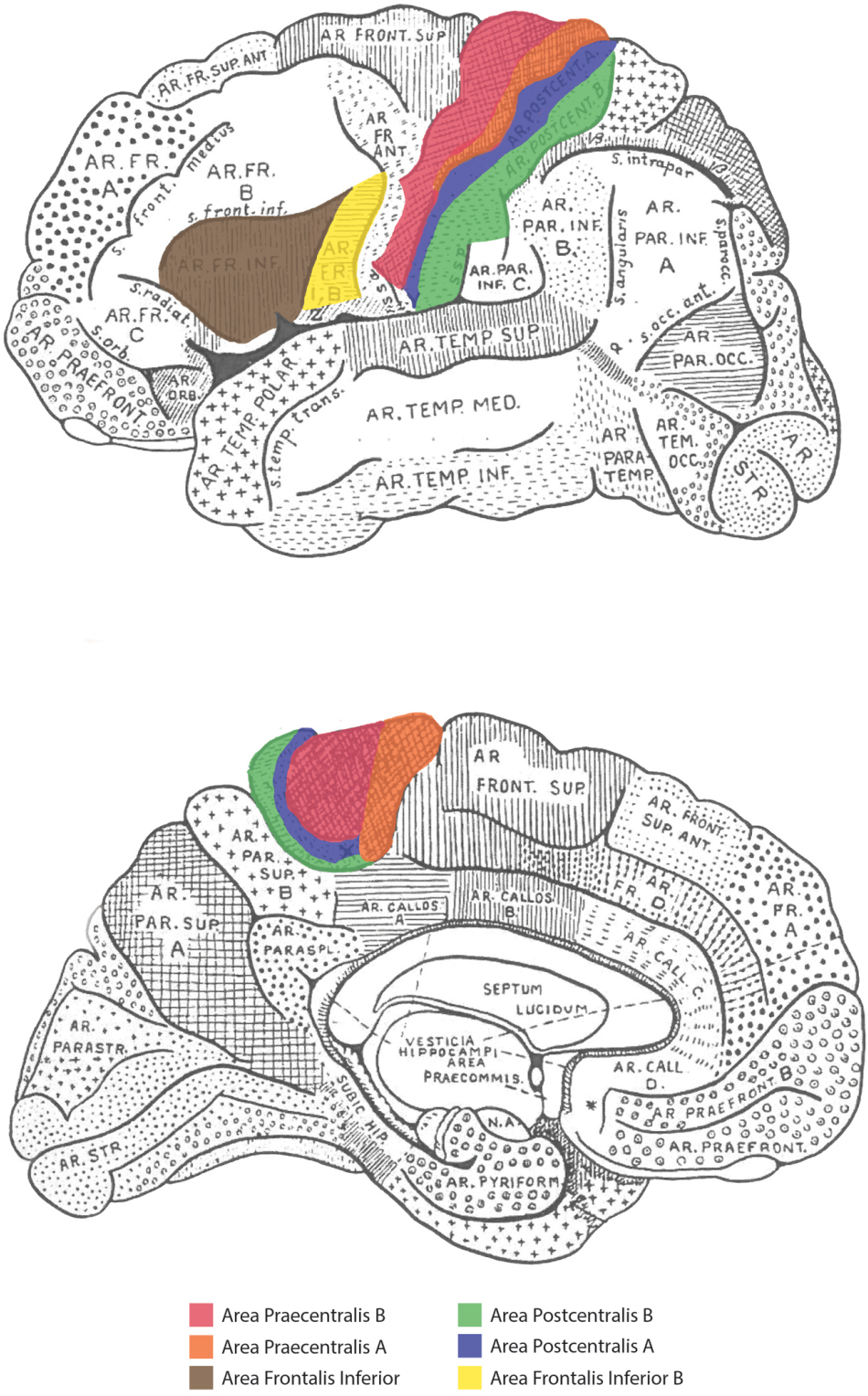

Figure A.2: Grafton Elliot Smith myeloarchitectonic parcellation of the cortical surface into 50 areas. Lateral view (top) and medial side view (bottom) onto the surface highlighting the primary motor-somatosensory areas 4, 3, 1 and 2, and Broca's region consisting of areas 44 and 45 (nomenclature and colour coding adopted from Fig. A.1). Image source: von Economo and Koskinas [1925].

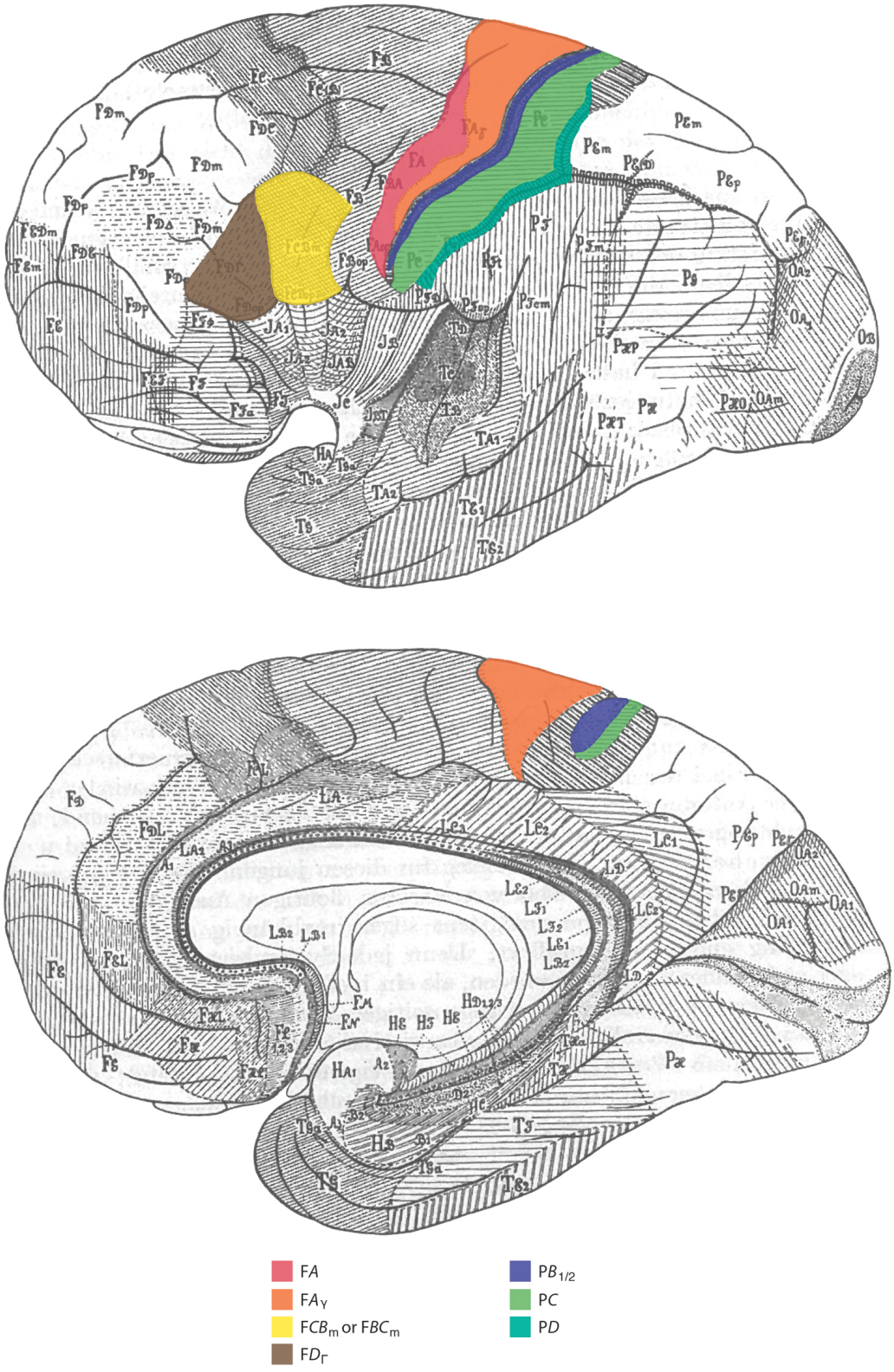

Figure A.3: Von Economos' and Koskinas' cytoarchitectonic parcellation consisting of 107 areas. Lateral view (top) and medial side view (bottom) onto the surface highlighting the primary motor-somatosensory areas 4, 3, 1 and 2, and Broca's region consisting of areas 44 and 45 (nomenclature and colour coding adopted from Fig. A.1). Image source: von Economo and Koskinas [1925].

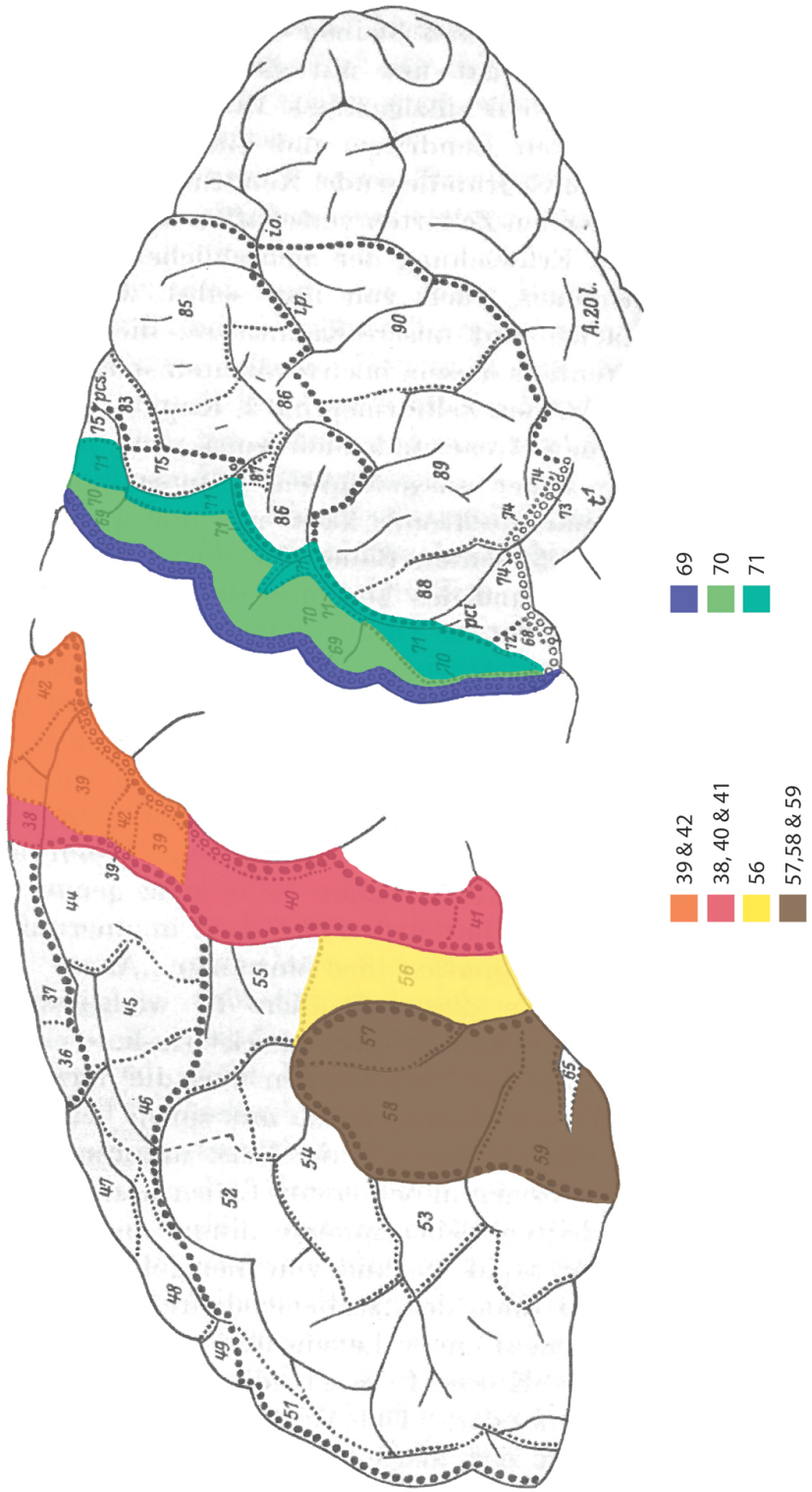

Figure A.4: Cécile and Oskar Vogts myeloarchitectonic parcellation of the brain surface into 200 areas in lateral view. The image depicts the primary motor-somatosensory areas 4, 3, 1 and 2, and Broca's region consisting of areas 44 and 45 (nomenclature and colour coding adopted from Fig. A.1). Image source:von Economo and Koskinas [1925].

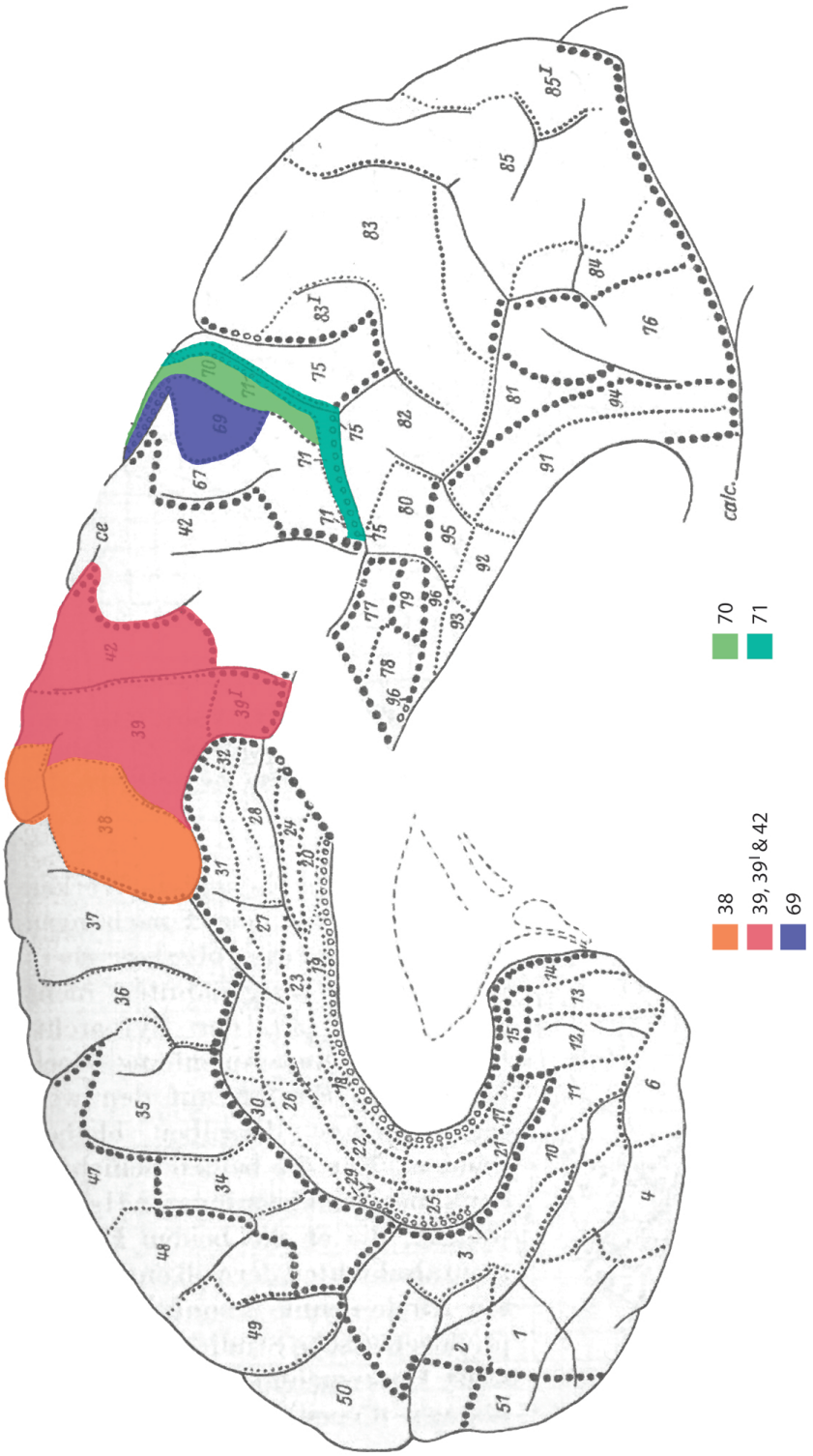

Figure A.5: Cécile and Oskar Vogts myeloarchitectonic parcellation of the brain surface in medial side view. The image highlights the primary motor-somatosensory areas 4, 3, 1 and 2 (nomenclature and colour coding adopted from Fig. A.1). Image source: von Economo and Koskinas [1925].

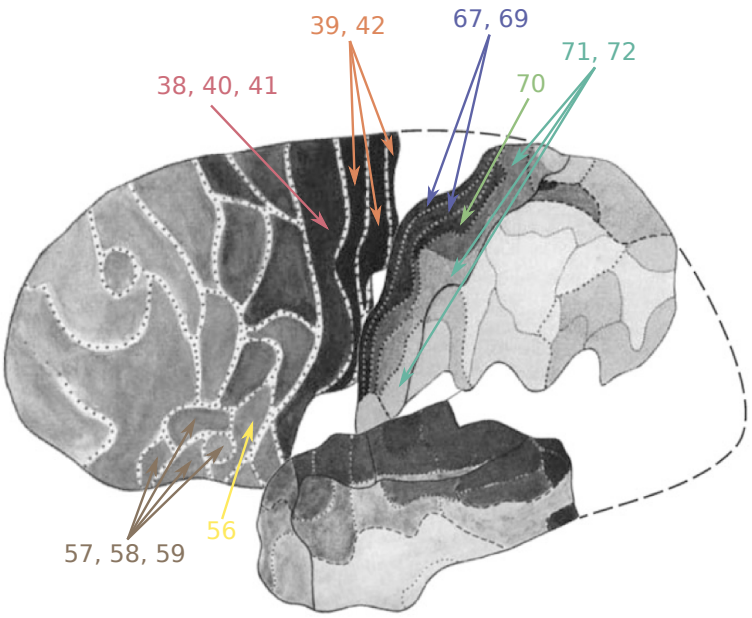

Figure A.6: Adaptation of Hopf's individual lobe maps as presented in Hopf [1955, 1956]; Hopf and Vitzthum [1957] merged to one single surface in lateral view (nomenclature and colour coding adopted from Fig. A.1). The separation agrees with structural changes in the myeloarchitecture described by the Vogts Vogt and Vogt [1919a,b,c]. The grey level codes the myelin concentration in each area with dark being strongly myelinated and light grey being less myelinated. (Image published in Geyer and Turner [2013] and by courtesy of Springer Verlag, Berlin-Heidelberg.)

B

CORTICAL LAYERING MODELS

Within the thesis a novel equivolume layering model was designed, implemented and validated. The model is based on the work by Bok [1929] and aims to generate a well-adapted coordinate system of the cortex.

In order to analyse layer architecture or function, it is desirable to define a conformal coordinate system. In this coordinate system, cortical depth values within a given cortical area remain constant, independent of cortical curvature. From surfaces spanning the coordinate system, cortical profiles can be constructed that traverse the cortex. Anatomically consistent profiles allow correct assessment of cortical thickness and enable accurate observer-independent mapping of structural brain areas.

The chapter briefly explains other existing layering approaches and includes a description of the validation experiments and their results. The content has previously been published in Waehnert et al. [2013c].

B.1 LAYERING MODELS

In previous studies, two different layering methods were mainly used: **Laplace** and **equidistant** models. In this section, the two models are briefly described. The main purpose of the well-adapted coordinate system is to provide profiles that are anatomically meaningful to study MR intensity patterns within cortical areas and their variation across area boundaries. Cortical profiles can be generated with computational techniques either by surface-based or voxel-based methods. Surface-based methods reconstruct cortical surfaces in order to generate the profiles, whereas voxel-based methods can generate the profiles directly from the segmentation.

B.1.1 *Laplace Models*

The Laplace method solves the Laplace equation between the inner and the outer cortical surfaces, setting each of these as an equipotential. Cortical profiles may then be constructed along the gradient of this layering [Jones et al., 2000]. Compared with straight profiles corresponding to nearest distance (from a point on one boundary surface to the closest on the opposite boundary surface) or orthogonal projection methods, Laplace profiles have been claimed to provide more accurate and stable cortical thickness estimates [Haidar and Soul, 2006]. Employing Laplace profiles to sample intensity values in the cortex is advantegous because they provide a one-to-one correspondence between the cortical boundary surfaces. In addition, they terminate perpendicularly at each boundary surface and do not intersect each other.

B.1.1.1 *Voxel-based Laplace Models*

Cortical thickness measurements based on Laplace profiles using the voxel-based approach have been made by: Yezzi and Prince [2003]; Hutton et al. [2008]; Geuze et al. [2008]; Nagy et al. [2011]; Strenziok et al. [2011]; van Swam et al. [2012]. This voxel-based approach is computationally more efficient than surface-based methods, sidestepping the need to reconstruct cortical boundary surfaces, and is especially important for large data sets of population studies. The main drawback of this is the lack of accuracy, which has been partly addressed by Acosta et al. [2009] and Querbes et al. [2009] by incorporating partial volume information.

Voxel-based Laplace profiles have been worked with extensively for cortical parcellation on two-dimensional histological sections. Schleicher et al. [2005] used Laplace profiles on cytoarchitectonic stained sections, quantifying the differences between mean profiles of a sliding window to provide observer-independent detection of areal borders. This approach has been employed to study striate and extrastriate areas [de Sousa et al., 2010], but also to analyse neurotransmitter receptor distribution patterns [Eickhoff et al., 2007]. Annese et al. [2004] applied Laplace profiles for myeloarchitectonic parcellation.

B.1.1.2 *Surface-based Laplace Models*

Surface-based methods employ the solution to the Laplace equation to generate one-to-one correspondences between the cortical boundary surfaces [Im et al., 2006] and even measure cortical thickness along the length of the links created by the Laplace profiles [Foster and Zatorre, 2010]. The Laplace equation has also been used to model cortical layers for high-resolution fMRI [Zimmermann et al., 2011].

B.1.1.3 *Laplace Models: Advantages and Disadvantages*

Laplace profiles have good mathematical properties, for instance they do not cross and are always perpendicular to the equipotentials they derive from. Because of this last property, the trajectory of the Laplacian profiles depends directly on the morphometry of the Laplacian equipotentials. The anatomy of the cortex also appears to have such a relationship: the cell columns running perpendicular to the cortical layers. Hence it is important to know whether observable cortical layers actually conform to the Laplace equation, or if a less mathematically constrained model is more appropriate to describe cortical anatomy. Schleicher et al. [2005] observed that some Laplace profiles follow cortical blood vessels on two-dimensional sections stained for cytoarchitectonics, and assumed that such profiles thus lie parallel to the cortical columns. Annese et al. [2004] asserted that the Laplace equipotentials lie parallel to myeloarchitectonic layers on their two-dimensional stained sections.

de Vos et al. [2004] studied the relationship between local curvature and areal boundaries in parcellations of two-dimensional sections stained for cytoarchitectonics. The areal boundaries were deduced from samplings along Laplace profiles.

They noted that the folding of the cortex can introduce artificial boundaries in observer-independent mapping. The challenge in these studies on two-dimensional

stained sections is that the cutting angle of the section must be normal to the cortical boundaries to provide an interpretable relationship between two-dimensional sections and the actual three-dimensional structure. It is clear that to address the cortical layering question thoroughly, it is vital to have access to a three dimensional image of the cortex, together with a spatial resolution sufficient to capture intracortical microstructure.

B.1.2 *Equidistant Models*

The computed intracortical surfaces describe a parameterised weighted average of the inner and outer cortical surfaces. The geometry of the surfaces depends on the choice of the parameter ρ which allows the final intracortical surface to be at any distance between the two boundary surfaces. If ρ is chosen to be constant, the resulting surface keeps a constant distance fraction from the segmented boundaries. Here, this is called the equidistant layering model. The intracortical surfaces are computed in the level set framework as described in Section 6.2.2.5 (see Equation 6.14).

The equidistant model has been used before by Trampel et al. [2012] for lamina-specific fMRI. Khan et al. [2011] also used weighted averages of the inner and pial surface level set functions to construct equidistant intracortical level set surfaces and from these constructed Euclidean depth profiles. Moreover, previously there have been other studies that use different implementations of equidistant laminae or that sample profiles at equally spaced Euclidean cortical depths [Olman et al., 2012; Polimeni et al., 2010b; Sereno et al., 2012]. However, Fig. 2.4 shows that the actual cortical layers do not maintain a constant distance from the inner and pial surfaces. Hence, the equidistant model is not appropriate.

B.1.3 *Equivolume Models*

The equivolume model is a novel approach for designing meaningful cortical profiles. It is explained in Section 6.2.2.5 and implemented according to the given descriptions.

B.2 VALIDATION OF THE LAYERING MODELS

The validation was carried out on high-resolution in-vivo and ex-vivo MRI data. It includes quantitative and qualitative comparisons between the models in different cortical areas to show that the proposed equivolume layering model provides a significant improvement both in precision and accuracy.

Intracortical layers extracted from the models are referred to in this study as computed laminae or laminae.

B.2.1 *Validation in Primary Visual and Somatosensory Regions*

The cortical areas were chosen such that they contain myelinated intracortical bands [Fatterpekar et al., 2002]. The bands of Baillarger are known to parallel the

cytoarchitectonic layers IV and V. In particular, the stria of Gennari, i. e., located in the calcarine sulcus in the primary visual area (Brodmann area 17), follows layer IVb [Vogt and Vogt, 1919a; Brodmann, 1909]. Therefore, comparing the location of the bands with computed surfaces indicates how well the established coordinate system describes the myelo- and cytoarchitectonics of the examined cortical area. Here, the models computed using the Laplace equation, the equidistant and the equivolume method are compared. Quantitative validation of the equivolume model consists of using manual delineations of the stria of Gennari as detected with in- and ex-vivo MRI data. The equivolume model is further validated qualitatively comparing the layers with the bands of Baillarger in an ex-vivo sample containing the postcentral gyrus.

B.2.2 *MR Data Acquisition and Preprocessing*

Scanning was performed using a 7 T whole-body MR system (Siemens, Germany) at the Max Planck Institute for Human Cognitive and Brain Sciences, Leipzig, Germany.

B.2.2.1 *Postmortem Scanning*

A formalin-fixed block of human postmortem brain containing the occipital pole was obtained from an autopsy with informed consent from the patient's relatives (postmortem time: 28 h). Another formalin-fixed block containing the pre- and post-central gyri was obtained with informed consent from the donor from the Netherlands Brain Bank Amsterdam (postmortem time: 8 h). No neurological pathologies were recorded for any of the brains.

The blocks were scanned using a specially-designed dual loop circularly polarised radio frequency coil. A gradient echo FLASH sequence was used to obtain a T_2^* weighted image of the occipital pole (150 µm cubic resolution, TE= 9 ms, TR=50 ms). Fig. B.1A shows the calcarine sulcus and the heavily myelinated stria of Gennari that characterise Brodmann area 17, also known as the primary visual area V1. Another gradient echo FLASH sequence was used to obtain a T_2^* weighted image of the pre- and postcentral gyri (70 µm cubic resolution, TE= 25 ms, TR=60 ms). Fig. B.1B shows the central sulcus with the precentral gyrus on the left, in its posterior wall containing Brodmann area 4 also known as primary motor cortex M1. On the right-hand side of the central sulcus is the post-central gyrus that contains Brodmann area 3b in its anterior wall also known as primary somatosensory cortex S1.

B.2.2.2 *Scanning of In-vivo Subject*

To acquire in-vivo images, a 24 channel phased array coil (Nova Medical Inc., USA) was used. The study was carried out with ethical approval from the local university and informed consent was obtained. Maps of the longitudinal relaxation time T_1 were obtained from one healthy subject using the MP2RAGE sequence [Marques et al., 2010; Hurley et al., 2010] (700 µm cubic resolution, TR = 5000 ms, TI_1 = 900 ms, α_1= 5°, TI_2 = 2750 ms, α_2=3°). The gradient echo FLASH sequence was used to obtain a T_2^* weighted image (Fig. B.5A, (400 µm cubic resolution, TE =

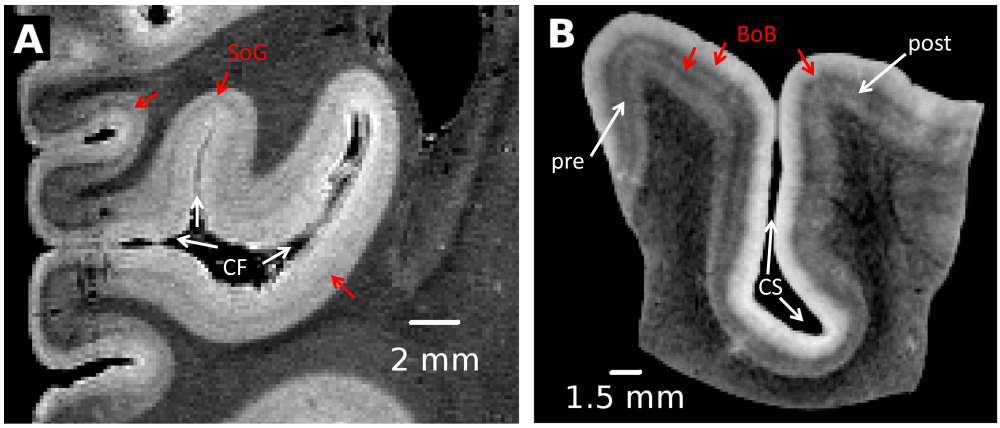

Figure B.1: T_2^* weighted image of postmortem samples: (A) Occipital pole sample with the calcarine fissure (CF) and the stria of Gennari (SoG), 150 µm cubic resolution; (B) pre- and post-central gyri sample with the precentral gyrus (pre), i. e., area 4, on the left showing two bands of Baillarger (BoB) and the post-central gyrus (post), i. e., area 3b, on the right containing one band. The image data were downsampled to 140 µm cubic resolution.

17.7 ms, TR = 35 ms, flip angle = 11°) of the same subject. The data was checked to have no serious motion artifacts. Both ex- and in-vivo data were also checked for ringing artifacts.

B.2.2.3 *Preprocessing of the Data*

Image preprocessing was done using MIPAV (NIH, Bethesda, USA) and the in house developed plug-ins described in Chapter 6. For segmentation of the postmortem images into grey and white matter (GM, WM), an automatic algorithm, Fantasm [Pham and Prince, 1999], was used to get a first crude estimation. Careful subsequent manual intervention was required to obtain a refined segmentation. From the segmented images, the inner GM/WM cortical surface and the outer GM/background surface were determined.

For the in-vivo data, the T_1 map was normalised into the Montreal's Neurological Institute (MNI) brain space and resampled to a cubic resolution of 400 µm. The normalisation consisted of a rigid registration and normalised mutual information as a cost function. Afterwards, the normalised image was segmented fully automatically and inner and the pial surfaces were reconstructed as described in Chapter 6. The T_2^* weighted image was then registered onto the segmentation of the T_1 map. This registration was landmark based and rigid to preserve the cortical geometry. Note that there are small distortions between the T_1 map and the T_2^* weighted image due to the different band widths during scanning.

B.3 RESULTS

B.3.1 *Postmortem Samples*

First, the layers in the primary visual cortex at the calcarine sulcus region (Fig. B.1A) was evaluated. A lamina estimated with the Laplace model is thinner at the highly

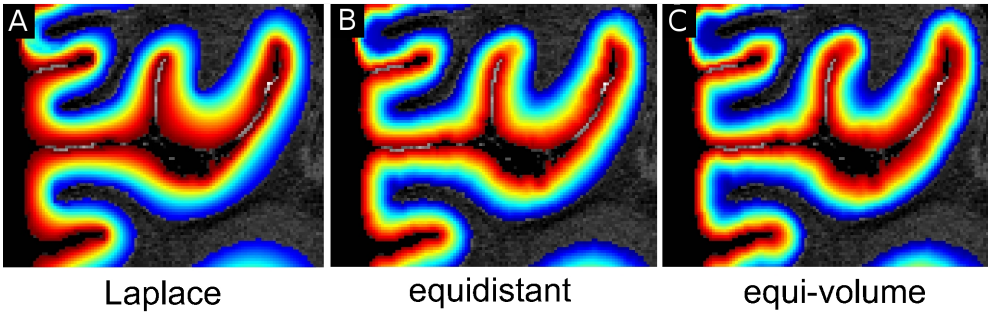

Figure B.2: Layering computed with the Laplace equation (A), the equidistant (B) and the equivolume model (C) on the postmortem occipital pole data shown in Fig. B.1A. Laminar thicknesses in the equivolume model change contrary to the thicknesses in the Laplace model with respect to curvature.

curved regions than at locations with low curvature (Fig. B.2A). Moreover, comparing the laminae that stratify the cortex from the inner to the pial surface, one notices that the laminae at the boundary surface with the higher curvature are thinner than the laminae at the boundary surface with lower curvature. The laminae from the equidistant model have equal thicknesses everywhere (Fig. B.2B), independent of curvature. The laminae in the equivolume model are thick when they are closer to the surface with greater curvature (Fig. B.2C) and thinner when they are closer to the little curved boundary surface. A lamina computed with the equivolume model, having a specific thickness at the flat part of the cortex, is thinner at locations of low curvature and thicker at locations of high curvature. Hence, the laminae thicknesses of the equivolume layers behave contrary with respect to curvature than the Laplace laminae thicknesses.

B.3.1.1 *Quantitative Comparison in Primary Visual Cortex using Ex-vivo MRI data*

To evaluate the three different models quantitatively, the respective laminar structure was investigated at the location of the stria of Gennari in the primary visual cortex. Brodmann [1909] described the stria of Gennari as located in cytoarchitectonic layer IVb. Von Economo and Koskinas [1925] measured the position of cytoarchitectonic layer IVb at different locations. In the sulcal wall it is between 0.47 and 0.61 relative Euclidean cortical depth. Our cortical depth values increase from the inner to the outer cortical boundary (the opposite of von Economo's convention). Therefore, we can model von Economo's values with a boxcar function that has a value of one between 0.39 and 0.53 and zero at other cortical depths. The cortex at the sulcal wall is flat, and hence the cortical depth values are undistorted. We can compare our cortical depth values even in highly curved cortex regions to von Economo's values, since the well-adapted coordinate system from the equivolume model compensates for curvature. To account for partial volume effects and the resolution of our data (150 µm), we convolved the boxcar function with a Gaussian that has a standard deviation of half the resolution with which the MR image was acquired. The convolved von Economo data is depicted in Fig. B.3C, D and E as an ochre curve. Its area was normalised to the area of the histogram of the equivolume model (Fig. B.3E). Mean and standard deviation are $\mu_{EG1} = 0.46 \pm 0.06$.

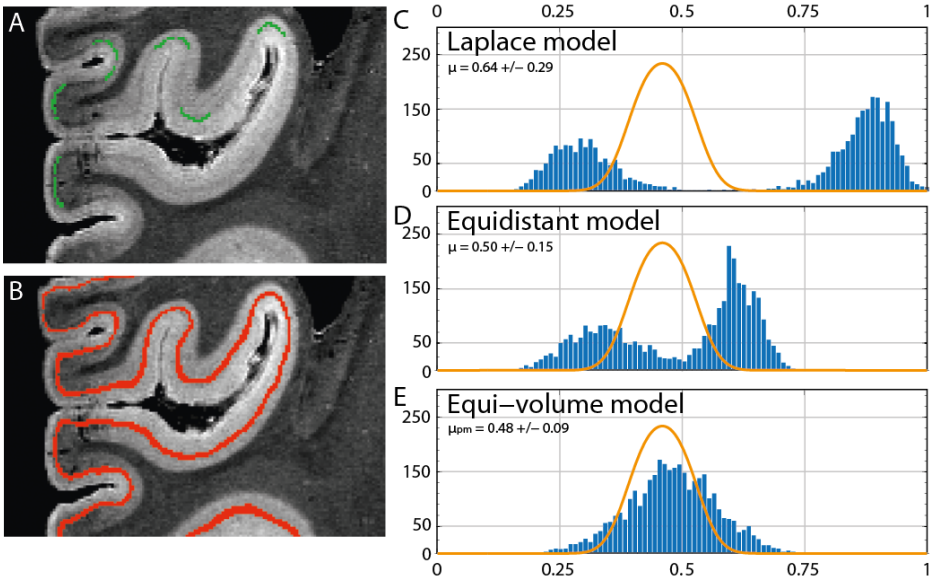

Figure B.3: Quantitative analysis of the Laplace method, the equidistant and the equivolume model on postmortem occipital pole data: (A) mask of the stria of Gennari on highly curved regions; (B) laminae with values $\mu_{pm} = 0.48 \pm 0.09$ of equivolume layering (Fig. B.2C); (C), (D), (E) blue bar plots: histograms of cortical depth values (Fig. B.2) at the stria of Gennari mask with respective means and standard deviations; ochre lines: convolution of von Economo's data with a Gaussian accounting for partial volume effects and a normalisation to the area of the histogram of E; (E) mean and standard deviation of the unimodal histogram: $\mu_{pm} = 0.48 \pm 0.09$.

To study the behavior of the different layering models quantitatively, the following technique was used. The stria was labelled in highly curved regions of the cortex, i.e. on the gyral crowns and in the fundi of the sulci (Fig. B.3A). This binary image is a mask of the stria of Gennari, with 1 at labelled stria locations and 0 everywhere else. This stria mask was multiplied voxel-wise with the layers of the model to be evaluated. The resulting image consists of the cortical depth values at the labelled stria and 0 everywhere else. A histogram of this resulting image is the last step of the analysis.

The layering of an ideal model would contain a thin laminae that follows the stria of Gennari everywhere. The histogram of the stria mask multiplied with the ideal layering would be a single narrow peak.

However, Fig. B.3C shows a bimodal histogram of the Laplace layering at labelled stria locations. The right mode represents the cortical depth values at the gyral crowns and the mode on the left-hand side are the values at the fundi of the sulci. This means, that there is no laminae that follows the stria all along the cortex. The same result was obtained in Waehnert et al. [2012] from a qualitative analysis of the same data. The bimodality of the histogram now is a quantitative description of the Laplace equation not being able to characterise the topology of the actual cortical layers. One implication of the striking mismatch between computed Laplace laminae and the anatomical layers is that cortical thickness measured along the Laplace profiles cannot be accurate, since these profiles do not parallel the corti-

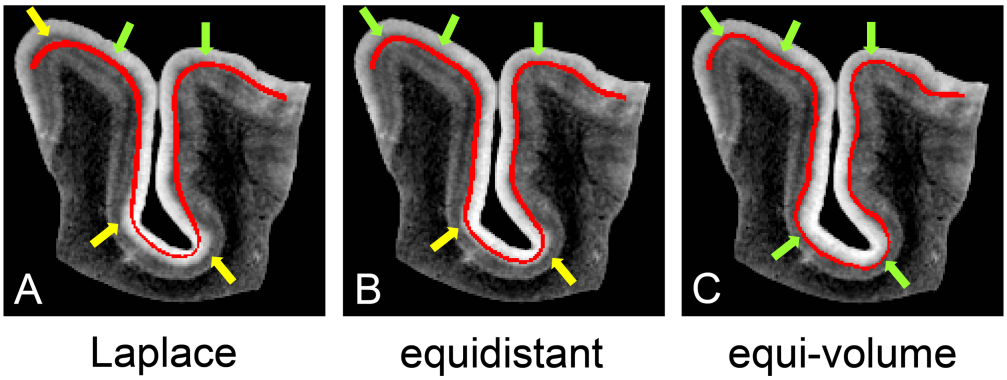

Figure B.4: Qualitative analysis of the Laplace method (A), the equidistant (B) and the equivolume model (C) on postmortem pre- and post-central gyri data: Each laminae was selected to follow the band of Baillarger in the gyral crown on the right-hand side (post-central gyrus). Green arrowheads mark locations where the laminae follows the myelinated band. Yellow arrows indicate that the chosen laminae fails to follow the band. The laminae was masked out towards the edge of the sample where it is influenced by boundary effects.

cal columns. Moreover, cortical parcellation performed using Laplace profiles may well dislocate boundaries between cortical areas.

Fig. B.3D shows that the histogram of the layering computed with the equidistant model at marked stria locations is also bimodal. Again, the cortical depth values at the gyral crowns make up one mode and the values at the fundi of the sulci give the other mode. But the two modes in the equidistant model are closer than in the Laplace model. Hence, the equidistant layering is closer to modelling the stria of Gennari than the Laplace one.

Fig. B.3E shows a different behavior of the histogram obtained with the equivolume model: this histogram is unimodal. This means that the equivolume layering does contain a single laminae that follows the stria of Gennari everywhere that is observable within the cortex, no matter how much it is curved. The mean and standard deviation of this histogram is $\mu_{pm} = 0.48 \pm 0.09$. Since it is unimodal it can be compared with the Gaussian distribution described by $\mu_{EG1} = 0.46 \pm 0.06$ (ochre curve in Fig. B.3 C, D, E). Vice versa, the location of the laminae of the values μ_{pm} is depicted in Fig. B.3B on the image, qualitatively showing that the laminae does follow the stria of Gennari everywhere that is observable within the cortex.

B.3.1.2 *Qualitative Comparison in Primary Motor Cortex using Ex-vivo MRI data*

Comparing the three models qualitatively was performed on the sample containing the pre- and post central gyri. The original very high resolution of 70 µm turned out to be computationally too expensive, so we subsampled the image to 140 µm (Fig. B.1B). Laminae that follow the bands of Baillarger in the crown of the post-central gyrus were chosen from the layering (right-hand side of Fig. B.4).

Fig. B.4A shows the Laplace laminae. It follows the band everywhere in the post-central gyrus and it follows the outer band in the flat part of the precentral gyrus. However, the laminae deviates from the band in the highly curved region of the precentral gyrus (extreme left of Fig. B.4A) and in the fundus of the central sulcus.

The laminae, chosen from the equidistant layering to follow the band of Baillarger in the crown of the post-central gyrus, also fits the upper band everywhere in the precentral gyrus (Fig. B.4B). Apparently, the distance between the band in the post-central gyrus and the pial surface is the same as the distance between the outer band and the pial surface in the precentral gyrus. In the sulcal walls the laminae follows the bands better than the Laplace laminae. In the sulcal fundus, the equidistant laminae is nearer to the band than the Laplace laminae. However, the thickness of the cortical layers changes with cortical curvature in order to keep the segment volume constant. Thus, the layers near the pial surface are thicker in the fundus than in the crowns. This results in the band in the fundus being deeper than the equidistant laminae.

The equivolume laminae selected to follow the band of Baillarger in the crown of the post-central gyrus, follows the slight curves of the band in the anterior wall of the post-central gyrus noticeably better than the equidistant laminae (Fig. B.4C). It also tracks the upper band in the precentral gyrus. Most importantly, the equivolume layering model compensates for the curvature in the sulcal fundus so that the laminae selected to follow the band in the crown, is also able to follow the band in the fundus.

B.3.2 *In-vivo Data*

Using the equidistant and the equivolume model, 20 intracortical laminae were computed. The laminae were interpolated to give continuous values stratifying the cortex. Fig. B.5B shows the equivolume layering on the T_2^* weighted image. Specially-developed software calculated the layering with the Laplace model in three dimensions [Waehnert et al., 2012], which already provides continuous cortical depth values.

Evaluation of the three different models was performed by comparing the respective layering with the location of the stria of Gennari in the primary visual cortex on the registered T_2^* weighted images. Like in the experiment with the post-mortem sample containing the calcarine sulcus (section B.3.1), a mask labelling the stria was created (inset of Fig. B.5A). The stria was labelled only in regions where it was clearly visible. Moreover, care was taken to label only regions where the cortical segmentation of the T1 map appeared accurate on the T_2^* weighted image. In contrast to the ex-vivo experiment, we labelled not only highly curved regions but had to include parts of flat cortex, in order to have enough values to establish a meaningful histogram.

The histograms shown in Fig. B.5C, D and E are obtained by multiplying the stria mask with the layering of the three different models, respectively. As described in section B.3.1, we convolve von Economo's data with a Gaussian that accounts for the resolution of the T_2^* weighted image (400 µm). This results in a curve that is normalised to the area of the equivolume histogram (Fig. B.5E) and has $\mu_{EG2} = 0.46 \pm 0.11$.

The Laplace model gives a histogram that is wide, flat and does not resemble a Gaussian distribution (Fig. B.5C). This means that the marked stria is equally often occuring at locations with many different values of the Laplace layering. Hence, the Laplace layering does not contain any laminae that follows the stria of Gennari

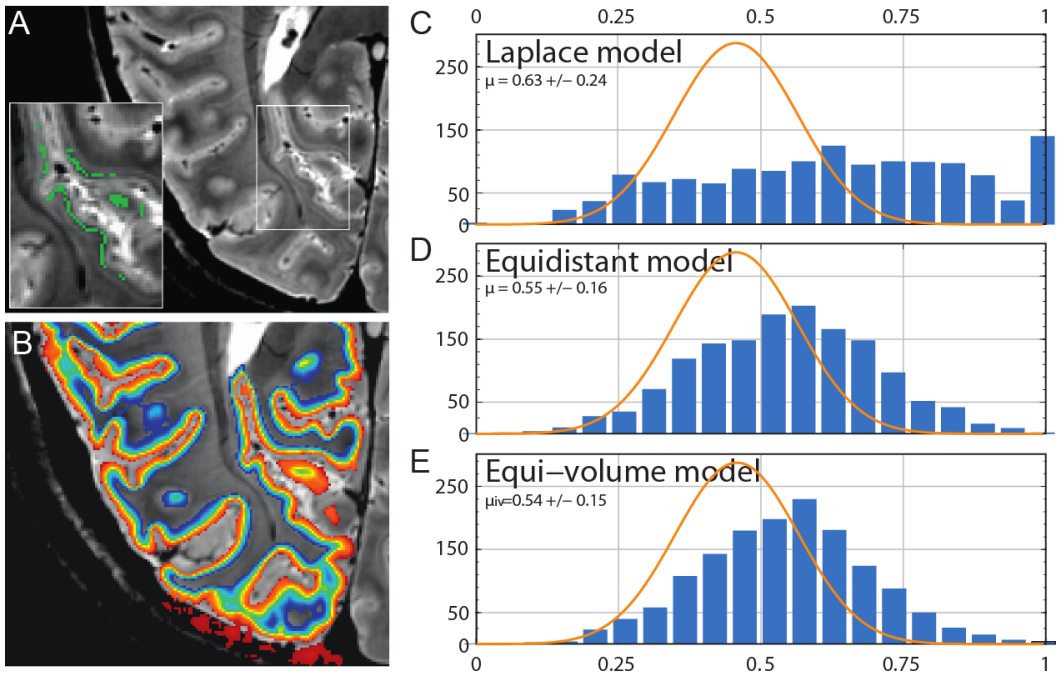

Figure B.5: Quantitative analysis of the Laplace, the equidistant and the equivolume model on in-vivo data: (A) T_2^* weighted image of the occipital pole, 400 µm cubic resolution, inset: mask of the stria of Gennari on well segmented cortex; (B) equivolume layering from interpolating 20 computed intracortical laminae; (C), (D), (E) blue bar plots: histograms of cortical depth values at the stria of Gennari mask for the different models with respective mean and standard deviation µ; ochre lines: convolution of von Economo's data with a Gaussian accounting for partial volume effects with a normalisation to the area of the histogram of E.

all along the cortex. It is possible though that the Laplace model would give a bimodal histogram if the stria contained only voxels from highly curved regions. Even then and given the fact of lower resolution, these findings confirm the result from the analysis of the postmortem data: The Laplace equation does not conform to observable cortical layers.

This is different in the case of the equidistant model. Here, the histogram looks almost unimodal (Fig. B.5D). The bimodality of the equidistant histogram of the postmortem data (Fig. B.3D) has vanished. This may be due to the values from the voxels in flat cortex and the lower resolution. The mean and the standard deviation is $\mu = 0.55 \pm 0.16$. This means that the equidistant layering contains a broad laminae that follows the stria of Gennari everywhere in the cortex.

However, the equivolume model gives the narrowest histogram and it is clearly unimodal. Mean and standard deviation are $\mu_{iv} = 0.54 \pm 0.15$. Hence, the equivolume layering contains a narrow laminae that follows the stria everywhere that is observable within the cortex. This confirms the result from the postmortem data: The equivolume model conforms to observable cortical layers.

B.4 DISCUSSION AND CONCLUSIONS

This study was motivated by the finding that the Laplace equation does not describe the morphology of the anatomical cortical layering [Waehnert et al., 2012]. The inspiration for a better model arises from Bok's (1929) study on the volume preservation of cortical segments. We do not aim to rebuild the six cytoarchitectonic layers, which in any case vary in relative thickness across cortical areas, but instead we intend to provide a coordinate system of depth on which to describe these layers, independently of the cortical folding. To our knowledge, this is the only implementation of the equivolume model so far using MRI data.

However, de Vos et al. [2004] were inspired by Bok's findings. They found that cortical curvature introduces artificial boundaries in the cytoarchitectonic mapping on two-dimensional stained slices. Therefore they tried to improve the Laplace profiles by applying Bok's ideas sampling at intervals of equal areas. In addition, histological studies of cortical geometry on two-dimensional stained sections depend strongly on the cutting angle of the section. To study the morphometry of cortical layers observed in histology most accurately one would also need to stack computationally the two-dimensional stained slices to three-dimensional volumes.

To validate our model, its performance on postmortem and in-vivo data was compared to those of the equidistant and the Laplace model. When assessed using the 150 µm postmortem data, the equivolume model is the only model that gives a *uni*modal histogram of layering values on the mask of gyral and sulcal locations of the stria of Gennari.

Mean and standard deviation of this histogram is $\mu_{pm} = 0.48 \pm 0.09$. Compared to $\mu_{EGI} = 0.46 \pm 0.06$, the equivolume model works impressively well, considering that it makes several simplifying assumptions in order to approximate Bok's cortical segments. These results indicate very clearly the need for the equivolume model in studies of cortical anatomy on 3D MRI and histology at resolutions of 150 µm or better.

It is also clear that the Laplace model is inaccurate even at lower resolutions, and will likely decrease sensitivity and introduce biased results in folded regions. Even in the 400 µm in-vivo data its estimation of the location of the stria of Gennari was far poorer than the one of the equidistant and the equivolume model. The equidistant model is better than the Laplace model, and for low resolutions it may be an acceptable approximation to the equivolume model. Still, even on our in-vivo data set with cortical boundary surfaces defined from 700 µm resolution data, the equivolume model was most successful.

The main weakness of this implementation of the equivolume model is the estimation of curvature. To give consistent values, the size of the curvature sampling neighborhood must be chosen appropriately. This requires some care at resolutions of 150 µm and better. When the sampling window is smaller than the scale of curvature the estimates become noisy and result in irregular laminae. When the sampling neighborhood is too large, the quadric approximation may not be adequate to model the surface locally and results in curvature estimates that go toward zero. In this case, the equivolume model turns into the equidistant model which may be an acceptable approximation. Moreover, the computation time increases cubically with the size of the curvature sampling neighborhood.

A quantitative measure for optimising the size of the curvature sampling neighborhood could be the standard deviation of an average profile. For a perfect layering it will be zero. Minimising it with varying curvature sampling neighborhood could provide a means of optimisation.

Profiles derived using the equivolume model are likely to improve cortical observer-independent parcellation. Bok warned against placing boundaries between cortical areas at locations where the layer structure is changed only by curvature and not by a really different architecture [Bok, 1929]. The equivolume model constructs an undistorted well-adapted coordinate system of the cortex. Thus, measuring cortical thickness and depth along profiles constructed with the equivolume model is neuro-anatomically more appropriate. Moreover, the approach offers itself for analysis of laminar-specific fMRI, where the data can be correlated with meaningful profiles and laminaes derived from structural images of the cortex.

Future work includes investigation of the impact of the equivolume layering model on measures of cortical thickness and the definition of cortical profiles, in particular as it assists in distinguishing cortical areas for architectonic parcellation.

BIBLIOGRAPHY

O. Acosta, P. Bourgeat, M.A. Zuluaga, J. Fripp, O. Salvado, and S. Ourselin. Automated voxel-based 3D cortical thickness measurement in a combined Lagrangia-Eulerian PDE approach using partial volume maps. *Medical Image Analysis*, 13 (5):730–743, 2009.

D. Adalsteinsson and J.A. Sethian. A fast level set method for propagating interfaces. *Journal of Computational Physics*, 118(2):269–277, 1995.

A. Aizerman, E.M. Braverman, and L.I. Rozoner. Theoretical foundations of the potential function method in pattern recognition learning. *Automation and Remote Control*, 25:821–837, 1964.

N.S. Altman. An introduction to kernel and nearest-neighbor nonparametric regression. *The American Statistician*, 46(3):175–185, 1992.

L. Alvarez, F. Guichard, P.-L. Lions, and J.-M. Morel. Axioms and fundamental equations of image processing. *Archive for Rational Mechanics and Analysis*, 123 (3):199–257, 1993.

Alzheimer's Disease International. Economoc impact - World Alzheimer Report 2010. September 2014. URL http://www.alz.co.uk/research/world-report.

A.A. Amini, T.E. Weymouth, and R.C. Jain. Using dynamic programming for solving variational problems in vision. *Pattern Analysis and Machine Intelligence, IEEE Transactions on*, 12(9):855–867, 1990.

P. Andlin-Sobocki, B. Jönsson, H.-U. Wittchen, and J. Olesen. Cost of disorders of the brain in EuropeÅ¿. *European Journal of Neurology*, 12:1–27, 2005.

J. Annese. The importance of combining MRI and large-scale digital histology in neuroimaging studies of brain connectivity and disease. *Frontiers in Neuroinformatics*, 6(13):1–6, 2012.

J. Annese, A. Pitiot, I.D. Dinov, and A.W. Toga. A myelo-architectonic method for the structural classification of cortical areas. *NeuroImage*, 21(1):15–26, 2004.

A. Anwander, M. Tittgemeyer, D.Y. von Cramon, A.D. Friederici, and T.R. Knösche. Connectivity-Based Parcellation of Broca's Area. *Cerebral Cortex*, 17(4):816–825, 2007.

Y. Assaf and O. Pasternak. Diffusion tensor imaging DTI-based white matter mapping in brain research: a review. *Journal of Molecular Neuroscience*, 34(1):51–61, 2008.

B. Aubert-Broche, M. Griffin, G.B. Pike, A.C. Evans, and D.L. Collins. Twenty new digital brain phantoms for creation of validation image data bases. *IEEE Transactions on Medical Imaging*, 25(11):1410–1416, 2006.

L. Axel and D. Morton. Correction of Phase Wrapping in Magnetic Resonance Imaging. *Medical Physics*, 16(2):284–287, 1989.

J.G.F. Baillarger. *Recherches sur la structure de la couche corticale des circonvolutions du cerveau*, volume 8. Mémoires de l'Académie Royale de Médecine, 1840.

P.J. Basser, J. Mattiello, and D. Le Bihan. Estimation of the effective self-diffusion tensor from the NMR spin echo. *Journal of Magnetic Resonance*, 103(3):247–254, 1994a.

P.J. Basser, J. Mattiello, and D. Le Bihan. MR diffusion tensor spectroscopy and imaging. *Biophysical Journal*, 66(1):259, 1994b.

P.-L. Bazin and D.L. Pham. Homeomorphic brain image segmentation with topological and statistical atlases. *Medical Image Analysis*, 12(5):616–625, 2008.

P.-L. Bazin, L.M. Ellingsen, and D.L. Pham. Digital homeomorphisms in deformable registration. In *Information Processing in Medical Imaging*, pages 211–222. Springer, 2007.

P.-L. Bazin, A. Schäfer, J. Dinse, C. Tardif, M. Waehnert, E. Hashim, L. Huber, S. Geyer, N. Bock, and R. Turner. Fine details of cortical and sub-cortical anatomy revealed in-vivo by ultra-high resolution quantitative T1 mapping. *Proceedings of the 19th Annual Meeting of the Organization for Human Brain Mapping*, 2013a.

P.-L. Bazin, M. Weiss, J. Dinse, A. Schäfer, R. Trampel, and R. Turner. A computational framework for ultra-high resolution cortical segmentation at 7 Tesla. *NeuroImage*, 93(0):201–209, 2013b.

M.F. Bear, B.W. Connors, and M.A. Paradiso. *Neuroscience: Exploring the Brain*. Lippincott Williams & Wilkins, 3 edition, 2007.

M. Beckmann, H. Johansen-Berg, and M.F.S. Rushworth. Connectivity-Based Parcellation of Human Cingulate Cortex and Its Relation to Functional Specialization. *The Journal of Neuroscience*, 29(4):1175–1190, 2009.

T.E.J Behrens and H. Johansen-Berg. Relating connectional architecture to grey matter function using diffusion imaging. *Philosophical Transactions of the Royal Society B: Biological Sciences*, 360(1457):903–911, 2005.

R. Berlin. *Beitrag zur Strukturlehre der Grosshirnwindungen*. Inaugural dissertation, 1858.

M. Bernstein, K. King, and X. Zhou. *Handbook of MRI pulse sequences*. Elsevier, 2004.

W. Betz. Anatomischer Nachweis zweier Gehirncentra. *Zentralblatt für die Medizinischen Wissenschaften*, 12(578–580; 595–599), 1874.

J.C. Bezdek. *Pattern recognition with fuzzy objective function algorithms*. Kluwer Academic Publishers, 1981.

Blausen Medical Communications, Inc. Wikiversity Journal of Medicine. *Blausen Gallery 2014*. URL https://en.wikiversity.org/wiki/Blausen_gallery_2014.

K.T. Block, M. Uecker, and J. Frahm. Suppression of MRI truncation artifacts using total variation constrained data extrapolation. *International Journal of Biomedical Imaging*, 2008, 2008.

T. Blumensath, S. Jbabdi, M. Glasser, D. Van Essen, K. Ugurbil, T. Behrens, and S. Smith. Spatially constrained hierarchical parcellation of the brain with resting-state fMRI. *NeuroImage*, 76:313–324, 2013.

N.A. Bock, A. Kocharyan, J.V. Liu, and A.C. Silva. Visualizing the Entire Cortical Myelination Pattern in Marmosets with Magnetic Resonance Imaging. *Journal of Neuroscience Methods*, 185(1):15–22, 2009. doi: 10.1016/j.jneumeth.2009.08.022.

J.A. Bogovic, J.L. Prince, and P.-L. Bazin. A multiple object geometric deformable model for image segmentation. *Computer Vision and Image Understanding*, 117(2): 145–157, 2013.

S.T. Bok. Der Einfluß der in den Furchen und Windungen auftretenden Krümmungen der Großhirnrinde auf die Rindenarchitektur. *Zeitschrift für die gesamte Neurologie und Psychiatrie*, 121(1):682–750, 1929.

B.E. Boser, I.M. Guyon, and V.N. Vapnik. A training algorithm for optimal margin classifiers. In *Proceedings of the 5th Annual Workshop on Computational Learning Theory*, pages 144–152. ACM, 1992.

P. Bradley, U. Fayyad, and C. Reina. Initialization of iterative refinement clustering algorithms. *Proceedings of ACMSIGKDD*, 1998.

V. Braitenberg. A Note on Myeloarchitectonics. *Journal of Comparative Neurology*, 118(2):141–156, 1962.

V. Braitenberg. Thoughts on the Cerebral Cortex. *Journal of Theoretical Biology*, 46 (2):421–447, 1974.

H. Bridge and S. Clare. High-resolution MRI: in vivo histology? *Philosophical Transactions of the Royal Society B: Biological Sciences*, 361(1465):137–146, 2006.

H. Bridge, S. Clare, M. Jenkinson, P. Jezzard, A.J. Parker, and P.M. Matthews. Independent anatomical and functional measures of the V1/V2 boundary in human visual cortex. *Journal of Vision*, 5(2):93–102, 2005.

K. Brodmann. *Vergleichende Lokalisationslehre der Großhirnrinde in ihren Prinzipien dargestellt auf Grund des Zellenbaues*. Leipzig: JA Barth, 1909.

R. Buckner, F. Krienen, and B. Yeo. Opportunities and limitations of intrinsic functional connectivity MRI. *Nature neuroscience*, 16(7):832–837, 2013.

A. Cachia, J.-F. Mangin, D. Riviére, D. Papadopoulos-Orfanos, F. Kherif, I. Bloch, and J. Régis. A generic framework for the parcellation of the cortical surface into gyri using geodesic Voronoï diagrams. *Medical Image Analysis*, 7(4):403–416, 2003. Medical Image Computing and Computer Assisted Intervention.

M.F. Callaghan, P. Freund, B. Draganski, E. Anderson, M. Cappelletti, R. Chowdhury, J. Diedrichsen, T.H.B. FitzGerald, P. Smittenaar, G. Helms, A. Lutti, and N. Weiskopf. Widespread age-related differences in the human brain microstructure revealed by quantitative magnetic resonance imaging. *Neurobiology of Aging*, 35(8):1862–1872, 2014.

A.W. Campbell. Histological studies on the localisation of cerebral function. *The British Journal of Psychiatry*, 50(211):651–662, 1904.

V. Caselles, F. Catté, T. Coll, and F. Dibos. A geometric model for active contours in image processing. *Numerische Mathematik*, 66(1):1–31, 1993.

V. Caselles, R. Kimmel, and G. Sapiro. Geodesic active contours. *International Journal of Computer Vision*, 22(1):61–79, 1997.

V. Caviness, J. Meyer, N. Makris, and D. Kennedy. MRI-based topographic parcellation of human neocortex: an anatomically specified method with estimate of reliability. *Cognitive Neuroscience, Journal of*, 8(6):566–587, 1996.

J. Charan and T. Biswas. How to calculate sample size for different study designs in medical research? *Indian Journal of Psychological Medicine*, 35(2):121, 2013.

E. Choi, B. Yeo, and R. Buckner. The organization of the human striatum estimated by intrinsic functional connectivity. *Journal of Neurophysiology*, 108(8):2242–2263, 2012.

S. Clare and H. Bridge. Methodological Issues Relating to In Vivo Cortical Myelography using MRI. *Human Brain Mapping*, 26(4):240–250, 2005.

V.P. Clark, E. Courchesne, and M. Grafe. In Vivo Myeloarchitectonic Analysis of Human Striate and Extrastriate Cortex using Magnetic Resonance Imaging. *Cerebral Cortex*, 2(5):417–424, 1992.

C. Clouchoux, O. Coulon, J.-L. Anton, J.-F. Mangin, and J. Régis. A New Cortical Surface Parcellation Model and Its Automatic Implementation. In R. Larsen, M. Nielsen, and J. Sporring, editors, *Medical Image Computing and Computer-Assisted Intervention – MICCAI 2006*, volume 4191 of *Lecture Notes in Computer Science*, pages 193–200. Springer, 2006.

C. Clouchoux, D. Riviére, J.-F. Mangin, G. Operto, J. Régis, and O. Coulon. Model-driven parameterization of the cortical surface for localization and inter-subject matching. *NeuroImage*, 50(2):552–566, 2010.

A. Cohen, D. Fair, N. Dosenbach, F. Miezin, D. Dierker, D. Van Essen, B. Schlaggar, and S. Petersen. Defining functional areas in individual human brains using resting functional connectivity MRI. *NeuroImage*, 41(1):45–57, 2008.

I. Cohen, L.D. Cohen, and N. Ayache. Using deformable surfaces to segment 3-d images and infer differential structures. *CVGIP: Image Understanding*, 56(2): 242–263, 1992.

L.D. Cohen. On active contour models and balloons. *CVGIP: Image Understanding*, 53(2):211–218, 1991.

L.D. Cohen and I. Cohen. Finite-element methods for active contour models and balloons for 2-d and 3-d images. *Pattern Analysis and Machine Intelligence, IEEE Transactions on*, 15(11):1131–1147, 1993.

J. Cohen-Adad. What can we learn from T_2^* maps of the cortex? *NeuroImage*, 93: 189–200, 2014.

J. Cohen-Adad, J.R. Polimeni, K.G. Helmer, T. Benner, J.A. McNab, L.L. Wald, B.R. Rosen, and C. Mainero. T_2^* mapping and B_0 orientation-dependence at 7T reveal cyto-and myeloarchitecture organization of the human cortex. *NeuroImage*, 60(2): 1006–1014, 2012.

M Colonnier and E Sas. An Anterograde Degeneration Study of the Tangential Spread of Axons in Cortical Areas 17 and 18 of the Squirrel Monkey (Saimiri Sciureus). *Journal of Comparative Neurology*, 179(2):245–262, 1978.

D. Coomans and D.L. Massart. Alternative k-nearest neighbour rules in supervised pattern recognition: Part 1. k-nearest neighbour classification by using alternative voting rules. *Analytica Chimica Acta*, 136:15–27, 1982a.

D. Coomans and D.L. Massart. Alternative k-nearest neighbour rules in supervised pattern recognition: Part 2. Probabilistic classification on the basis of the kNN method modified for direct density estimation. *Analytica Chimica Acta*, 138:153–165, 1982b.

C. Cortes and V. Vapnik. Support-vector networks. *Machine Learning*, 20(3):273–297, 1995.

R. Courant and D. Hilbert. *Methods of Mathematical Physics*, volume 1. New York: Interscience, 1953.

O.D. Creutzfeldt, L.J. Garey, R. Kuroda, and J.-R. Wolff. The Distribution of Degenerating Axons after Small Lesions in the Intact and Isolated Visual Cortex of the Cat. *Experimental Brain Research*, 27(3-4):419–440, 1977.

P. Croxson, H. Johansen-Berg, T. Behrens, M. Robson, M. Pinsk, C. Gross, W. Richter, M. Richter, S. Kastner, and M. Rushworth. Quantitative investigation of connections of the prefrontal cortex in the human and macaque using probabilistic diffusion tractography. *The Journal of Neuroscience*, 25(39):8854–8866, 2005.

L.F. Czervionke, J.M. Czervionke, D.L. Daniels, and V.M. Haughton. Characteristic features of MR truncation artifacts. *American Journal of Neuroradiology*, 9(5):815–824, 1988.

A.M. Dale, B. Fischl, and M.I. Sereno. Cortical Surface-Based Analysis: I. Segmentation and Surface Reconstruction. *NeuroImage*, 9(2):179–194, 1999.

J. Damoiseaux and M. Greicius. Greater than the sum of its parts: a review of studies combining structural connectivity and resting-state functional connectivity. *Brain Structure and Function*, 213(6):525–533, 2009.

F. De Martino, F. Esposito, P. Van de Moortele, N. Harel, E. Formisano, R. Goebel, K. Ugurbil, and E. Yacoub. Whole brain high-resolution functional imaging at ultra high magnetic fields: an application to the analysis of resting state networks. *NeuroImage*, 57(3):1031–1044, 2011.

A.A. de Sousa, C.C. Sherwood, A. Schleicher, K. Amunts, C.E. MacLeod, P.R. Hof, and K. Zilles. Comparative cytoarchitectural analyses of striate and extrastriate areas in hominoids. *Cerebral Cortex*, 20(4):966–981, 2010.

K. de Vos, C.W. Pool, E.J. Sanz-Arigita, and H.B.M. Uylings. Curvature effects in observer independent cytoarchitectonic mapping of the human cerebral cortex. In *Proceedings of the Second Vogt-Brodmann Symposium, Research Center Jülich, Germany*, 2004.

G. Deco and V. Jirsa. Ongoing cortical activity at rest: criticality, multistability, and ghost attractors. *The Journal of Neuroscience*, 32(10):3366–3375, 2012.

A. Deistung, A. Schäfer, F. Schweser, U. Biedermann, R. Turner, and J.R. Reichenbach. Toward in vivo histology: A comparison of quantitative susceptibility mapping (QSM) with magnitude-, phase-, and R_2^*-imaging at ultra-high magnetic field strength. *NeuroImage*, 65:299–314, 2013.

R.S. Desikan, F. Ségonne, B. Fischl, B.T. Quinn, B.C. Dickerson, D. Blacker, R.L. Buckner, A.M. Dale, R.P. Maguire, B.T. Hyman, M.S. Albert, and R.J. Killiany. An automated labeling system for subdividing the human cerebral cortex on MRI scans into gyral based regions of interest. *NeuroImage*, 31(3):968–980, 2006.

C. Destrieux, B. Fischl, A. Dale, and E. Halgren. Automatic parcellation of human cortical gyri and sulci using standard anatomical nomenclature. *NeuroImage*, 53 (1):1–15, 2010.

A. Di Martino, A. Scheres, D. Margulies, A. Kelly, L. Uddin, Z. Shehzad, B. Biswal, J. Walters, F. Castellanos, and M. Milham. Functional connectivity of human striatum: a resting state fMRI study. *Cerebral Cortex*, 18(12):2735–2747, 2008.

F. Dick, A. Tierney, A. Lutti, O. Josephs, M. Sereno, and N. Weiskopf. In Vivo Functional and Myeloarchitectonic Mapping of Human Primary Auditory Areas. *The Journal of Neuroscience*, 32(46):16095–16105, 2012.

J. Dinse, P. Martin, A. Schäfer, S. Geyer, R. Turner, and P.-L. Bazin. Quantifying Differences Between Primary Cortical Areas in Humans Based on Laminar Profiles in In-Vivo MRI Data. In H.-P. Meinzer, T.M. Deserno, H. Handels, and T. Tolxdorff, editors, *Bildverarbeitung für die Medizin 2013*, Informatik aktuell 2013, pages 39–44. Springer, 2013a.

J. Dinse, M. Waehnert, C.L. Tardif, A. Schäfer, S. Geyer, R. Turner, and P.-L. Bazin. A Histology-Based Model of Quantitative T1 Contrast for In-vivo Cortical Parcellation of High-Resolution 7 Tesla Brain MR Images. In *Medical Image Computing and Computer-Assisted Intervention–MICCAI 2013*, volume 8150 of *Lecture Notes in Computer Science*, pages 51–58. Springer, 2013b.

J.C. Dunn. A fuzzy relative of the ISODATA process and its use in detecting compact well-separated clusters. *Journal of Cybernetics*, 30:32–57, 1973.

R. Ďurikovič, K. Kaneda, and H. Yamashita. Dynamic contour: a texture approach and contour operations. *The Visual Computer*, 11(6):277–289, 1995.

H.M. Duvernoy. *The human brain: surface, three-dimensional sectional anatomy with MRI, and blood supply*. Springer Science & Business Media, 2012.

H.M. Duvernoy, E.A. Cabanis, and J.L. Vannson. *The Human Brain. Surface, Three-Dimensional Sectional Anatomy and MRI*. Springer, 1991.

J. Duyn. The future of ultra-high field MRI and fMRI for study of the human brain. *NeuroImage*, 62(2):1241–1248, 2012.

S. Eickhoff, N.B. Walters, A. Schleicher, J. Kril, G.F. Egan, K. Zilles, J.D.G. Watson, and K. Amunts. High-Resolution MRI Reflects Myeloarchitecture and Cytoarchitecture of Human Cerebral Cortex. *Human Brain Mapping*, 24(3):206–215, 2005a.

S.B. Eickhoff, K.E. Stephan, H. Mohlberg, C. Grefkes, G.R. Fink, K. Amunts, and K. Zilles. A new SPM toolbox for combining probabilistic cytoarchitectonic maps and functional imaging data. *NeuroImage*, 25(4):1325–1335, 2005b.

S.B. Eickhoff, A. Schleicher, F. Scheperjans, N. Palomero-Gallagher, and K. Zilles. Analysis of neurotransmitter receptor distribution patterns in the cerebral cortex. *NeuroImage*, 34(4):1317–1330, 2007.

M. Eltibi and W. Ashour. Initializing k-means clustering algorithm using statistical information. *International Journal of Computer Applied Technology*, 29(7):51–55, 2011.

L.J. Erasmus, D. Hurter, M. Naudé, H.G. Kritzinger, and S. Acho. A short overview of MRI artefacts: review article. *SA Journal of Radiology*, 8(2):p–13, 2004.

X. Fan, P.-L. Bazin, and J.L. Prince. A multi-compartment segmentation framework with homeomorphic level sets. In *Computer Vision and Pattern Recognition, 2008. CVPR 2008. IEEE Conference on*, pages 1–6. IEEE, 2008.

Girish M Fatterpekar, Thomas P Naidich, Bradley N Delman, Juan G Aguinaldo, S Humayun Gultekin, Chet C Sherwood, Patrick R Hof, Burton P Drayer, and Zahi A Fayad. Cytoarchitecture of the Human Cerebral Cortex: MR Microscopy of Excised Specimens at 9.4 Tesla. *American Journal of Neuroradiology*, 23(8):1313–1321, 2002.

B. Fischl, M.I. Sereno, and A.M. Dale. Cortical Surface-Based Analysis: II. Inflation, Flattening, and a Surface-Based Coordinate System. *NeuroImage*, 9(2):195–207, 1999a.

B. Fischl, M.I. Sereno, R.B.H. Tootell, A.M. Dale, et al. High-Resolution Intersubject Averaging and a Coordinate System for the Cortical Surface. *Human Brain Mapping*, 8(4):272–284, 1999b.

B. Fischl, D.H. Salat, A.J.W. van der Kouwe, N. Makris, F. Ségonne, B.T. Quinn, and A.M. Dale. Sequence-independent segmentation of magnetic resonance images. *NeuroImage*, 23:S69–S84, 2004a.

B. Fischl, A. Van Der Kouwe, C. Destrieux, E. Halgren, F. Ségonne, D.H. Salat, E. Busa, L.J. Seidman, J. Goldstein, D. Kennedy, V. Caviness, N. Makris, R. Bruce, and A.M. Dale. Automatically Parcellating the Human Cerebral Cortex. *Cerebral Cortex*, 14(1):11–22, 2004b.

B. Fischl, N. Rajendran, E. Busa, J. Augustinack, O. Hinds, BT Yeo, H. Mohlberg, K. Amunts, and K. Zilles. Cortical Folding Patterns and Predicting Cytoarchitecture. *Cerebral Cortex*, 18(8):1973–1980, 2008.

M.A. Fischler and R.A. Elschlager. The representation and matching of pictorial structures. *IEEE Transactions on Computers*, 22(1):67–92, 1973.

P.E. Flechsig. *Anatomie des menschlichen Gehirns und Rückenmarks auf myelogenetischer Grundlage*, volume 1. G. Thieme, 1920.

N.E.V. Foster and R.J. Zatorre. Cortical structure predicts success in performing musical transformation judgments. *NeuroImage*, 53(1):26–36, 2010.

A.F. Frangi, W.J. Niessen, K.L. Vincken, and M.A. Viergever. Multiscale vessel enhancement filtering. In *Medical Image Computing and Computer-Assisted Interventation-MICCAI'98*, pages 130–137. Springer, 1998.

M. Fukunaga, T. Li, P. van Gelderen, J.A. de Zwart, K. Shmueli, B. Yao, J. Lee, D. Maric, M.A. Aronova, G. Zhang, R.D. Leapman, J.F. Schenck, H Merkle, and J.H. Duyn. Layer-specific variation of iron content in cerebral cortex as a source of MRI contrast. *Proceedings of the National Academy of Sciences*, 107(8):3834–3839, 2010.

K.C. Gatter, J.J. Sloper, and T.P. Powell. The intrinsic connections of the cortex of area 4 of the monkey. *Brain*, 101(3):513–541, 1978.

D. Geiger, A. Gupta, L.A. Costa, and J. Vlontzos. Dynamic programming for detecting, tracking, and matching deformable contours. *Pattern Analysis and Machine Intelligence, IEEE Transactions on*, 17(3):294–302, 1995.

M. Gerlach, D. Ben-Shachar, P. Riederer, and M. Youdim. Altered brain metabolism of iron as a cause of neurodegenerative diseases? *Journal of Neurochemistry*, 63 (3):793–807, 1994.

E. Geuze, H.G.M. Westenberg, A. Heinecke, C.S. de Kloet, R. Goebel, and E. Vermetten. Thinner prefrontal cortex in veterans with posttraumatic stress disorder. *NeuroImage*, 41(3):675–681, 2008.

S. Geyer and R. Turner. *Microstructural Parcellation of the Human Cerebral Cortex*. Springer, 2013.

S. Geyer, A. Schleicher, and K. Zilles. Areas 3a, 3b, and 1 of Human Primary Somatosensory Cortex: 1. Microstructural Organization and Interindividual Variability. *NeuroImage*, 10(1):63–83, 1999.

S. Geyer, M. Weiss, K. Reimann, G. Lohmann, and R. Turner. Microstructural Parcellation of the Human Cerebral Cortex–From Brodmann's Post-Mortem Map to in vivo Mapping with High-Field Magnetic Resonance Imaging. *Frontiers in Human Neuroscience*, 5, 2011.

Matthew F Glasser, Manu S Goyal, Todd M Preuss, Marcus E Raichle, and David C Van Essen. Trends and properties of human cerebral cortex: correlations with cortical myelin content. *Neuroimage*, 93:165–175, 2014.

M.F. Glasser and D.C. Van Essen. Mapping Human Cortical Areas In Vivo based on Myelin Content as Revealed by T1-and T2-Weighted MRI. *The Journal of Neuroscience*, 31(32):11597–11616, 2011.

A. Goulas, H. Uylings, and P. Stiers. Unravelling the intrinsic functional organization of the human lateral frontal cortex: a parcellation scheme based on resting state fMRI. *The Journal of Neuroscience*, 32(30):10238–10252, 2012.

W. Graumann and D. Sasse. *Compact Lehrbuch Anatomie: in 4 Bänden*, volume 2. Schattauer Verlag, 2005.

H. Gray. *Anatomy of the human body*. Lea & Febiger, 1918.

M.A. Grayson. Shortening embedded curves. *Annals of Mathematics*, pages 71–111, 1989.

C. Grefkes, S. Geyer, T. Schormann, P. Roland, and K. Zilles. Human Somatosensory Area 2: Observer-Independent Cytoarchitectonic Mapping, Interindividual Variability, and Population Map. *NeuroImage*, 14(3):617–631, 2001. doi: 10.1006/nimg.2001.0858.

A. Gustavsson, M. Svensson, F. Jacobi, C. Allgulander, J. Alonso, E. Beghi, R. Dodel, M. Ekman, C. Faravelli, L. Fratiglioni, et al. Cost of disorders of the brain in europe 2010. *European Neuropsychopharmacology*, 21(10):718–779, 2011.

M. Guye, G. Parker, M. Symms, P. Boulby, C. Wheeler-Kingshott, A. Salek-Haddadi, G. Barker, and J. Duncan. Combined functional MRI and tractography to demonstrate the connectivity of the human primary motor cortex in vivo. *NeuroImage*, 19(4):1349–1360, 2003.

H. Haidar and J.S. Soul. Measurement of Cortical Thickness in 3D Brain MRI Data: Validation of the Laplacian Method. *Journal of Neuroimaging*, 16(2):146–153, 2006.

J. Hale, M. Brookes, E. Hall, J. Zumer, C. Stevenson, S. Francis, and P. Morris. Comparison of functional connectivity in default mode and sensorimotor networks at 3 and 7T. *Magnetic Resonance Materials in Physics, Biology and Medicine*, 23(5-6): 339–349, 2010.

B. Hallgren and P. Sourander. The effect of age on the non-haemin iron in the human brain. *Journal of Neurochemistry*, 3(1):41–51, 1958.

C. Hammarberg. *Studien über Klinik und Pathologie der Idiotie, nebst Untersuchungen über die normale Anatomie der Hirnrinde*. Berling, Akademische Buchdruckerie, Upsala, 1895.

X. Han, C. Xu, and J.L. Prince. A Topology Preserving Level Set Method for Geometric Deformable Models. *Pattern Analysis and Machine Intelligence, IEEE Transactions on*, 25(6):755–768, 2003.

X. Han, D.L. Pham, D. Tosun, M.E. Rettmann, C. Xu, and J.L. Prince. CRUISE: Cortical reconstruction using implicit surface evolution. *NeuroImage*, 23(3):997–1012, 2004.

M. Hearst, S. Dumais, E. Osman, J. Platt, and B. Schölkopf. Support vector machines. *Intelligent Systems and their Applications, IEEE*, 13(4):18–28, 1998.

B. Hellwig. How the Myelin Picture of the Human Cerebral Cortex can be computed from Cytoarchitectural Data. A Bridge between von Economo and Vogt. *Journal für Hirnforschung*, 34(3):387–402, 1993.

G. Henderson, B.E. Tomlinson, and P.H. Gibson. Cell Counts in Human Cerebral Cortex in Normal Adults Throughout Life using an Image Analysing Computer. *Journal of the Neurological Sciences*, 46(1):113–136, 1980.

C.C. Henery and T.M. Mayhew. The cerebrum and cerebellum of the fixed human brain: efficient and unbiased estimates of volumes and cortical surface areas. *Journal of Anatomy*, 167:167–180, 1989.

K. Heuer, R. Schurade, J. Böttger, D.S. Margulies, T.R. Knösche, A.D. Friederici, and A. Anwander. Browsing the connectome: 3D functional and structural brainnetworks in the cloud. In *20th Annual Meeting of the Organization for Human Brain Mapping (OHBM)*, 2014.

O. Hinds, N. Rajendran, J. Polimeni, J. Augustinack, G. Wiggins, L. Wald, H. Rosas, A. Potthast, E. Schwartz, and B. Fischl. Accurate prediction of V1 location from cortical folds in a surface coordinate system. *NeuroImage*, 39(4):1585–1599, 2008.

O. Hinds, J.R. Polimeni, N. Rajendran, M. Balasubramanian, K. Amunts, K. Zilles, E.L. Schwartz, B. Fischl, and C. Triantafyllou. Locating the functional and anatomical boundaries of human primary visual cortex. *NeuroImage*, 46(4):915–922, 2009.

L.J. Hogstrom, L.T. Westlye, K.B. Walhovd, and A.M. Fjell. The Structure of the Cerebral Cortex Across Adult Life: Age-Related Patterns of Surface Area, Thickness, and Gyrification. *Cerebral Cortex*, 23(11):2521–2530, 2013.

A. Hopf. Über die Verteilung myeloarchitektonischer Merkmale in der isokortikalen Schläfenlappenrinde beim Menschen. *Journal für Hirnforschung*, 2(1):36–54, 1955.

A. Hopf. Über die Verteilung myeloarchitektonischer Merkmale in der Stirnhirnrinde beim Menschen. *Journal für Hirnforschung*, 2(4):311–333, 1956.

A Hopf. Registration of the Myeloarchitecture of the Human Frontal Lobe with an Extinction Method. *Journal für Hirnforschung*, 10(3):259–269, 1967.

A Hopf. Photometric studies on the myeloarchitecture of the human temporal lobe. *Journal für Hirnforschung*, 10(4):285–297, 1968.

A Hopf. Photometric studies on the myeloarchitecture of the human parietal lobe. I. Parietal region. *Journal für Hirnforschung*, 11(4):253–265, 1969.

A. Hopf. Photometric studies on the myeloarchitecture of the human parietal lobe. II. Postcentral region. *Journal für Hirnforschung*, 12(1):135–141, 1970.

A. Hopf and H. Gräfin Vitzthum. Über die Verteilung myeloarchitektonischer Merkmale in der Scheitellappenrinde beim Menschen. *Journal für Hirnforschung*, 3(2/3):79–104, 1957.

L. Huber, J. Goense, A.J. Kennerley, R. Trampel, M. Guidi, E. Reimer, D. Ivanov, N. Neef, C.J. Gauthier, R. Turner, and H. Möller. Cortical lamina-dependent blood volume changes in human brain at 7T. *NeuroImage*, 2014.

L. Huber, J. Goense, A. Kennerly, R. Trampel, M. Guidi, D. Ivanov, N. Neef, C. Gauthier, R. Turner, and H. Möller. Cortical lamina-dependent blood volume changes in human brain at 7 T. *NeuroImage*, 107:22–33, 2015.

A.C. Hurley, A. Al-Radaideh, L. Bai, U. Aickelin, R. Coxon, P. Glover, and P.A. Gowland. Tailored RF pulse for Magnetization Inversion at Ultrahigh Field. *Magnetic Resonance in Medicine*, 63(1):51–58, 2010.

J.B. Hursh. Conduction velocity and diameter of nerve fibers. *American Journal of Physiology*, 127(9), 1939.

C. Hutton, E. De Vita, J. Ashburner, R. Deichmann, and R. Turner. Voxel-based cortical thickness measurements in MRI. *NeuroImage*, 40(4):1701, 2008.

K. Im, J. Lee, J. Lee, Y. Shin, I. Kim, J. Kwon, and S. Kim. Gender difference analysis of cortical thickness in healthy young adults with surface-based methods. *NeuroImage*, 31(1):31–38, 2006.

C. Jäger, D. Lendvai, G. Seeger, G. Brückner, R.T. Matthews, T. Arendt, A. Alpar, and M. Morawski. Perineuronal and perisynaptic extracellular matrix in the human spinal cord. *Neuroscience*, 238:168–184, 2013.

M. Jenkinson and S. Smith. A global optimisation method for robust affine registration of brain images. *Medical Image Analysis*, 5(2):143–156, 2001.

H. Johansen-Berg and T.E.J. Behrens. Diffusion MRI: From Quantitative Measurement to In vivo Neuroanatomy, 2009.

H. Johansen-Berg, T.E.J. Behrens, M.D. Robson, I. Drobnjak, M.F.S. Rushworth, J.M. Brady, S.M. Smith, D.J. Higham, and P.M. Matthews. Changes in connectivity profiles define functionally distinct regions in human medial frontal cortex. *Proceedings of the National Academy of Sciences of the United States of America*, 101(36): 13335–13340, 2004.

H. Johansen-Berg, T.E.J. Behrens, E. Sillery, O. Ciccarelli, A.J. Thompson, S. M. Smith, and P.M. Matthews. Functional-Anatomical Validation and Individual Variation of Diffusion Tractography-based Segmentation of the Human Thalamus. *Cerebral Cortex*, 15(1):31–39, 2005.

S.C. Johnson. Hierarchical clustering schemes. *Psychometrika*, 32(3):241–254, 1967.

D.K. Jones and A. Leemans. Diffusion tensor imaging. In *Magnetic Resonance Neuroimaging*, pages 127–144. Springer, 2011.

S.E. Jones, B.R. Buchbinder, and I. Aharon. Three-dimensional mapping of cortical thickness using Laplace's Equation. *Human Brain Mapping*, 11(1):12–32, 2000.

J. Karbowski. How does connectivity between cortical areas depend on brain size? Implications for efficient computation. *Journal of Computational Neuroscience*, 15 (3):347–356, 2003.

M. Kass, A. Witkin, and D. Terzopoulos. Snakes: Active Contour Models. *International Journal of Computer Vision*, 1(4):321–331, 1988.

D.N. Kennedy, N. Lange, N. Makris, J. Bates, J. Meyer, and V.S. Caviness. Gyri of the human neocortex: an MRI-based analysis of volume and variance. *Cerebral Cortex*, 8(4):372–384, 1998.

R. Khan, Q. Zhang, S. Darayan, S. Dhandapani, S. Katyal, C. Greene, C. Bajaj, and D. Ress. Surface-based analysis methods for high-resolution functional magnetic resonance imaging. *Graphical Models*, 73(6):313–322, 2011.

J. Kim, J. Lee, H. Jo, S. Kim, J. Lee, S. Kim, S. Seo, R. Cox, D. Na, S. Kim, and Z. Saad. Defining functional SMA and pre-SMA subregions in human MFC using resting state fMRI: functional connectivity-based parcellation method. *NeuroImage*, 49 (3):2375–2386, 2010.

B.B. Kimia, A. Tannenbaum, and S.W. Zucker. *Toward a computational theory of shape: An overview*. Springer, 1990.

B.B. Kimia, A.R. Tannenbaum, and S.W. Zucker. Shapes, shocks, and deformations i: the components of two-dimensional shape and the reaction-diffusion space. *International Iournal of Computer Vision*, 15(3):189–224, 1995.

R. Kimmel, A. Amir, and A.M. Bruckstein. Finding shortest paths on surfaces using level sets propagation. *Pattern Analysis and Machine Intelligence, IEEE Transactions on*, 17(6):635–640, 1995.

J.C. Klein, T.E.J. Behrens, M.D. Robson, C.E. Mackay, D.J. Higham, and H. Johansen-Berg. Connectivity-based parcellation of human cortex using diffusion MRI: Establishing reproducibility, validity and observer independence in BA 44/45 and SMA/pre-SMA. *NeuroImage*, 34(1):204–211, 2007.

V.A. Klyachko and C.F. Stevens. Connectivity optimization and the positioning of cortical areas. *Proceedings of the National Academy of Sciences*, 100(13):7937–7941, 2003.

S.H. Koenig. Cholesterol of myelin is the determinant of gray-white contrast in MRI of brain. *Magnetic Resonance in Medicine*, 20(2):285–291, 1991.

D. Le Bihan, J.-F. Mangin, C. Poupon, C.A. Clark, S. Pappata, N. Molko, and Hughes Chabriat. Diffusion tensor imaging: concepts and applications. *Journal of Magnetic Resonance Imaging*, 13(4):534–546, 2001.

G. Le Goualher, E. Procyk, D. L. Collins, R. Venugopal, C. Barillot, and A.C. Evans. Automated extraction and variability analysis of sulcal neuroanatomy. *Medical Imaging, IEEE Transactions on*, 18(3):206–217, 1999.

W.E. Le Gros Clark and S. Sunderland. Structural changes in the isolated visual cortex. *Journal of Anatomy*, 73(4):563–574, 1939.

Y. Leprince, C. Fischer, J.-F. Mangin, B. Larrat, S. Meriaux, C. Poupon, I. Reillo, V. Borrell, O. Foubet, R. Toro, and D. Riviere. Architectonics-informed partition of the cortex at sub-millimetre resolution. *Proceedings of the 20th Annual Meeting of the Organization for Human Brain Mapping*, 2014.

W.B Lewis. On the Comparative Structure of the Cortex Cerebri. *Brain*, 1(1):79–96, 1878.

W.B. Lewis. Researches on the comparative structure of the cortex cerebri. *Philosophical Transactions of the Royal Society of London*, 171:35–64, 1880.

G. Li, L. Guo, J. Nie, and T. Liu. Automatic cortical sulcal parcellation based on surface principal direction flow field tracking. *NeuroImage*, 46(4):923–937, 2009.

P. Lintl and H. Braak. Loss of intracortical myelinated fibers: a distinctive age-related alteration in the human striate area. *Acta neuropathologica*, 61(3-4):178–182, 1983.

S. Lobregt and M.A. Viergever. A discrete dynamic contour model. *Medical Imaging, IEEE Transactions on*, 14(1):12–24, 1995.

G. Lohmann. Extracting line representations of sulcal and gyral patterns in MR images of the human brain. *Medical Imaging, IEEE Transactions on*, 17(6):1040–1048, 1998.

G. Lohmann and D.Y. von Cramon. Automatic labelling of the human cortical surface using sulcal basins. *Medical Image Analysis*, 4(3):179–188, 2000.

Lohmann, G. and von Cramon, D. and Colchester, A. Deep Sulcal Landmarks Provide an Organizing Framework for Human Cortical Folding. *Cerebral Cortex*, 18(6):1415–1420, 2008.

H. Lu, L.M. Nagae-Poetscher, X. Golay, D. Lin, M. Pomper, and P. van Zijl. Routine clinical brain MRI sequences for use at 3.0 Tesla. *Journal of Magnetic Resonance Imaging*, 22(1):13–22, 2005.

B.C. Lucas, J.A. Bogovic, A. Carass, P.-L. Bazin, J.L. Prince, D.L. Pham, and B.A. Landman. The Java Image Science Toolkit (JIST) for Rapid Prototyping and Publishing of Neuroimaging Software. *Neuroinformatics*, 8(1):5–17, 2010.

A. Lutti, F. Dick, M.I. Sereno, and N. Weiskopf. Using high-resolution quantitative mapping of R_1 as an index of cortical myelination. *NeuroImage*, 93:176–188, 2014.

J. MacQueen. Some methods for classification and analysis of multivariate observations. In *Proceedings of the fifth Berkeley symposium on mathematical statistics and probability*, volume 1, pages 281–297. California, USA, 1967.

J.E. Makris, N and. Schlerf, S.M. Hodge, C. Haselgrove, M.D. Albaugh, L.J. Seidman, S.L. Rauch, G. Harris, J. Biederman, V.S. Caviness Jr, D.N. Kennedy, and J.D. Schmahmann. MRI-based surface-assisted parcellation of human cerebellar cortex: An anatomically specified method with estimate of reliability. *NeuroImage*, 25(4):1146–1160, 2005.

N. Makris, J. Kaiser, C. Haselgrove, L.J. Seidman, J. Biederman, D. Boriel, E.M. Valera, G.M. Papadimitriou, B. Fischl, V.S. Caviness Jr, and D.N. Kennedy. Human cerebral cortex: A system for the integration of volume-and surface-based representations. *NeuroImage*, 33(1):139–153, 2006.

A. Malikovic, K. Amunts, A. Schleicher, H. Mohlberg, S.B. Eickhoff, M. Wilms, N. Palomero-Gallagher, E. Armstrong, and K. Zilles. Cytoarchitectonic analysis of the human extrastriate cortex in the region of V5/MT+: a probabilistic, stereotaxic map of area hOc5. *Cerebral Cortex*, 17(3):562–574, 2007.

R. Malladi, J.A. Sethian, and B.C. Vemuri. Shape modeling with front propagation: A level set approach. *Pattern Analysis and Machine Intelligence, IEEE Transactions on*, 17(2):158–175, 1995.

J.-F. Mangin, V. Frouin, I. Bloch, J. Régis, and J. López-Krahe. From 3D magnetic resonance images to structural representations of the cortex topography using topology preserving deformations. *Journal of Mathematical Imaging and Vision*, 5 (4):297–318, 1995.

J.P. Marques and R. Gruetter. New Developments and Applications of the MP2RAGE Sequence - Focusing the Contrast and High Spatial Resolution R_1 Mapping. *PloS one*, 8(7):e69294, 2013. doi: 10.1371/journal.pone.0069294.

J.P. Marques, T. Kober, G. Krueger, W. van der Zwaag, P.F. Van de Moortele, and R. Gruetter. MP2RAGE, a self bias-field corrected sequence for improved segmentation and T_1-mapping at high field. *NeuroImage*, 49(2):1271–1281, 2010.

R. Mars, S. Jbabdi, J. Sallet, J. O'Reilly, P. Croxson, E. Olivier, M. Noonan, C. Bergmann, A. Mitchell, M. Baxter, et al. Diffusion-weighted imaging tractography-based parcellation of the human parietal cortex and comparison with human and macaque resting-state functional connectivity. *The Journal of Neuroscience*, 31(11):4087–4100, 2011.

T. Mauss. Die faserarchitektonische Gliederung des Cortex cerebri der anthropomorphen Affen. *J Psychol Neurol*, 18:410–467, 1911.

J. Mayhew. Sedation for MRI. *Pediatric Anesthesia*, 15(10):900–900, 2005.

M. McAuliffe, F. Lalonde, D. McGarry, W. Gandler, K. Csaky, and B. Trus. Medical image processing, analysis and visualization in clinical research. In *Computer-Based Medical Systems, 2001. CBMS 2001. Proceedings. 14th IEEE Symposium on*, pages 381–386. IEEE, 2001.

T. McInerney and D. Terzopoulos. A dynamic finite element surface model for segmentation and tracking in multidimensional medical images with application

to cardiac 4D image analysis. *Computerized Medical Imaging and Graphics*, 19(1): 69–83, 1995a.

T. McInerney and D. Terzopoulos. Topologically adaptable snakes. In *Computer Vision, 1995. Proceedings., Fifth International Conference on*, pages 840–845. IEEE, 1995b.

G. McLachlan and D. Peel. *Finite mixture models*. John Wiley & Sons, 2004.

MedlinePlus. *Degenerative Nerve Diseases*. National Institute of Health, 2014. URL http://www.nlm.nih.gov/medlineplus/degenerativenervediseases.html.

A. Merbach and E. Tóth. *The chemistry of contrast agents in medical magnetic resonance imaging*, volume 46. Wiley Online Library, 2001.

T.H. Meynert. Neue Untersuchungen über den Bau der Grosshirnrinde und ihre örtlichen Verschiedenheiten. *Allgemeine Wiener Medizinische Zeitung*, 13:419–428, 1868.

M.I. Miller, G.E. Christensen, Y. Amit, and U. Grenander. Mathematical textbook of deformable neuroanatomies. *Proceedings of the National Academy of Sciences*, 90 (24):11944–11948, 1993.

E.M. Mirkes. K-NN and Potential Energy. University of Leicester, 2011. URL http://www.math.le.ac.uk/people/ag153/homepage/KNN/KNN3.html.

T. Moon. The expectation-maximization algorithm. *Signal Processing Magazine, IEEE*, 13(6):47–60, 1996.

A. Moore. The Andrew Moore Tutorial slides. 2001. URL http://www.autonlab.org/tutorials/gmm14.pdf.

D.A. Mouritzen. Shrinkage of the brain during histological procedures with fixation in formaldehyde solutions of different concentrations. *Journal für Hirnforschung*, 20(2):115–119, 1978.

M. Mulisch and U. Welsch, editors. *Romeis - Mikroskopische Technik*. Springer, 18th edition, 2010.

Z. Nagy, H. Lagercrantz, and C. Hutton. Effects of preterm birth on cortical thickness measured in adolescence. *Cerebral Cortex*, 21(2):300–306, 2011.

Z. Nagy, D. Alexander, D. Thomas, N. Weiskopf, and M. Sereno. Using high angular resolution diffusion imaging data to discriminate cortical regions. *PloS one*, 8(5):e63842, 2013.

L. Nanetti, L. Cerliani, V. Gazzola, R. Renken, and C. Keysers. Group analyses of connectivity-based cortical parcellation using repeated k-means clustering. *NeuroImage*, 47(4):1666–1677, 2009.

C. Nastar and N. Ayache. Frequency-based nonrigid motion analysis: Application to four dimensional medical images. *Pattern Analysis and Machine Intelligence, IEEE Transactions on*, 18(11):1067–1079, 1996.

R. Nieuwenhuys. The myeloarchitectonic studies on the human cerebral cortex of the Vogt–Vogt school, and their significance for the interpretation of functional neuroimaging data. *Brain Structure and Function*, 218(2):303–352, 2013.

R. Nieuwenhuys, C.A.J. Broere, and L. Cerliani. A new myeloarchitectonic map of the human neocortex based on data from the Vogt–Vogt school. *Brain Structure and Function*, pages 1–23, 2014.

C.A. Olman, N. Harel, D.A. Feinberg, S. He, P. Zhang, K. Ugurbil, and E. Yacoub. Layer-specific fMRI reflects different neuronal computations at different depths in human V1. *PLoS ONE*, 7(3):e32536, 03 2012.

M. Ono, S. Kubik, and C.D. Abernathey. *Atlas of the cerebral sulci*. Thieme, 1990.

B. Pakkenberg and H. J.G. Gundersen. Neocortical neuron number in humans: effect of sex and age. *Journal of Comparative Neurology*, 384(2):312–320, 1997.

B. Pakkenberg, D. Pelvig, L. Marner, M.J. Bundgaard, H.J.G. Gundersen, J.R. Nyengaard, and L. Regeur. Aging and the human neocortex. *Experimental Gerontology*, 38(1):95–99, 2003.

AM Paldino and E. Harth. Some quantitative results on golgi impregnated axons in rat visual cortex using a computer assisted video digitizer. *The Journal of comparative neurology*, 176(2):247–261, 1977.

H.-J. Park, J.J. Kim, S.-K. Lee, J.H. Seok, J. Chun, D.I. Kim, and J.D. Lee. Corpus callosal connection mapping using cortical gray matter parcellation and DT-MRI. *Human Brain Mapping*, 29(5):503–516, 2008.

J. Pena, J. Lozano, and P. Larranaga. An empirical comparison of four initialization methods for the k-means algorithm. *Pattern Recognition Letters*, 20(10):1027–1040, 1999.

A. Peters. The effects of normal aging on myelin and nerve fibers: a review. *Journal of Neurocytology*, 31(8-9):581–593, 2002.

D.L. Pham and J.L. Prince. Adaptive fuzzy segmentation of magnetic resonance images. *IEEE Transactions on Medical Imaging*, 18(9):737–752, 1999.

J.R. Polimeni, B. Fischl, and D. Greve. Laminar-specific functional connectivity: distinguishing directionality in cortical networks. In *Proceedings of the 16th Annual Meeting of the Organization for Human Brain Mapping*, 2010a.

J.R. Polimeni, B. Fischl, D.N. Greve, and L.L. Wald. Laminar analysis of 7T BOLD using an imposed spatial activation pattern in human V1. *NeuroImage*, 52(4): 1334–1346, 2010b.

C.S. Poon and M. Braun. Image segmentation by a deformable contour model incorporating region analysis. *Physics in Medicine and Biology*, 42(9):1833, 1997.

C. Preibisch and R. Deichmann. Influence of RF spoiling on the stability and accuracy of T_1 mapping based on spoiled FLASH with varying flip angles. *Magnetic Resonance in Medicine*, 61(1):125–135, 2009.

O. Querbes, F. Aubry, J. Pariente, J. Lotterie, J. Démonet, V. Duret, M. Puel, I. Berry, J. Fort, P. Celsis, and The Alzheimer's Disease Neuroimaging Initiative. Early diagnosis of alzheimer's disease using cortical thickness: impact of cognitive reserve. *Brain*, 132(8):2036–2047, 2009.

M.E. Rettmann, X. Han, C. Xu, and J.L. Prince. Automated Sulcal Segmentation Using Watersheds on the Cortical Surface. *NeuroImage*, 15(2):329–344, 2002.

J.L. Ringo. Neuronal interconnection as a function of brain size. *Brain, Behavior and Evolution*, 38(1):1–6, 1991.

J.L. Ringo, R.W. Doty, S. Demeter, and P.Y. Simard. Time is of the essence: a conjecture that hemispheric specialization arises from interhemispheric conduction delay. *Cerebral Cortex*, 4(4):331–343, 1994.

D. Riviere, J. Mangin, D. Papadopoulos-Orfanos, J. Martinez, V. Frouin, and J. Régis. Automatic recognition of cortical sulci of the human brain using a congregation of neural networks. *Medical Image Analysis*, 6(2):77–92, 2002.

E.C. Robinson, S. Jbabdi, J.L.R. Andersson, S.M. Smith, M.F. Glasser, D.C. Van Essen, G.C. Burgess, M.P. Harms, D.M. Barch, and M. Jenkinson. Multimodal Surface Matching: Fast and Generalisable Cortical Registration Using Discrete Optimisation. In J.C. Gee, S. Joshi, K.M. Pohl, W.M. Wells, and L. Zöllei, editors, *Information Processing in Medical Imaging*, volume 7917 of *Lecture Notes in Computer Science*, pages 475–486. Springer, 2013.

R. Ronfard. Region-based strategies for active contour models. *International Journal of Computer Vision*, 13(2):229–251, 1994.

W.D. Rooney, G. Johnson, X. Li, E.R. Cohen, S.G. Kim, K. Ugurbil, and C.S. Springer. Magnetic Field and Tissue Dependencies of Human Brain Longitudinal ^1H_2O Relaxation In Vivo. *Magnetic Resonance in Medicine*, 57(2):308–318, 2007.

M. Ruschel, T. Knösche, A. Friederici, R. Turner, S. Geyer, and A. Anwander. Connectivity architecture and subdivision of the human inferior parietal cortex revealed by diffusion MRI. *Cerebral Cortex*, 24(9):2436–2448, 2014.

R.M. Sánchez-Panchuelo, S.T. Francis, D. Schluppeck, and R.W. Bowtell. Correspondence of human visual areas identified using functional and anatomical MRI in vivo at 7 T. *Journal of Magnetic Resonance Imaging*, 35(2):287–299, 2012.

F. Sanides. *Die Architektonik des menschlichen Stirnhirns: zugleich eine Darstellung der Prinzipien seiner Gestaltung als Spiegel der stammesgeschichtlichen Differenzierung der Grosshirnrinde*. Springer, 1962.

A. Schleicher, K. Amunts, S. Geyer, P. Morosan, and K. Zilles. Observer-Independent Method for Microstructural Parcellation of Cerebral Cortex: A Quantitative Approach to Cytoarchitectonics. *NeuroImage*, 9(1):165–177, 1999.

A. Schleicher, K. Amunts, S. Geyer, T. Kowalski, T. Schormann, N. Palomero-Gallagher, and K. Zilles. A stereological approach to human cortical architecture:

identification and delineation of cortical areas. *Journal of Chemical Neuroanatomy*, 20(1):31–47, 2000.

A. Schleicher, N. Palomero-Gallagher, P. Morosan, S.B. Eickhoff, T. Kowalski, K. Vos, K. Amunts, and K. Zilles. Quantitative architectural analysis: a new approach to cortical mapping. *Anatomy and Embryology*, 210(5):373–386, 2005.

J. Schulz, T. Siegert, E. Reimer, C. Labadie, J. Maclaren, M. Herbst, M. Zaitsev, and R. Turner. An embedded optical tracking system for motion-corrected magnetic resonance imaging at 7T. *Magnetic Resonance Materials in Physics, Biology and Medicine*, 25(6):443–453, 2012.

R. Schweizer, G. Helms, and J. Frahm. Revisiting a historic human brain with magnetic resonance imaging–the first description of a divided central sulcus. *Frontiers in Neuroanatomy*, 8, 2014.

M. Sereno, A. Lutti, N. Weiskopf, and F. Dick. Mapping the Human Cortical Surface by Combining Quantitative T_1 with Retinotopy. *Cerebral Cortex*, 23(9): 2261–2268, 2012.

J.A. Sethian. Curvature and the evolution of fronts. *Communications in Mathematical Physics*, 101(4):487–499, 1985.

J.A. Sethian. A fast marching level set method for monotonically advancing fronts. *Proceedings of the National Academy of Sciences*, 93(4):1591–1595, 1996.

J.A. Sethian. *Level set methods and fast marching methods: evolving interfaces in computational geometry, fluid mechanics, computer vision, and materials science*. Number 3. Cambridge University Press, 1999.

R. Sharma. 21 Tesla MRI of Mouse Brain: Structural Segmentation and Volumetrics. *Nanotechnology Research Journal*, 2(2):33–38, 2009.

N. Shental, A. Bar-Hillel, T. Hertz, and D. Weinshall. Computing Gaussian mixture models with EM using equivalence constraints. *Advances in Neural Information Processing Systems*, 16(8):465–472, 2004.

Y. Shi, P.M. Thompson, I. Dinov, and A.W. Toga. Hamilton-Jacobi Skeleton on Cortical Surfaces. *Medical Imaging, IEEE Transactions on*, 27(5):664–673, 2008.

K. Siddiqi, S. Bouix, A. Tannebaum, and S.W. Zucker. Hamilton-jacobi skeletons. *International Journal of Computer Vision*, 48(3):215–231, 2002.

I.S. Sigalovsky, B. Fischl, and J.R. Melcher. Mapping an intrinsic MR property of gray matter in auditory cortex of living humans: a possible marker for primary cortex and hemispheric differences. *NeuroImage*, 32(4):1524–1537, 2006.

G.E. Smith. A new Topographical Survey of the Human Cerebral Cortex, being an account of the Distribution of the Anatomically Distinct Cortical Areas and their Relationship to the Cerebral Sulci. *Journal of Anatomy and Physiology*, 41(Pt 4):237–254, 1907.

J. Sobotta and J. Playfair McMurrich. Atlas and text-book of human anatomy. volume iii. *Annals of Surgery*, 48(2):318, 1908.

K. Somasundaram and P. Kalavathi. Analysis of imaging artifacts in MR brain images. *Orient. J. Comput. Sci. Technol*, 5:135–141, 2012.

M. Strenziok, F. Krueger, A. Heinecke, R.K. Lenroot, K.M. Knutson, E. van der Meer, and J. Grafman. Developmental effects of aggressive behavior in male adolescents assessed with structural and functional brain imaging. *Social Cognitive and Affective Neuroscience*, 6(1):2–11, 2011.

C. Stüber, M. Morawski, A. Schäfer, C. Labadie, M. Wähnert, C. Leuze, M. Streicher, N. Barapatre, K. Reimann, S. Geyer, D. Spemann, and R. Turner. Myelin and iron concentration in the human brain: A quantitative study of MRI contrast. *NeuroImage*, 93:95–106, 2014.

C. Stueber, M. Morawski, K. Reimann, N. Barapatre, S. Geyer, and R. Turner. Iron, Ferritin, Myelin and MR-Contrast: Proton-Induced X-Ray Emission (PIXE) Maps of Cortical Iron Content . *Proceedings of the 19th Annual Meeting of the International Society for Magnetic Resonance in Medicine*, 2011.

C.L. Tardif, J. Dinse, A. Schäfer, R. Turner, and P.-L. Bazin. Multi-modal Surface-Based Alignment of Cortical Areas Using Intra-Cortical T1 Contrast. In L. Shen, T. Liu, P.-T. Yap, H. Huang, D. Shen, and C.-F. Westin, editors, *Multimodal Brain Image Analysis*, volume 8159, pages 222–232. Springer, 2013.

H. Tek and B.B. Kimia. Volumetric segmentation of medical images by three-dimensional bubbles. In *Physics-Based Modeling in Computer Vision, 1995., Proceedings of the Workshop on*, page 9. IEEE, 1995.

D. Teraopoulos. On matching deformable models to images. *Topical Meeting on Machine Vision, Technical Digest Series*, 12:160–167, 1987.

G.R. Terrell and D.W. Scott. Variable kernel density estimation. *The Annals of Statistics*, pages 1236–1265, 1992.

R.D. Terry, R. DeTeresa, and L.A. Hansen. Neocortical Cell Counts in Normal Human Adult Aging. *Annals of Neurology*, 21(6):530–539, 1987.

D. Terzopoulos and K. Fleischer. Deformable models. *The Visual Computer*, 4(6): 306–331, 1988.

D. Terzopoulos, A. Witkin, and M. Kass. Constraints on deformable models: Recovering 3D shape and nonrigid motion. *Artificial Intelligence*, 36(1):91–123, 1988.

D.L. Thomas, E. De Vita, R. Deichmann, R. Turner, and R.J. Ordidge. 3D MDEFT imaging of the human brain at 4.7 T with reduced sensitivity to radiofrequency inhomogeneity. *Magnetic Resonance in Medicine*, 53(6):1452–1458, 2005.

V. Tomassini, S. Jbabdi, J.C. Klein, T.E.J. Behrens, C. Pozzilli, P.M. Matthews, M.F.S. Rushworth, and H. Johansen-Berg. Diffusion-Weighted Imaging Tractography-Based Parcellation of the Human Lateral Premotor Cortex Identifies Dorsal and

Ventral Subregions with Anatomical and Functional Specializations. *The Journal of Neuroscience*, 27(38):10259–10269, 2007.

R. Toro and Y. Burnod. Geometric atlas: modeling the cortex as an organized surface. *NeuroImage*, 20(3):1468–1484, 2003.

D. Tosun, M.E. Rettmann, X. Han, X. Tao, C. Xu, S.M. Resnick, D.L. Pham, and J.L. Prince. Cortical surface segmentation and mapping. *NeuroImage*, 23:S108–S118, 2004.

R. Trampel, D. Ott, and R. Turner. Do the congenitally blind have a stria of gennari? first intracortical insights in vivo. *Cerebral Cortex*, 21(9):2075–2081, 2011.

R. Trampel, P.-L. Bazin, A. Schäfer, R. Heidemann, D. Ivanov, G. Lohmann, S. Geyer, and R. Turner. Laminar-specific BOLD fingerprints of sensorimotor areas during imagined and actual finger tapping. *Proceedings of the 18th Annual Meeting of the Organization for Human Brain Mapping*, 2012.

R Turner. Neuroscientific applications of high-field MRI in humans. In *High-Field MR Imaging*, pages 137–149. Springer, 2012.

R. Turner. MRI methods for in-vivo cortical parcellation. In *Microstructural Parcellation of the Human Cerebral Cortex*, pages 197–220. Springer, 2013.

R. Turner, A.-M. Oros-Peusquens, S. Romanzetti, K. Zilles, and N.J. Shah. Optimised in vivo visualisation of cortical structures in the human brain at 3 T using IR-TSE. *Magnetic Resonance Imaging*, 26(7):935–942, 2008.

M. Vaillant and C. Davatzikos. Finding parametric representations of the cortical sulci using an active contour model. *Medical Image Analysis*, 1(4):295–315, 1997.

P.F. Van de Moortele, E.J. Auerbach, C. Olman, E. Yacoub, K. Ugurbil, and S. Moeller. Unbiased high resolution T1 weighted brain images at high field with a new interleaved 3D-MPRAGE/proton density GE sequence. *Proceedings of the 14th Annual Meeting of the Organization for Human Brain Mapping*, 2008.

P.F. Van de Moortele, E.J. Auerbach, C. Olman, E. Yacoub, K. Ugurbil, and S. Moeller. T1 weighted brain images at 7 Tesla unbiased for proton density, T_2^* contrast and RF coil receive B_1 sensitivity with simultaneous vessel visualization. *NeuroImage*, 46(2):432–446, 2009.

D.C. Van Essen. A tension-based theory of morphogenesis and compact wiring in the central nervous system. *Nature*, 385:313–318, 1997.

D.C. Van Essen and D.L. Dierker. Surface-Based and Probabilistic Atlases of Primate Cerebral Cortex. *Neuron*, 56(2):209–225, 2007. ISSN 0896-6273.

C. van Swam, A. Federspiel, D. Hubl, R. Wiest, C. Boesch, P. Vermathen, R. Kreis, W. Strik, and T. Dierks. Possible dysregulation of cortical plasticity in auditory verbal hallucinations: A cortical thickness study in schizophrenia. *Journal of Psychiatric Research*, 46(8):1015–1023, 2012.

V. Vapnik. Pattern recognition using generalized portrait method. *Automation and Remote Control*, 24:774–780, 1963.

V. Vapnik and A.J. Chervonenkis. On the one class of the algorithms of pattern recognition. *Automation and Remote Control*, 25(6), 1964.

T. Vercauteren, X. Pennec, A. Perchant, and N. Ayache. Diffeomorphic demons: Efficient non-parametric image registration. *NeuroImage*, 45(1):S61–S72, 2009.

C. Vogt and O. Vogt. Allgemeinere Ergebnisse unserer Hirnforschung. Erste Mitteilung. Ziele und Wege unserer Hirnforschung. *Journal für Psychologie und Neurologie*, 25:281–291, 1919a.

C. Vogt and O. Vogt. Allgemeinere Ergebnisse unserer Hirnforschung. Zweite Mitteilung. Das Wesen der topischen architektonischen Differenzen des Cortex cerebri. *Journal für Psychologie und Neurologie*, 25:292–360, 1919b.

C. Vogt and O. Vogt. Allgemeinere Ergebnisse unserer Hirnforschung. Dritte Mitteilung. Die architektonische Rindenfelderung im Lichte unserer neuesten Forschungen. *Journal für Psychologie und Neurologie*, 25:361–398, 1919c.

O. Vogt. Die myeloarchitektonische Felderung des menschlichen Stirnhirns. *Journal für Psychologie und Neurologie*, 15(4/5):221–232, 1910.

O. Vogt. Furchenbildung und architektonische Rindenfelderung. *Journal für Psychologie und Neurologie*, 29:438–439, 1923.

C. von Economo and G.N. Koskinas. *Die Cytoarchitektonik der Hirnrinde des Erwachsenen Menschen*. Textband und Atlas. Wien und Berlin, 1925.

M. Waehnert, M. Weiss, M. Streicher, P.-L. Bazin, S. Geyer, and R. Turner. Do cortical layers conform to the laplace equation? *Proceedings of the 18th Annual Meeting of the Organization for Human Brain Mapping*, 2012.

M. Waehnert, J. Dinse, C. Tardif, A. Schäfer, S. Geyer, P. Bazin, and R. Turner. How Much Resolution Is Needed for in-vivo Analysis of Cortical Myeloarchitecture? *Proceedings of the 21th Annual Meeting of the International Society for Magnetic Resonance in Medicine*, 2013a.

M. Waehnert, J. Dinse, C. Tardif, A. Schäfer, S. Geyer, P.-L. Bazin, and R. Turner. Identifying heavily myelinated areas of the cortex using subject-specific cortical profiles of T1. *Proceedings of the 19th Annual Meeting of the Organization for Human Brain Mapping*, 2013b.

M.D. Waehnert, J. Dinse, M. Weiss, M.N. Streicher, P. Waehnert, S. Geyer, R. Turner, and P.-L. Bazin. Anatomically motivated modeling of cortical laminae. *NeuroImage*, 93(2):210–220, 2013c. ISSN 1053-8119.

G. Wagenknecht and S. Winter. Volume-of-interest segmentation of cortical regions for multimodal brain analysis. In *Nuclear Science Symposium Conference Record, 2008. IEEE*, pages 4368–4372. IEEE, 2008.

N.B. Walters, G.F. Egan, J.J. Kril, M. Kean, P. Waley, M. Jenkinson, and J.D.G. Watson. In vivo identification of human cortical areas using high-resolution MRI: an approach to cerebral structure–function correlation. *Proceedings of the National Academy of Sciences*, 100(5):2981–2986, 2003.

N.B. Walters, S.B. Eickhoff, A. Schleicher, K. Zilles, K. Amunts, G.F. Egan, and J.D.G. Watson. Observer-Independent Analysis of High-Resolution MR Images of the Human Cerebral Cortex: In Vivo Delineation of Cortical Areas. *Human Brain Mapping*, 28(1):1–8, 2007.

J.P. Wansapura, S.K. Holland, R.S. Dunn, and W.S. Ball. NMR relaxation times in the human brain at 3.0 Tesla. *Journal of Magnetic Resonance Imaging*, 9(4):531–538, 1999.

E. Waters and S. Wickline. Contrast agents for MRI. *Basic Research in Cardiology*, 103(2):114–121, 2008.

N. Weiskopf, J. Suckling, G. Williams, M.M. Correia, B. Inkster, R. Tait, C. Ooi, E.T. Bullmore, and A. Lutti. Quantitative multi-parameter mapping of R1, PD*, MT, and R_2^* at 3T: a multi-center validation. *Frontiers in Neuroscience*, 7, 2013.

B. Widrow. The "rubber-mask" technique - I. Pattern measurement and analysis. *Pattern Recognition*, 5(3):175–197, 1973a.

B. Widrow. The "rubber-mask" technique - II. pattern storage and recognition. *Pattern Recognition*, 5(3):199–211, 1973b.

G. Wig, T. Laumann, and S. Petersen. An approach for parcellating human cortical areas using resting-state correlations. *NeuroImage*, 93:276–291, 2014.

H. Wilms, L. Zecca, P. Rosenstiel, J. Sievers, G. Deuschl, and R. Lucius. Inflammation in Parkinson's diseases and other neurodegenerative diseases: cause and therapeutic implications. *Current Pharmaceutical Design*, 13(18):1925–1928, 2007.

A. Worth, C. Haselgrove, and D. Kennedy. The Internet Brain Segmentation Repository (IBSR) on NITRC. November 1996. URL http://www.nitrc.org/projects/ibsr/.

P.J. Wright, O.E. Mougin, J.J. Totman, A.M. Peters, M.J. Brookes, R. Coxon, P.E. Morris, M. Clemence, S.T. Francis, R.W Bowtell, and P.A. Gowland. Water proton T1 measurements in brain tissue at 7, 3, and 1.5 T using IR-EPI, IR-TSE, and MPRAGE: results and optimization. *Magnetic Resonance Materials in Physics, Biology and Medicine*, 21(1-2):121–130, 2008.

C. Xu and J.L. Prince. Generalized gradient vector flow external forces for active contours. *Signal processing*, 71(2):131–139, 1998a.

C. Xu and J.L. Prince. Snakes, shapes, and gradient vector flow. *Image Processing, IEEE Transactions on*, 7(3):359–369, 1998b.

C. Xu, D.L. Pham, and J.L. Prince. *Medical Image Segmentation using Deformable Models*, chapter 6.

C. Xu, D.L. Pham, and J.L. Prince. Image segmentation using deformable models. *Handbook of Medical Imaging*, 2:129–174, 2000.

L. Yang, J. Effler, B. Kutscher, S. Sullivan, D. Robinson, and P. Iglesias. Modeling cellular deformations using the level set formalism. *BMC Systems Biology*, 2(1): 68, 2008.

J.D. Yeatman, B.A. Wandell, and A.A. Mezer. Lifespan maturation and degeneration of human brain white matter. *Nature Communications*, 5, 2014.

B. Yeo, F. Krienen, J. Sepulcre, M. Sabuncu, D. Lashkari, M. Hollinshead, J. Roffman, J. Smoller, L. Zöllei, J. Polimeni, B. Fischl, H. Liu, and L. Buckner. The organization of the human cerebral cortex estimated by intrinsic functional connectivity. *Journal of neurophysiology*, 106(3):1125–1165, 2011.

A. Yezzi and J.L. Prince. An Eulerian PDE approach for computing tissue thickness. *IEEE Transactions on Medical Imaging*, 22(10):1332–1339, 2003.

X. Zeng, L.H. Staib, R.T. Schultz, H. Tagare, L. Win, and J.S. Duncan. A new approach to 3D sulcal ribbon finding from MR images. In *Medical Image Computing and Computer-Assisted Intervention–MICCAI'99*, pages 148–157. Springer, 1999.

D. Zhang, L. Guo, G. Li, J. Nie, F. Deng, K. Li, X. Hu, T. Zhang, X. Jiang, D. Zhu, Z. Qun, and T. Liu. Automatic cortical surface parcellation based on fiber density information. In *Proceedings of the 2010 IEEE international Conference on Biomedical Imaging: from nano to macro*, pages 1133–1136. IEEE Press, 2010.

Y. Zhou, P. Thompson, and A. Toga. Extracting and representing the cortical sulci. *Computer Graphics and Applications, IEEE*, 19(3):49–55, 1999.

J. Zimmermann, R. Goebel, F. De Martino, P.-F. van de Moortele, D. Feinberg, G. Adriany, D. Chaimow, A. Shmuel, K. Ugurbil, and E. Yacoub. Mapping the Organization of Axis of Motion Selective Features in Human Area MT Using High-Field fMRI. *PLoS ONE*, 6(12):e28716, 2011.